Spring 1-1-2010

Earth's Outer Radiation Belt Electrons: Identifying Sources, Improving Forecasts, and a New Particle Detector Design

Drew Lawson Turner
turnerd@colorado.edu

Earth's Outer Radiation Belt Electrons: Identifying Sources, Improving Forecasts, and a New Particle Detector Design

by

Drew L. Turner

B.S., Embry-Riddle Aeronautical University, 2005

M.S., University of Colorado, 2008

A thesis submitted to the

Faculty of the Graduate School of the

University of Colorado in partial fulfillment

of the requirements for the degree of

Doctor of Philosophy

Department of Aerospace Engineering Sciences

2010

This thesis entitled:
Earth's Outer Radiation Belt Electrons: Identifying Sources, Improving Forecasts, and a New Particle Detector Design
written by Drew L. Turner
has been approved for the Department of Aerospace Engineering Sciences

_____
Xinlin Li

_____
Prof. Fran Bagenal

_____
Prof. Dan Baker

_____
Dr. Scot Elkington

_____
Prof. Scott Palo

Date _____

The final copy of this thesis has been examined by the signatories, and we find that both the content and the form meet acceptable presentation standards of scholarly work in the above mentioned discipline.

Turner, Drew L. (Ph.D., Aerospace Engineering Sciences)

Earth's Outer Radiation Belt Electrons: Identifying Sources, Improving Forecasts, and a New Particle Detector Design

Thesis directed by Prof. Xinlin Li

Earth's outer radiation belt is a highly dynamic region composed primarily of relativistic electrons, which can pose a threat to spacecraft and astronauts. Despite decades of acquiring data and conducting research, the exact mechanisms and relative importance of outer belt electron source, loss, and transport processes are still not fully understood. Here, I follow the full cycle of outer belt electron data, from acquiring it in situ to analysis and practical use. I start by discussing a new instrument designed to measure relativistic particles from a low-cost picosatellite in low-Earth orbit, which will provide complementary data to NASA's Radiation Belt Storm Probes mission. Next, I discuss data analysis studies of the source of relativistic electrons in the outer belt conducted using electron data from existing instruments. I provide a detailed discussion of the results of these studies, which reveal clear evidence that there are two distinct populations of electrons in the outer belt, each with a different source region: 1) low-energy electrons with energy below a few hundred keV and source in the magnetotail, and 2) relativistic electrons with energy greater than around 500 keV that most often have a source within geosynchronous orbit. These results indicate the importance of substorms and wave-particle interactions for the acceleration of relativistic electrons. I finish with the details of an improved forecast system for these electrons, which demonstrates how outer belt electron data are used for practical applications.

Dedication

For always encouraging me to follow my dreams, I dedicate this work to my parents, Fran and Larry Turner.

Acknowledgements

First and foremost, I thank my advisor, Professor Xinlin Li. Xinlin has proven to be an ideal advisor. He encouraged me to complete my course requirements early to allow me to focus more on my research, and he has always been available to approach for advice on any topic. He has remained open to new ideas and together we have worked through the various research I describe here. I am forever indebted to Xinlin for his excellent tutelage, which has truly opened the doors for my future career. I want to next thank my PhD committee. I have had experience with and advice from each of you throughout my time at CU, and I am honored to have such a prestigious committee. There are too many people to thank individually from both the ASEN department and LASP, but I want to express my thanks for how supportive both institutions are to their graduate students. LASP, in particular, has been an incredible place to work. It is phenomenal to have so many researchers from a variety of specialties within space physics all so accessible and nearby. For example, my work has benefitted greatly from the knowledgeable input and support from Edward Burin des Roziers, James McCollough, Steve Monk, and Stefan Erikson, and I would be next to nowhere today without the advice and support from my colleague and friend, Weichao Tu. I want to thank Quintin Schiller for his enthusiasm and thirst for knowledge; his many questions on the magnetosphere, Sun, and solar wind have really helped to reinforce my own understanding. Last, but not least, I want to express how grateful I am to my family, friends, and fiance, Missy, who never fail to provide emotional and personal support.

Contents

Chapter

Tables

Table

Figures

Figure

Chapter 1

Introduction

Earth's magnetosphere is a highly dynamic and complex system consisting of a central, internally generated magnetic field, several distinct plasma regions, and a series of particle populations that form current systems and thus alter the magnetic topology. Much of this system's complexity arises from the fact that Earth's magnetic field also interacts with the Sun's interplanetary magnetic field (IMF) and turbulent solar wind, which act as primary drivers of magnetospheric weather. As humans continue to explore space and become more and more dependent on space based platforms, primarily for communication, navigation, defense, and scientific purposes, the ability to understand and forecast this complex solar-terrestrial weather system becomes increasingly more important.

Of particular interest in the magnetosphere is the outer radiation belt, a population of mostly electrons with energies that range from hundreds of keV up to several MeV and fluxes that can fluctuate by orders of magnitude in a matter of minutes. This belt, located equatorially around 3-7 Earth radii, encompasses a vast region of space that is used by a great number of spacecraft, particularly many of those for communication, navigation, and terrestrial weather monitoring, and these energetic electrons can pose a significant threat by way of deep dielectric charging of spacecraft electronics. Despite decades of research, the true nature of these outer belt electrons, namely all of their source, loss, and transport mechanisms and their relative importance under different conditions, continues to be intriguing to scientists.

This thesis is concerned with the relativistic electron data process, from making in-situ measurements, to developing a better understanding of the system through data analysis, and using

that better understanding to develop more accurate system models. Throughout, the underlying focus is primarily on the following question: what is the source of electrons in the outer radiation belt and how does this source become energized to relativistic energies? I begin with a chapter providing a detailed introduction to particles in the magnetosphere with particular emphasis on the outer radiation belt electrons. A discussion of the current understanding of the nature of the outer belt electrons follows, and this leads into the importance of radiation belt observations and model development. Next, I introduce the importance and difficulty of making accurate measurements of relativistic particles, with an overview of several spacecraft missions that have provided radiation belt datasets and the instruments used to do so. A brief review of some of the more successful radiation belt models, many of which I refer to throughout the thesis, finishes up Chapter 2, and overall, this introduction should provide an adequate summary of the background necessary to fully understand my work, which is presented in the subsequent chapters.

In Chapter 3, I introduce the Relativistic Electron and Proton Telescope integrated little experiment (REPTile) instrument, which has been designed for the Colorado Student Space Weather Experiment (CSSWE) CubeSat mission. REPTile will measure outer radiation belt electrons and solar energetic protons from a highly-inclined low-Earth orbit. I discuss my work on the instrument design, which accounts for electron scattering and noise from shield-penetrating protons. I also stress the significance of the CSSWE CubeSat mission, which will prove scientifically complementary for NASA's Radiation Belt Storm Probes mission. Multi-point measurements of the outer belt electrons are critical to addressing the question of source and energization as well as understanding loss and transport processes, and the CSSWE mission is a clear example of how small, relatively simple and inexpensive spacecraft can be employed for valuable science and to complement larger and much more complex and expensive space missions.

Chapters 4 and 5 present studies on outer belt electron phase space density radial gradients and the population near the belt's outer boundary. These studies provide insight into the source regions for the outer belt electrons and the conditions under which different acceleration mechanisms are dominant. I find that the outer belt consists of two distinct populations of electrons, those with

energy below a few hundred keV at geosynchronous orbit (GEO) with a source in the plasma sheet and the relativistic population with its primary source internal to the belt inside of GEO. This study also reveals the importance of substorms and enhanced convection to outer belt dynamics, particularly internal acceleration of electrons to relativistic energies.

Concerning the practical application of outer belt data, I discuss my work on relativistic electron forecasting at GEO in Chapters 6 and 7. I describe several forecast models that I have developed, one of which operates independent of any solar wind inputs and another that includes an internal source that is a function of the AL index. This model with a source term reflects the results from 4, and its strong performance further exemplifies the importance of internal acceleration processes to relativistic electrons in the outer belt. I also present an innovative technique to estimate solar wind speed several days in advance, which I show can be used to extend solar wind based space weather forecasts. I finish with an introduction to a new and improved system of forecasts for relativistic electrons at GEO that includes a tool to forecast electron fluxes at a local hour resolution around GEO. This accounts for the range of fluxes observed around GEO, which has not been done before. This system is currently operational and running in real-time.

Chapter 8 summarizes my conclusions from this work and also discusses potential extensions to several of the studies as well as my plans for additional studies in the future. The appendices cover additional work from several of the chapters and also a study on an interesting magnetopause disturbance event that I have conducted, which fits outside of the scope of Earth's outer radiation belt electrons.

Chapter 2

Relevant Background

2.1 Particles in Earth's Magnetosphere

Earth's magnetosphere is a massive cavity that the magnetic field generated inside the Earth has carved out of the surrounding space, which is dominated by solar wind plasma and the IMF. The outer boundary of this cavity is called the magnetopause, and its location is determined by the balance of the solar wind dynamic pressure and the magnetosphere's magnetic pressure. From this balance, Earth's magnetic field, which is intrinsically dipolar, is distorted; it is compressed by the solar wind on the dayside and stretched out on the nightside. The magnetopause is not a solid boundary. It is quite dynamic, and though it deflects 99.5% of the mass and energy incident upon it, it does allow solar wind particles to leak in at certain places (i.e. the cusps and flanks) [*Tascione*, 1988].

Many of the particles in the magnetosphere belong to distinct current systems, but for a discussion of the radiation belts, it is most important to understand how individual particles behave in the magnetosphere. The behavior of energetic, charged particles in electric and magnetic fields is described by the Lorentz force law:

$$\frac{d\mathbf{p}}{dt} = q\gamma\left(\mathbf{E} + \mathbf{v} \times \mathbf{B}\right) \tag{2.1}$$

where $\mathbf{p}$ is relativistic momentum, q is particle charge, $\gamma = \left(1 - \left(\frac{v}{c}\right)^2\right)^{-\frac{1}{2}}$ is the relativistic Lorentz factor with v being the particle speed and c the speed of light, $\mathbf{E}$ is the local electric field, $\mathbf{v}$ is the particle's velocity vector, and $\mathbf{B}$ the local magnetic field. It is this law that is used to show

how charged particles can be trapped, or "bottled", in a non-uniform magnetic field like that of a magnetic dipole. Once trapped in Earth's quasi-dipolar field, charged particles undergo three types of motion: 1) gyration (gyro-motion) about a field line, 2) bounce along field lines between magnetic mirror points, which are determined by a particle's energy and velocity parallel to the field, and 3) azimuthal drift perpendicular to field lines and around the entire system. The gyro-motion simply occurs when a particle's velocity vector has some perpendicular component to the local magnetic field vector, and a $\mathbf{v} \times \mathbf{B}$ force results in the particle gyrating about the field line. If the particle's velocity vector also has a parallel component to the local field vector, the gyrating particle will also travel along the field line. Particles drift due to the field configuration and $\mathbf{F} \times \mathbf{B}$ velocities for any external force $\mathbf{F}$ (discussed further below). See Figure 2.1 for a cartoon depicting these motions and Figures 2.9 and 2.10 for simulation results showing how these motions can trap protons and electrons in the inner and outer radiation belts.

It is important here to introduce the three adiabatic invariants of charged particles in the magnetosphere. Each of these parameters is associated with one of the three types of motion introduced above, and these remain constant for a particle so long as changes in the field occur on timescales greater than the timescale of the associated motion. The first adiabatic invariant is the magnetic moment, μ. A magnetic moment is defined for any current loop, and its value is the product of the current itself and the area of the loop. So μ for a charged particle gyrating about a magnetic field line is:

$$\mu = \frac{qv_\perp}{2\pi r_c} \cdot \pi r_c^2 = \frac{qv_\perp}{2} \cdot \frac{mv_\perp}{qB} = \frac{m\left(v \sin\alpha\right)^2}{2B} \tag{2.2}$$

where m is the particle mass, v is the particle velocity, α is the pitch angle between the velocity and magnetic field vectors, and B is the local magnetic field strength. Equation 2.2 starts with the current created by the gyrating particle multiplied by the area of its current loop then goes on to replace the gyro-radius, r_c, with its form derived from the balance of the centripetal force to the Lorentz force to develop the final (rightmost) form of μ. So, if the magnetic field is not changing faster than a gyro-period, then μ is conserved. It is important to note that M is often used to

symbolize the first adiabatic invariant of relativistic particles, but throughout this work, only μ is used. Now going back to the particle motion, as a gyrating particle travels along a field line away from the equator, the magnetic field it encounters gets stronger. Since μ is conserved, as B increases the pitch angle must also increase. If the pitch angle increases to 90° before the particle encounters the upper atmosphere (where it would be lost due to collisions), the particle's motion along the field line stops and the particle is reflected back toward the equator. This point in a particle's trapped trajectory is called a mirror point, and it will encounter these mirror points in both the northern and southern hemispheres, which leads to the bounce motion of the particle. The invariant associated with the bounce motion is J, which is the integral of the parallel momentum over one bounce between mirror points. From J, one can also derive another parameter, denoted K, used often when discussing the second adiabatic invariant. K is related to both J and μ and remains invariant so long as they do [see *Green and Kivelson*, 2004, Appendix A].

Drift motion is primarily a result of two mechanisms. The first is that when a particle is closest to Earth in its gyration about a field line, it encounters a stronger field than that at its farthest point from Earth. Since r_c is inversely proportional to B, the gyro-radius is going to change slightly during a particle's gyro-motion: it will be smaller when B is stronger and larger when B is weaker. This results in what is known as gradient-B drift. The second mechanism is that since a field line is curved, a particle "feels" a centrifugal force. The particle reacts to this force by drifting perpendicular to the field line in such a way that the perpendicular component of the electric field, or $\frac{F}{q}$, goes to zero in the electron's rest frame. These two drifts together are the primary cause of particle longitudinal drift in the magnetosphere, which is referred to as gradient-curvature drift, but any other external force or electric field will also cause drift. The third and last adiabatic invariant is the flux invariant (denoted with Φ) which states that the total geomagnetic flux enclosed by a drift orbit is constant so long as the magnetic field is not changing on timescales faster than a drift period. Figure 2.1 depicts the three characteristic particle motions associated with the adiabatic invariants, and this discussion of particle motions and adiabatic invariants is fully described in texts by *Hargreaves* [1992] and *Kivelson and Russell* [1995].

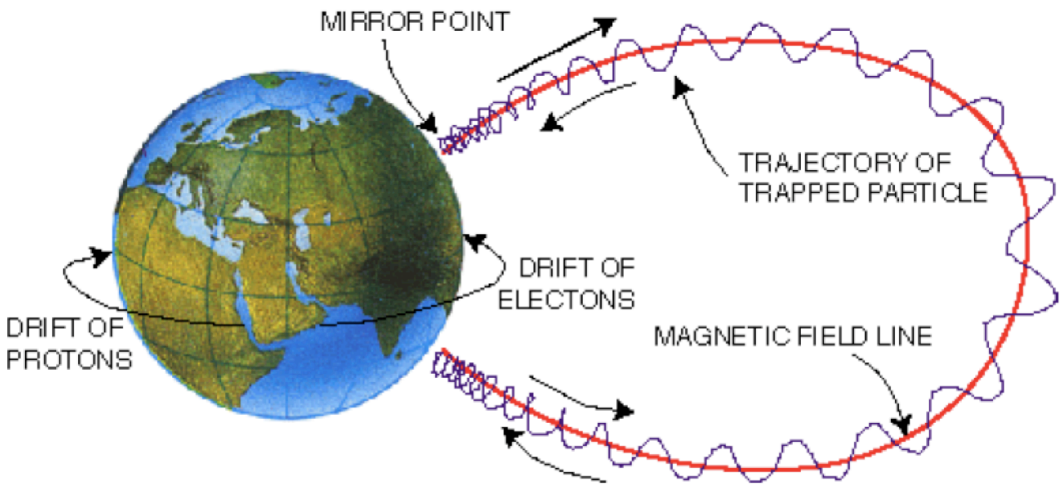

Figure 2.1: Cartoon depicting the three characteristic motions associated with energetic charged particles trapped in Earth's magnetosphere. From *Stern and Ness* [1981].

McIlwain [1961] introduced the L parameter to magnetospheric physics. The L parameter is defined as the distance from the center of the Earth to a field line at its equatorial crossing point in a dipole magnetic field. It is measured in units of Earth radii, R_E, and given the geometry of the magnetosphere and that particles bounce along field lines, it is useful for describing particle locations. McIlwain-L can also be used to define invariant latitude, which is the latitude where a field line intersects the surface of the Earth [*Kivelson and Russell*, 1995, pg 166]. *Roederer* [1970] defined another L parameter, L^*. L^* is directly related to the third adiabatic invariant and is often used analogously to it. This parameter describes the radial distance to a field line's equatorial crossing point if all external magnetic fields were slowly turned off leaving only Earth's internal dipole field [*Green and Kivelson*, 2004].

Schulz and Lanzerotti [1974] went into great detail discussing various forms of the Fokker-Planck equation, which is the governing equation of particle distributions, and how it applies to particle diffusion in the radiation belts. The general Fokker-Planck equation is:

$$\frac{\partial f}{\partial t} + \sum_i \frac{\partial}{\partial J_i}\left[\left(\frac{dJ_i}{dt}\right) f\right] = \sum_{i,j} \frac{\partial}{\partial J_i}\left(D_{ij}\frac{\partial f}{\partial J_j}\right) - \frac{f}{\tau} + S \tag{2.3}$$

where f is the particle distribution function, or phase space density (PSD), J are the fundamental action integrals (related to the adiabatic invariants), the first term on the left side is just the PSD time rate of change, the second term represents coherent terms, like friction, the first term on the right side represents diffusion, the second is loss, and the last is source. When one is concerned primarily with radial diffusion, as is the case for many radiation belt investigations, Equation 2.3 simplifies to:

$$\frac{\partial f}{\partial t} = L^2 \frac{\partial}{\partial L}\left(\frac{D_{LL}}{L^2}\frac{\partial f}{\partial L}\right) - \frac{f}{\tau} \tag{2.4}$$

where L in this equation is the invariant L^* parameter, D_{LL} is the diffusion coefficient, and τ is a loss timescale. Diffusion acts by smoothing out gradients in PSD. Finally, PSD is used in radiation belt studies primarily because of the implications of Liouville's theorem, which shows that a phase space volume (consisting of both position and velocity space) containing a particular density of particles moves incompressibly through phase space [the entire paragraph above is in reference to:

Schulz and Lanzerotti, 1974]. This is important in that the phase space density remains constant along a particle trajectory.

2.2 The Outer Radiation Belt

In 1958, *Explorer 1* was the first satellite launched into orbit by the United States of America. It was put into an elliptical orbit and its instrumentation consisted of a Geiger counter, which allowed it to take measurements of the radiation environment around the Earth. It was from these measurements (and also measurements from following missions) that James Van Allen discovered that there were two distinct belts of highly energetic particles around the Earth, which are separated by a region of lower particle densities called the slot [*Kivelson and Russell*, 1995]. The inner radiation belt, at around L = 1.2 - 2.5, consists primarily of high energy protons (E > 100 MeV), and this belt is relatively stable. Its source is thought to be the decay of energetic neutrons produced by the interaction of cosmic rays with the atmosphere. The outer belt, consisting mostly of energetic electrons (E from 100's keV to 10's MeV) with a total system energy ranging from $10^{10} \sim 10^{13}$ J ($10^{23} \sim 10^{26}$ MeV) [*Baker et al.*, 1998c], is much more dynamic. Figure 2.2 shows SAMPEX electron fluxes for more than a full solar cycle (> 11 years). Notice how both the inner and outer boundaries are not rigid in L but quite jagged. Also, note the flux variation seen at various timescales, particularly near the heart of the belt at L $\sim$ 4. To give some sense of just how energetic these electrons are, a 1 MeV electron with an equatorial pitch angle of 60° near geosynchronous orbit (GEO) has a gyro-period of 10^{-3} seconds, a bounce period of 10^{0} seconds, and a drift period of 10^{3} seconds [*Li and Temerin*, 2001]. This example electron is moving near the speed of light; it travels around the planet, at a radial distance of 6.6 R_E, in less than 20 minutes.

Two sources provide the electrons that feed the outer belt: electrons from 1) the solar wind and 2) Earth's ionosphere [*Li and Temerin*, 2001]. However, neither of these sources is energetic enough to account for the energies of electrons in the outer belt; solar wind electrons are on the order of 10 eV while ionospheric electrons are on the order of 1 eV. So, some acceleration mechanism (or mechanisms) is active in the magnetosphere itself and is responsible for energizing the electrons

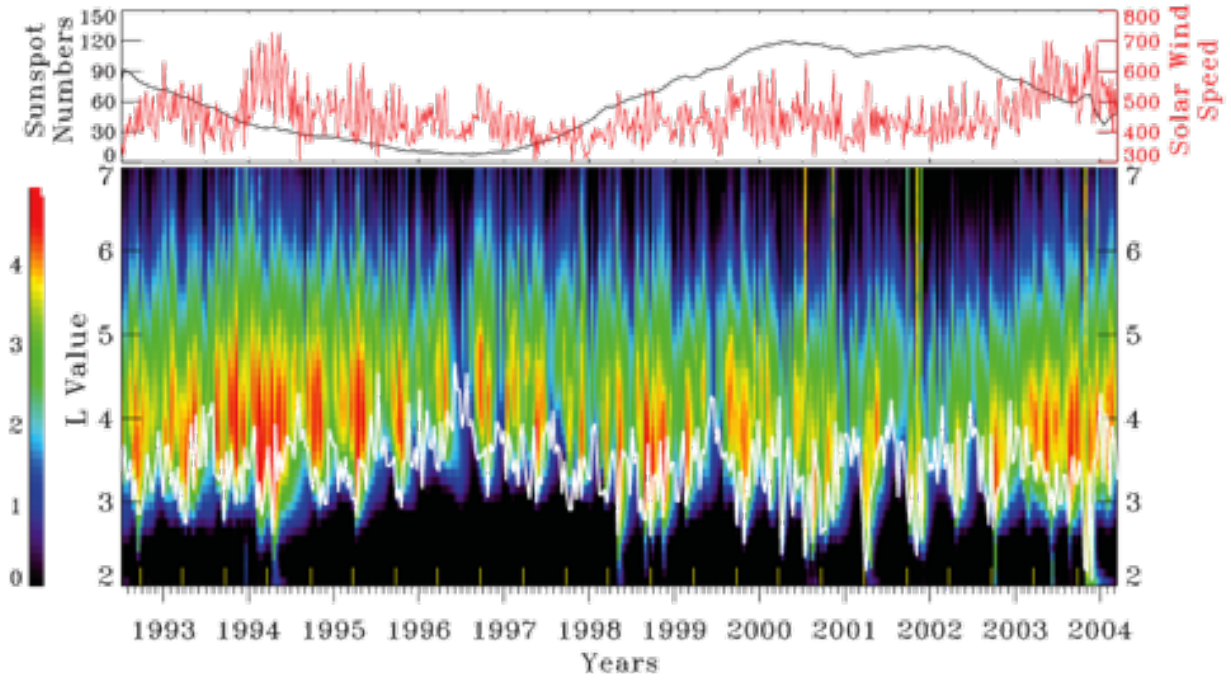

Figure 2.2: Figure 1 from *Li et al.* [2006]. Top: Yearly window-averaged sunspot numbers in black and weekly window-averaged solar wind speed (units km/s) in red. Bottom: Monthly window-averaged SAMPEX electron fluxes (units $cm^{-2}s^{-1}sr^{-1}$) from its launch in on 3 July 1992 to 2004. Logarithm of flux is shown in color and is binned by McIlwain-L. The white curve superimposed is every 10-days minimum plasmapause location determined with an empirical model.

by up to seven orders of magnitude.

Flux variations in the outer belt have been related to both changes in the solar wind [e.g. *Paulikas and Blake*, 1979; *Baker et al.*, 1979; *Baker*, 1996; *Li et al.*, 2001a] and geomagnetic activity [e.g. *Reeves*, 1998; *Rostoker et al.*, 1998; *Reeves et al.*, 2003]. These variations can be quite extreme, with fluxes increasing or decreasing by 1 to 2 orders of magnitude in a matter of hours [*Friedel et al.*, 2002]. Based on an extensive study of 276 geomagnetic storms,*Reeves et al.* [2003] found that surprisingly, only about half of all storms result in a net flux increase of relativistic electrons, about a fifth result in a net loss, and the rest result in no net change in flux. This is indicative of the complex nature of relativistic electron acceleration and loss, which has continued to puzzle researchers. *Reeves et al.* [2003] went on to describe the effect of geomagnetic storms on relativistic electrons as "a delicate and complicated balance between the effects of particle acceleration and loss." Figure 2.3 is a cartoon summarizing many of these complex acceleration, loss, and transport processes with their approximate locations in the magnetosphere. Many of these processes will be discussed in the following section.

2.3 Acceleration, Loss, and Transport of Relativistic Electrons

2.3.1 Acceleration

Flux enhancement events of radiation belt electrons are often associated with fast solar wind streams [*Paulikas and Blake*, 1979; *Baker et al.*, 1979] and coronal mass ejections [*Baker et al.*, 1998b] impinging on the Earth's magnetosphere and also with the geomagnetic storms associated with these events [e.g. *Reeves et al.*, 2003]. It is well accepted that the solar wind is the driving force of electron acceleration [e.g. *Baker et al.*, 1998b], but it is complex processes, internal to the magnetosphere, that are directly responsible for electron energization. In addition to the solar wind driving, it is also known that at a given location, electron enhancements at different energies are observed to occur usually with successively longer delays for higher energy: lower energy electron fluxes increase first, then higher energy electrons [*Li et al.*, 2005; *Turner and Li*, 2008a]. This

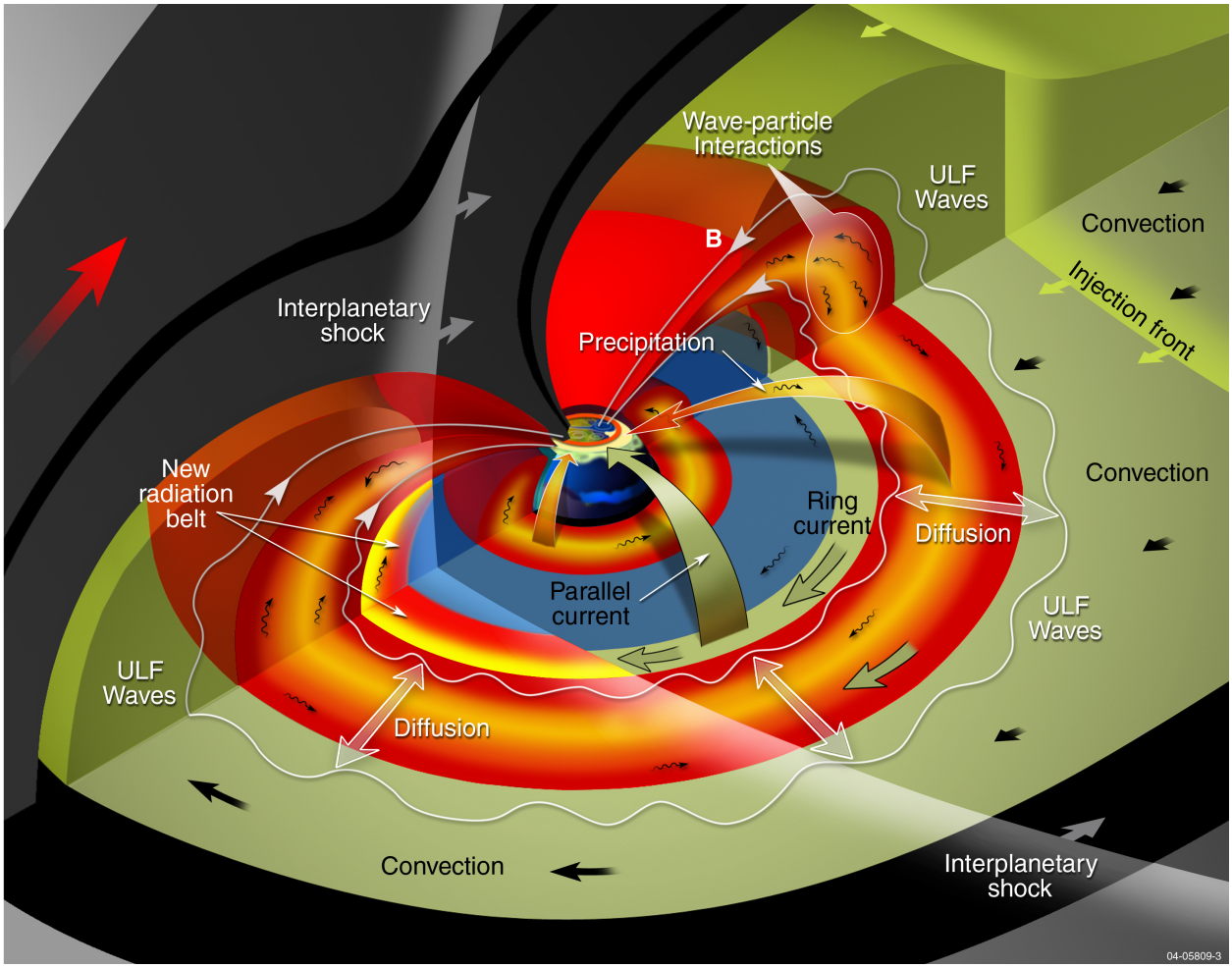

Figure 2.3: Image from RBSP's homepage at: http://rbsp.jhuapl.edu/gallery/artist.php. A cartoon of Earth's magnetosphere displaying many of the processes that have been identified as important to radiation belt dynamics.

energy delay for flux enhancements indicates that the source of the radiation belt electrons is low energy electrons within the magnetosphere, which agrees with the results of *Li et al.* [1997], and that the acceleration mechanism takes some time to occur. These two relations are important both for the following discussion about acceleration and for the forecast models described in Chapters 6 and 7.

Several theories for energizing outer radiation belt electrons have been proposed that involve breaking one or more of the electrons' adiabatic invariants. These theories can be categorized into two classes: 1) inward radial transport and 2) in situ acceleration. The inward radial transport theory says that radial diffusion/transport energizes electrons when the third adiabatic invariant is broken allowing less-energetic electrons to diffuse inward from higher L-shells, assuming that there is a continual supply of these electrons in the outer magnetosphere and that they have higher phase space density than electrons with the same first and second adiabatic invariants closer to Earth. Energization occurs since this process conserves the particles' first adiabatic invariants, and when the magnetic field becomes stronger as they diffuse in towards Earth, their momentum, and thus their kinetic energy, must increase to conserve μ. Early work in this area focused primarily on inward radial diffusion and was conducted by *Fälthammar* [1965] and *Schulz and Lanzerotti* [1974]. More recent studies show that this process can be enhanced by elevated fluctuations in magnetospheric electric and magnetic fields with frequencies comparable to the electrons' drift frequencies (in mHz range) [*Rostoker et al.*, 1998; *Elkington et al.*, 1999; *Hudson et al.*, 2000; *O'Brien et al.*, 2001, 2003; *Mann et al.*, 2004; *Sarris et al.*, 2006] and by enhanced inductive electric fields due to a strong interplanetary shock impacting the magnetosphere [*Li et al.*, 1993, 2003; *Gannon et al.*, 2005]. The former is usually referred to as enhanced radial diffusion, and the latter as sharp solar wind pressure enhancement-associated acceleration and transport, which occurs on fast time scales, with the whole energization process occurring on a time scale of less than the particle's drift period.

In situ acceleration occurs by violating the first and second adiabatic invariants of less-energetic electrons, and electron energization can be realized locally via wave-particle interactions in the inner magnetosphere. Both theory and model results show that the waves that are particularly

adept at accelerating a source population of electrons up to outer belt energies of hundreds of keV to MeV are whistler mode chorus [*Temerin et al.*, 1994; *Horne and Thorne*, 1998; *Summers et al.*, 1998; *Roth et al.*, 1999b; *Meredith et al.*, 2002; *Bortnik and Thorne*, 2007] and fast magnetosonic waves [*Horne et al.*, 2007; *Meredith et al.*, 2008].

Concerning whistler-mode chorus, *Horne and Thorne* [1998] showed that chorus waves could interact with electrons from a wide range of energy levels via Doppler-shifted cyclotron resonance and that it is theoretically possible to accelerate these seed populations up to relativistic (MeV) energies. *Bortnik and Thorne* [2007] provided a brief review of chorus' role in Earth's outer radiation belt dynamics and also defined an "anchor point" at a few hundred keV above which chorus tends to accelerate electrons and below which it tends to cause electrons to precipitate and be lost to the atmosphere. This is in accordance with *Summers et al.* [1998] and *Meredith et al.* [2002], who found that a seed population of electrons with energies of a few 100 keV can be significantly energized by interactions with chorus waves. Gyro- (or cyclotron) resonant wave-particle interactions satisfy the following condition:

$$\omega - k_{\|} v_{\|} + \frac{n|\Omega_e|}{\gamma} = 0 \tag{2.5}$$

where ω is the Doppler-shifted wave frequency, $k_{\|}$ is the wavenumber parallel to the local magnetic field, $v_{\|}$ is the velocity component parallel to the field, $n = \pm 1$ for the first harmonic number of electrons interacting with right- and left-handed electromagnetic waves propagating parallel to the magnetic field (note that chorus is a right-handed, i.e. R mode, wave), Ω_e is the electron gyrofrequency, and γ is the relativistic Lorentz factor.

Horne et al. [2007] introduced magnetosonic waves as a potential accelerator of radiation belt electrons. They discussed how these waves, which are generated by unstable ring current distributions, cause electron acceleration via Landau resonance (i.e. $n = 0$ in Eq. 2.5) and how this process can energize electrons from a source population at 10's of keV up to several MeV. *Meredith et al.* [2008] continued this investigation by looking at wave and particle data from the Combined Release and Radiation Effects Satellite (CRRES), and they found that the intensity of

fast magnetosonic waves increases with increased magnetic activity, implying that they may be related to times of enhanced convection or substorm activity. They suggested that while the true source of these waves is yet to be determined, these waves may indeed transfer significant amounts of energy from the ring current to the outer belt electrons.

A combination of both local acceleration and radial transport has also been used to explain energization of outer belt electrons. These combinations are mentioned in *O'Brien et al.* [2003], who discussed how electron flux enhancements are associated with both ULF and VLF/ELF wave activity and *Tu et al.* [2009], who found that they can best simulate observed PSD during storms when they included both radial diffusion and internal heating in their model. *Boscher et al.* [2000] proposed a localized recirculation model in which inward radial diffusion acts near the equator while outward radial diffusion occurs for higher latitudes. In this model, electrons are energized by circulating through the system repeatedly near the plasmapause, where plasmaspheric hiss pitch-angle scatters them to higher latitudes. *Brautigam and Albert* [2000] found that for the 9 October 1990 storm, radial diffusion alone is not enough to fully explain the observed increase in >1 MeV electron flux and suggested that wave-particle interaction with enhanced chorus waves may provide an explanation for the inconsistency, and *Taylor et al.* [2004] found from a multi-satellite PSD study of a small to moderate geomagnetic storm that there is sufficient source for inward radial diffusion during the storm but also that there is evidence of a local PSD peak between the GPS ($\sim$4 R_E) and POLAR ($\sim$8 R_E) observations, implying that local acceleration still plays a role. Others described similar types of events but draw different conclusions about the principle accelerating mechanism: *Horne et al.* [2005a] concluded that whistler mode chorus is a viable explanation for electron flux increases around L = 4.5 during geomagnetically active periods, while *Loto'aniu et al.* [2006] and *Li et al.* [2008] showed that inward radial diffusion can explain most of the observations during the great October-November 2003 storms, which geomagnetically were extremely active events.

Several recent studies into the PSD radial gradient of outer belt electrons yield evidence that local acceleration mechanisms play a very significant role in relativistic electron generation. *Selesnick and Blake* [2000] found that a local source of relativistic electrons may exist around L =

4 based on PSD calculations, implying that some local acceleration is occurring there. *Green and Kivelson* [2004] went on to explain how a peak in PSD at L $\approx$ 5 could diffuse outwards to account for the correspondence between flux enhancements at GEO and increased ULF wave power. More recently using a multi-satellite study, *Chen et al.* [2007b] found that, on average, electron PSD peaks inside of GEO during storm times and non-storm times alike. They also found an instance where the PSD increased first around GEO then later at higher and lower L, which is strong evidence of internal heating by wave-particle interactions. They concluded that wave-particle interactions are the dominant source of relativistic electrons in the outer radiation belt. *Turner and Li* [2008b] and *Turner et al.* [2010b] used sharp solar wind pressure enhancements to calculate instantaneous PSD gradients beyond GEO for a very broad range of μ and various geomagnetic and solar wind conditions, and they found that for electrons with energies above a couple of hundred keV at GEO, the PSD gradient is negative, which indicates that local heating is causing a PSD peak inside of GEO prior to these events. When this peak forms near the heart of the outer belt, radial diffusion can still play an important role, causing electrons to drift away from the peak in PSD. Those electrons that diffuse inwards, gain energy but most likely interact with plasmaspheric hiss and are scattered into the loss cone [*Lyons et al.*, 1972; *Abel and Thorne*, 1998], while those electrons that diffuse outwards, lose some energy but may retain enough to be measured as relativistic by satellites at GEO, which are closer to the outer edge of the outer belt.

2.3.2 Loss

As discussed above, relativistic electrons experience both sudden enhancements and losses. Like enhancements, an observed decrease in electron flux can be caused by adiabatic effects [*McIlwain*, 1966; *Kim and Chan*, 1997], but true loss of radiation belt electrons occurs through precipitation into the atmosphere or magnetopause shadowing [*Millan and Thorne*, 2007]. Magnetopause shadowing is the term used for particles that are lost by drifting into the magnetopause, and this can become important for lower L shells as the magnetopause is compressed inwards due to high speed solar wind streams or pressure pulses.

Many different processes can lead to precipitation of relativistic electrons into the atmosphere. *Millan and Thorne* [2007] provided a full review of these loss processes, and the following is mostly a summary of their work. When extremely high energy electrons precipitate into the atmosphere they cause increased ionization in the D-region of the ionosphere [*Bailey*, 1968] and bremsstrahlung X-ray production from collisions with neutrals [*Rosenberg et al.*, 1972]. *O'Brien* [1964] discussed how electron precipitation is a highly energy-dependent process by showing that precipitation of E $>$ 40 keV electrons did not correspond to precipitation of $>$ 1 MeV electrons. *Onsager et al.* [2002] investigated the response of electrons to a -80 nT Dst magnetic storm, and they too find that there is an energy-dependence to non-adiabatic electron loss.

Most precipitation is due to scattering by wave-particle interactions. Wave-particle interactions occur when there is a Doppler shifted resonance between an electromagnetic wave's frequency and the electron gyro-frequency (see Eq. 2.5 for electron interactions with electromagnetic waves). By violating the first and/or second adiabatic invariants, wave-particle interactions can respectively lead to energy diffusion and/or pitch angle scattering of radiation belt electrons. There are particular waves that are naturally present in the magnetosphere that are known to be able to interact with relativistic electrons.

Earth's plasmasphere is a cold, dense region of plasma that co-rotates with the Earth [*Kivelson and Russell*, 1995, pg 298-300]. *Lyons et al.* [1972] and *Lyons and Thorne* [1973] discussed how the slot region between the radiation belts is a result of pitch-angle scattering by plasmaspheric hiss, which is a broadband ELF (100 Hz several kHz) whistler-mode wave emission observed throughout the plasmasphere [*Millan and Thorne*, 2007]. Recently, *Bortnik et al.* [2008] showed how whistler-mode chorus generated at higher L shells can propagate into the plasmasphere where it then decays into hiss. The plasmasphere is a dynamic region; its outer boundary varies based on geomagnetic and solar wind activity [*Kivelson and Russell*, 1995]. *Li et al.* [2006] showed that there is good correlation between the inner edge of the outer radiation belt and the outer edge of the plasmasphere (see Figure 2.2), which further confirms the importance of plasmaspheric hiss to relativistic electron loss.

Whistler-mode chorus are discrete emissions with frequencies ranging from ~100 Hz to 5 kHz. They are observed outside the plasmasphere, and are mostly observed to have frequencies that rise in tone, though falling tones are also possible [*Millan and Thorne*, 2007]. *Kennel and Petschek* [1966] discussed how it is believed that chorus is generated by electron-cyclotron instabilities associated with freshly injected plasma sheet electrons, and *Meredith et al.* [2001] showed that chorus intensity increases during enhanced substorm activity. Electrons can be pitch angle scattered by chorus, which can result in loss, however, *Bortnik and Thorne* [2007] discussed how VLF chorus tends to preferentially accelerate electrons with energy above a couple of hundred keV.

Electromagnetic ion cyclotron (EMIC) waves are believed to be generated by anisotropy in the proton ring current, which is associated with protons injected during times of strong geomagnetic activity (i.e. storms and substorms) [*Jordanova et al.*, 2001a, b]. Also, *McCollough et al.* [2009] used test-particle simulations of protons in MHD fields calculated from actual solar wind conditions to show how EMIC wave-growth rates are enhanced when off-equatorial minimum-B pockets form on the dayside magnetosphere. These minimum-B pockets can be produced by solar wind dynamic pressure enhancements and can cause sufficient temperature anisotropy as the ring current protons move along special "Shabansky" drift-orbits in the distorted field [*Shabansky*, 1971]. EMIC waves are particularly effective for wave-particle interactions with electrons with energy above a couple hundred keV [*Thorne and Andreoli*, 1980], and this makes them ideal for loss of outer belt electrons. This electron loss by EMICs occurs when the waves pitch-angle scatter the electrons into the loss cone, resulting in electron precipitation [*Millan and Thorne*, 2007]. Near the heart of the radiation belts, L = 3.5-5, EMIC waves have their largest amplitudes in the dusk sector and their occurrence rate is significantly higher during geomagnetically active times [*Erlandson and Ukhorskiy*, 2001]. *Bortnik et al.* [2006] showed the effectiveness of EMIC waves to relativistic electron loss by relating a rapid flux dropout during a storm on 20 November 2003 to the telltale signs of scattering by EMICs.

Another potential loss mechanism, which has not been extensively studied, is the breaking of electrons adiabatic invariants due to current sheet scattering. This loss process occurs when the

radius of curvature of the magnetic field is on the same order as the electron gyro-radius. This occurs primarily on the nightside because of the stretched nature of the field lines there [*Imhof et al.*, 1991; *Selesnick and Blake*, 2002; *Millan and Thorne*, 2007].

2.3.3 Transport

Electrons in Earth's magnetosphere ultimately come from sources in either the solar wind or Earth's ionosphere [*Li and Temerin*, 2001], and transport processes are critical not only to get these particles into the inner magnetosphere but also in the acceleration of these electrons to relativistic energies in the outer radiation belt. A variety of transport processes can introduce electrons into the outer belt zone, but it is well accepted that injections and convection of electrons from the plasma sheet are most important as a source for the outer radiation belt [*Friedel et al.*, 2002]. Two of the primary acceleration theories rely on source electrons from the plasma sheet. For inward radial diffusion, electrons in the sheet represent a source of high PSD, and when the third adiabatic invariant is broken, these particles can diffuse inwards in L^* gaining energy in the process. For in-situ acceleration by wave particle interactions, substorm injections and enhanced convection are responsible for introducing a seed population of 10's to low-100's keV electrons. These injected particles also generate the plasma waves that can be responsible for gyro-resonant acceleration of electrons to relativistic energies.

As discussed previously in the Acceleration section, the radial distributions of electron PSD for fixed first and second invariants are telltale of the dominant acceleration mechanism and also reveal regions of loss. Figure 2.4 shows different PSD distributions resulting from a) a source at high L^* leading to inward radial diffusion, b) in-situ acceleration resulting in a peak in the distribution and subsequent inward and outward radial diffusion, and c) a peak resulting from either an on-off source at high L^* or a loss at high L^* like that due to magnetopause shadowing. In each of these cases, radial transport due to diffusion plays a critical role in redistributing the electrons throughout the outer belt. For the first and second cases, radial transport results in an overall enhancement of the belt, while for the third case the overall result can be either an enhancement or a deflation

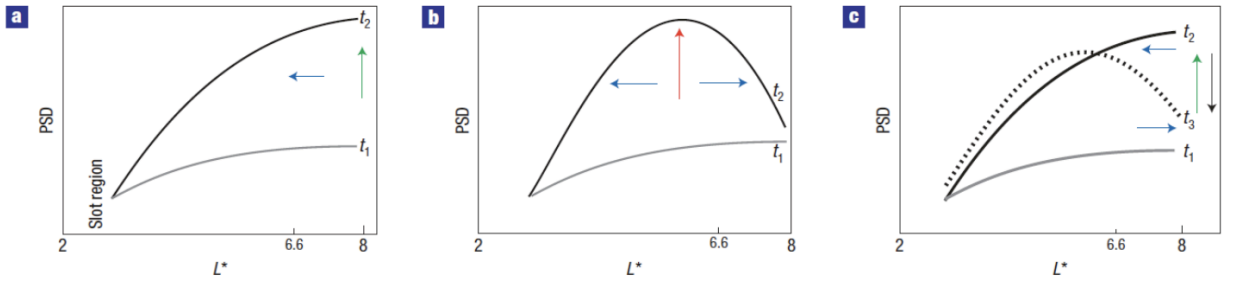

Figure 2.4: Figure 1 from *Chen et al.* [2007b] showing different PSD radial profiles: a) a profile exhibiting a positive gradient, which would be conducive to inward radial diffusion; b) a peaked profile resulting from an internal source; c) a peaked profile resulting from variable conditions or loss at higher L-shells.

of the belt depending on the magnitude and nature of the source or loss at higher L^*.

Concerning radiation belt transport, it is important to study to separate the adiabatic from non-adiabatic motions. For instance, *Kim and Chan* [1997] discussed the Dst effect in which compressions and expansions of the Earth's magnetic field on slow time scales result in fully adiabatic motion of the trapped particles. This motion however can result in drastic changes of electron flux measured by in-situ spacecraft and can be mistaken for true losses or enhancements. Really though, the spacecraft is just measuring particles, which were originally at either lower or higher energy (since the first adiabatic invariant is conserved), from elsewhere in the radiation belt. If all three invariants truly are conserved, then by Liouville's theorem there should be no change in PSD for fixed μ, K, and L^* even if the fluxes are changing. For this reason, it is important to look at changes not in flux, but in PSD for fixed invariants, which provide a better estimate of true non-adiabatic losses or sources instead of just adiabatic transport. Some events that can be truly complicated in this matter are geomagnetic storms and substorms, both of which can involve various levels of electron source, loss, and transport processes.

2.4 The Complex Roles of Geomagnetic Storms and Substorms

Geomagnetic storms are global magnetospheric disturbances associated with enhanced solar wind - magnetosphere coupling and enhancements of the ring current, and they are known to be

associated with drastic changes to the intensities of outer belt electrons [e.g. *Reeves*, 1998; *O'Brien et al.*, 2001; *Reeves et al.*, 2003; *Tu et al.*, 2009]. *Reeves* [1998] investigated geomagnetic storms from 1992-1995, which coincided with the transition from solar maximum to minimum. He found that all of the relativistic electron enhancements during the time period was associated with a geomagnetic storm, but there was little correlation between the strength of storms (characterized by minimum Dst during the storm main-phase) and the intensity of an associated radiation belt enhancement. He also noted that there were several storms during the period that resulted in no relativistic electron enhancement. *Reeves* [1998] concluded that there were additional processes at work during storms that decoupled the radiation belt electrons from the ring current. He presented the possibilities that an internal acceleration mechanism for the electrons and the state of the source populations could explain the decoupling between the two systems.

O'Brien et al. [2001] and *Reeves et al.* [2003] both conducted statistical surveys of geomagnetic storms and their effects on the outer radiation belt electrons. *O'Brien et al.* [2001] used statistical asynchronous regression (see *O'Brien et al.* [2001] and Chapter 7 for details) to map GEO measurements to local noon and performed cross correlation and superposed epoch analyses to try and determine which quantities are most important to relativistic electron enhancements during storms. They found that sustained high solar wind speeds and enhanced ULF wave power in the magnetosphere best distinguished between the storms with electron flux enhancements compared to those without. Figure 2.5 shows the results from their superposed epoch analysis. Note here that the largest separations between the sets of data for the enhancement and non-enhancement sets prior to Dst minimum (0 epoch time) is for the solar wind speed, ULF wave power, and the AE index.

Reeves et al. [2003] looked at the effects of 276 moderate and intense magnetic storms on relativistic electrons at GEO for a full solar cycle (1989-2000). They built up statistics of how many of the storms result in increases, decreases, or no change in electron fluxes. Their results are summarized in Figure 2.6, which reveal that only 53% of the storms resulted in net electron flux enhancements. The remaining storms were divided between 28% in which there was no significant

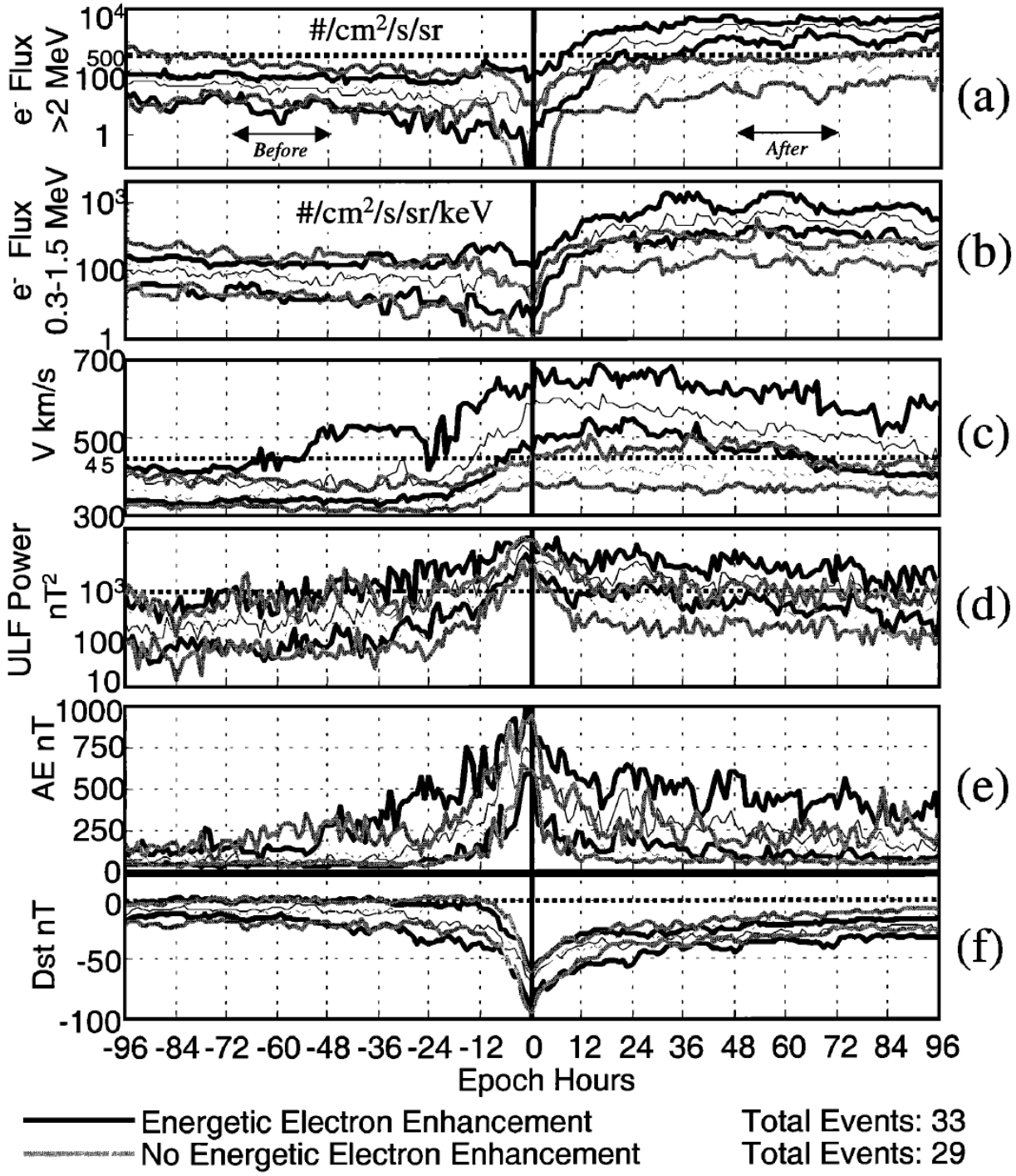

Figure 2.5: Figure 2 from *O'Brien et al.* [2001] showing the results of a superposed epoch analysis for geomagnetic storms that result in relativistic electron enhancements (black lines) and those that result in no enhancements (gray lines). Epoch time is set to minimum Dst during storm main-phase. Thick lines are the upper and lower quartiles, while the thin lines are the medians.

change in electron fluxes and 19% in which there was a net loss of electrons at GEO. They also showed that the pre-storm and post-storm fluxes were highly uncorrelated, indicating that storms do not simply "pump up" the outer belt electrons. They concluded that these results indicated that the outer radiation belt is the result of a complex balance between electron source and loss mechanisms.

A potentially important type of event that often seems somewhat neglected compared to geomagnetic storms are substorms. Substorms are the result of reconnection events in the magnetotail that cause global field reconfigurations by way of dipolarization of the inner magnetosphere and the ejection of plasmoids down the tail. Associated with the dipolarization of the field are particle injections of energetic electrons and protons (up to several 10's of keV). As discussed above, *Meredith et al.* [2001] and *Meredith et al.* [2008] showed that enhanced convection or substorm activity results in enhancements in whistler-mode chorus and magnetosonic wave activity, which can potentially accelerate seed electrons to relativistic energies in the inner magnetosphere. *Meredith et al.* [2002] went on to show that relativistic electron enhancements are associated with enhanced substorm activity and chorus intensities. They presented three cases using CRRES data: 1) a strong storm resulting in an electron flux enhancement, 2) a strong storm resulting in no flux enhancement, and 3) an electron flux enhancement with no associated storm. They found that for the cases involving net electron flux enhancements, there was enhanced substorm (from the AE index and signatures of substorm particle injections) and chorus activity (from the CRRES fields instruments). The strong storm with no flux enhancement was characterized by a recovery period displaying few substorm injections of subreletivistic particles, weak chorus amplitudes, and a net loss of radiation belt electrons. They concluded that substorm activity is critical to the several-day enhancement of relativistic electrons in the outer belt. This picture is summarized nicely in *Horne* [2007], and a schematic from this work is shown in Figure 2.7. Here, substorms inject both the seed population of subrelativistic electrons (∼10's to a few 100 keV) and energetic protons (∼10's keV). These substorm injected particles create the anisotropy conditions necessary for whistler-mode chorus wave growth as well as the production of magnetosonic waves, both of which can accelerate the seed

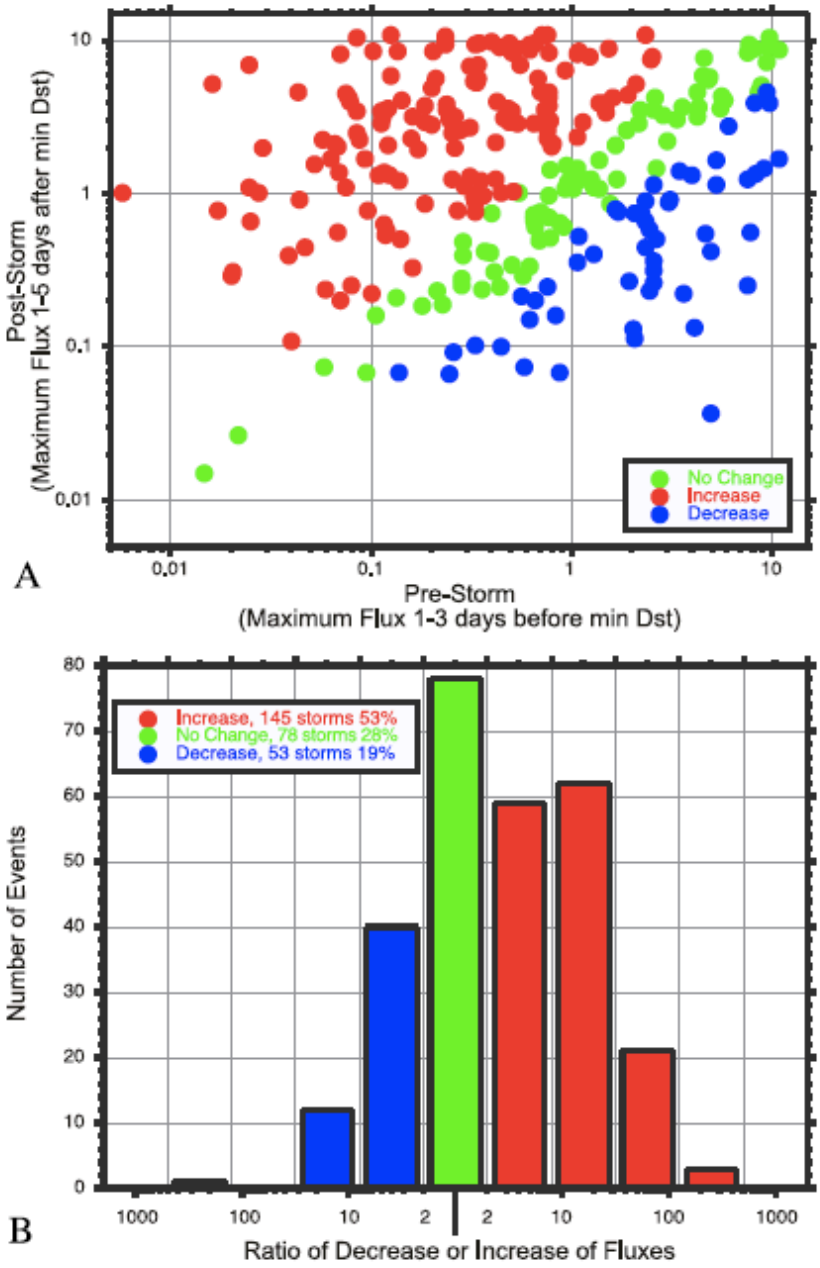

Figure 2.6: Figure 3 from *Reeves et al.* [2003] showing the results of a statistical study of geomagnetic storm effects on relativistic electrons in the outer belt.

electrons to relativistic energies over 1∼2 days. Such internal acceleration processes would result in a peak in the PSD and subsequent inward and outward radial diffusion towards the "sinks" at the magnetopause and the slot region. Such diffusion would be enhanced in the presence of magnetic field disturbances like ULF waves. The overall effect of this process would be a net enhancement of relativistic electrons throughout the outer radiation belt.

Overall, the dynamics of the outer radiation belt are very complex, and spacecraft instruments that provide in-situ data are immensely useful for addressing outstanding questions as well as validating theories and models. Thus, it is important to understand what instruments are available, how they work, and what range of data they provide.

2.5 Relativistic Electron Instruments

This work is on the acquisition, analysis, and practical use of outer radiation belt data, so it is important to discuss some of the important spacecraft missions that have provided, or will provide, this data. One of the first missions to really alter our concepts concerning the extreme dynamics of the outer radiation belt was the Combined Release and Radiation Effects Satellite (CRRES) [*Brautigam*, 2002]. Despite its short mission lifetime (launched 25 July 1990, failed 12 October 1991 presumably due to battery failure), the dataset provided by the waves and particles instruments on this satellite are still being used for new science today [e.g *Ni et al.*, 2009]. In addition to waves sensors capable of detecting a range of waves from ULF to VLF, CRRES carried the High-Energy Electron Fluxmeter (HEEF) and the Medium Electron Sensor-A (MEA), which could measure differential electron fluxes in channels ranging from below 50 keV up to 10 MeV. This suite of instruments and it's low inclination GEO transfer orbit made CRRES ideal for studying outer belt electron dynamics.

Another mission from the early 90's is the Solar, Anomalous, and Magnetospheric Particle Explorer (SAMPEX) [*Baker et al.*, 1993]. SAMPEX is still operational and has provided electron flux measurements from low-Earth orbit (LEO) since its launch in July 1992. Unlike CRRES, SAMPEX is in a high-inclination LEO allowing it to pass through the "horns" of both radiation

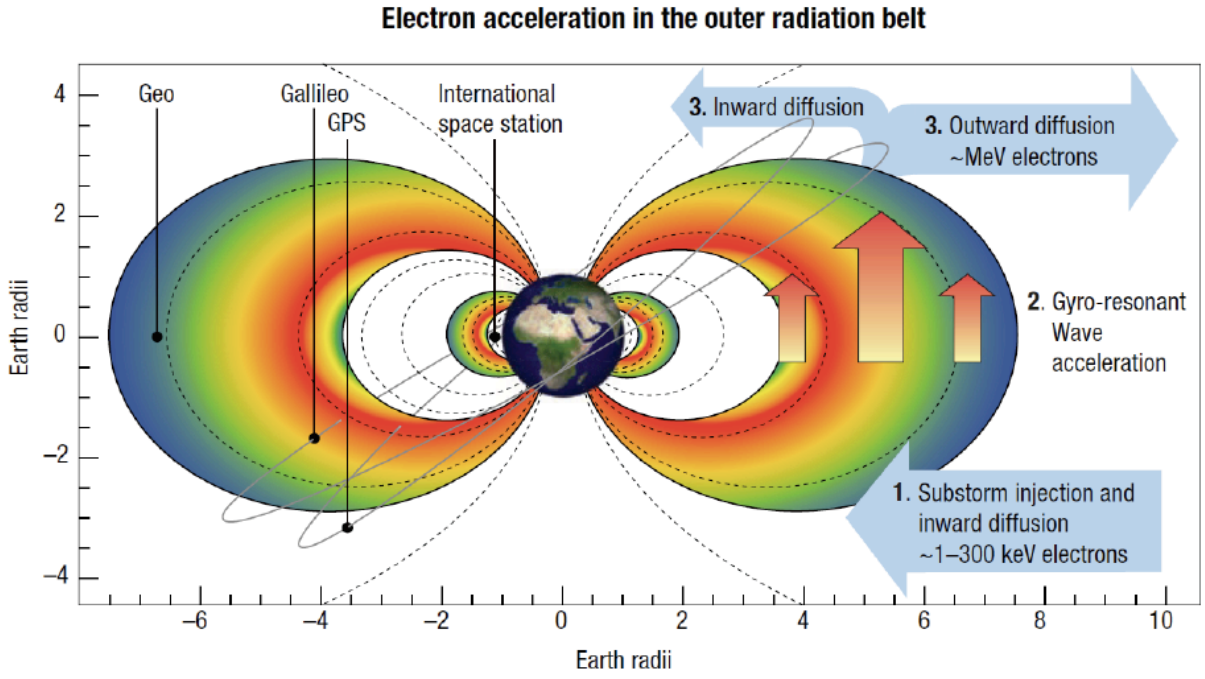

Figure 2.7: Figure 1 from *Horne* [2007] showing the role of seed particles to the outer radiation belt electrons: 1. Medium energy particles are injected into the inner magnetosphere from the tail, providing a seed population and exciting wave instabilities. 2. Wave-particle interactions preferentially accelerate some of the seed electrons to relativistic energies. 3. Radial diffusion redistributes the relativistic electrons and fills the outer radiation belt.

belts. SAMPEX's instrument suite consists of four particle instruments: 1) the Mass Spectrometer Telescope (MAST), 2) the Proton/Electron Telescope (PET), 3) the Low Energy Ion Composition Analyzer (LEICA), and the Heavy Ion Large Telescope (HILT) [*Cook et al.*, 1993]. For energetic electrons, PET was designed to nominally measure electrons in one integral count rate channel at >0.4 MeV and four differential channels at ∼1-4 MeV, ∼4-20 MeV, and two ∼12-30 MeV channels (each with a different geometric factor). This instrument can be used to study radiation belt losses, and *Blake et al.* [1996] used it to study the temporal and spatial characteristics of electron microbursts, which are now believed to be the result of enhanced scattering and loss of outer belt electrons by wave-particle interactions with EMICs [*Millan and Thorne*, 2007]. SAMPEX, being NASA's first Small Explorer (SMEX) mission, is a prime example of how a small spacecraft in a high-inclination LEO can be particularly effective for certain complementary studies of Earth's outer radiation belt electrons, and I will discuss more on this in Chapter 3.

GEO is an immensely popular orbit, and spacecraft here have provided some very important measurements of outer belt electrons. NOAA's Geostationary Operational Environment Satellites (GOES) have provided integral fluxes of relativistic electrons at GEO for close to three decades. The earlier GOES spacecraft used the Energetic Particle Sensors (EPS) to measure electrons in three integral flux channels: >600 keV, >2 MeV and >4 MeV, while the latest GOES spacecraft carry the Magnetospheric Electron Detectors (MAGED) that measure differential fluxes in five energy channels covering a range of energies from 30 - 600 keV. The MAGED instruments also have a field of view (FOV) of ∼30°, so they can resolve pitch angle information. Like the energetic electron instruments on CRRES and SAMPEX, the MAGED employs solid state detectors to provide the electronic signal to be processed into the final count rates. These detectors are protected from light by a thin foil covering the instrument aperture, and this foil also serves as a shield that blocks all lower energy electrons from entering the detector stack. The instruments do however suffer from proton contamination, which is accounted for via algorithms in post-processing of the data [all GOES information is referenced from the *GOES Databook - Section 5. Space Environment Monitor*, which is available online at goes.gsfc.nasa.gov]. All of the GOES spacecraft also carry

onboard magnetometers, which makes them additionally useful for radiation belt studies. Also at GEO are the Los Alamos National Laboratories (LANL) spacecraft with their Synchronous Orbit Particle Analyzer (SOPA) instruments capable of measuring energetic electrons from 50 keV to >1 MeV in nine differential flux energy channels. Data from the various GOES and LANL spacecraft at GEO are used extensively in this work, particularly in Chapters 4, 6, and 7.

Very recently, the Time History of Events and Microscale Interactions during Substorms (THEMIS) mission [*Angelopoulos*, 2008] has been operating and providing a plethora of data that is useful to a wide range of space physics topics (for example, see Appendix C). This mission consists of five spacecraft in highly-elliptic Earth orbits, with apogees ranging from 10 to 30 R_E, and they carry identical suites of instruments including a comprehensive particles suite consisting of the Electrostatic Analyzer (ESA) and Solid-State Telescope (SST) instruments. The ESA instrument covers low-energy, thermal protons and electrons up to ∼30 keV, and the SST covers energetic protons and electrons from ∼25 keV to several MeV. The SST is an interesting design (see Fig. 2.8, consisting of two identical instruments side-by-side, each with one collimator specifically for electrons and one specifically for ions. The electron side uses a thin foil to block protons below a certain energy (a few hundred keV), while the ion side uses a magnet to deflect away the much less massive electrons. Both sides share the same detector stack, and the type and energy of incident particles are determined using coincidence logic. Mechanically activated attenuators, which consist of a metal plate with a pin-hole, are used to limit the geometric factor of the instrument in the case of very high environmental fluxes to prevent saturation of the electronics. The shielding on this instrument consists only of aluminum, which can be problematic concerning detector noise from shield-penetrating particles, which is discussed in Chapter 3.

NASA's Radiation Belt Storm Probes mission (RBSP) is being designed specifically to study Earth's radiation belts environment. The mission [see website for details: http://rbsp.jhuapl.edu/] will consists of two identical spacecraft in highly-elliptic, low-inclination orbits similar to that of CRRES. The instrument suite on each spacecraft will provide measurements of the waves, fields, and particles relevant to all aspects of radiation belt acceleration, loss, and transport processes.

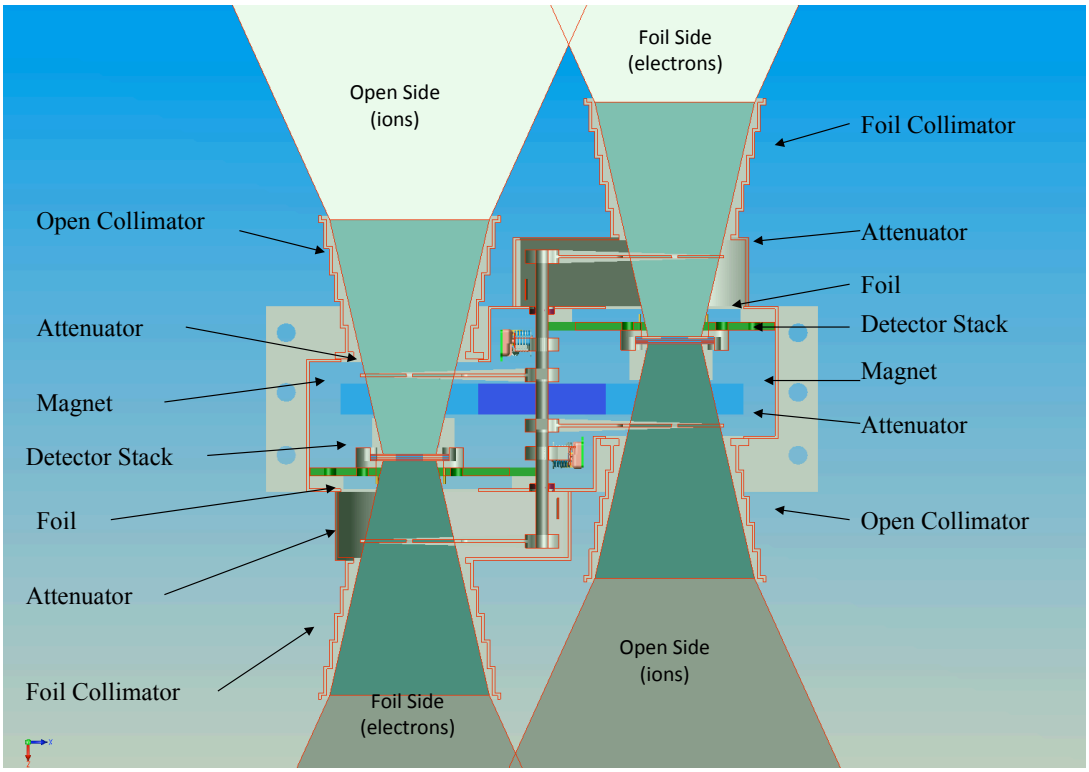

Figure 2.8: Conceptual design and key components of the THEMIS Solid State Telescope instruments. See THEMIS website for source of image and additional information on the SST instrument.

The Relativistic Electron and Proton Telescope (REPT) is being designed and manufactured here at the University of Colorado's Laboratory for Atmospheric and Space Physics. REPT will measure relativistic electrons from 4 to 10 MeV and protons from 20 to 75 MeV. This instrument provides the basis for the design of the instrument described in Chapter 3. Hopefully, RBSP will provide the data necessary to answer many of the outstanding questions concerning Earth's outer radiation belt electrons.

2.6 Outer Radiation Belt Models

Spacecraft data are very useful for understanding the outer belt system, but it is limited in that: 1) the observations are extremely sparse and 2) often temporal and spatial changes are difficult to distinguish. System models can thus prove very useful to develop a better understanding of full system dynamics. Sometimes models can be used to explain puzzling features in data sets, while data provides a metric for physics-based model parameter tuning and validation. Here, I briefly review some of the more common and successful types of models for outer radiation belt electron dynamics.

One of the more popular types of model for the outer belt electrons is the diffusion model that solves for the phase-averaged PSD (f) in Equation 2.3 or its derivatives. Earliest work with diffusion models involved one-dimensional forms, where electrons could only diffuse radially in L^*. Radial diffusion models numerically solve Equation 7.1 given specific boundary and initial conditions. Some examples include *Brautigam and Albert* [2000], *Li et al.* [2001b], and *Shprits and Thorne* [2004]. Recently, *Subbotin and Shprits* [2009] and *Subbotin et al.* [2010] extended diffusion modeling into three dimensions. *Subbotin and Shprits* [2009] described the UCLA-VERB model, which solves a modified Fokker-Planck equation including radial, pitch-angle, and energy diffusion and discussed its numerical performance and results when the diagonal terms of diffusion are included. *Subbotin et al.* [2010] also included the mixed-diffusion terms (i.e. the off-diagonal terms). These models all assume there are no advective terms (referred to as coherent terms in Equation 2.3), and the next step will be including these terms to accommodate for waves in the

system that might break the assumptions made for quasi-linear theory (i.e. large amplitude plasma waves).

Increasingly popular in radiation belt modeling are data-assimilative models that use observed data to adjust model results and parameters. *Rigler et al.* [2004] used a Kalman filter to improve upon the results of a linear prediction filter by reanalysis. The Kalman filter is a recursive, data-assimilative algorithm that provides the optimal estimate of the state variables for a modeled system, which can include model coefficients, by fitting model output to actual observations. Kalman filters have been used in other fields, like spacecraft orbit determination, terrestrial weather, and atmospheric and oceanic research, for more than two decades [see references in *Kondrashov et al.*, 2007], and only recently has this technique been applied to radiation belt studies. *Rigler et al.* [2004] found that applying the Kalman filter significantly improves the results from a linear prediction filter used to predict outer belt electron flux, and they also discuss how a Kalman filter can be applied to improve a real-time forecast model. Others have employed the Kalman filter to radiation belt studies as well. *Shprits et al.* [2007a] applied the Kalman filter to a one-dimensional radial diffusion model and energetic electron PSD observations from the CRRES spacecraft. They found that the results of the reanalysis show peaks in the PSD near the heart of the outer belt, which are impossible to produce by the radial diffusion model itself due to its nature (it has no internal acceleration terms) and constant boundary conditions. *Kondrashov et al.* [2007] also use a Kalman filter with a one-dimensional radial diffusion model and CRRES observations to study the systematic differences in the effects on radiation belt electron lifetimes from storms driven by coronal mass ejections and co-rotating interaction regions. *Koller et al.* [2007] used an ensemble Kalman filter to estimate the locations where additional source or loss is required to minimize the error between observations and a 1-D radial diffusion model. Overall, the Kalman filter is a powerful tool that can be used to improve radiation belt studies and models.

Test-particle simulations are another type of model useful for studying radiation belt dynamics. These models capture some of the most basic physics associated with the energetic particles' motions. For example, Figures 2.9 and 2.10 are generated using a very simple code that numer-

ically solves for a test-particle's position and velocity in time using only the relativistic Lorentz force (see Eq. 2.1) in the IGRF field model. Note that with only this one equation and a realistic field model, a particle's three characteristic motions automatically emerge. When even more realistic fields are included, like the dynamic electric and magnetic fields produced by MHD models, full-system energetic particle dynamics can be simulated. MHD/particle simulations are discussed in detail in *Elkington et al.* [2002], where the Lyon-Fedder-Mobarry (LFM) MHD code is employed to establish the global magnetic and electric fields, and the test-particle system was evolved using a fully 3-dimensional Lorentz integrator to determine particle trajectories in those fields. For any particular event, the MHD simulations can be run using actual solar wind measurements as input. Figure 2.11 (from *Elkington et al.* [2004]) shows how a source population of 60 keV electrons in the plasma sheet can be transported into the trapping region via enhanced convection during a geomagnetic storm. By conserving their first adiabatic invariant, these electrons become more energetic as they move radially inwards, which can explain how the MeV population in the outer belt becomes enhanced during some storms. Test-particle simulations can also be used for studying radial diffusion associated with enhanced ULF activity [e.g. *Elkington et al.*, 1999, 2003].

Finally, *Fok et al.* [2008] used kinetic theory to develop a full-system radiation belt environment (RBE) model. The RBE model solves a bounce-averaged Boltzmann transport equation to determine the PSD of radiation belt electrons. To best simulate full-system dynamics and the coupled nature of the radiation belts, RBE is coupled to realistic magnetic and electric field models, plasma sheet and plasmasphere models, and wave-particle interactions via pitch-angle and energy diffusion. The model has been compared to spacecraft measurements during storms and substorms, and it captured many of the general features associated with outer belt flux changes. A simplified version of RBE is currently running online in real-time to provide a "nowcast" of the radiation belts. It relies on solar wind speed, density, IMF, and Dst as inputs, and it represents one of the most comprehensive operational radiation belt models currently available.

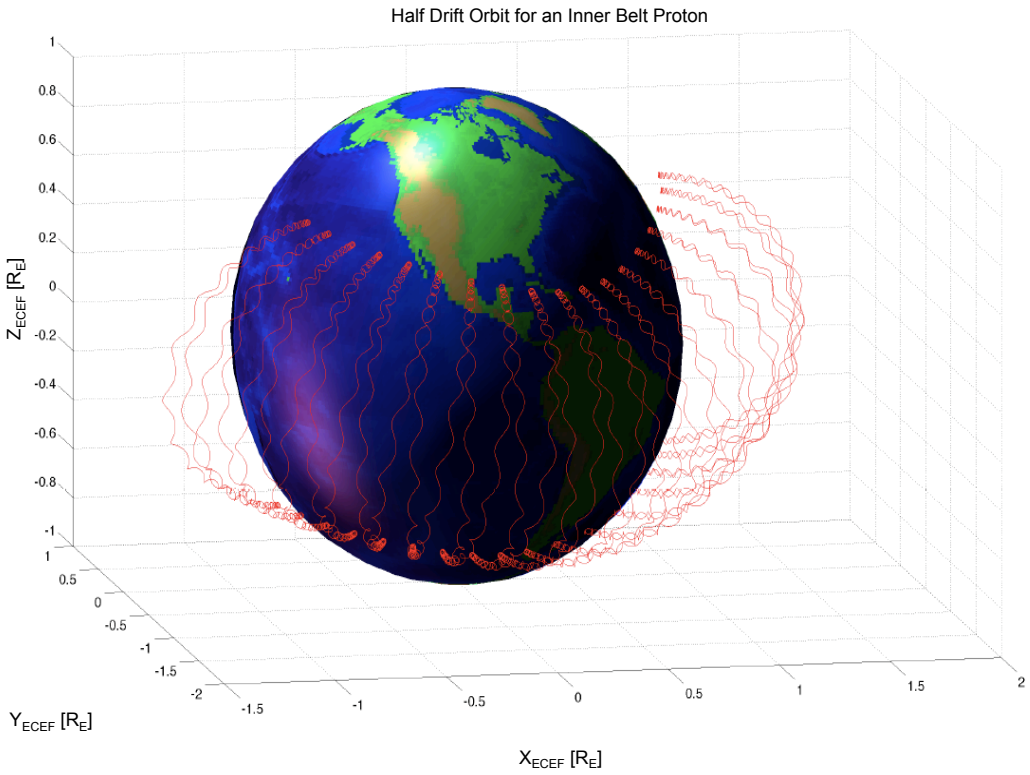

Figure 2.9: Results from a full Lorentz force, relativistic test particle simulation for an inner belt proton. The background magnetic field is the IGRF field, and the proton's energy is 10 MeV. Half a drift orbit is shown here.

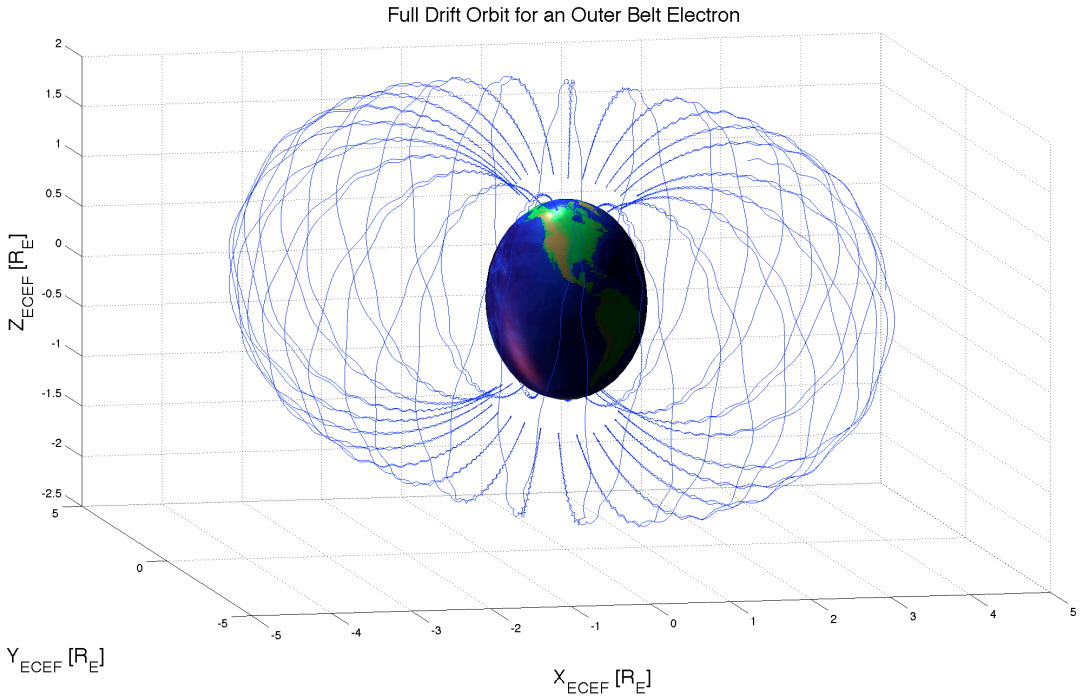

Figure 2.10: Results from a full Lorentz force, relativistic test particle simulation for an outer belt electron. The background magnetic field is the IGRF field, and the electron's energy is 1 MeV. A full drift orbit is shown here.

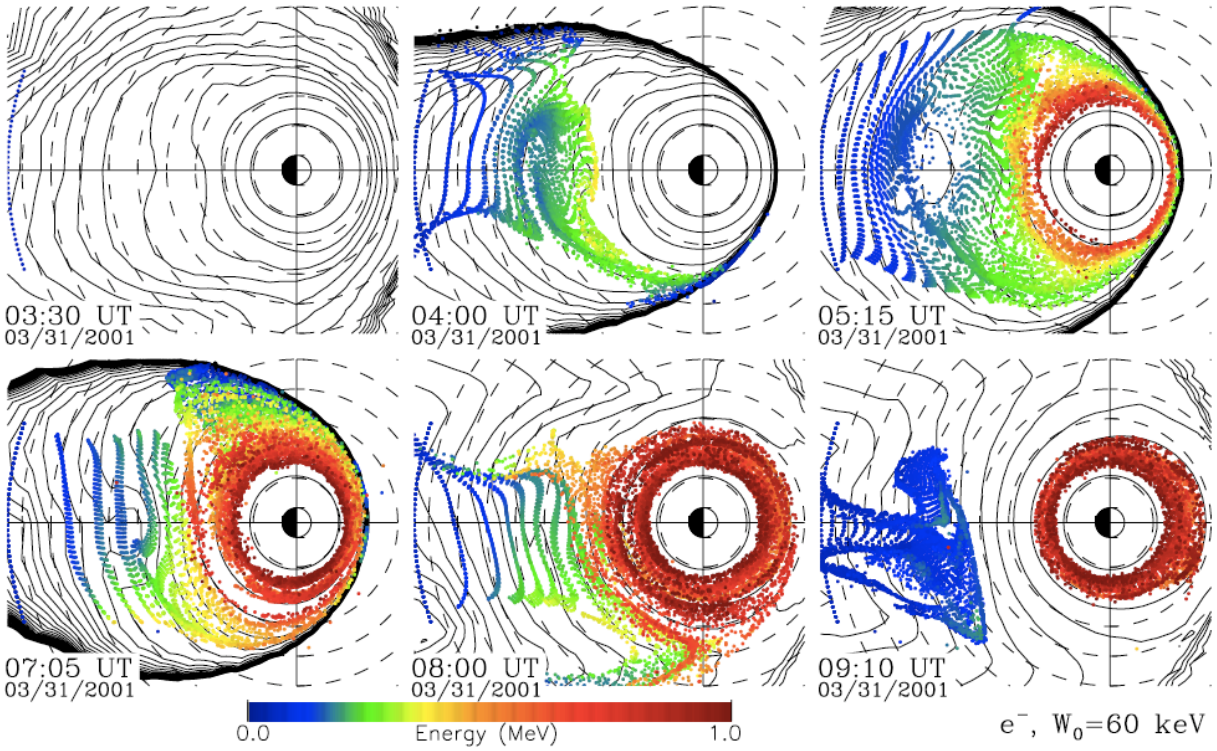

Figure 2.11: Figure from *Elkington et al.* [2004]: Results from MHD/test-particle simulations showing how 60 keV electrons in the plasma sheet can be injected into the trapping region via enhanced convection and diffuse inwards to enhance the MeV population in the radiation belt during a storm.

Chapter 3

REPTile: the Relativistic Electron and Proton Telescope - integrated little experiment

3.1 Introduction

For the past three and a half years, I have been involved with a graduate level design course focussed on spacecraft instrumentation provided through the Department of Aerospace Engineering Sciences and taught by Profs. Xinlin Li and Scott Palo. I first took the course for credit in 2007, when myself and a team of fellow students redesigned and manufactured a working mass spectrometer for interstellar dust. Prof. Li allowed me to stay involved with the class in the following years as a course assistant, and this has allowed me to become heavily involved with the current project, which fits in well with my research since it consists of a small spacecraft mission to study relativistic particles in Earth's magnetosphere. With our second round of proposals to the NSF, the project was accepted for funding by the NSF-CubeSat program in 2009. I have contributed mostly to the design of the mission's instrument, and Prof. Li has supervised my independent study in this particle detector design, which I describe here. Note that this chapter includes work conducted by myself and several colleagues including: Carl Seubert, Ian Crocker, Joey Espejo, Ben Fell, Jianbao Tao, Abhishek Mahendrakumar, and Quintin Schiller. Also, I would like to recognize the rest of the students who have helped with various other aspects of the Colorado Student Space Weather Experiment project, particularly our current project manager, Tyler Redick, and our systems engineer, David Gerhardt. Here, I focus primarily on my contributions to this work, but being a design project, much of the team's work is also included. I would just like to start by

recognizing that this was a group effort and thanking each of them for their hard work in helping to make this project so successful. Additionally, the format and content of this chapter is similar to a paper for the 2010 SmallSat conference that I helped Quintin and Abhishek write, for which they were awarded 3^{rd} place and $3250.00 each in the conference's student paper competition.

Society has become dependent on space-based technology. Spacecraft are used for bank transactions, intercontinental communications, navigation for commercial trade, national defense, and some people can no longer even get from one place to another without a satellite telling their navigation computers where they are. Our societal reliance on space-borne technology has led to the realization that the understanding and ability to forecast space weather is of critical importance. We know that solar events, like solar flares or coronal mass ejections (CMEs), can have serious effects at Earth, from the space environment in Earth's magnetosphere to the terrestrial atmosphere and even in the ground itself. A solar flare, for example, unleashes bursts of X-rays and relativistic protons and electrons (solar energetic particles, SEPs). When such an event is pointed at the Earth, SEPs arrive in less than ten minutes, just shortly after the light that warned us there was a flare in the first place. When these particles hit the Earth, they precipitate near the poles since they are guided there by Earth's magnetosphere. Here, they interact with the atmosphere, which can result in reduced transmission of radio signals (affecting the accuracy of GPS) and increased levels of radiation for people in the polar regions. Sometimes associated with solar flares, CMEs are another piece of space weather that can have adverse affects on manmade systems. These massive, explosive events on the Sun release great amounts of solar material into the solar wind, and when Earth's magnetosphere is impacted by a CME, it often results in a magnetospheric storm. Storms are associated with enhanced ring currents, which alter Earth's magnetic field and can result in induced currents around the planet. Such currents have the potential to overload power grid systems, resulting in power outages on a continental scale. Also during storms, spacecraft are at additional risk from the potential for strong enhancements in outer radiation belt fluxes. These electrons are energetic enough to embed themselves in sensitive electronic components (for an overview of the various negative effects particles can have on spacecraft, see Figure 3.1; deep-

dielectric charging can result from outer belt electrons), which can lead to dielectric breakdown by way of electrical discharging in sensitive, semiconductor components.

To address important space weather questions such as: 1) what are the important electron source, loss, and transport mechanisms and under what conditions are they most effective? and 2) given a solar flare at a certain location on the solar disk, what is the atmospheric penetration depth and latitude range for the associated SEP event at Earth?, it is critical to provide in situ data to the scientific community so that it may be analyzed and incorporated into models. These models can further be developed into real-time forecasts, which mitigate the various societal risks related to space weather. Unfortunately, however, most space missions are extremely expensive and only provide single-point measurements of very large and complex systems. In this chapter, I introduce the Colorado Student Space Weather Experiment (CSSWE) with its sole instrument, the Relativistic Electron and Proton Telescope integrated little experiment (REPTile). CSSWE is a small, inexpensive spacecraft mission that will provide measurements of Earth's outer radiation belt electrons ranging in energy from 500 keV to >3 MeV and SEP protons from 10-40 MeV. CSSWE exemplifies the concept of simpler and smaller spacecraft to provide inexpensive multi-point perspectives to larger, orders of magnitude more expensive missions. The focus of this chapter is on REPTile since I have been heavily involved with the design of this instrument. I begin with a brief introduction to the CSSWE mission to set the context, and I follow this with an introduction to the complexities of energetic particle detection. I then get into the design process of the instrument by discussing the initial design and issues with it followed by an exploration of the instrument's design space and subsequent redesign to address the various problems. I discuss the current design in detail with an emphasis on the various simulations we have run to estimate the instrument performance. I finish with brief sections on the manufacturing and testing of the instrument before concluding on the importance of such small, inexpensive missions to provide complementary data to larger missions.

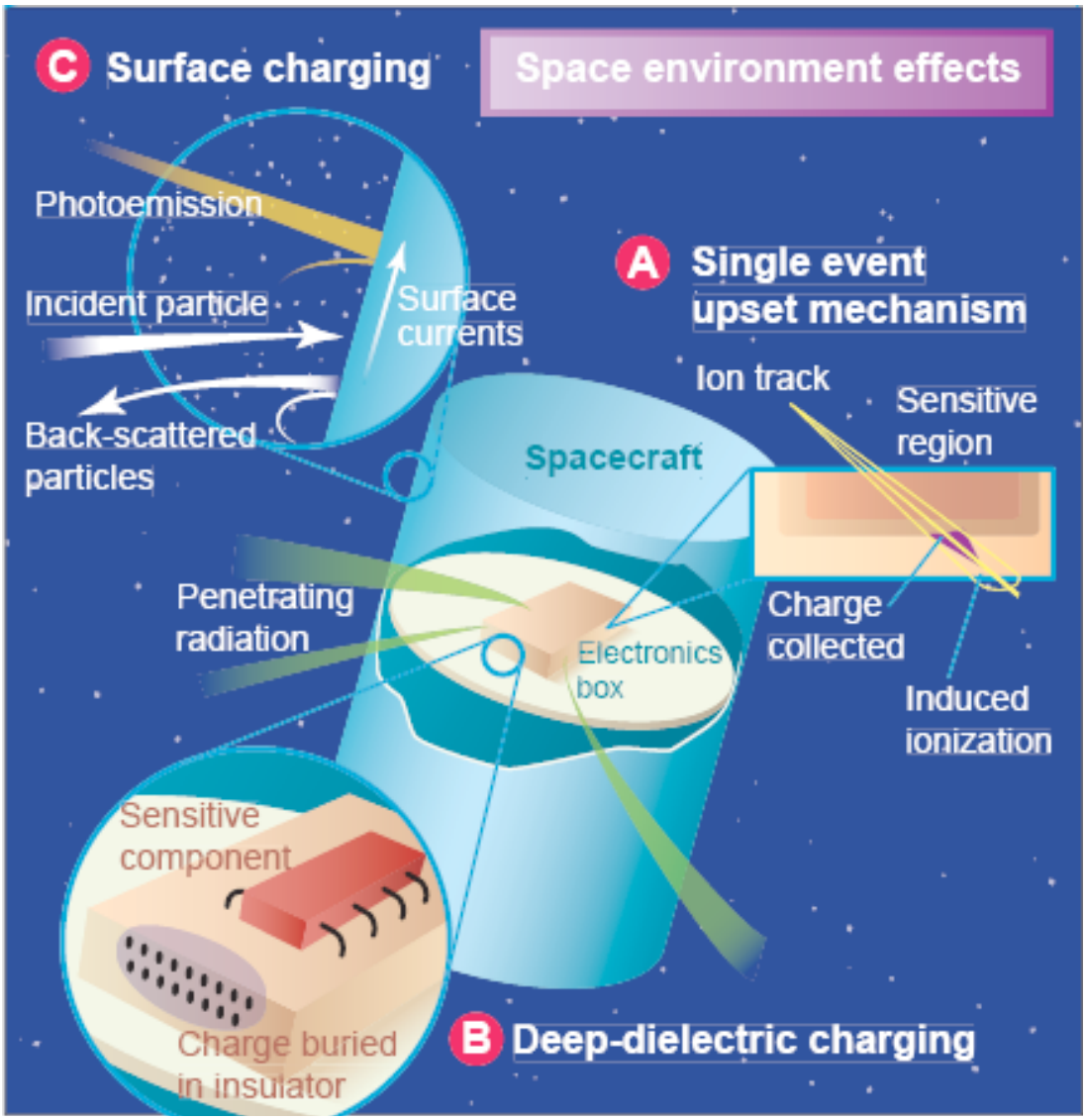

Figure 3.1: Various space environment effects encountered by spacecraft. From *Baker* [2002].

3.2 CSSWE: Big Science from a Small Spacecraft

By measuring SEP protons and outer belt electrons to address the above-mentioned science questions, CSSWE will be helping to prove that significant science can be achieved from small, inexpensive space missions, like CubeSat missions. CubeSat requirements and specifications are defined by Cal-Poly, and they define a small 10x10x34 cm box-like spacecraft with a total system mass of no greater than 4 kg and a center of mass within 2 cm of the geometric center of the spacecraft. These requirements are primarily to produce spacecraft that conform to the Poly Picosatellite Orbital Deployer (P-POD), which is used to interface a group of CubeSats to a launch vehicle and eject them with little risk to any primary payload or the launch vehicle itself.

Figure 3.2 shows the CSSWE systems block diagram. In this figure, each subsystem is colored differently and command, power, and data interfaces are shown with the color-coded arrows defined in the legend. The primary science instrument, REPTile, resides in the center of the CubeSat bus (structure subsystem represented by the rectangular box housing the other spacecraft subsystems). The REPTile electronics processes the proton and electron hits in the detectors to produce count rate data. Command and Data Handling (C&DH) is the "brains" of the system. It consists of a micro-processor (MCU) and flash memory. It collects and stores the science and housekeeping data and commands and regulates the other subsystems. The Communications (COMM) subsystem consists of a micro-processor, a radio, and antennas. It communicates with the ground via a 433 MHz UHF link. The Ground Network is external to the system in this figure since it resides in Boulder at LASP. Solar arrays provide power to the system while the spacecraft is on orbit. The power is stored, regulated, and distributed to the other subsystems by the Power subsystem (EPS). There are two passive subsystems on the spacecraft. The first is the Thermal Control System (TCS), which passively regulates the temperature throughout via thermally absorptive and emissive surfaces and mechanical interfaces. The other passive subsystem is the Magnetic Attitude Control System (MACS). This subsystem consists of a small bar magnet and hysteresis rods. When the bar magnet's moment is not aligned with Earth's field at the spacecraft location, a torque will

be induced on the system, and the hysteresis rods, which are made of a semi-magnetic material, will act as a dampening torque due to their time-lagged response to magnetic field changes. The passive MACS will line the long axis of the spacecraft up with Earth's local field direction within around $\pm 10°$. A magnetometer measures the local field direction to confirm that the MACS is properly working and to provide additional science data that is useful with particle flux measurements.

CSSWE's system configuration is shown in its actual form in Figure 3.3. This shows the structural layout of the entire spacecraft. Starting with the exterior (left image), the CubeSat bus is commercially available from Pumpkin Inc., and we currently have two of these CubeSat structures in house (one for the engineering model and one for the flight model). Each of the spacecraft's long sides are covered with solar panels. On the side with the REPTile aperture and the side opposite this, there are six solar panels, while on the other two sides there are eight. These provide $\sim$4.5 W of orbit average power given the spacecraft attitude alignment with the local magnetic field direction. The solar panels are mounted on printed circuit board (PCB) material with the appropriate connections etched in them. These clip onto the side via commercially available parts designed specifically for this use. Also, gaps are left in the PCB substrates to allow for thermal emission from the electronics stacks inside the spacecraft. The two steel tape antennas are also visible on the exterior. These will be coiled up and stored in slots in the end caps prior to launch. Then, once the CubeSat is released from the P-POD and becomes activated, a resistor will burn through a thin wire holding the coils in place. This will release the antennas, which will unfurl into the configuration shown in the figure.

The interior of the spacecraft (shown on the right in Figure 3.3) starts at the top with the four, thin hysteresis rods (shown here in pink). The batteries sit at the top of the electronics stack and are shown in yellow. These are simple lithium-ion batteries, very similar to those found in iPods. The positioning of these batteries also adds additional shielding for the electronics stack. The EPS and COMM boards lie directly under the batteries, and the C&DH board is at the bottom of the electronics stack. These boards interface via a 104-pin standard connector. REPTile, being by far the most massive component in the system, requires significant support. Two aluminum

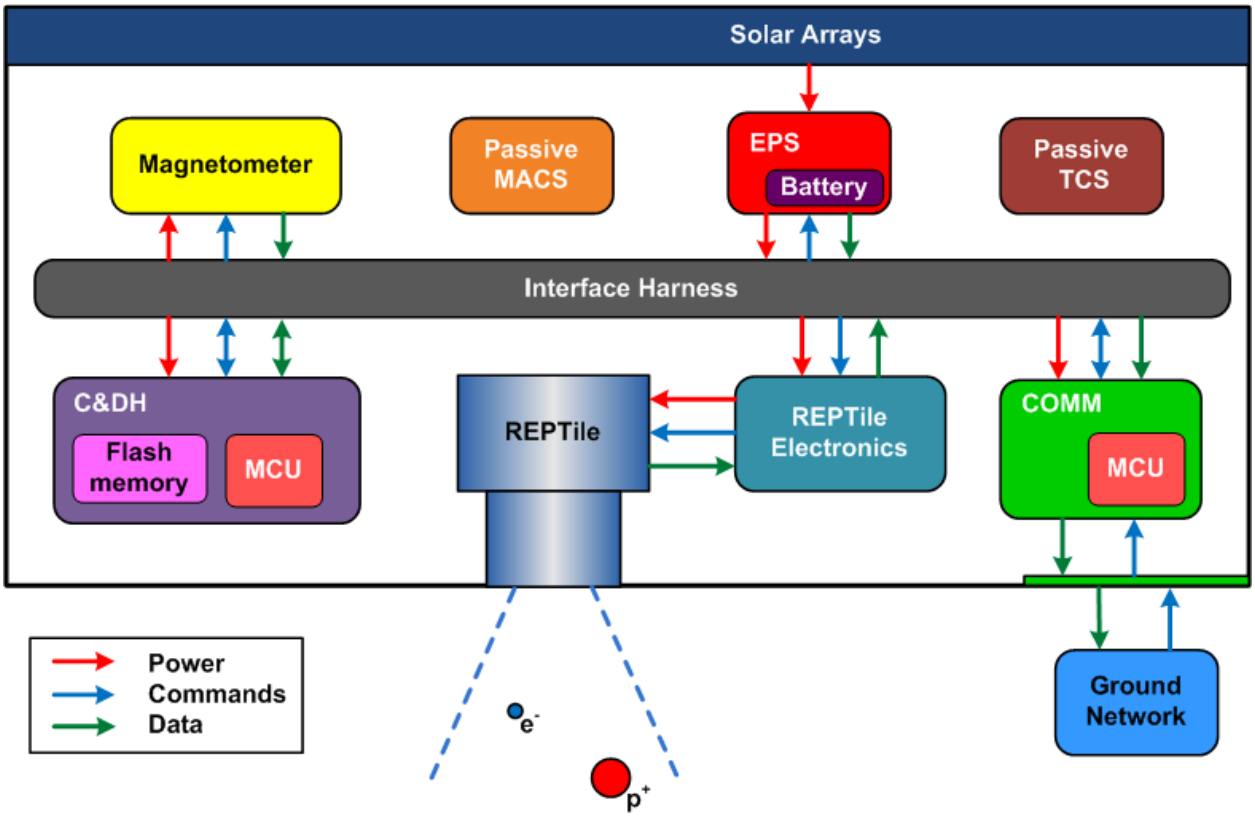

Figure 3.2: CSSWE's system block diagram. Data, power, and commands links between various subsystems are shown with color-coded arrows. See text for subsystem details.

mounting brackets support the instrument and are connected to the outer structure by both the bottom end cap and two of the long walls. REPTile (described further below) mounts into these and so does the REPTile electronics board. The bar magnet and magnetometer are positioned in the bottom portion of the spacecraft below REPTile. The benefit of this configuration is that the interior structure can be removed from the outer shell by simply unfastening the side wall connectors and removing the bottom end cap. This allows for accessibility to the interior for integration and systems testing without risk to the fragile solar cells on the exterior of the spacecraft.

One of the potential problems concerning the system design that I worked on exclusively was the effect of the bar magnet on the particle measurements. Simply put, a magnet nearby the instrument will affect the trajectories of incoming particles that are supposed to be measured by REPTile, and we were concerned that the bar magnet might significantly affect the instrument performance. To simulate this effect in our system, I resorted to test particle simulations integrated using the magnetic component of the relativistic Lorentz force. Figure 3.4 shows the simulation configuration and results for electrons (left) and protons (right) of various incident energies. The plots are shown on a 10 cm by 10 cm grid with a cross-section of REPTile superposed. For both plots, the bar magnet is represented by the black circle at the [0, 0]. The strength of this magnet is 0.3 A-m^2, which is the same as we are using for the MACS, and the field from this magnet is estimated as that of a dipole. Test particle trajectories are shown for the incident energies labeled in the legends, and the initial conditions for these particles are an initial position of +1 meter in the X-direction with a velocity corresponding to their energy and in the negative X-direction. From the results, it is clear that the trajectories for the energies we are concerned with (i.e. 500 keV to >3 MeV for electrons and 10 to 40 MeV for protons) are not significantly affected through the detector stack. Additionally, this simulation represented a worst-case scenario in which the bar magnet was placed only 2 cm behind the center of the instrument. In the current configuration, the bar magnet is more than 6 cm away and far off-center from the instrument. We have re-run these simulations using this configuration and have shown that the resulting particle trajectories are affected even less (as expected concerning the extra distance between the detector stack and

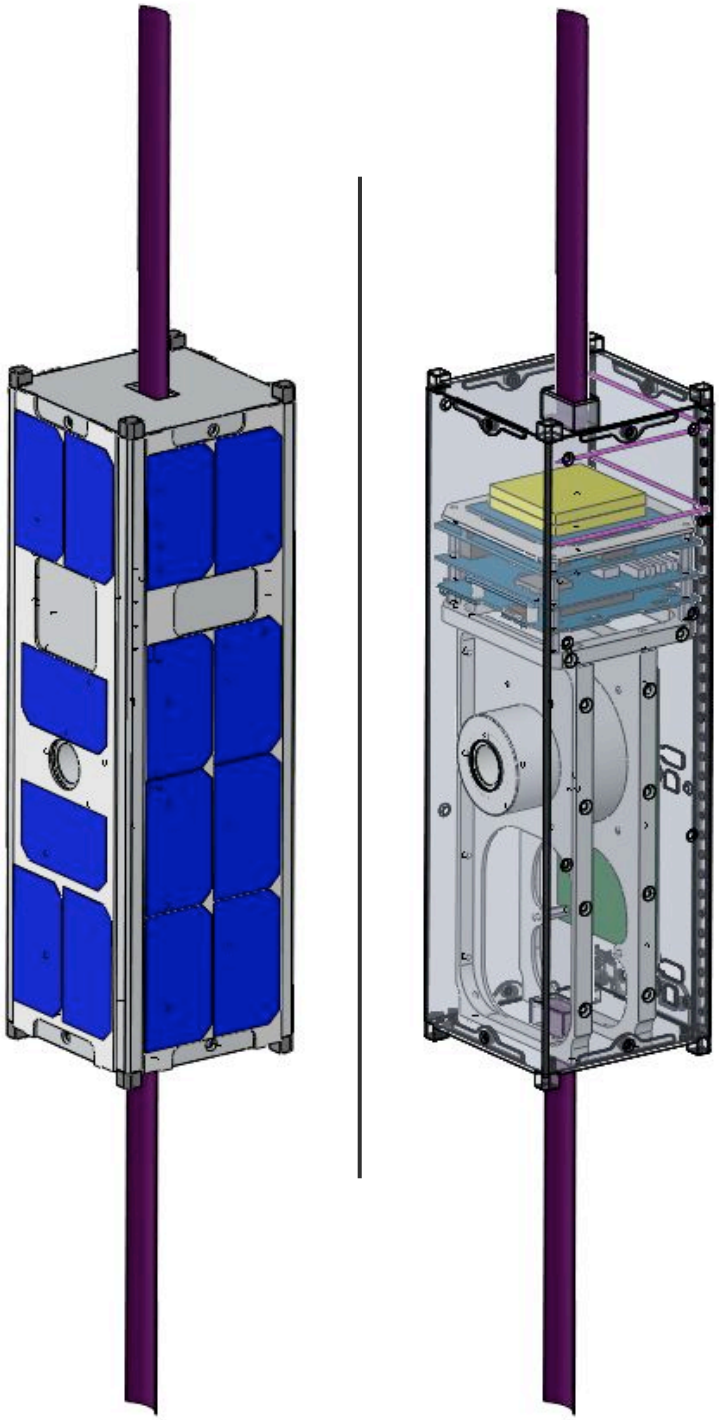

Figure 3.3: CSSWE's CubeSat bus showing the exterior (left) and interior (right). See text for details.

the bar magnet) and are more than acceptable concerning the instrument performance.

CSSWE is one of six CubeSat missions to be selected for funding and support from the National Science Foundation (NSF). We need to have a flight model ready for delivery by the end of 2011 for an early 2012 launch date. One of the reasons for this NSF support is that CSSWE with REPTile will be able to provide complementary scientific data for NASA's Radiation Belt Storm Probes (RBSP) mission, which is also scheduled to launch in early 2012. The REPT instrument on RBSP provided the basis for the REPTile instrument design, and REPT will measure outer radiation belt electrons from 4 to 10 MeV and protons from 20 to 75 MeV. However, being in low-inclination, highly-eccentric orbits with altitude of perigee near 500 km and altitude of apogee near 30,600 km, the two RBSP spacecraft will stay near the equatorial zone and their instruments will be unable to fully resolve the outer belt electron loss cone. For example, the loss cone near the magnetic equator at L = 4.5 is only around 5 or 6 degrees while the field of view for REPT is around 30 degrees. However, CSSWE will provide SAMPEX-like measurements from its high-inclination low-Earth orbit, and this data can be used to study electron loss. Figures 3.5 and 3.6 show an estimate of the RBSP spacecraft orbits with the CSSWE orbit simulated in Satellite Tool Kit. In these figures, the two spacecraft are at similar longitudes with CSSWE being at high latitude and thus in or near the horn of the outer belt and the RBSP spacecraft near their apogees in the heart of the outer belt. During such conjunctions, even more interesting science can be conducted, like the scattering effects of various waves on outer belt electrons for example. Whenever the two spacecraft are in conjunction concerning electron PSD for fixed first and second invariants, the data will also be very useful for data reanalysis efforts [e.g. *Shprits et al.*, 2007a; *Kondrashov et al.*, 2007; *Koller et al.*, 2007].

3.3 Measuring Energetic Particles

Accurately measuring energetic particles is complicated due to the complex interactions of individual particles moving through a material. Protons, being relatively massive compared to electrons and positrons, are generally well behaved, and their energy loss through a material can

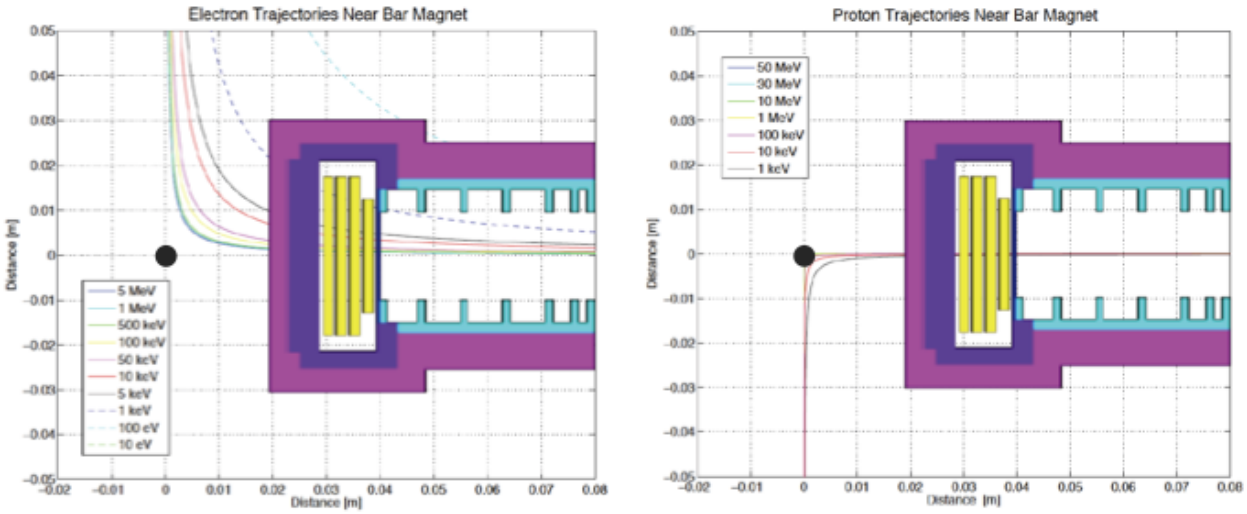

Figure 3.4: Results from relativistic test particle simulations for the MACS bar magnet near the REPTile instrument. Results are given for both electrons (left) and protons (right) of various incident energies (as labeled in legend). The bar magnet is located at the origin with the black circle, and a REPTile model has been included to show the particle tracks with respect to the detector stack.

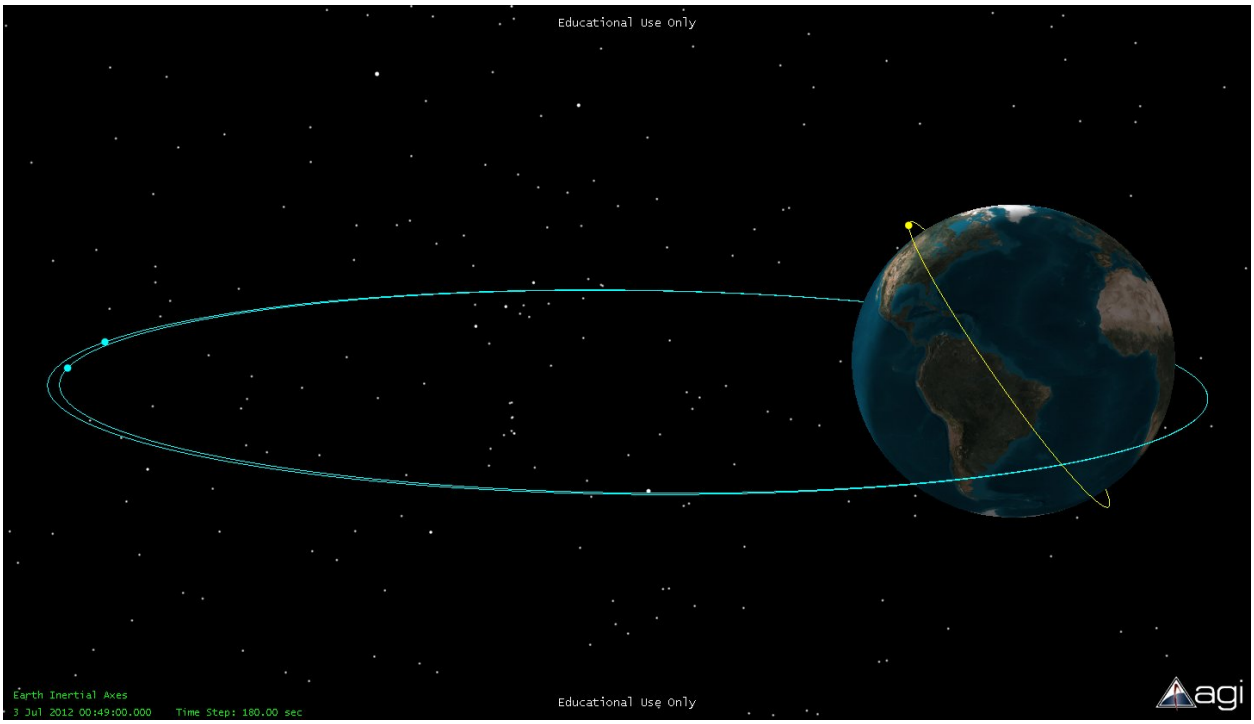

Figure 3.5: Satellite Tool Kit simulation showing the two RBSP spacecraft in their low-inclination, highly-elliptical orbit (light blue) with the CSSWE mission in its high-inclination, low-Earth orbit (yellow). Dots mark the current spacecraft positions here. CSSWE with its REPTile instrument will provide a complementary data set to RBSP.

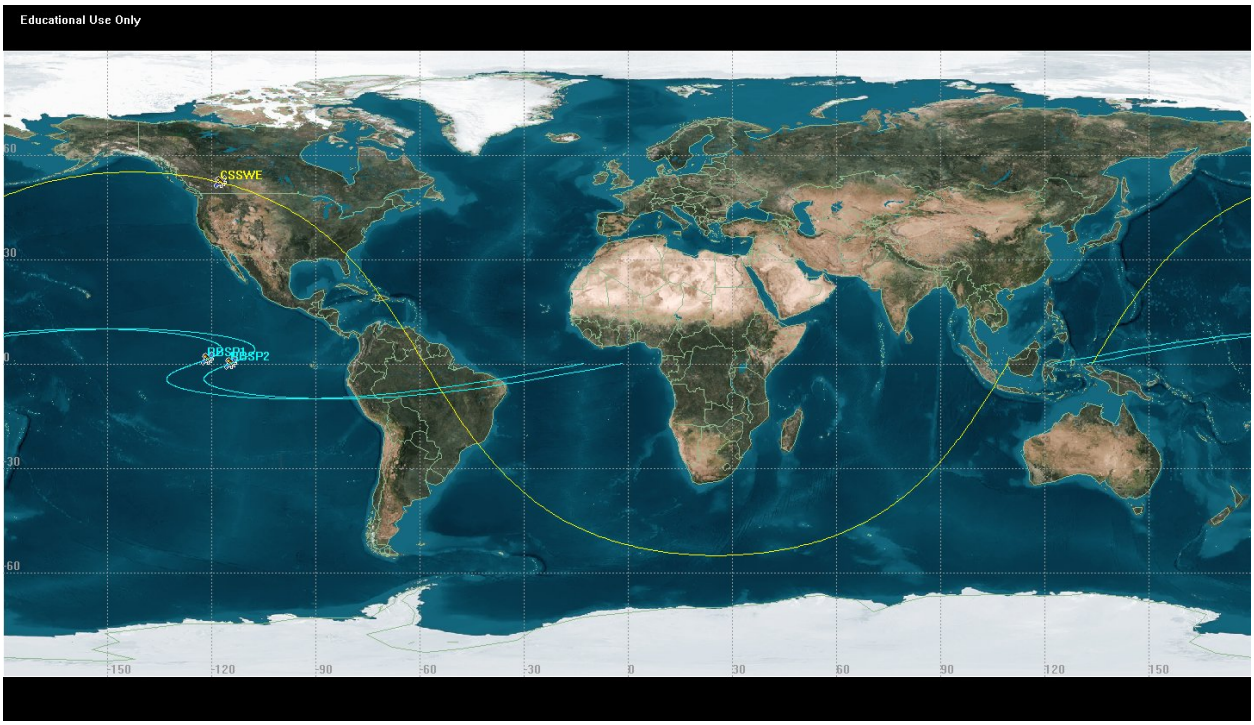

Figure 3.6: Ground tracks of the Satellite Tool Kit simulation from Figure 3.5.

be estimated statistically by the quantum mechanics based Bethe-Bloch formula [*Leo*, 1987]. This formula estimates energy loss as a result of inelastic collisions with atomic electrons and is only valid for "heavy" particles (e.g. protons, α-particles, and heavier ions). However, this formula is not valid for electrons and positrons, which are significantly more affected by deflections from their incident path than are protons. These deflections are primarily the results of: inelastic collisions with atomic electrons in the material (which can result in excitation or ionization of the host atom); elastic scattering from nuclei; emission of Cherenkov radiation; nuclear reactions; and bremsstrahlung emissions (i.e. the generation of high-energy photons caused by an electron accelerated in a curved trajectory) [*Leo*, 1987].

Vampola [1998] discusses the difficulties in measuring energetic particles such as electrons and protons. As mentioned above, protons will pass through a material with minimal deflection from their original trajectories and depositing calculable amounts of their incident energy. However, very high energy protons have the ability to penetrate through any reasonable amount of instrument shielding and can thus contribute a significant amount of noise to a detector. On the other hand, energetic electrons up to around 10 MeV are easily shielded by reasonable amounts of material, but their trajectories scatter erratically through a material. For example: when incident upon an aluminum surface, up to 25% of electrons will be diffusely backscattered from the surface [*Vampola*, 1998]. Due to this scattering of incident electrons, the response of a detector to individual, mono-energetic electrons is highly inconsistent. For this reason, the response of an instrument to energetic electrons must be treated in a statistical sense.

A properly designed relativistic particle instrument should consider the scattering properties of electrons as well as the shield-penetrating capabilities of energetic protons. Unfortunately, these can sometimes be overlooked in instrument design. As *Vampola* [1998] points out bluntly: "Few investigators who have flown energetic electron spectrometers have really understood the behavior of their instruments", and this is primarily due to a lack of understanding of their instruments' responses to electron scattering and shield penetrating particles.

Vampola [1998] and *Leo* [1987] discuss different types of instruments and the strengths and

shortcomings of each. Of these, collimated and shielded "telescopes" encasing solid-state detector stacks are the most common type of instruments used for indirect energy measurement and classification of relativistic particles. However, these high-energy particle telescopes can be particularly sensitive to shield-penetrating protons, particularly from very high energy protons that can penetrate directly through the detector stack from outside of the field of view, effectively deceiving any coincidence logic that may be in use. Heavy shielding surrounding the detector stack will minimize shield-penetrating particles, but due to mass restrictions for space missions, a balance between shield thickness and detector noise must be accommodated and accounted for in the resulting data. Another significant source of noise can arise from the collimator design. A poorly designed collimator will allow electrons from outside of the field of view to scatter into the detector stack where they can then be falsely included as signal electrons.

The generation of secondary particles in shield alloys must also be taken into account. High-Z materials, when bombarded by incident radiation, produce larger amounts of energetic secondary particles compared to those generated in low-Z materials. Unfortunately in this regard, dense materials, which serve as the best shields for blocking high-energy particles, tend to also be high-Z materials. Thus, an adequate shield design must take thickness and density (i.e. mass) and molecular or atomic composition into account, and the noise from any secondary particles generated in the shields should be estimated and accounted for in the resulting data.

The most common types of detectors used in energetic particle telescopes are made of a semiconducting material, like doped silicon[*Leo*, 1987]. When an incoming energetic particle hits a silicon detector, it results in an electron-hole pair generation consisting of a free electron and the remaining ion from which it was released (i.e. the "hole"). A bias voltage applied across one of these detectors accelerates the freed electrons to an anode where they can be measured and amplified by appropriate sensitive electronics. This amplified electronic signal can then be analyzed further to determine particle type and approximate incident energy in incremental counting bins, which are the raw data produced by an instrument.

In the following sections, I introduce the REPTile instrument, which accounts for all of

the above-mentioned design difficulties, yet is small enough to be incorporated onto the CSSWE CubeSat.

3.4 Early Design Issues and Probing the Design Space

The first iteration of the REPTile instrument (first several iterations designed by myself, Ian Crocker, Joey Espejo, and Carl Seubert) consisted simply of a scaled down version of the REPT instrument. The field of view remained the same, while the instrument dimensions were reduced and the shield thicknesses scaled by a factor of one half. The original design included 8 detectors like REPT. The SolidWorks image shown on the left in Figure 3.7 shows one of the first iterations of the instrument design including only 4 detectors. The image on the right in Figure 3.7 shows a later iteration, which was a redesign to account for commercially available detectors. The detectors required for the first iteration would have to have been custom design and fabrication, which was impossible given the project budget. Note that the collimator in this iteration is long, which closed the field of view, and at 5 mm each, the detector casings were twice as thick as those used for REPT (even though their diameter was much less), which elongated the instrument significantly, even when the number of detectors was reduced to 4.

This second iteration was designed to measure electrons from 1 to 5 MeV and protons from 19 to 51 MeV. These energy ranges were achieved given the thickness of the silicon detectors (1.5 mm) and a 2 mm thick beryllium window at the entrance to the detector stack, which regulated the cutoff energy at which each type of particle could penetrate into the detector stack. Data from particle instruments are most often provided as flux, which has units ($\# \cdot cm^{-2} \cdot sr^{-1} \cdot s^{-1} \cdot keV^{-1}$) (for differential flux; integral flux is also used and is similar but without the energy units, i.e. keV) and can be thought of as a measurement of particle irradiance. A critical instrument parameter for particle flux measurements is the geometric factor, which is defined by the geometry of the instrument's field of view, collimator, and detector stack. The geometric factor is determined by approximating the entrance aperture as a surface source of area A_1 that radiates onto the detector of area A_2 using the appropriate surface and solid angle double-integral that accounts for the areas

shapes and distance of separation. A measurement of flux from an instrument consists of the raw data (i.e. particle intensity in the form of detector count rates) divided by the geometric factor of the instrument. The geometric factor for the first iteration of the REPTile design was 0.05 cm^2sr.

To estimate the instrument performance, we once again followed what was done for REPT and resorted to using Geant4. Geant4 was developed by physicists at the European Organization for Nuclear Research (CERN) to use Monte Carlo techniques to simulate particle interactions in matter. As a design tool, it has been employed throughout the realm of energetic particle physics, including the Large Hadron Collider (LHC), the Tevatron at FermiLab, the Gamma Ray Large Area Space Telescope (GLAST), and of course REPT for RBSP. It has been shown again and again to very accurately model complex particle interactions *in a statistical sense*, and it is ideal for our requirements to estimate REPTile's response to the relativistic electrons and protons found in LEO since we are unable to take any prototype instruments to a particle beam facility for testing. For further details on Geant4, which is freely available, see CERN's website for the toolkit: geant4.web.cern.ch.

With this powerful toolkit in hand, we (myself, Ian Crocker, Jianbao Tao, and Quintin Schiller were all involved in Geant4 testing at different points in the development) started to get a sense for the performance of our instrument given its design. Figure 3.8 shows an example of Geant4's visual output, which is useful to verify that the simulation is set up properly. In the top part of the figure, a beam of 12 MeV electrons (e^-) is being shot from the bottom left up into the instrument through the shields. This clearly shows the random behavior of electrons. Note that upon entering the aluminum shielding on the outside of the instrument (purple) the electron beam fans out as the individual electrons are scattered in different directions. A couple of the electrons even backscatter fully out of the aluminum and exit the view to the bottom and left parts of the view screen. Also, all of the green lines represent bremsstrahlung photons generated by electrons as they are redirected by near-misses with atomic nuclei. Note that the tungsten inner shielding (light blue) successfully blocks most of the electrons that make it through the aluminum layer. Only a few of the incident electrons penetrate into the detector stack (yellow rectangles). Protons, however, behave quite

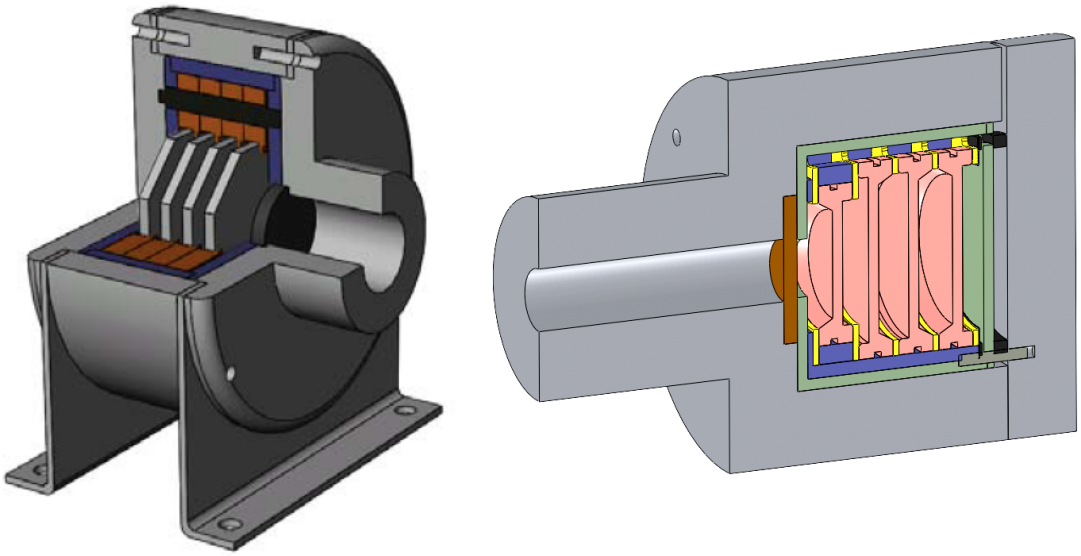

Figure 3.7: Two previous iterations of the REPTile instrument design. See text for additional details.

different, as can be seen in the bottom part of the figure. Here, a beam of 100 MeV protons is shot at the same angle as the electrons were in the top half. Upon encountering the aluminum shielding, the protons penetrate through it with minimal deflection. They also generate a cloud of electrons (shown in red in the material sections) around them as they pass through the material and knock electrons off of the atoms they pass close to. They continue through the tungsten shielding and detector stack in much the same manner before fully depleting their energy and embedding themselves in the back shielding. The electrons that they free in the detectors are those that are collected and measured by the electronics. This is a simple example of how energetic protons can be a significant source of noise in a particle instrument.

By setting up Geant4 simulations using thousands of particles, we developed a sense for the statistical behavior of our instrument. One of the first challenges was to determine how the instrument electronics could distinguish between protons and electrons. To do this, we decided to use the energy deposition. Based on the simulations, signal protons with energies in the 10's of MeV range consistently deposited above a certain energy in the detectors. Similarly, the majority of electrons deposited energy within a range that was lower than this proton energy. This can be seen more clearly with the energy deposition histograms in Figure 3.9. Here, energy deposited is on the X-axis, while the Y-axis is the number of particles (with fixed incident energies, electrons in black, protons in red) to deposit that energy in each detector, numbered D1-D8. So, for 4 MeV electrons, the majority will penetrate through to the fifth detector depositing somewhere between 0.35 and 2 MeV in each detector. Obviously, an incident particle can only deposit as much energy as it has initially, so those 4 MeV electrons that deposit 2 MeV or more in a detector have probably scattered a lot in that detector and expend most of their energy there. Next, notice that the protons deposit much more energy in each detector, and until the 4th and 5th detectors, their deposition energy range is not as spread out as it is for the electrons. Note too that the deposited energy in each detector actually increases as the protons pass further into the detector stack. These results are as expected for protons. High energy protons will initially pass through a material depositing very little energy in it due to their very high momentum. However, as they begin to slow down, they

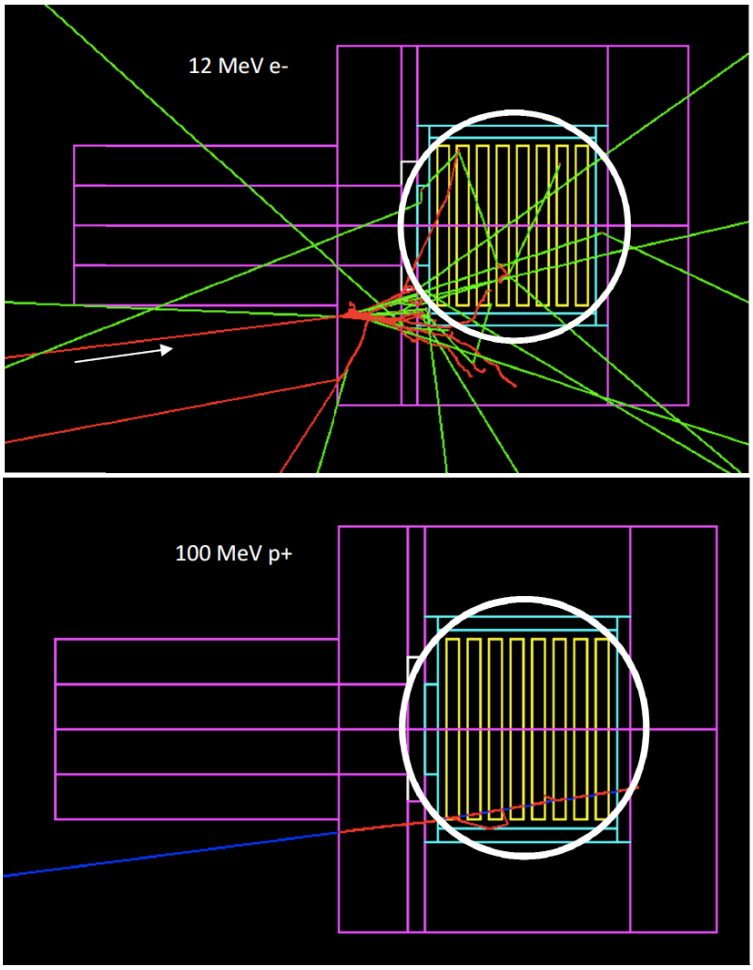

Figure 3.8: Shield penetrating shots through an early iteration (note the 8 detectors like REPT) of the REPTile design. Incident particle types and energies are listed in the upper left of each simulation, and the detector stack is circled in white. Electrons are shown in red, protons in blue, high energy photons in green, and the various instrument materials in the other colors. The arrow in the electron image denotes the incident beam from a reflected electron track below it. Note that this is a 2-dimensional projection of 3-dimensional model and results. Figure from Ian Crocker's Spring 2008 final report.

are more affected by the electrostatic forces from atomic nuclei in the material and begin to lose more energy and eventually scatter. Based on these deposition profiles for particles in the energy range to be detected by REPTile, we established a set of logic to determine the particle type based simply on the energy deposited in each detector. Basically, if a particle deposits energy between two lower-energy bands (e.g. 0.35 and 2.5 MeV for the example in Fig. 3.9), then the particle is classified as an electron. Meanwhile, if a particle deposits above some specified higher-energy threshold (e.g. 4.5 MeV from Fig. 3.9), then the particle is classified as a proton. This is the logic we decided to employ for REPTile, and it is discussed in detail in the Current Design section.

Geant4 simulations were also used to determine the energy bins for each particle. Once again referring to Figure 3.9, it is clear that the 4 MeV electrons and 40 MeV protons only penetrate through the detector stack to the fifth detector. Some of the electrons get through to the 6th and 7th detector, which is a result of the more erratic behavior of electrons, and the consequence of this is more uncertainty in the electron measurements. However, the majority of the 4 MeV and practically all of the 40 MeV protons penetrate through to the 5th detector *and* deposit the appropriate amount of energy to classify the particle type as was just discussed. This is exactly how the instrument's energy bins were determined. When the simulations are run over the full range of energies, the energy bins can be classified by finding the range of energies for both types of particles that are fully stopped by each detector. So for the example here, 4 MeV electrons and 40 MeV protons would be classified into the fifth energy bin since the majority of them pass through the detector stack and are stopped in the fifth detector. Note that this incorporates coincidence logic into it. In order to count as a fifth energy bin proton in this example, an incident proton would have to deposit more than 4.5 MeV in not only detector 5, but each detector in the stack before that too (i.e. D1-D4). This coincidence logic is particularly useful at reducing noise and will be discussed further in the Current Design section.

With this logic established, we could start estimating count rates for each detector by as-

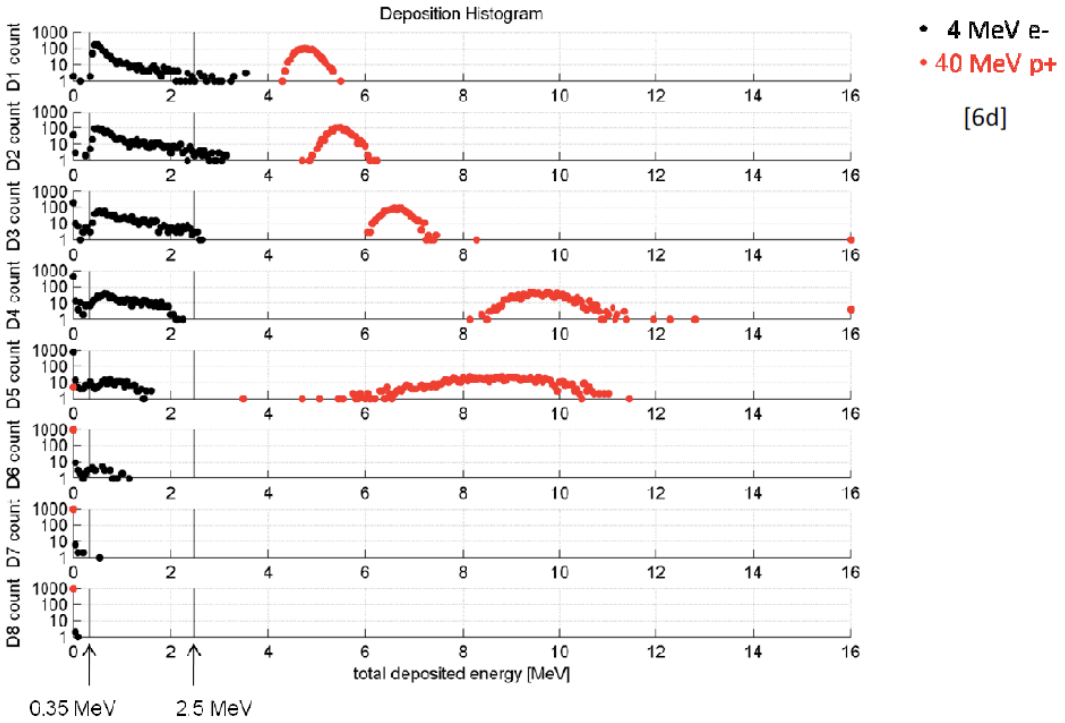

Figure 3.9: Energy deposition histograms for the early iteration, 8-detector configuration of REP-Tile. Plots are ordered by detector number with D1 being at the front of the stack adjacent to the collimator and D8 at the back adjacent to the shields. Electrons with incident energy of 4 MeV are shown in black and protons with incident energy of 40 MeV are shown in red. Figure from Ian Crocker's Spring 2008 final report.

suming environmental fluxes and using the following equation:

$$C_i = \int_0^\infty j\left(E\right) \cdot \gamma \cdot \epsilon_i\left(E\right) \cdot dE \tag{3.1}$$

where C_i is the count rate on the i^{th} detector in units of number per second, $j\left(E\right)$ is the environmental differential flux for particles of energy E (same units as mentioned above), γ is the instrument's geometric factor (units of cm^2sr), and $\epsilon_i\left(E\right)$ is the i^{th} detector's efficiency to particles of energy E (unitless). The environmental fluxes used for all our analyses are the AE-8 Max model and a solar energetic proton spectra from *Mewaldt et al.* [2005]. These flux spectra can be seen in Figures 3.10 and 3.11. The geometric factor was calculated using the instrument geometry, and the detector efficiencies were calculated using Geant4 with the appropriate particle-type, coincidence, and binning logic applied to the results. With all this in place, we estimated the expected signal count rates on each detector and ensured that the instrument electronics would be fast enough to process these without significant bunching.

Once we established the instrument's performance for signal particles, we had to determine how it would perform if it were irradiated with energetic particles from all directions. Basically, we needed to determine the instrument's signal-to-noise ratios (SNR). Our first attempt at this was to take shots through the shields from one angle and assume the response from the detectors would be similar to particles entering in from other angles. As two worst-case scenarios, we started by shooting "noise" particles directly through the back shields and on an angle through the shields below the collimator (as can be seen in the proton shots in Fig. 3.8). These represent worst-cases since particles along these trajectories that can penetrate through the shields have direct access to the detector stack in such a way that they can penetrate into several detectors and possibly trick the electronic logic into thinking they are signal particles. To handle the case where particles would come in through the shields at the front of the instrument, we decided to use a smaller first detector. This way, very few particles would hit it after penetrating through the front shields, and with the coincidence logic in place, if the first detector was not triggered, then the remaining hits on the other detectors would not be counted. Using the geometry shown in Figure 3.12 with the smaller

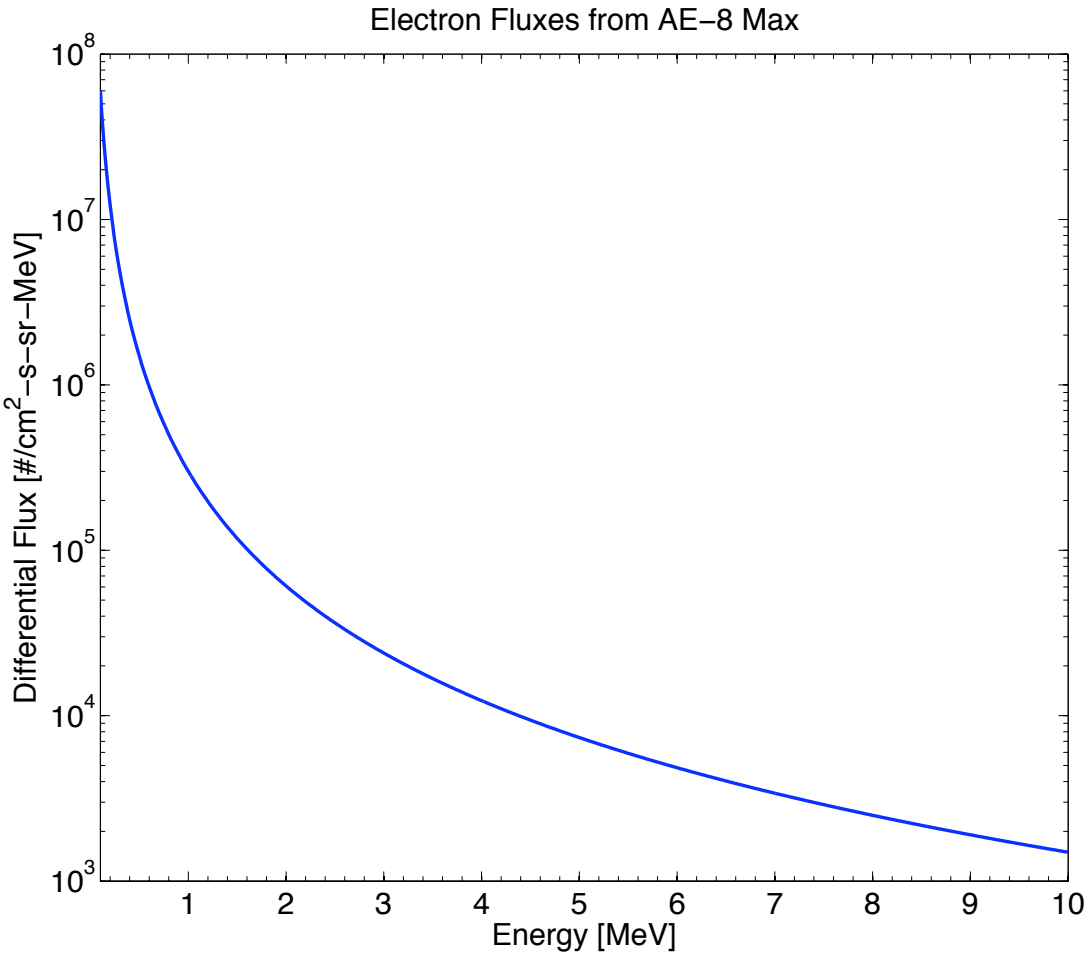

Figure 3.10: Electron fluxes used to simulate the spacecraft environment. These are from the AE-8 Max model.

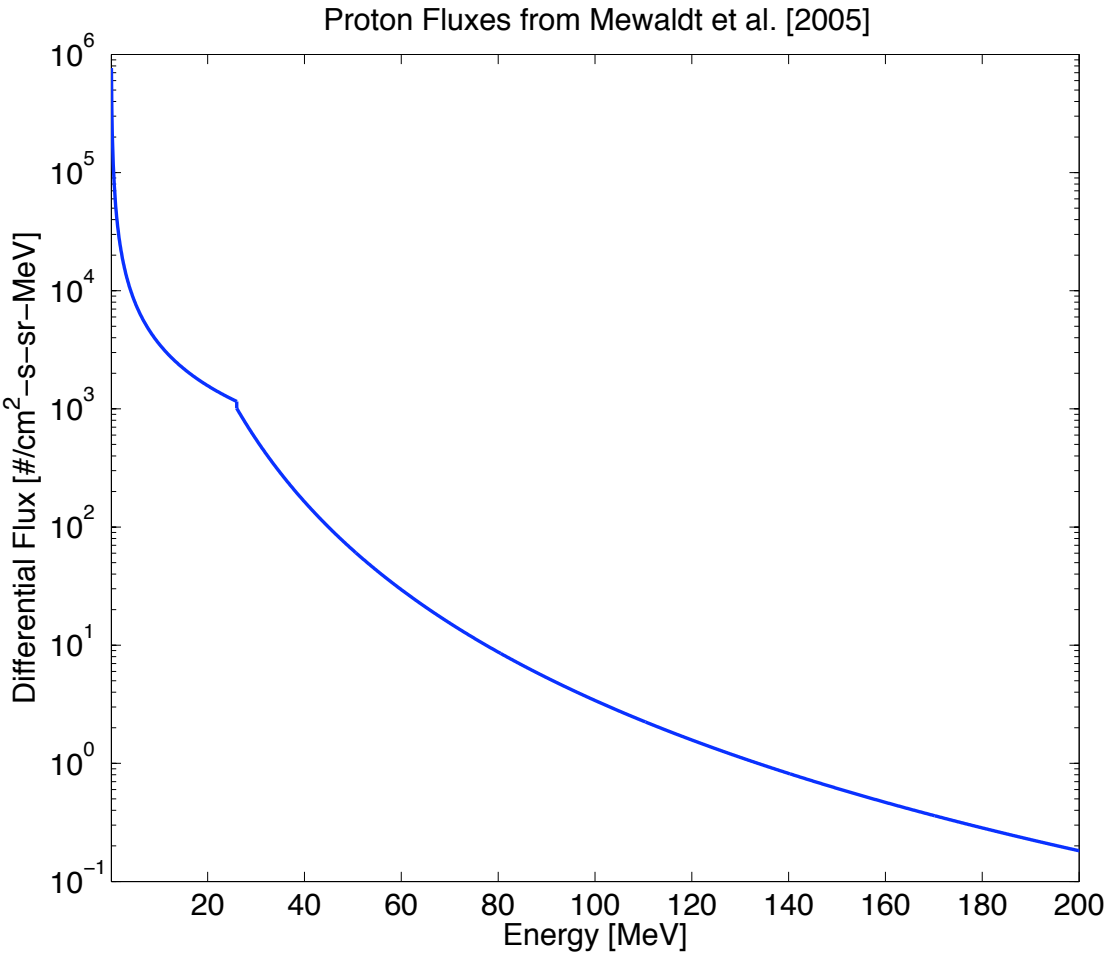

Figure 3.11: Proton fluxes used to simulate the spacecraft environment during SEP events. These are from the observations made by *Mewaldt et al.* [2005] for the Halloween storms in 2003.

first detector and only four commercially available detectors in the stack, it became very quickly apparent that our shielding was insufficient concerning the particles that could come in through the back of the instrument. The simulations showed us that protons from around 80 - 100 MeV were at just the right energy to pass through the shields and give up enough energy to then pass through all four detectors and appear as signal protons. This problem was not an issue for the electrons, but the instrument as designed in Figures 3.12 and 3.7 (right) would not work for protons. Based on the *Mewaldt et al.* [2005] fluxes for SEPs and the geometric factors for the collimator (signal) and back shield plates (noise), the count rates would range from 6 - 32 protons per second from the collimator (in large part due to the thick Be-window and small geometric factor) and 500 - 600 protons per second through the rear shields (primarily due to their inadequate thickness and large geometric factor). A serious redesign was required to make REPTile work for solar energetic protons.

To address the redesign, I spent a considerable amount of time probing the instrument design space. The critical parameters that I identified were: the instrument mass; the geometric factor; the diameter of the detectors; the collimator length; the collimator inner diameter; the field-of-view; the tungsten shielding thickness; the aluminum shielding thickness; the instrument's total length; the number of detectors; and the thickness of the detectors. From these I developed a system of equations to determine the dependent and independent variables in the system. For example, the detector mass depended on the shielding thicknesses, the number of detectors, the thickness and diameter of the detectors, and the collimator length and inner diameter. The other dependent variables were the instrument length (dependent on the collimator length, detector thickness, number of detectors, and shielding thicknesses), the geometric factor (dependent on the collimator length and diameter, the detectors' thickness and diameter, and the number of detectors), and the field-of-view (dependent on the collimator length and diameter). Another factor that played a critical role was the beryllium window, which has a large role in controlling the signal count rates. Basically, a thinner window allows lower-energy particles to penetrate into the detector stack, and there are many more particles at lower energies than there are at higher-energies, which

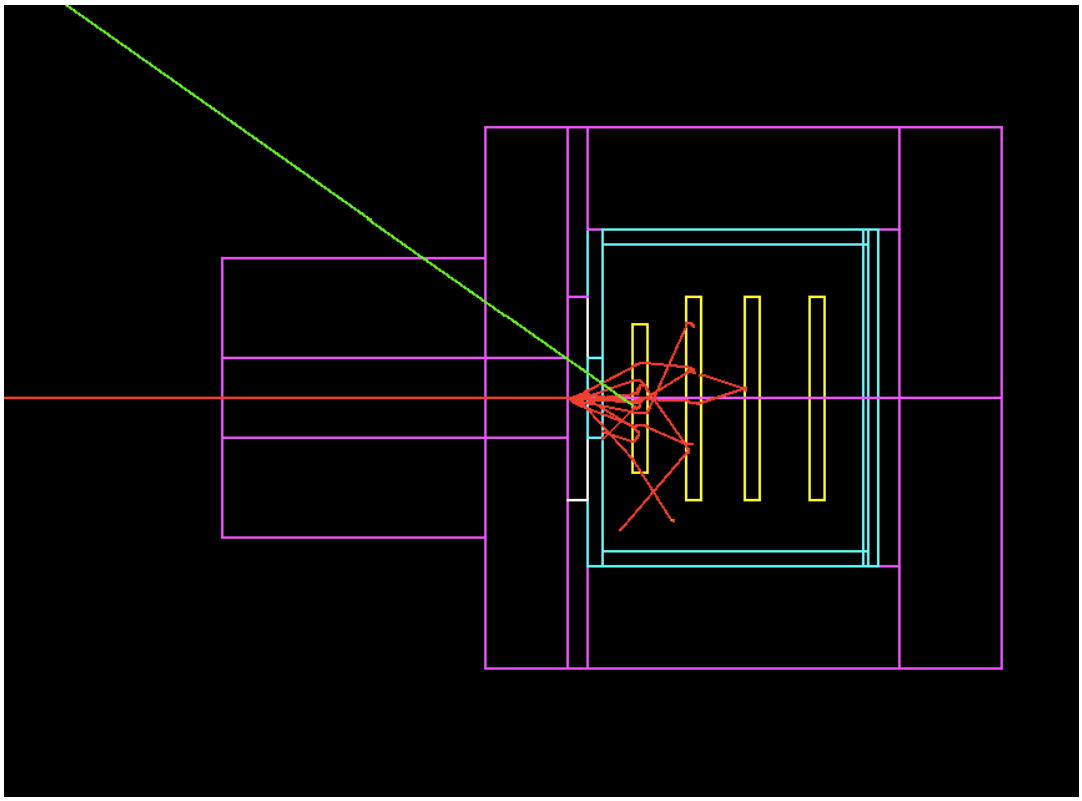

Figure 3.12: 2 MeV electrons shot down the bore-sight of an early iteration of the REPTile design. It was with this design that we used Geant4 to prove that the instrument would not perform adequately based on the requirements. Figure from Ian Crocker's Fall 2008 final report.

are responsible for the noise.

There were many constraints to consider as well. For example, the instrument mass and volume were strictly restricted because of the requirements for the CubeSat. This seriously restricted the amount of shielding we could use, particularly the more effective tungsten inner shielding. Also, we wanted to maintain a reasonable field-of-view. After discussions with Professor Li, it was decided that we should aim to have a field-of-view that was less than or equal to that of SAMPEX (i.e. 58 degrees), since this is important to resolving electrons in the loss cone. Since there were so many factors and variables involved with no hard constraints and the process involved going back and continually recalculating new SNR based on each new design, I decided not to handle this with numerical optimization schemes but with an exploration of the available design space. This allowed me to converge on an intelligent solution that satisfied the requirements for our problem, namely, an instrument with reasonable mass, volume, and field-of-view that allowed for an acceptable level of SNR for the proton and electron channels.

To do this, I developed a series of MATLAB scripts and functions that used the following variables as input: aluminum and tungsten shield thicknesses, number of detectors, detector thickness, and the length and inner diameter of the collimator. These functions output a total instrument mass estimate, total instrument length, geometric factor, diameter of the last detector (which really defined the inner diameter of the shielding around the detector stack), and the field-of-view. I employed NIST's eStar and pStar tools (see: $http://www.nist.gov/physlab/data/star/index.cfm$) to get initial estimates for shield thicknesses. These online tools use the Bethe-Bloch formula to estimate penetration depths and energy deposition for electrons and protons through certain materials. Figure 3.13 shows examples of the results from these estimates. The plots show the energy of a particle versus its incident energy for various aluminum/tungsten layered shield configurations provided in the legend. The layered combinations for aluminum (blue) and tungsten (black) are denoted by the same symbol, and all of the runs have a total shielding thickness of 1.15 cm. The numbers before the material type in the legend show the thickness of that material for each run. For example, given 1.0 cm of Al and 0.15 cm of W (denoted by the circle symbols; these thicknesses

are the same as those in the first iterations of the REPTile design), a 60 MeV proton loses around 30 MeV in the Al-shielding and around 15 MeV in the W-shielding. This leaves it with around 15 MeV of energy after passing through all the shielding and entering into the detector stack, which is more than enough energy to trigger as valid hits on the detectors. Note that above a few hundred MeV, protons lose minimal amounts of energy through even a full 1.15 cm of tungsten shielding. This is a good example of how protons above a certain energy can simply not be adequately shielded with reasonable amounts of material. The eStar (electron) tool is not nearly as accurate as pStar (protons) because of the Bethe-Bloch approximations mentioned previously.

Based on what we had learned from the Geant4 simulations given our previous geometry (i.e. Fig. 3.12), we knew that we had to make the shields thicker, particularly the tungsten inner shield as this was most effective at stopping and slowing protons. The pStar energy loss curves (e.g. Fig. 3.13) combined with the reference proton flux-energy spectrum (Fig. 3.11) and the MATLAB tools for the instrument parameters allowed me to estimate a shield combination that could work for our system. Another large improvement to the SNR came when I decided to make the beryllium window thinner, allowing for a significantly higher signal count rate for both electrons and protons though changing our energy ranges. Since we were also restricted to commercially available detectors, I decided that we should aim to get the thinnest detectors possible, as this minimized the instrument length and thus significantly affected the mass because of the shielding materials. This led us to go with the same detectors that are being used for RBSP's REPT, which was also beneficial given the amount of experience the LASP engineers had with these detectors. Finally, I settled upon a geometry for the instrument that satisfied our various requirements, including the SNR. The latest version of this design is described in the following sections.

3.5 Current Design

The current design of the REPTile sensor is shown in Figure 3.14. The sensor comprises a stack of silicon solid-state detectors in a telescope configuration enclosed in aluminum and tungsten shields. A collimator sets the field of view to a circular cone of ∼52°. A 0.5 mm beryllium (Be) disc

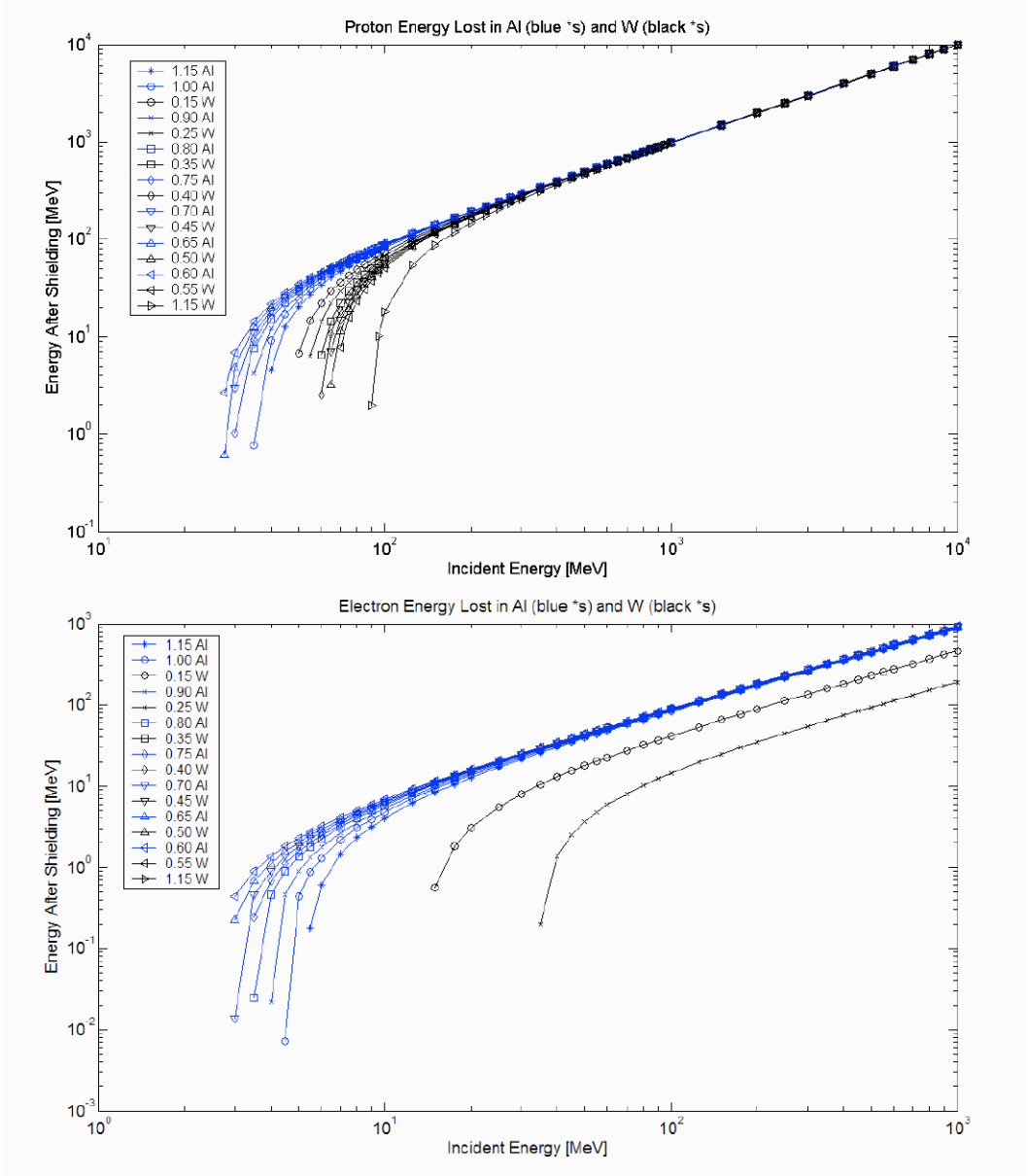

δ_{Al} [cm]	1.15	1.00	0.90	0.80	0.75	0.70	0.65	0.60	0.00
δ_{W} [cm]	0.00	0.15	0.25	0.35	0.40	0.45	0.50	0.55	1.15
m [g]	261.4	379.4	470.9	573.4	628.9	687.5	749.1	813.8	1864

Figure 3.13: pStar and eStar estimates for energy lost by protons (top) and electrons (bottom) through various shield thicknesses (in cm) and combinations of material as specified in the legends. The particle incident energy is plotted along the X-axis, while the energy after passing through each layer of shielding is plotted on the Y-axis. Aluminum (blue) and tungsten (black) curves that use the same symbol imply that a layered shield was employed consisting of an outer layer of aluminum and an inner laying of tungsten. Estimates for the mass of the instrument for each combination of thickness/material are shown in the table at the bottom.

located at the detector-end of the collimator (shown in light blue in Fig. 3.14) stops electrons below ∼400 keV and protons below ∼10 MeV (initially from continuous stopping distance approximations and confirmed or corrected with Geant4 simulations). The solid-state detector stack is made up of 4 separate detectors with a total thickness of 1 cm (6 mm total of silicon, shown as light green discs: 4 discs at 1.5mm thickness each) and can measure electrons in four energy channels starting at 0.5 MeV to >3 MeV and protons in four channels with energies from 10 MeV up to 40 MeV. These silicon detectors are the same as those developed for the REPT instrument and are available from Micron Semiconductor. A 3.5 mm thick tungsten (W) layer of shielding surrounds the detector stack (dull green in Fig. 3.14), which is further encased by an outer aluminum (Al) layer that is 5 mm thick (shown in dull blue-gray). This shielding effectively stops energetic electrons below ∼20 MeV and protons below ∼90 MeV from entering the detector stack from the sides, while thicker tungsten shielding (an extra 2 mm) in the back further increases the particle energy needed to penetrate the stack and significantly improves the signal to noise ratios. Higher energy (>15 MeV) electron flux is low along CSSWEs reference orbit in LEO and most protons with sufficient energy to penetrate the shields will pass through both the shielding and the sensor leaving only minimal deposited energy. The collimator acceptance angle, cross section, and the Be-window limit the flux at the detector to rates manageable by a standard electronics design, nominally on the order of 10^4 per second rising to less than $\sim 5 \times 10^5$ per second during population enhancement events.

Figure 3.15 shows an exploded view of the instrument, revealing all of its components. There are 27 individual components in the instrument assembly, and of these 15 are unique pieces. By unique pieces, I mean that the remaining 12 pieces are identical copies of one of the unique pieces. I discuss the assembly in more detail in the Manufacturing section.

The above design is based heavily on simulations using Geant4. We carried out full sensor simulations to estimate the amount of energy particles lose through their various interactions with the instrument materials, with numerous consultations with and reviews by LASP engineers and scientists. Figure 3.16 shows the current REPTile instrument built-up in Geant4 for four different simulation runs. We estimated the instrument's performance using these simulations. Figure 3.16

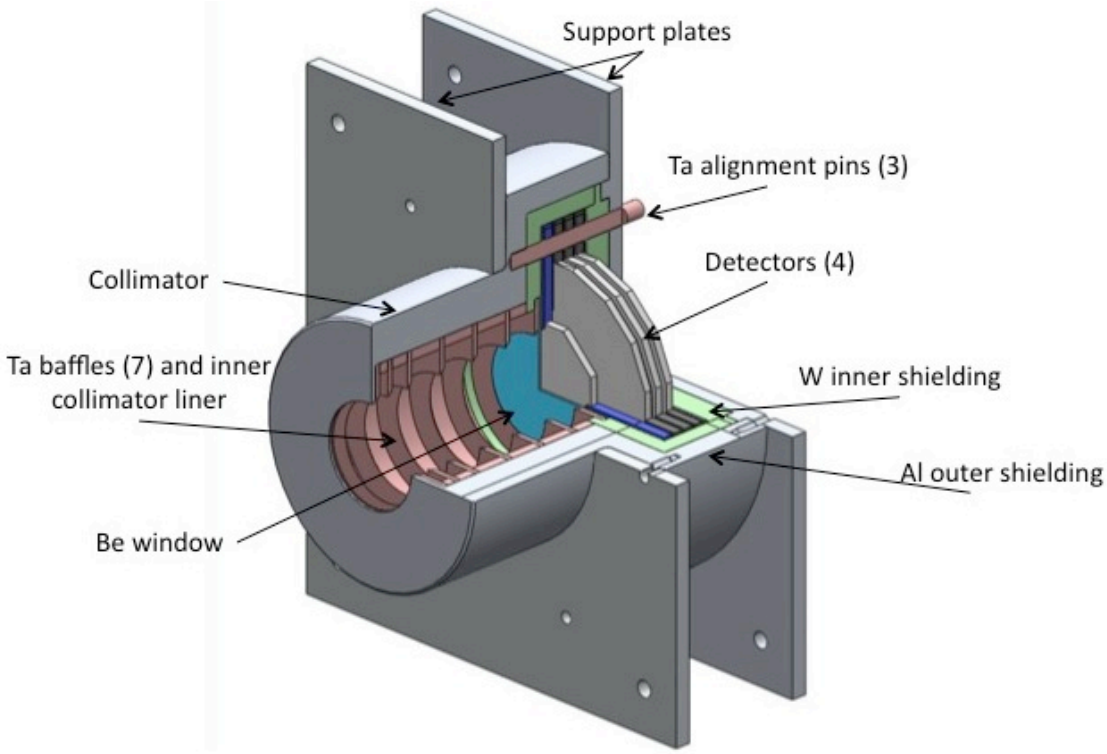

Figure 3.14: Cross section of the REPTile instrument. Different materials are shown in different colors and labeled. See text for additional details.

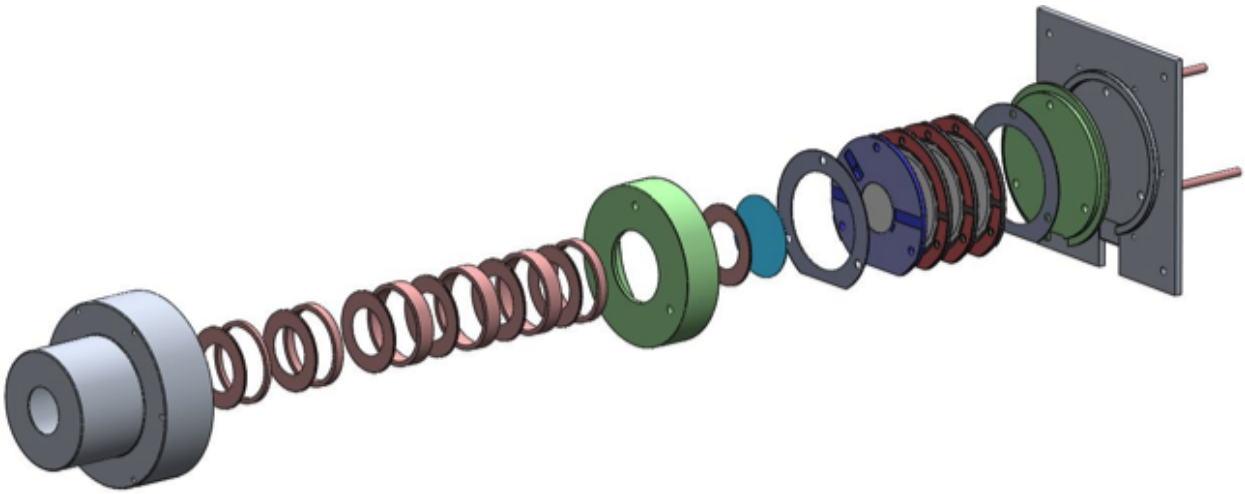

Figure 3.15: Exploded view of the REPTile instrument. See text for additional details.

Table 3.1: REPTile instrument binning logic to determine particle type and energy range. Particle type is determined based on the deposited energy (E_{dep}) logic in the header. A "1" counts as a valid hit on any given detector (Det.) given the logic in the header and a "0" is an invalid hit.

	Electrons 1 if 0.25MeV $\leq E_{dep} \leq$ 1.4MeV		Protons 1 if $E_{dep} \geq$ 4.5MeV	
	Det. 1	Det. 2	Det. 3	Det. 4
Bin 1:	1	0	0	0
Bin 2:	1	1	0	0
Bin 3:	1	1	1	0
Bin 4:	1	1	1	1

clearly shows several examples of some of the effects we have discussed previously. For example, Fig. 3.16 b) shows how some high-energy shield-penetrating protons can fool the electronics into thinking they are lower-energy protons through the field-of-view. Shield-penetrating protons can also appear as electrons at higher energies since they deposit less energy in the instrument materials as they pass through. It also shows how narrow the proton scattering cone is and how that cone spreads as the protons lose more energy. Fig. 3.16 c) is another example showing how electrons scatter and backscatter and generate bremsstrahlung radiation, and Fig. 3.16 d) shows the effectiveness of the collimator baffles at stopping electrons from outside of the field-of-view from scattering into the detector stack.

The two types of particles will be distinguished by the amount of energy they deposit and their deposition profile. Based on the simulations, an incoming particle will be determined to be an electron if it deposits between 0.25 MeV and 1.4 MeV in the first detector and a proton if it deposits at least 4.5 MeV in the first detector. This logic is applied to each detector in the stack, and for a particle to be counted as a valid hit, it must register on all the detectors in front of it in the stack. For example, for a particle to be classified as a proton in the fourth energy bin, it must deposit at least 4.5 MeV of energy in the first through fourth detectors. Given this energy classification for particle type, this binning logic can be summed up easily with a table (i.e. Table 3.1), where a "1" counts as a valid hit on a detector and a "0" is an invalid hit on each detector:

Using the Geant4 simulations with this logic, we have generated statistics curves of detector

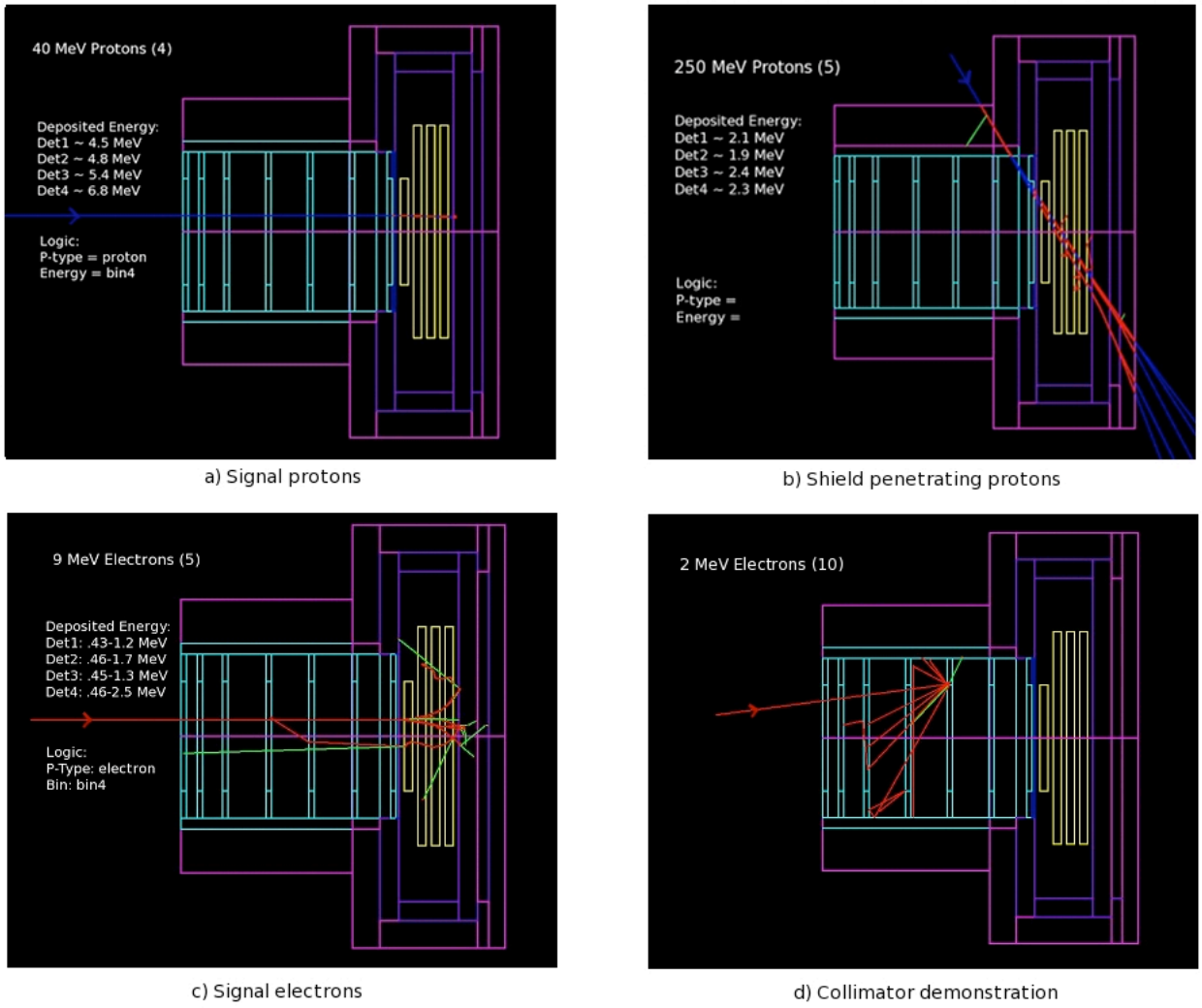

Figure 3.16: Four different particle beams incident on the REPTile instrument. For each, the average energy deposited on each detector and the instrument electronics interpretation of the detector signals in the form of particle type and energy bin is provided. The first (top left) shows signal protons incident through the field of view. Top right shows protons penetrating through the collimator and shielding and passing through the detector stack. The bottom left are signal electrons through the field of view, and the bottom right are electrons scattered in the collimator.

Table 3.2: REPTile energy bins for protons and electrons

	Bin 1	Bin 2	Bin 3	Bin 4
Electrons:	0.5 - 1.5 MeV	1.5 - 2.2 MeV	2.2 - 2.9 MeV	>2.9 MeV
Protons:	10 - 18 MeV	19 - 25 MeV	26 - 30 MeV	31 - 40 MeV

efficiency for particles at different incident energies, and from these curves, we have determined the electron and proton energy bins. Figure 3.17 shows detector efficiencies for electrons and protons of various incident energies coming through the collimator.

From the results in Figure 3.17, we determined REPTile's effective energy bins for both protons and electrons. These are shown in Table 3.2. Thus, from its high-inclination low-Earth orbit, REPTile will be able to measure electrons from 500 keV to greater than 3 MeV, which will provide outer radiation belt data for relativistic electrons with very low equatorial pitch angles when CSSWE is at high latitudes in the horns of the belt. With its proton capabilities ranging from 10 to 40 MeV in four differential energy channels, REPTile will also be able to provide SEP proton (and electrons) flux spectra related to different solar flares. Through the inner belt, REPTile may become significantly affected by shield-penetrating protons.

To better quantify the SNR for the current design, we chose a more elaborate technique that the one used for the previous iterations and described above. Once again, Geant4 was used to simulate the particle interactions with the various instrument materials. This time however, we shot the full range of particles through various different parts of the shields and throughout the collimator, both in the field-of-view and outside of it. In this way, we could get a much more realistic sense for the signal and noise count rates by calculating them for each of the different shooting angles. Using Equation 3.1 and a look-up table of geometric factors courtesy of the University of Texas' Howell Catalog (see: me.utexas.edu/∼howell/index.html), we established SNR estimates that took into account particles coming into the detector stack through all parts of the shields as well as scattering off of different parts of the collimator. These SNR estimates can be seen for each detector (D1-D4) in Table 3.3. Note that the electron SNRs are significantly higher than those for

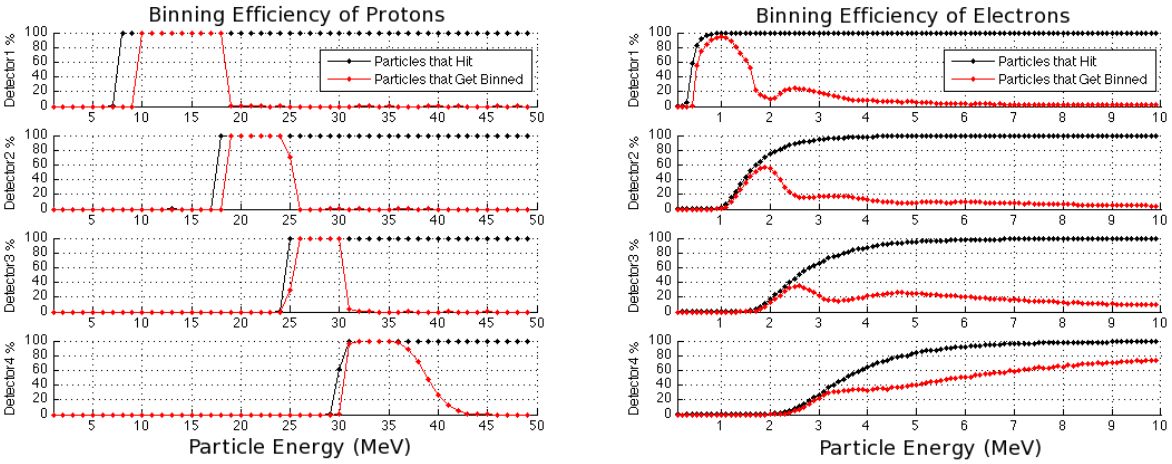

Figure 3.17: REPTile binning efficiencies by particle type and detector number for various energies of incident particles. The black curves show the efficiency of all particles of a given incident energy that hit each detector, while the red curves show the detector efficiencies when the instrument logic is applied. Thus, the red curves represent the instrument binning efficiencies.

Table 3.3: REPTile signal-to-noise ratios for both electron and proton signals on detectors 1 through 4.

Particle	D1	D2	D3	D4
Electrons	87.9	42.2	28.9	23.8
Protons	13.6	8.5	6.4	2.2

the protons. This is largely because the shields are very effective at stopping electrons up to very high energies and the shield-penetrating protons that look like electrons are so energetic that there are just too few of them to affect the electron signals. Note too that these are worst case estimates. The *Mewaldt et al.* [2005] spectrum for SEPs is based on the Halloween 2003 events, which were very large and uncommon.

3.6 Manufacturing

Currently (i.e. at the time of writing), REPTile is in the Engineering Model (EM) stage of development. Figure 3.18 shows a picture of the assembled EM. Most of the components in the EM are made of aluminum with the exception of the empty detector casings and flex-cables, 12 steel bolts, and the tantalum threaded rods, which align the detector stack. We decided to use aluminum since this was manufactured primarily by myself and Quintin Schiller with the assistance of Matt Rhode of the Aerospace Engineering machine shop and we didn't have the resources or experience to machine the interior parts out of tungsten and tantalum. However, this mostly aluminum model is more than sufficient to establish our machining tolerances, design feasibility, and assembly plan, which were the primary goals for the EM development.

The EM is shown disassembled in Figure 3.19. The assembly process starts by loading the collimator baffles and spacers into the main outer aluminum shielding. The inner tungsten shielding is put in next, and it is aligned so that the tantalum threaded rods can be put in and connected to three tapped and helicoiled holes in the inside of the aluminum shielding. When the threaded rods are inserted, they serve to align the inner parts and serve as guide rails for assembling the detector stack. Since the detectors are very sensitive devices, we use empty detector casings for the

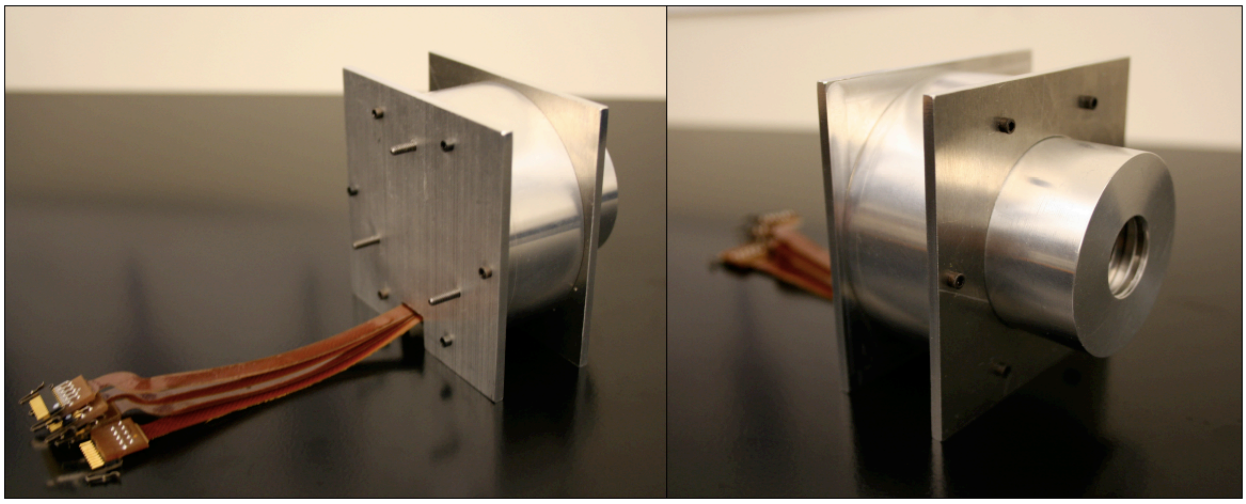

Figure 3.18: REPTile engineering model (EM), back and front views.

EM. The assembly continues with the detectors, which are enclosed in the stack by the tungsten end-cap, all of which slide down over the threaded rods. The aluminum end-cap is then placed over the back of the assembly and bolted into place.

For the flight model, we will outsource the machining to LASP personnel to ensure the finest quality and precision. Of course for the flight version, the appropriate metals (tungsten and tantalum) will be used for the inner shields and collimator pieces.

3.7 Electronics and Testing

REPTile's electronics (electronics work led by Abhishek Mahendrakumar and Ben Fell) are required for detector signal processing including: particle identification and energy binning, incrementing count rates for each particle type and energy bin, and sending these count rates to C&DH when requested. Figure 3.20 shows a block diagram of the instrument electronics chain for an individual detector. Each time a particle hits one of the detectors, it will generate a small amount of charge that will appear as a voltage spike in the electronics circuit. For the example shown at the top of Figure 3.20, the 20-33 mV spike is what would be generated for a typical electron hit, however this will vary based on the amount of energy deposited in the detector. This signal from the detector is very sensitive to noise, and it is for this reason that the instrument electronics resides so close to the back of the instrument, which keeps the flex circuits (and thus the length of wire that the signal must pass over) short. This signal undergoes two stages of amplification, first via a charge sensitive amplifier (CSA) and next via a pulse-shaping amplifier (PSA). For the CSA, we have decided to use an integrated circuit available from Amptek Inc., the A225, which is a space graded circuit. This CSA is also highly sensitive to noise, and we will take extra care to quantify this during testing. If it is found to be problematic due to the other electronics around it in the system, we will have to shield this portion of the instrument electronics board.

The PSA stage of amplification further enhances the amplitude of the signal so that proton and electron hits can be clearly distinguished. The PSA is a commercially available part that will amplify the signal to somewhere between 2.6 and 4.3 V. Three discriminators are used to

Figure 3.19: REPTile EM disassembled to show individual components.

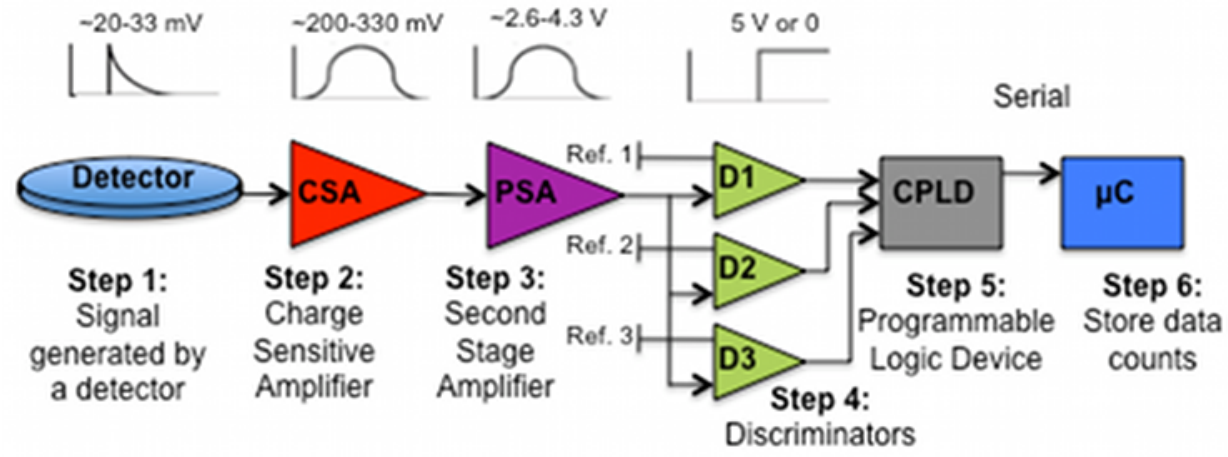

Figure 3.20: REPTile electronics block diagram. Each detector has a chain like this up to the CPLD.

determine particle-type based on three reference voltages corresponding to the particle-definition energies discussed in the Current Design section (i.e. 0.25, 1.5, and 4.5 MeV). These voltages will be determined by calibration and testing using radioactive sources and assuming a linear relation between incident energy and voltage response, which is an accurate assumption based on the results from the REPT instrument development. At this point in the circuit, the signal becomes digital, with the output from the discriminators being either a 1 (5 V) or a 0 (0 V) depending on if the signal voltage exceeds or does not exceed the corresponding reference voltage.

The digital combinations from the three discriminators are received and interpreted by a complex programmable logic device (CPLD), which determines the particle type and energy bin and increments the appropriate counter. For example, if D1-D2-D3 returns 1-0-0 from the first detector only, then the CPLD will interpret the particle as an electron with energy between 0.5 and 1.5 MeV and will increment the count in the first energy bin for electrons. If a particle doesn't meet the electron or proton logic for one of the pre-determined energy bins, then a hit will not be counted. Once again, all of this logic is based on the detailed Geant4 simulations discussed in the previous sections. If commanded to do so from the ground network, the C&DH will be able to change the reference voltages if they are later determined to be inaccurate.

C&DH (μC in Fig. fig:REPTileElectronics) controls the CPLD and the digital to analog converters (DACs) required to set the reference voltages via an I2C interface. Every six seconds during normal science operations, C&DH will request the CPLD for the eight count rates (4 energy bins for each type of particle) and tell it to reset the counts on those bins. Additionally, there are housekeeping sensors on the instrument electronics board which will also communicate with C&DH via an I2C interface. These will report current, voltage, and temperature data to C&DH to provide data about the instrument electronics' health and state.

Currently, an EM for the instrument electronics board has been produced and populated with the necessary components. To test the electronics, we will start from the digital end of the board with the CPLD code and work backwards down the chain towards the detectors. With the CPLD logic coded onto the circuit, we can inject digital pulses into the inputs of the CPLD and confirm

that the appropriate bins are being incremented by the circuit's logic. The discriminators can be individually tested before board integration, and once installed on the board, various analog voltage pulses can be input into them to further confirm the correct operation of the signal chain. We can simulate the output from the CSA using analog inputs into the PSA. We have already started CSA testing using analog inputs of the appropriate voltage and shape to simulate a detector response to an electron hit. Finally, we will first test the detectors individually and apart from the EM board to verify their functionality. Once this is established, we can plug detectors into the board and test the full board operation using radioactive sources to activate the detectors. This step will also help to establish the reference voltages. After the EM board testing is complete, the full REPTile EM will be ready for integration into the "flatsat" version of the system.

3.8 Conclusion

Here, I have introduced and discussed the Colorado Student Space Weather Experiment, a CubeSat with its primary payload consisting of the REPTile instrument. I have been involved with this project since it started in Spring 2008, and as this chapter reflects, I have been focussed primarily on the design of REPTile. CSSWE should launch in early 2012, which aligns it well with NASA's RBSP mission. If successful, CSSWE with REPTile will provide an additional measurement of relativistic electrons in Earth's outer radiation belt. Multi-point measurements are particularly useful to scientists trying to make sense of such a massive, dynamic, and complex system. In particular, CSSWE will be able to measure relativistic electrons with very low equatorial pitch angles, including those that are in the loss cone and are precipitating into the atmosphere. Being much closer to the magnetic equator, RBSP is unable to resolve the loss cone, and thus, CSSWE will be able to fill in this gap at certain times. This makes CSSWE a true example of how small, inexpensive, and relatively simple spacecraft can be employed to benefit and enrich the science results of larger and orders of magnitude more expensive and complex space missions.

Many factors must be taken into account when designing an instrument for measuring relativistic particles. Secondary particles, electron scattering, and shield-penetrating particles must all

be taken into account. For REPTile, we employed Geant4 to help us quantify our instrument performance. With this tool, we have gone through several iterations of the instrument design before settling with the current design described in this chapter. Based on the analyses using Geant4, we are confident that REPTile will be able to satisfy the requirements for measuring solar energetic protons and outer belt electrons from LEO.

This chapter has focussed on how energetic particle data is acquired in situ using spacecraft instrumentation, and in the next couple chapters, I focus on how those data are analyzed to develop a better understanding of the system.

Chapter 4

Identifying outer belt electron sources I: Phase space density radial gradients of outer belt electrons

4.1 Introduction

Now that I have introduced how outer radiation belt data are acquired, I will discuss how I have analyzed such data to answer important outstanding questions concerning outer belt electrons. In this chapter, I present two publications on my work concerning the radial gradients in the phase space density of outer belt electrons, which are important for identifying source and loss regions and determining the direction of radial transport via diffusion. The first section consists of a letter published in GRL, which introduces the methodology and initial results from the study, which involves converting flux measurements from GEO to PSD for fixed first invariant during very sudden solar wind pressure enhancements. I use the PSD data at these times to determine the sign of the PSD radial gradient beyond GEO immediately prior to the events. The second section consists of a paper published in JGR that details a comprehensive case study, with statistical, superposed epoch, and individual case results provided. In the Conclusions section, I summarize the new scientific results from these studies and their implications for our overall understanding of Earth's outer radiation belt electrons.

4.2 *Radial gradients of phase space density of the outer radiation belt electrons prior to sudden solar wind pressure enhancements* by D. L. Turner and X. Li, published in GRL in 2008

4.2.1 Abstract

When Earth's magnetosphere is impacted by a sudden solar wind pressure enhancement, day-side trapped electrons are transported radially inwards, conserving their first and second adiabatic invariants (μ and K). Thus, with magnetic field and particle flux measurements at geosynchronous orbit (GEO) before and after the impact, the phase space density (PSD) radial gradients of the particles prior to the impact can be reconstructed. We show two examples, in which the PSD of low-μ electrons, which correspond to energies less than ~100 keV, increases slightly with increasing radial distance for one event and remains unchanged for the other, while that of high-μ electrons decreases significantly with increasing radial distance from GEO for both events. These results suggest that the PSD radial gradients are μ dependent, and a significant heating, which violates μ and K, occurs inside GEO for the high energy electrons for the two cases examined.

4.2.2 Introduction

Phase space density radial gradients are suggestive of the source regions of the outer belt electrons and thus, the dominant acceleration mechanisms as well. These gradients have been investigated intensively [e.g. *Selesnick and Blake*, 2000; *Green and Kivelson*, 2004; *Onsager et al.*, 2004; *Iles et al.*, 2006; *Chen et al.*, 2005, 2006, 2007a]. A critical process in determining the magnitude of the PSD radial gradient is to calculate the L^* (L^* throughout is the Roederer L^* parameter and is related to the third adiabatic invariant) on which the electrons are assumed to drift while conserving their first and second adiabatic invariants. Most researchers apply empirical magnetic field models to calculate L^*, but it is known that empirical models have some uncertainties. For example, using different empirical models may lead to different values of L^* for the same events [e.g. *Green and Kivelson*, 2004; *McCollough et al.*, 2008]. Multisatellite techniques [i.e. *Onsager*

et al., 2004; *Chen et al.*, 2005, 2006, 2007a], which are used to determine instantaneous values of the PSD radial gradient, are field model dependent since a corresponding L^* must be calculated for each spacecraft, and single satellite techniques [i.e. *Selesnick and Blake*, 2000; *Green and Kivelson*, 2004; *Iles et al.*, 2006], which are used to determine values of the PSD radial gradient over a portion of the spacecraft orbit, are also field model dependent and assume that changes during the spacecraft transit time are insignificant. *Onsager et al.* [2004], utilizing the fact that two GOES satellites are at different L^* because of their different magnetic latitudes, studied the PSD of electrons with $\mu =$ 6000 MeV/G, and they found that the PSD radial gradient is positive around GEO. However, other researchers, as referenced above, found that the PSD for high-μ electrons usually peaks inside of GEO. We have developed a new method that determines the direction of the PSD radial gradient nearly instantaneously and without relying on a magnetic field model to determine the actual L^*. This method is complementary to the above mentioned studies, and results from it are consistent with the results of several of these previous studies.

Here, we demonstrate this new method, which determines the direction of the electron PSD radial gradient at and beyond GEO prior to a sudden solar wind pressure impact based on the fact that such an event causes a magnetic field compression and dayside trapped particles to be transported radially inwards, conserving μ and K [*Li et al.*, 1993, 2003; *Lee et al.*, 2005; *Shi et al.*, 2009]. As we know, a satellite at dayside GEO measures electrons initially at larger L^* immediately after the impact and electrons at a smaller L^* before the impact. Based on the electron measurements as well as the magnetic information before and after the impact, a PSD radial gradient prior to the impact can be reconstructed. Using this method, we have investigated several events, and we present the results from two of them here. From these, we find that the PSD radial gradients are μ (or energy) dependent. For low-μ electrons, corresponding to energies less than ~100 keV at GEO, the PSD increases slightly or stays relatively constant with increasing radial distance, while that of high-μ electrons, which correspond to energies greater than ~200 keV, generally decreases with increasing radial distance from GEO. For the remainder of this discussion, a gradient that increases with increasing radial distance shall be referred to as a positive gradient,

while one that decreases with increasing radial distance shall be referred to as a negative gradient.

4.2.3 Analysis Method

We use two solar wind pressure enhancement events to determine the PSD radial gradient for electrons at and beyond GEO. Figure 4.1 shows the Dst index and B_z, V, and dynamic pressure of the solar wind from ACE measurements for 12 hour periods before and after sudden solar wind pressure enhancements on 26 August 1998 and 23 June 2000. To employ this method, the sudden pressure enhancements should occur on timescales much shorter than the drift periods of the particles being studied to ensure that the particle measurements accurately reflect particles from the same local time but a different L^*. Also, note that the solar wind conditions prior to the events are relatively calm. This is not necessarily an event criterion, but for these events, it does correspond to a more uniform magnetic field response, which makes the μ calculation easier and is further discussed below.

For particle data, we use energetic electron flux measurements from the Los Alamos National Laboratory (LANL) satellites in GEO. The LANL satellites' SOPA instruments have nine differential electron flux channels, and we use 10-second resolution SOPA flux data for this study. Flux measurements from several energy channels at this resolution for two hours before and after the events are shown in Figure 4.2. Here, we only show the measurements from three LANL satellites for each event. For the 1998 event, all three satellites shown are on the dayside, and for the 2000 event, only the three satellites with data available are shown, of which two are also on the dayside. In Figure 4.2, event times are marked with a vertical dashed line. Note how the response varies for each satellite, yet most see a flux increase in the lowest energy channels and a decrease in the higher energy channels immediately following the solar wind pressure impact. However, because the local magnetic field is compressed by the solar wind pressure enhancement, one cannot infer the PSD radial gradient just based on the flux variations. The PSD has to be carefully calculated as described below.

To capture only these initial effects and mitigate ambiguity due to particle drifts, we use only

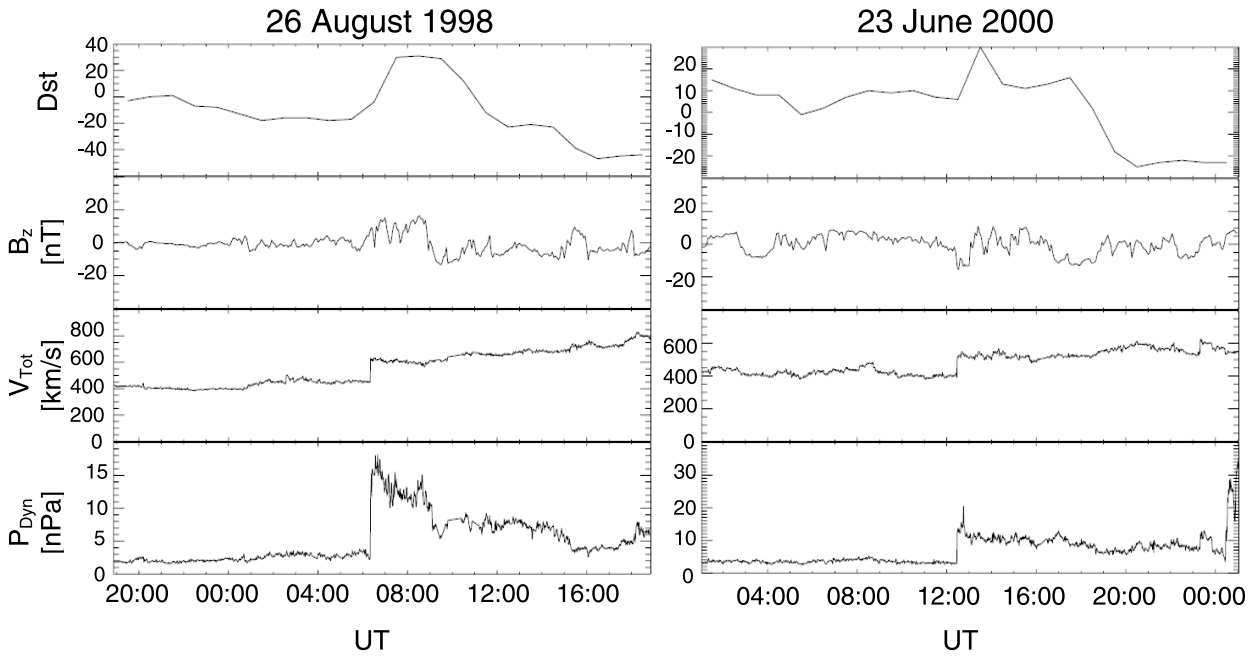

Figure 1

Figure 4.1: Dst and ACE solar wind data for both events. Note that the date at the top of Figures 4.1 (left) and 4.1 (right) is that of the event itself, but both show a time range of more than one day.

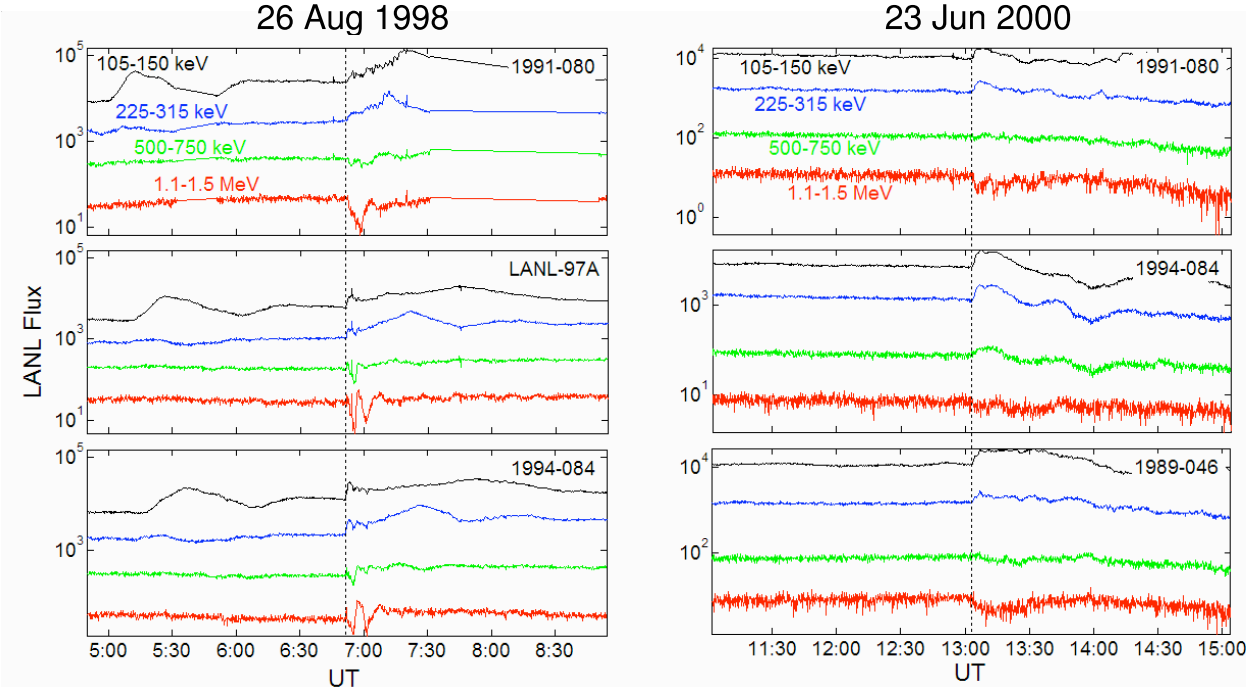

Figure 4.2: LANL flux [$cm^{-2}s^{-1}sr^{-}1keV^{-}1$] measurements for both events. Event times are shown with dotted lines. For the 1998 event, 1991-080, LANL-97A, and 1994-084 are at 07:27, 11:30, and 13:45 local time (LT) respectively, and for the 2000 event, 1991-080, 1994-084, and 1989-046 are at 13:36, 19:59, and 02:01 LT respectively.

the flux measured three minutes before and after the pressure enhancement. The fluxes from the nine differential energy channels from each satellite are fit with a power law using the equivalent energy for each channel:

$$E_{ch} = \sqrt{E_{min}^{ch} \cdot E_{max}^{ch}} \tag{4.1}$$

where the *min* and *max* energies are the lower and upper bounds of the channel as discussed by *Chen et al.* [2005]. The power law fit provides a good approximation of the energy spectrum at each time and allows us to determine a flux for any given energy. PSD is then calculated for each time from these fluxes using:

$$f = 3.325 \times 10^{-8} \frac{j}{E\left(E + 2m_0c^2\right)} \left[\left(\frac{c}{MeV \cdot cm}\right)^3\right] \tag{4.2}$$

where f is PSD in units seen in brackets, j is flux in units of $\mathrm{cm^{-2}s^{-1}sr^{-1}keV^{-1}}$, E is energy in MeV, m_0 is the rest mass of an electron, and c is the speed of light in a vacuum. For detail of the equation form, see *Chen et al.* [2005].

To calculate μ, the magnitude of the magnetic field is required, but LANL satellites do not have onboard magnetometers. Before the pressure impacts, magnetic field models such as the Tsyganenko 2001-storm (Ts01-S) model [*Tsyganenko et al.*, 2003] prove to be quite accurate when compared to GOES magnetic field measurements. However, during and after the pressure impacts, all field models are unable to capture the resulting compression of the field, and as has been mentioned in much of the previous research, accurate PSD results are highly dependent on the accuracy of the field model [*Selesnick and Blake*, 2000; *Green and Kivelson*, 2004]. Figure 4.3 shows the GOES magnetic field measurements during both events. These field measurements are 1-minute resolution data from the Coordinated Data Analysis Web (CDAWeb) and NOAA's SPIDR data archive (see Acknowledgments for site URLs), and the known offsets for GOES-8 and GOES-10 measurements [*Tsyganenko et al.*, 2003] are corrected. For both events, the Ts01-S model was run at GOES-8 positions, and the results are shown by the dotted blue line. Notice that before the event, the Ts01-S model and the GOES-8 measurements are very close, but when the event occurs, the Ts01-S model does not capture the immediate field enhancement.

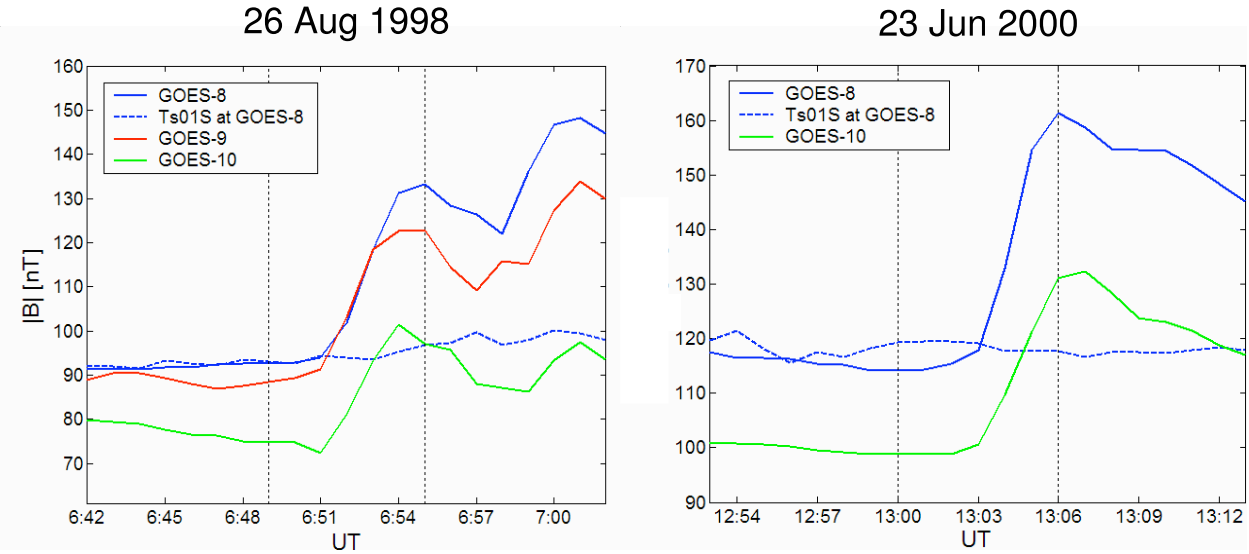

Figure 4.3: GOES B-fields for both events. Tsyganenko 2001-Storm model results for GOES-8 are shown with the dashed blue lines for both events. Dotted vertical lines show the times used for this study. For the 1998 event, GOES-8, -9, and -10 are at ∼02:50, ∼00:50, and ∼22:50 LT respectively, and for the 2000 event, GOES-8 and -10 are at ∼09:00 and ∼05:00 LT respectively.

We have chosen events in which the magnetic field response is similar at different local times, meaning that the GOES satellites see very similar relative increases in the magnitude of the magnetic field. For the 26 August 1998 event, the percent increases observed by GOES 8 and 10 differ by ∼2%, while GOES-8 and -9 and -9 and -10 increases differ by ∼1%. For the 23 June 2000 event, GOES 8 and 10 percent increases differ by ∼4%. Since the fields measured by GOES behave very similarly during the event, we assume the same relative change for the magnetic fields at the LANL locations. To approximate the field strength at the LANL spacecraft positions, we use the Ts01-S model before the event and scale the compressed field from the nearest GOES measurements for the rest of the event. First, GOES field measurements are interpolated from their 1-min resolution to the same 10-s resolution as the LANL particle measurements. The scaling then involves calculating the ratio of the Ts01-S field at the LANL spacecraft to the initial measured field at GOES and multiplying the remaining GOES measurements with this ratio to get the field at the corresponding times for the LANL satellite:

$$B\left(t_i\right)_{LANL} = \left(\frac{B\left(t_0\right)_{Ts01-S}}{B\left(t_0\right)_{GOES}}\right) B\left(t_i\right)_{GOES} \tag{4.3}$$

where t_i is a time index with t_0 being the initial time, $B(t)_{GOES}$ is the GOES measured field, $B(t_0)_{Ts01-S}$ is the Ts01-S result at the LANL spacecraft position prior to the event, and $B(t)_{LANL}$ is the scaled field at the LANL position throughout the event. Given this, we can now compute μ for each time step with:

$$\mu = \frac{E\left(E + 2m_0c^2\right)\sin^2\alpha}{B_{LANL}\left(2m_0c^2\right)} \times 10^5 \left[\frac{MeV}{G}\right] \tag{4.4}$$

where B_{LANL} is the field magnitude in nT, α is the pitch angle, and the other parameters are as defined for equation 4.2. Note that for this study, we are calculating this for equatorial electrons with pitch angles close to 90 degrees, which is representative of the majority of dayside energetic electrons [*Gannon et al.*, 2007].

4.2.4 Results and Discussion

Figure 4.4 shows the results for both events. Each event is displayed with three plots showing the logarithm of PSD for fixed values of μ. These are the results derived from the LANL satellites closest to noon: LANL-97A at ∼11:30 LT for the 1998 event and 1991-080 at ∼13:30 LT for the 2000 event. We only show the results from the satellites closest to noon since it is there that the electrons are most likely transported radially inwards. Event times are displayed with the dashed vertical lines, and the time scale for all is six minutes. It is evident in the first event that the PSD for high μ (results above ∼100 MeV/G) drops significantly, up to a full order of magnitude for the PSD of μ = 3608 MeV/G, after the event, but for μ = 51 MeV/G, the PSD slightly increases after the event and then returns to approximately initial levels. This low-μ behavior is markedly different from that of higher μ's, and the results from the other two LANL satellites for this event have similar features. Thus, it is apparent that immediately prior to this event the PSD radial gradient for fixed μ above ∼100 MeV/G is negative, while for lower μ's, it is relatively flat.

For the 2000 event, 1991-080 observes similar results. The PSD for low μ (51 and 107 MeV/G) is unchanged after the shocks impact, while that for the highest μ's (2226 and 3608 MeV/G) decrease drastically after the event. In general, a flat PSD radial profile could be the result of two different reasons: one in which the profile reflects a steady situation with no PSD radial gradient and another in which diffusion may have been so strong that it has smoothed out any gradients in the PSD. For the PSD with μ = 168 MeV/G, a slight decrease is observed, and this decrease is also seen in the PSD for all μ's higher than this, with the decrease in PSD for μ = 3608 MeV/G being almost an order of magnitude. The behavior is distinctly different between the PSD for lowest and highest μ's. Similar to the 1998 event, immediately prior to this event, the PSD gradient for fixed μ above ∼110 MeV/G is negative, while the gradient for fixed μ lower than this is relatively flat.

We have investigated more than 15 other events using this new method, and we have found that in most cases, the results are similar to the ones presented here. In two cases, the low μ

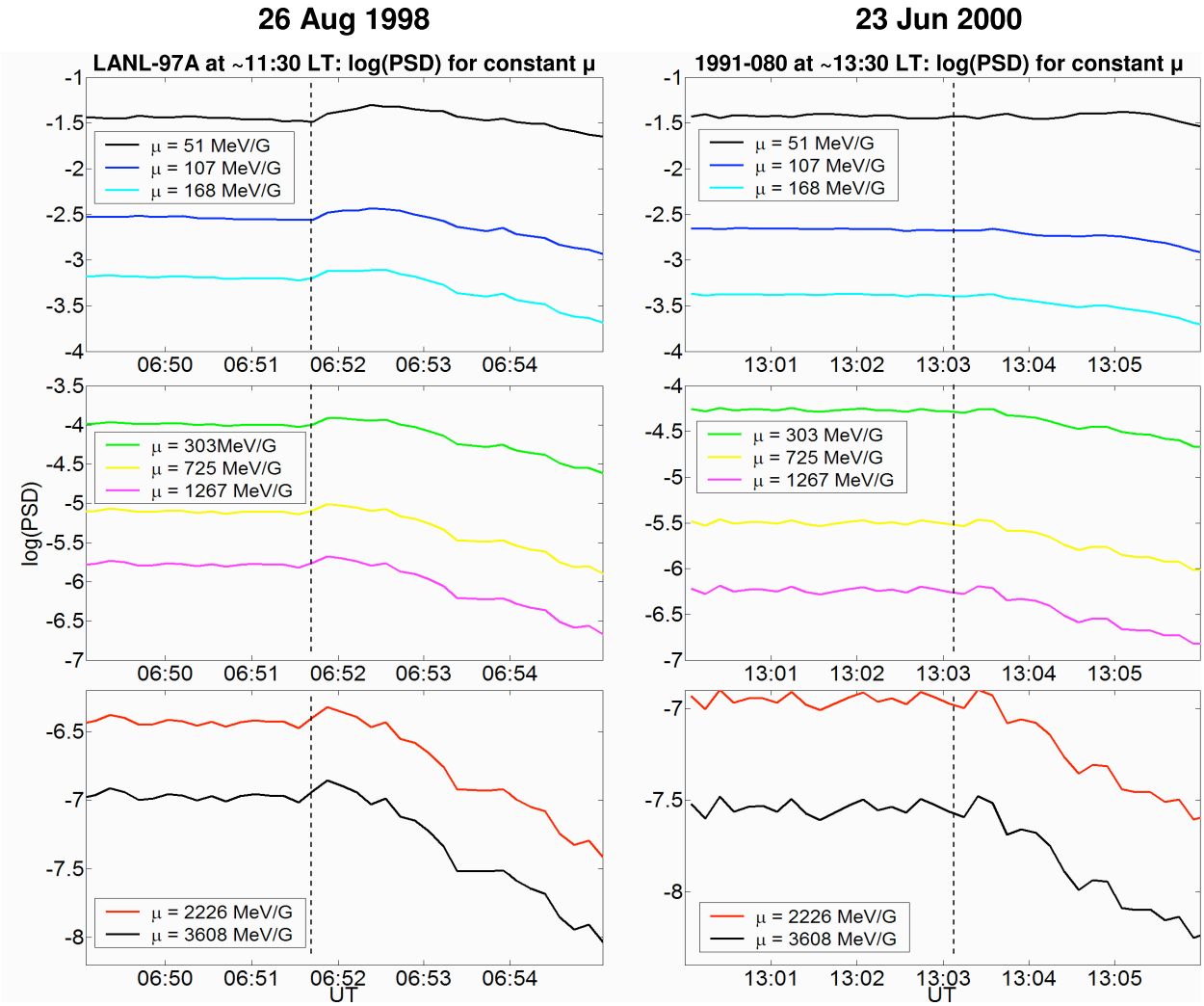

Figure 4.4: PSD results from the LANL satellite closest to noon for each event. Colored lines show the logarithm of PSD for constant values of μ for three minutes before and after each event, the times of which are shown with dashed lines.

gradient is also negative. In some others cases, the gradient for high μ electrons is relatively flat, and there is one case in which the PSD gradient is positive for high μ electrons. However, in the majority of cases for high μ electrons, the PSD radial gradient is negative. Also, in the vast majority of cases, there is a distinctive difference in the behavior of electrons with μ less than ~100-200 MeV/G when compared to those with μ greater than ~200-300 MeV/G.

Overall, we find for the cases presented here that the dayside PSD radial profile immediately prior to two sudden solar wind pressure enhancements decreases with increasing radial distance for electrons with μ greater than around 100-200 MeV/G and is relatively flat for lower μ's. These results imply that the PSD for μ greater than a couple of hundred MeV/G peaks inside of GEO prior to these events. These results are consistent with those of *Chen et al.* [2005, 2006, 2007a] and *Iles et al.* [2006]. *Chen et al.* [2005, 2007a] find that for both quiet and storm times, the electron PSD gradient for L-shells centered about L^* ~6 is negative for high energy electrons. These results are somewhat consistent with those of *Brautigam and Albert* [2000] as well; they find for one storm that electrons with μ <~315 MeV/G can be modeled well by radial diffusion, while those with μ >~700 MeV/G cannot. They suggest that wave particle heating, which would cause a negative PSD radial gradient beyond GEO, might explain the inconsistency for the high-μ electrons. It is also interesting to note here the findings of *Bortnik and Thorne* [2007]; they discuss an "anchor point" energy at a couple of hundred keV at which whistler-mode chorus tends to accelerate electrons with greater energy and scatter those with lower energy. This too is consistent with our findings here; for electrons at GEO, μ of ~200 MeV/G corresponds to energy of a couple of hundred keV.

4.2.5 Conclusion

Here, we have discussed a new method for calculating the direction of the equatorial PSD radial gradient immediately prior to sudden solar wind pressure enhancements using particle and magnetic field data from spacecraft in GEO. Based on the results of this method applied to two events in 1998 and 2000, we found that the PSD radial gradient is μ dependent; it is negative for electrons with μ greater than ~100-200 MeV/G and either slightly positive or flat for electrons

with μ lower than this. These results are consistent with those of several previous independent studies and suggest that prior to these events higher energy electrons had a PSD peak inside of GEO, implying a significant heating occurs for these high energy electrons.

4.3 *On phase space density radial gradients of Earth's outer-belt electrons prior to sudden solar wind pressure enhancements: Results from distinctive events and a superposed epoch analysis* by D. L. Turner, X. Li, G. D. Reeves, and H. J. Singer, published in JGR in 2010

4.3.1 Abstract

Here, we present the results of a study of phase space density radial gradients for outer-belt electrons at and beyond geosynchronous orbit prior to 86 sudden solar wind pressure enhancements from 1993 through 2007. All of the events are classified and analyzed based on the results for equatorial electrons with first adiabatic invariants of 50, 200, 750, and 2000 MeV/G. Examples of three distinctive events are compared, and the results from a superposed epoch analysis are presented. We find that the radial gradients are dependent on the first adiabatic invariant (i.e., energy), and that for the majority of cases, the gradient is negative for electrons with energies above a couple of hundred keV, while it is either positive or relatively flat for electrons with energies lower than this, which is evidence of two distinct populations. In the cases where a positive gradient is observed for 2000 MeV/G electrons, the solar wind and geomagnetic conditions are very quiet for at least two days prior to the event, but for the events when the gradient for the same electrons is negative, there is a consistent evidence of enhanced substorm activity and/or convection in the days leading up to the events. Overall, this study puts previous observations of phase space density (PSD) gradients into a broader context of solar wind and geomagnetic conditions, while encompassing a broad range of energies, from the source population of tens to hundreds of keV electrons to relativistic electrons with energies exceeding 1 MeV. We discuss how 41 of the 86 events are consistent with and can be explained by local heating by wave-particle interactions, and we provide evidence of the solar wind and geomagnetic conditions that are important to different types

of sources of outer-belt electron PSD.

4.3.2 Introduction

4.3.2.1 Historical Context

Despite five decades of research, the exact nature of the processes that control the Earth's outer radiation belt remains elusive. This region, which makes a torus-shaped "belt" around the Earth with inner and outer radial boundaries along the magnetic equator of around 3 R_E and 7 R_E, respectively, consists primarily of highly energetic electrons, the dynamics of which are affected by changes in the solar wind, magnetospheric field configurations, and other plasma populations. Many questions concerning the primary source and loss processes for these electrons remain unanswered. One such question, how electrons are accelerated to relativistic energies within the magnetosphere, was thought to be addressed with the inward radial diffusion theory presented in *Particle Diffusion in the Radiation Belts* [*Schulz and Lanzerotti*, 1974], but later spacecraft measurements and new analysis techniques implied that the radial diffusion theory alone could not account for electron acceleration in this complex region [e.g. *Reeves et al.*, 1998; *Li et al.*, 1999; *Brautigam and Albert*, 2000, also see discussions in review by *Friedel et al.* [2002]].

The problem of electron acceleration has been reexamined within the past 15 years, and a new theory has arisen to explain the discrepancies between observations and the radial diffusion theory. *Temerin et al.* [1994] proposed a new mechanism in which plasma waves interact with the gyrating, trapped electrons, thus transferring energy to result in net electron acceleration. *Summers et al.* [1998] and *Horne and Thorne* [1998] expanded upon this theory and identify whistler mode chorus waves as the energy donor for electrons with energies from hundreds of keV to several MeV. The theory of electron energization by wave-particle interactions has since been further examined and refined.

At the heart of the acceleration question lie the electron phase space density (PSD) distributions. At any given time, the radial distribution of electron PSD for fixed values of the first

and second adiabatic invariants (μ and K, respectively) is telltale of the acceleration mechanism responsible for electron energization [see discussion in *Green and Kivelson*, 2004]. Energization by inward radial diffusion requires the electron PSD for fixed μ and K to be higher at higher radial distances (referred to from now on as L^*, the Roederer L-star parameter, which is related to the third adiabatic invariant and describes the radial distance in Earth radii to an electron's drift shell in the equatorial plane of Earth's magnetic field [see *Roederer*, 1970; *Selesnick and Blake*, 2000; *Green and Kivelson*, 2004]). In the other case, in situ acceleration by wave-particle interactions would result in a local peak in PSD around the L^* where the interactions are taking place. Thus, the radial gradient of outer-belt electron PSD can be used to imply the acceleration mechanism.

Several previous studies have been conducted in attempts to identify the dominant mechanism using PSD radial gradients [i.e. *Selesnick et al.*, 1997; *Brautigam and Albert*, 2000; *Hilmer et al.*, 2000; *Selesnick and Blake*, 2000; *McAdams and Reeves*, 2001; *Green and Kivelson*, 2004; *Onsager et al.*, 2004; *Taylor et al.*, 2004; *Chen et al.*, 2005, 2006, 2007a, b; *Iles et al.*, 2006; *Turner and Li*, 2008b; *Tu et al.*, 2009]. Among these studies, *Hilmer et al.* [2000] used GPS dosimeter measurements and Los Alamos National Laboratory (LANL) flux measurements from geosynchronous orbit (GEO) to estimate the radial gradient of electrons with ~90° pitch angles and μ = 2100 MeV/G during high-speed solar wind streams. They found that the gradient between GPS (r~4.2 R_E) and GEO (r~6.6 R_E) was positive (i.e., increasing with increasing radial distance) for 27 out of 31 cases studied. *Brautigam and Albert* [2000] found that for one storm, using CRRES data to calculate electron PSD for μ from 500 to 1000 MeV/G, the radial gradient was positive for smaller μ (<700 MeV/G) and negative for larger μ (>700 MeV/G), and they discussed several possible explanations for this, one of which is that an internal acceleration source existed for higher-energy electrons. *Selesnick and Blake* [2000] found evidence of PSD peaks between L of 4 and 6 from Polar data, and they discussed how PSD peaks can form either from local acceleration or from inward radial diffusion with a variable source at the outer boundary. They also discussed how PSD gradient calculations depend heavily on the magnetic field model used in the calculation. *Green and Kivelson* [2004] used data from the Polar spacecraft and the Tsyganenko models to calculate electron PSD

gradients. They found that their results are best explained by acceleration from an internal source at L∼5, but the results are also strongly model-dependent. *Onsager et al.* [2004] calculated electron PSD gradients using two GOES measurements at different L^* around GEO (being at different magnetic latitudes, the GOES satellites are also located on different L^*). They limited their study to equatorially mirroring, ∼90° pitch angles, $\mu = 6000$ MeV/G electrons, and their results indicate that the PSD radial gradient is positive for times of quiet geomagnetic conditions, meaning inward radial diffusion may be the primary energization mechanism under quiet conditions. Recently, *Chen et al.* [2007b] used Polar, LANL, and GPS satellite measurements to calculate the electron PSD at different radial distances. Their analysis covers two years, 2001-2002, and μ in the range 462-2083 MeV/G. They found frequent and sometimes persistent PSD peaks inside of GEO with no evidence of variations in the PSD at higher L^*, suggesting that local acceleration by wave-particle interactions is the primary acceleration mechanism for electrons in the outer belt.

4.3.2.2 Development and Application of a New Technique

In the past, independent works by *Li et al.* [2003] and *Lee et al.* [2005] on particle injections resulting from interplanetary shocks found that the energetic (i.e. >225 keV) electron response can be an immediate decrease in the flux measured at GEO. *Li et al.* [2003] explained this as a result of weaker source population at larger radial distances for an event on 26 August 1998, and refer to previous test-particle simulation results, which show how particles are transported radially inward when the shock impacts the magnetosphere, as further evidence [i.e. *Li et al.*, 1993, 1998]. In *Lee et al.* [2005], they also found that for "compression-only" injections of high-energy electrons, there are often immediate dropouts in electron fluxes. They discussed that a decrease or little change in particle flux due to an injection from a dynamic pressure impulse is evidence that the particle distribution function (i.e., PSD) at constant first and second adiabatic invariants decreased or was approximately constant with increasing radial distance. *Shi et al.* [2009] conducted a more comprehensive study of the energetic flux response to 128 solar wind dynamic pressure enhancements from 2000 to 2003, and they found that the dominant response for

relativistic electrons measured at GEO is a decrease in flux.

Recently, *Turner and Li* [2008b] introduced a new analysis technique to determine the direction of the PSD radial gradient at and beyond GEO, immediately prior to sharp solar wind pressure enhancements, referred to, throughout this paper, as pressure pulses. When the magnetosphere is impacted by a solar wind pressure pulse, the impulse in the dynamic pressure results in a magnetic field compression and the inward radial transport of trapped outer-belt electrons, which conserve their respective μ and K in the process [*Li et al.*, 1993, 2003; *Lee et al.*, 2005]. Thus, immediately after such a pressure pulse, magnetic field and electron flux measurements from GEO are used to determine the PSD at increasingly higher L^* (i.e., at a fixed location, L^* before the compression is less than L^* after the event). *Turner and Li* [2008b] used flux data from the Los Alamos spacecraft in GEO to calculate electron PSD for a broad energy range, and they calculated μ for all energies by scaling the magnetic field measured by the nearest GOES satellite to the LANL satellite being used to get the PSD. From this, the PSD for near-equatorial electrons with fixed μ can be calculated before and after the pressure pulse to determine the sign of the PSD gradient beyond GEO. This process requires that specific criteria be met, which is discussed further in the Event Criteria section. Two of the significant advantages of this new technique are that it does not rely on empirical magnetic field models for long periods of time or when the models become highly inaccurate (i.e., after the pressure pulse impact) and that it can be used to determine the direction of the PSD gradient nearly instantaneously using particle measurements from only a single spacecraft. *Turner and Li* [2008b] found that the direction of the PSD gradient for ~1 MeV electrons at GEO prior to the events is negative for the majority of events examined. Also, they discussed how the PSD gradient is μ-dependent: the gradient for higher-μ electrons is often significantly different than that for lower-μ electrons.

Here, we employ the method of *Turner and Li* [2008b] to determine the direction of the PSD radial gradients of equatorially mirroring electrons over a wide range of μ at and beyond GEO prior to 86 solar wind pressure pulse events that occurred over more than one full solar cycle (1993-2007). We first discuss the data used to conduct this study and the criteria we use to determine our set

of events. A case study of three individual events, each displaying a distinctive type of PSD result, follows. The results of a superposed epoch analysis are then presented prior to a comprehensive discussion of the results, which focus on the various solar wind and geomagnetic preconditions that lead to different types of PSD gradients beyond GEO, and their implications. We also discuss how these results provide important insight and context to the results from previous PSD gradient studies while expanding our understanding of not only the gradients for relativistic electrons, but those for the source population of tens to hundreds of keV electrons as well. Finally, conclusions are presented, followed by a discussion of potential future work.

4.3.3 Data Set Description

This study requires various types of data from several different sources. Electron flux data from the synchronous orbit particle analyzer (SOPA) instruments on various LANL spacecraft in GEO have been obtained from the LANL online data request system (available at: $http://leadbelly.lanl.gov/lanl\_ep\_data/$). For this study, flux data at a 10 s resolution is used from the SOPA instruments' nine differential energy channels, which cover a full energy range from 50 keV to 1.5 MeV. These data are used to calculate the PSD during each event, as well as for the electron population characteristics in the superposed epoch analysis. GOES magnetic field measurements are used to determine event eligibility based on the study criteria (discussed in section 3), as well as to determine the field compression during each event. These data were obtained at a 1 min resolution from NASA's coordinated data analysis web site (CDAWeb; available at: $http://cdaweb.gsfc.nasa.gov/$) [*McGuire et al.*, 2000].

For the individual event studies and the superposed epoch analysis, we used data from the following sets: solar wind velocity; number density; Bx, By, and Bz from in-house ACE data sets (for 1998-2007); and IMP-8 and OMNI data sets, which are both available from CDAWeb (for 1993-1997) (see $http://omniweb.gsfc.nasa.gov/$); AL, AU, AE, Dst, and Kp geomagnetic index data sets from the World Data Center for Geomagnetism, Kyoto, Japan (AL, AU, AE, and Dst sets available at: $http://swdcwww.kugi.kyoto-u.ac.jp/index.html$) and from CDAWeb (Kp,

courtesy of the National Geophysical Data Center). Solar wind data from ACE and OMNI (1995-1997) are available at 1 min resolution, while OMNI data for 1993-1994 are available only at hourly resolution. AL, AU, AE, and Dst are used at 1 h resolution, while 3 hourly Kp is used.

Solar wind dynamic pressure is calculated directly from the velocity and number density data, approximating the proton to alpha ratio to be 4:1 (i.e., 80% protons and 20% alphas). GSE magnetic field measurements are converted to GSM using the Office National dEtudes et de Recherche Aerospatiales (ONERA) Deployment Environmental Surveillance Program (DESP) library tools ($http://craterre.onecert.fr/support/user\_guide.html$). Other parameters (e.g., magnetic field magnitude (B_{tot}), solar wind V-Bsouth (VB_s), plasmapause location (L_{pp}), and the Akasofu ε parameter) are also calculated from the appropriate data sets and were examined for this study, though not all of the parameters examined are presented here. Two additional parameters that we discuss throughout are AE^* and Dst_{min}, which are defined, respectively, at any particular time as the maximum value of the AE index from the previous 3 h and the minimum value of the Dst index from the previous 3 h.

4.3.4 Event Criteria

As discussed by *Turner and Li* [2008b], this study requires that we use only sudden pressure enhancement events in which the solar wind pressure pulses occur on timescales significantly shorter than the electrons' drift periods (i.e., rise times less than ~2 min). This requirement ensures that the spacecraft flux measurements after the pressure pulse impact are of electrons that were at approximately the same local time but a higher L^* prior to the pressure pulse. After identifying these types of pressure pulses in the solar wind data set, we further narrow the events down by the magnetic compression observed by the GOES spacecraft in GEO. We only use events in which there is a positive overall compression of the magnetic field that is also relatively uniform over different local times. To test the uniformity of the compressions, we compare the percent increase from two or more spacecraft, which are most often two GOES satellites separated by approximately 4 h in local time, and only use events in which the percent increases of the measured compressions differ

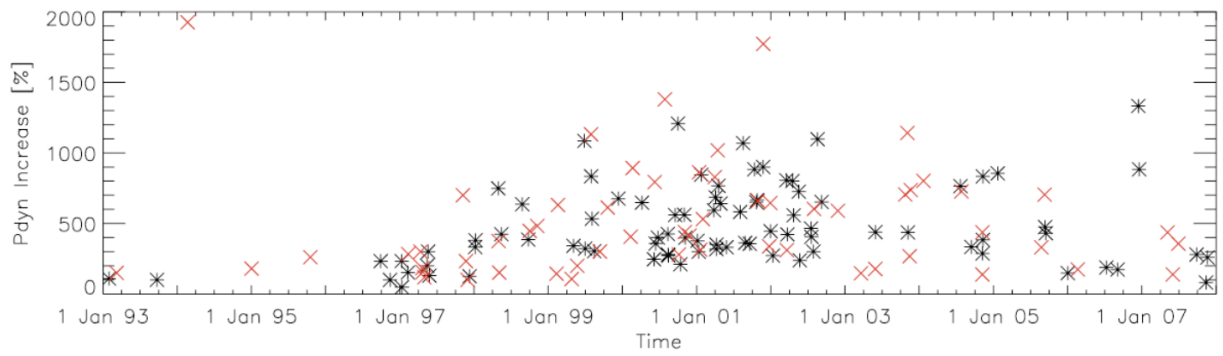

Figure 4.5: Event distribution in time from 1993 to 2007 and scaled by the pressure pulse percent increase. Pressure pulses that meet the event criteria are shown with black asterisks, while those that do not are shown with red crosses.

by less than 25%. Finally, to qualify as a useable event, at least one LANL spacecraft must be on the dayside, between 0600 LT and 1800 LT, at the time of the pressure pulse impact.

We have identified over 145 sudden pressure pulse events in which the solar wind dynamic pressure (from IMP-8, ACE, and OMNI data sets) increases by more than half of its original level in less than 2 min. After the geosynchronous magnetic field compression criteria are applied to this set, the number of useable pressure pulses is reduced to 86. Figure 4.5 shows how these events are distributed over the period from 1 January 1993 to 1 January 2008. In Figure 4.5, events are plotted on the y-axis by their respective percent increase in solar wind dynamic pressure. Events that are used in this study are marked by the black asterisks, while other events that were identified but not used due to the event criteria are marked by the red crosses. Notice how the events are mostly concentrated around solar maximum, with half of the events used in the study (43 of the 86) occurring between January 2000 and September 2002.

4.3.5 Study of Distinctive Events

In this section, we discuss the characteristics of distinct types of events that we have identified through this analysis. We classify each type of event based on the behavior of the PSD for four fixed values of μ: μ = 50, 200, 750, and 2000 MeV/G, which correspond to electrons near dayside

Table 4.1: Amount of Events in Which the Phase Space Density Gradient for Electrons With m = 50, 200, 750, and 2000 MeV/G Are Negative, Flat, or Positive with Percentage of Total Displayed in Parentheses

	Negative	Flat	Positive
50 MeV/G	24 (28%)	29 (34%)	33 (38%)
200 MeV/G	39 (45%)	28 (33%)	19 (22%)
750 MeV/G	50 (58%)	29 (34%)	7 (8%)
2000 MeV/G	65 (75%)	16 (19%)	5 (6%)

GEO with energies around 50 keV, 200 keV, 600 keV, and 1 MeV, respectively. Table 4.1 shows the number of events in which the PSD gradients for each of these four μ values are negative, flat, and positive. To be considered as a "negative gradient event," the PSD for some fixed μ after the event must drop to less than 90% of the PSD (for the same μ) averaged two-and-a-half minutes before the event, whereas to be classified a "positive gradient event," the PSD must increase to more than 110% of the before-event PSD average. Those events classified as "flat" fall in between these two other types. Note that for 75% of events, the PSD gradient for electrons with $\mu = 2000$ MeV/G is negative, while the gradient for electrons with $\mu = 50$ MeV/G is positive or flat for 72% of events. Meanwhile, the PSD gradient for electrons with $\mu = 200$ MeV/G, which have energies near GEO of around a couple of hundred keV, are split almost evenly between negative and positive/flat events. These results are consistent with the results of *Chen et al.* [2007b] for relativistic electrons and with the initial findings of *Turner and Li* [2008b], who discussed how the PSD gradient beyond GEO is μ-dependent and there is some transition from mostly positive or flat gradients to mostly negative gradients for electrons with energies near GEO around a couple of hundred keV.

The majority of the events can be more generally classified based on their overall PSD gradient results into the following four categories: (1) the PSD gradients for all μ's examined are negative, (2) the PSD gradients for all μ's examined are positive, (3) the PSD gradients for all μ's examined are flat, and (4) the PSD gradients for high-energy electrons are different than those for lower-energy electrons. There are two exceptional cases, both of which exhibit evidence of a peak in the high-energy electron PSD gradients beyond GEO. However, these exceptional case results are

Table 4.2: Amount of Events by Overall Gradient Category with Percentage of Total Displayed in Parentheses

All-Negative	All-Positive	All-Flat	Mixed Gradients	Evidence of a Peak
23 (26.7%)	4 (4.7%)	9 (10.5%)	48 (55.8%)	2 (2.3%)

somewhat ambiguous since the observed peaks may be the result of either a brief dip in the dynamic pressure during the compression or an actual peak in the PSD gradient. Table 4.2 lists how many events can be classified into each of these categories.

Three example cases will be discussed in the following subsections. The first example exhibits several events, but we pay attention primarily to two of these: an event where all gradients are negative and an event where all gradients are flat. The second example exhibits an event where all gradients are positive, and the third is for a "mixed" event exhibiting a negative gradient for 2000 MeV/G electrons, but a positive gradient for 50 MeV/G electrons. Figure 4.6 shows the PSD results for four different μ's (50, 200, 750, and 2000 MeV/G) from the three events used to set the epoch times (ETs) in each of the examples. In Figure 4.6, each event is color- and symbol-coded, and time is given in epoch minutes for 3 min before and after the pressure pulse impact time, which is the time used to determine the PSD gradient to avoid ambiguities due to electron drift (discussed by *Turner and Li* [2008b]).

For each example, corresponding Figures 4.7-4.12 show several solar wind parameters (i.e., dynamic pressure P, total velocity V, interplanetary magnetic field (IMF) magnitude B, IMF B_z in GSM, and VB_s), geomagnetic indices (i.e., Kp, AE, and Dst), LANL electron fluxes, and the derived PSD for different μ. For the solar wind and geomagnetic indices plots, time is given in epoch hours, where the epoch is defined as the impact time. Note, however, that the ET is different for ACE and the magnetosphere (since the solar wind passes ACE at its L1 orbit shortly before it hits the magnetosphere), but they have been aligned throughout for Figures 4.7, 4.9, 4.11, and 4.13. The date and time at the top of Figures 4.7, 4.9, and 4.11 is the ET of the pressure pulse impacts with the magnetosphere. Figures 4.7, 4.9, and 4.11, comparing the different types of events, have

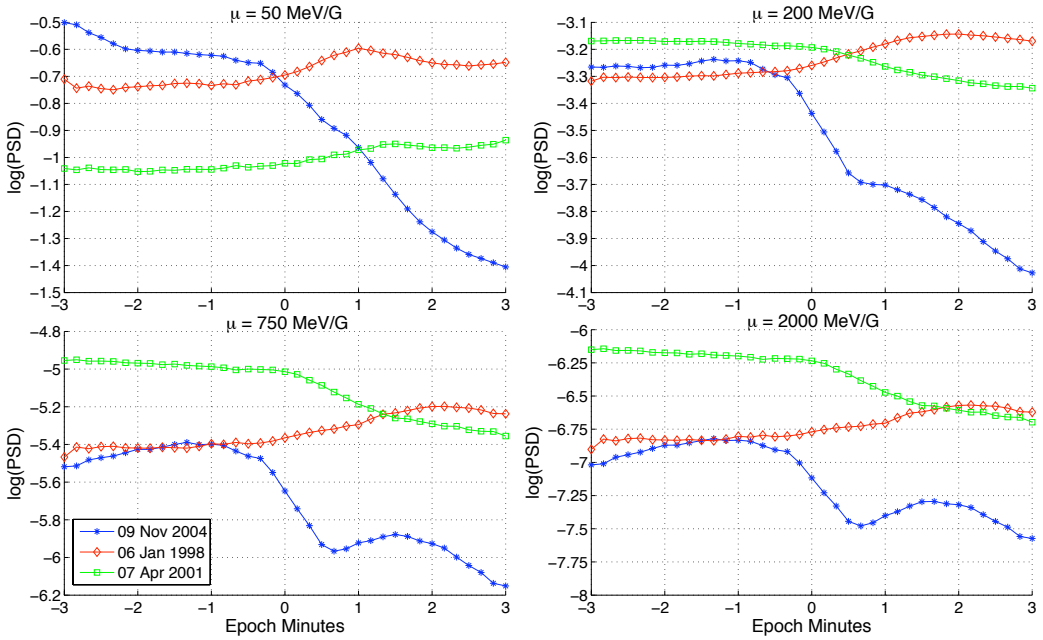

Figure 4.6: Phase space density (PSD) results (PSD units: $c^3MeV^{-3}cm^{-3}$, where c is the speed of light) from three example events. Logarithm of phase space density is shown for four different values of μ (top left) 50 MeV/G, (top right) 200 MeV/G, (bottom left) 750 MeV/G, and (bottom right) 2000 MeV/G. Events are color- and symbol-coded (see embedded legend).

the same range for each of the plotted parameters for comparison purposes. Also note, solar wind number density is not displayed since its characteristics are so similar to dynamic pressure. Figures 4.8, 4.10, and 4.12 show electron fluxes from four differential energy channels: 50-75 keV, 150-225 keV, 500-750 keV, and 1.1-1.5 MeV. For the first and third examples, the flux measurements that are used to calculate the PSD, which is, in turn, used to classify each event, are examined. For the second example, flux measurements from the spacecraft used to calculate the PSD have several large gaps in the days leading up to the event, so measurements from another spacecraft are displayed instead. For this study, we use 10 s resolution flux data, but for these event flux plots, we have smoothed the data for clarity. Time is given in epoch hours, where the ET is the time of the pressure pulses impact with the magnetosphere, and is the same as that used in the solar wind and geomagnetic index plots. With the exception of the first example, ETs for these flux plots only go back to ~48 h due to a combination of missing days in the data and results from the superposed epoch analysis that are discussed in the next section. Finally, the PSD results from each event are also shown individually in the same format as in Figure 4.6.

4.3.5.1 Example Event 1: All-Negative and All-Flat PSD Gradients

The first example to be discussed is actually an interesting series of several different events. Figure 4.7 shows the solar wind parameters and geomagnetic indices for this series of events. ET here is set to an event that is used in this study and reveals a decrease in PSD (i.e., negative gradients) over a full range of μ's immediately following the pressure pulse impact. For this event, the negative gradients, which result from a lack of source populations for electrons at all energies, are likely due to loss at higher L^*'s from the pressure pulse that occurs ~9 h before the ET, where the dynamic pressure spikes to more than 10 nPa and stays high up to the ET. The series of pressure pulses in the days leading up to this event present an interesting, though complex, scenario to this study. Two of the pressure pulses on 7 November (at -64 and -56 h ET) are not used for this study, since they do not meet the event criteria due to the lack of a large pressure enhancement in the first event, as well as inconsistencies in the associated magnetic field compressions measured by GOES 10

and GOES 12. However, looking only at the LANL data in Figure 4.8 (top), we can infer that prior to the second pressure pulse (first dash-dot vertical line from the left at about -56 h ET), the PSD gradient was negative for electrons with energies greater than a couple hundred of keV, since their fluxes either stay relatively the same or decrease significantly immediately after the pressure pulse impact. Also, the fluxes for lower-energy electrons increase immediately after this pressure pulse, but it is impossible to say what the direction of their PSD gradient was without more confidence in the magnitude of the magnetic field compression. This flux behavior is also the same for three LANL satellites on the dayside for this event. The third pressure pulse on 7 November (shortly before -48 h ET and marked with the second dash-dot line from the left in Figure 4.8) does meet all the criteria, and this pressure pulse reveals all negative PSD gradients, which is possibly due to enhanced magnetopause losses from the previous two events. Two days later, the pressure pulse at -9 h ET (third dash-dot line from left in Figure 4.8) results in flat PSD gradients for μ's of 2000, 750, and 200 MeV/G, and a positive PSD gradient for $\mu = 50$ MeV/G. This is significant because it shows that in the two days between pressure pulses, the source populations at higher L^* have been replenished. Concerning this, notice the sudden flux increase at around -33 h ET, where the flux for all channels increases abruptly by more than an order of magnitude, and then stay at these new levels. These flux data are from LANL satellite 1991-080, which is at 07:49 LT at 0 h ET; therefore, at -33 h ET, 1991-080 was on the nightside at 22:49 LT. Here, the 500-750 keV and 1.1-1.5 MeV levels increase together with the 50-75 and 150-225 keV channels, but for the large fluctuations seen in the lower channels before this time, which are probably associated with enhanced substorm activity evident from the very high AE index levels, there are only small, similar variations in the 500-750 keV flux and absolutely no similar variations in the 1.1-1.5 MeV flux. This increase is likely due to a couple of substorm injections of both lower energy and relativistic electrons similar to the event discussed in *Ingraham et al.* [2001], who find that prolonged substorm activity during the recovery phase of the large storm that occurred on 24 March 1991 resulted in substorm injections of two different electron populations: one with energies ranging from 50 to 300 keV that are commonly injected by substorms and the other with energies from 0.3 to several MeV, to GEO within a few

hours of local midnight. Similar to the 1991 event, at -33 h ET in Figures 4.7 and 4.8, 1991-080 is near ∼23:00 LT in GEO during the recovery phase of a large storm and a prolonged period of high substorm activity, when it observes a sudden injection of electrons over a broad range in energy from tens of keV to greater than 1 MeV. This injection likely explains how the source population at higher L^* is replaced prior to the all-flat gradients event that occurred one day later at around -9 h ET.

It should be noted here that very different preconditions seem to be able to result in all-flat PSD gradients. In contrast to the example discussed previously, many of the all-flat gradient events have very calm solar wind and geomagnetic conditions in the days leading up to the event times. Part of this may be from event misclassification if the PSD after the pressure pulse does not change by at least 10% of the prepressure pulse average. However, nearly flat gradients imply that radial diffusion, either inward or outward, has smoothed the radial gradient and that radial diffusion will not be significant at and beyond GEO.

4.3.5.2 Example Event 2: All-Positive PSD Gradients

As can be seen from Figure 4.10 (bottom), the PSD for all four μ's increases for this example, an event that occurred on 6 January 1998. This type of event, in which the gradients for the full range of μ's is positive, is one of the more uncommon types, with only 4 of the 86 events examined being classified as such (see Table 4.2 for numbers of each type of event). From Figure 4.9, we see that the solar wind conditions in the days leading up to the event are very calm, with no large enhancements in dynamic pressure, below-average velocity, low magnetic field magnitude, and only a few significant periods of southward IMF. This lack of activity is also apparent in the magnetosphere from the geomagnetic index data. The flux data in Figure 4.10 reflect these calm conditions, particularly in the 1.1-1.5 MeV channel (red). Figure 4.10 shows the fluxes measured by LANL-97A because the flux from 1990-095, which was at ∼11:45 LT at the pressure pulse impact time and is used to calculate the PSD for this event, has several large data gaps in the days leading up to the event. Thus, fluxes from LANL-97A, at ∼18:55 LT at the pressure pulse impact time,

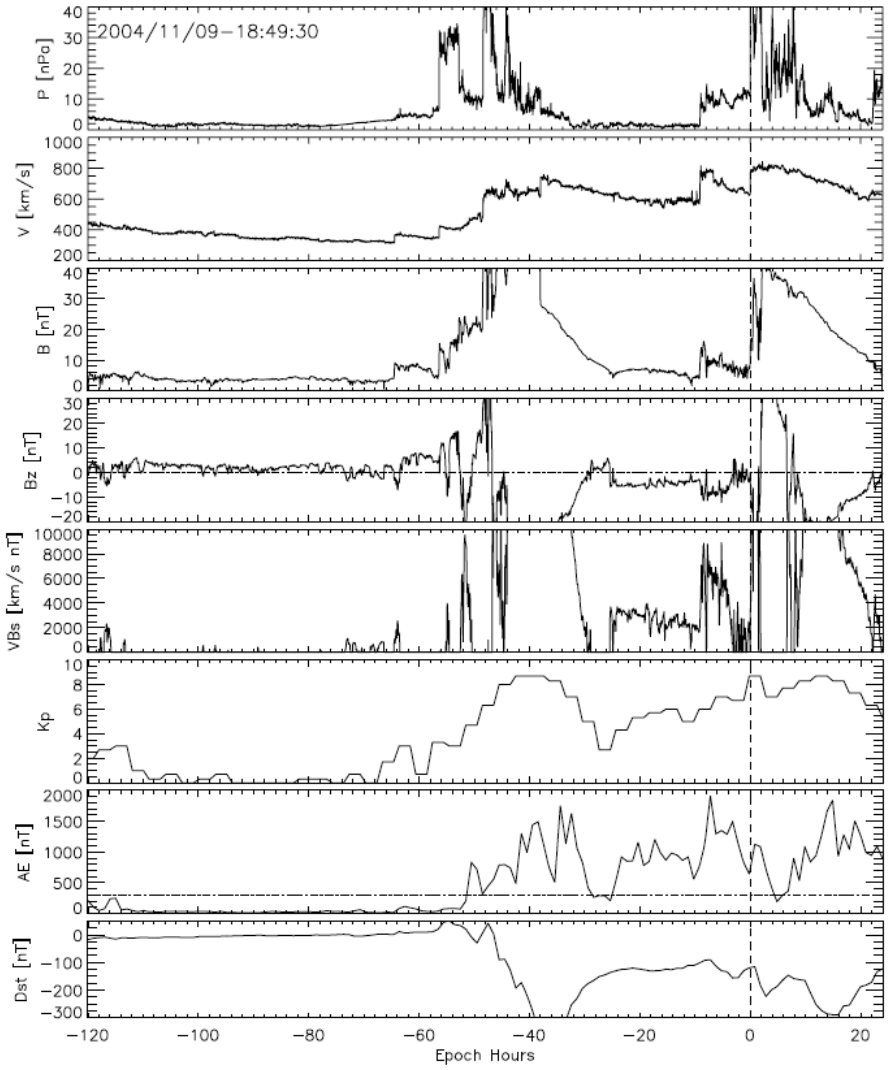

Figure 4.7: Solar wind and geomagnetic conditions for five days before and one day after an event on 9 November 2004. Epoch time is given in the top left.

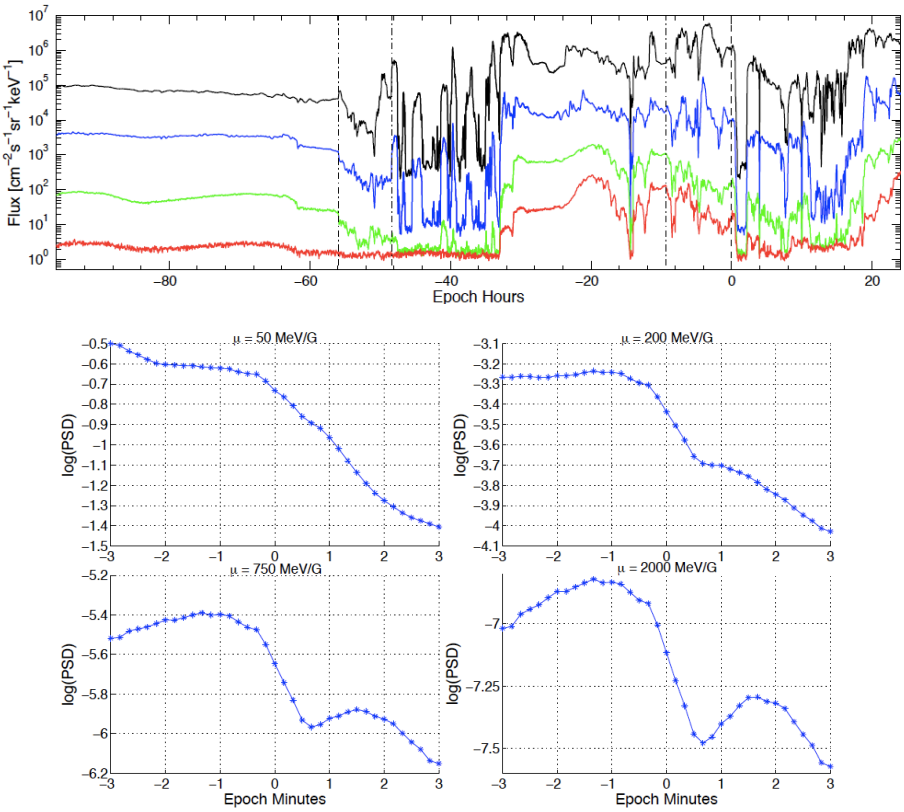

Figure 4.8: (top) Electron fluxes from LANL satellite 1991-080 for the 9 November 2004 event. Epoch time is the same as that for Figure 4.7. Fluxes are shown from four different energy channels: 50-75 keV (black), 150-225 keV (blue), 500-750 keV (green), 1.1-1.5 MeV (red). For further details, see discussion in text. (bottom) Phase space density results from this event shown in the same format as Figure 4.6.

are shown to better illustrate the flux preconditions. From this, note that the lower-energy fluxes see particle injections at around -11 and -21 h, which correspond nicely with the minor AE activity around those same times and are probably substorm injections, but the higher-energy flux is quite constant other than the normal, diurnal variation. This quiet time and positive gradient scenario is consistent with the results of *Onsager et al.* [2004], who found that during a several-day period of low solar wind and magnetospheric activity in February 1996, the PSD gradient around GEO was positive.

It is of interest here to briefly discuss how the PSD results can differ when using fluxes from different LANL spacecraft, which are at different local times around GEO, to derive the results. For this event, using fluxes from the spacecraft closest to noon (1990-095), which is how events are classified in this paper, the results are classified as an all-positive gradients event. However, when the same analysis is performed using fluxes from LANL-97A, the results are different; the PSD over the full range of μ remains relatively flat. This local time difference is potentially significant; it may result either because the two spacecraft are at different L^* or because LANL-97A was on the nightside and particles are not necessarily transported radially inward there. For further discussion on these local time differences, refer to *Lee et al.* [2005] and *Shi et al.* [2009], where the flux responses to sudden solar wind pressure pulses as measured by multiple LANL spacecraft are examined.

4.3.5.3 Example Event 3: Mixed PSD Gradients

Figures 4.11 and 4.12 show the conditions for the most common type of event, in which there is a difference in the PSD gradients when those for electrons with μ of 50 MeV/G are compared to those for electrons with μ of 2000 MeV/G. Of this type of event, there are 23 cases where the PSD gradient is negative for 2000 MeV/G electrons but positive for 50 MeV/G electrons, 18 cases where it is negative for 2000 MeV/G electrons but flat for 50 MeV/G electrons, and 7 cases where it is flat for 2000 MeV/G electrons but positive for 50 MeV/G electrons. There are no cases where the gradient is negative or flat for 50 MeV/G electrons but positive for 2000 MeV/G electrons.

From Figure 4.11, one can see that there were three sudden pressure pulse events during

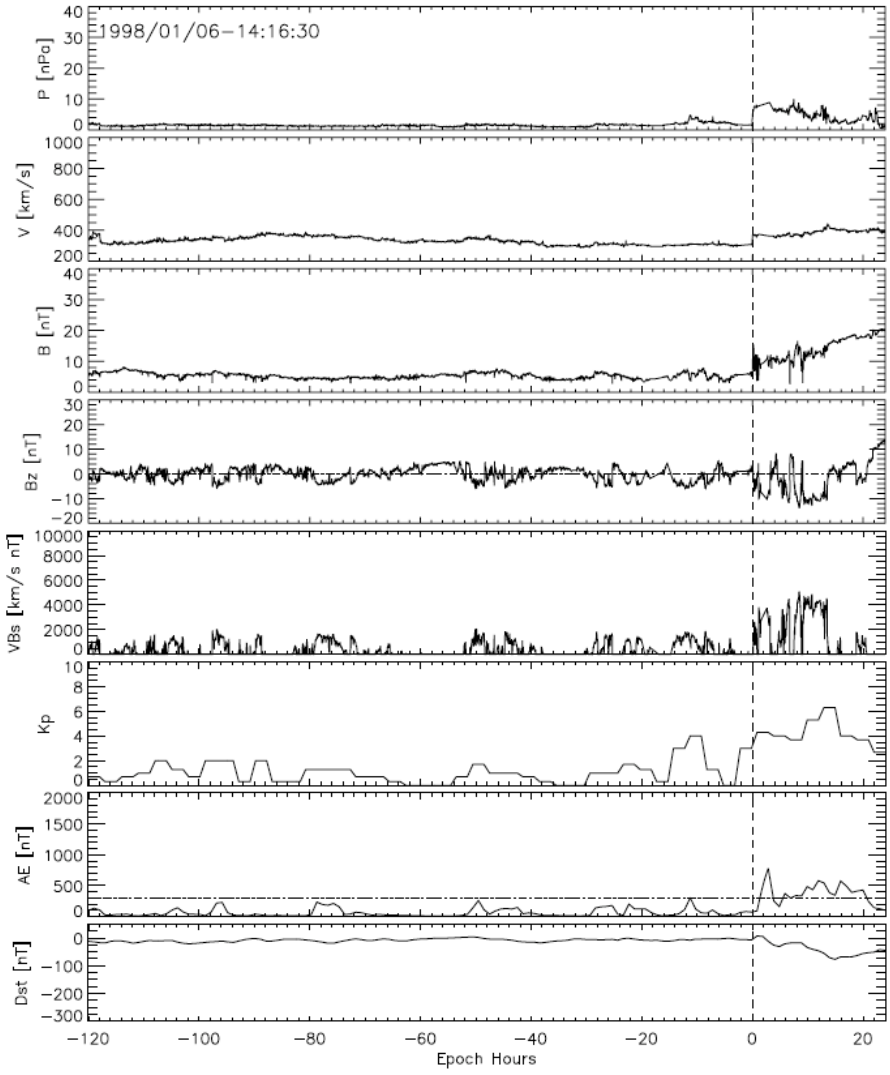

Figure 4.9: Solar wind and geomagnetic conditions for five days before and one day after an event on 6 January 1998. Epoch time is given in the top left.

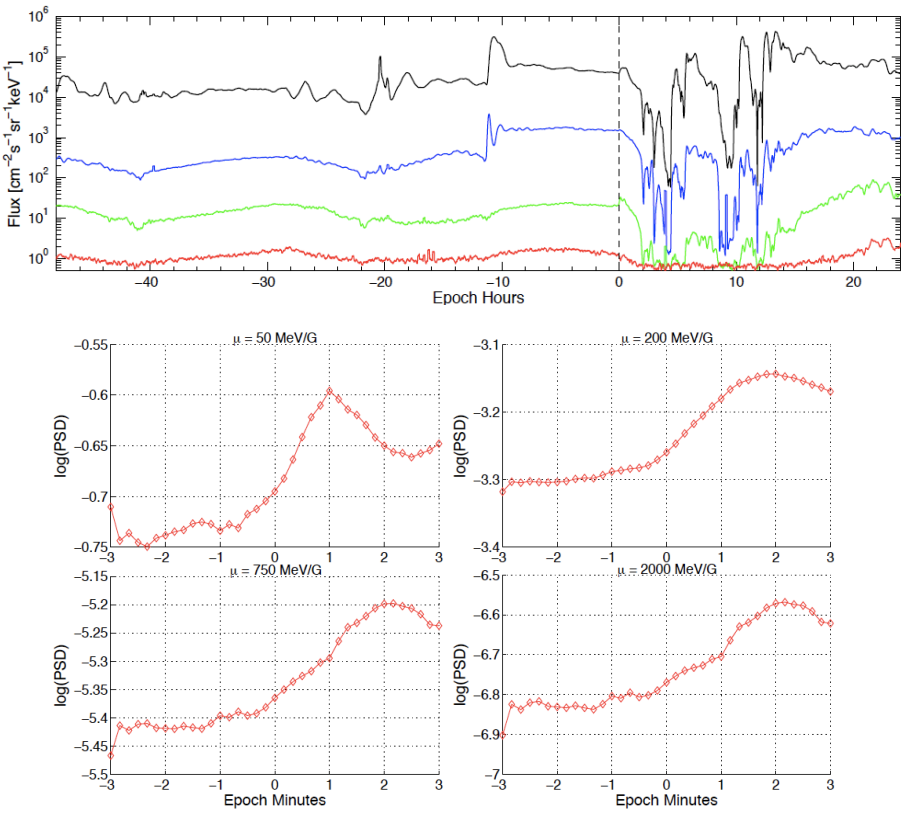

Figure 4.10: (top) Electron fluxes from LANL-97A for the 6 January 1998 event. Epoch time is the same as that for Figure 4.9. Colors correspond to the same four energy channels as in Figure 4.8. (bottom) Phase space density results from this event shown in same format as Figure 4.6.

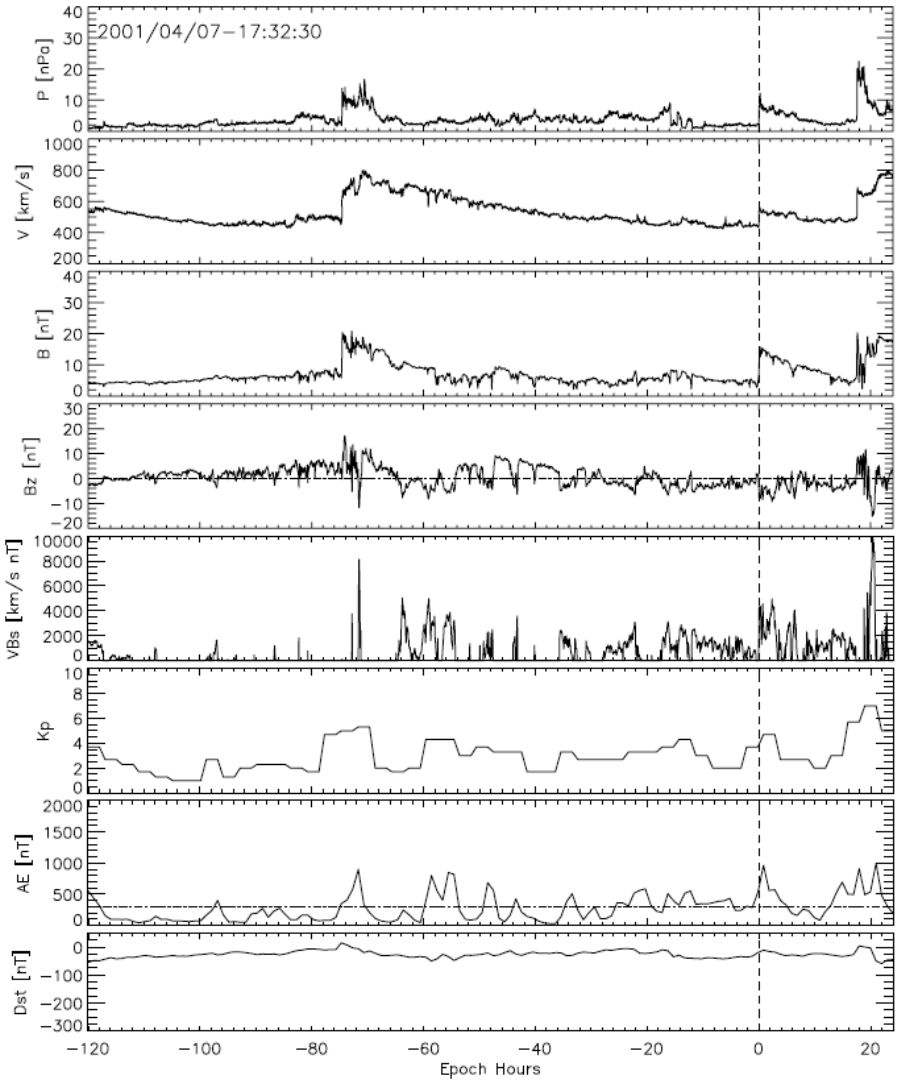

Figure 4.11: Solar wind and geomagnetic conditions for five days before and one day after an event on 7 April 2001. Epoch time is given in the top left.

the six days of time displayed. The first event, shortly after -75 h ET, is used in this study and classified as an all-negative gradients event. This event spawns some nearly continuous activity in the magnetosphere, which is evident in the Kp and AE indices, but no large storm prior to the second pressure pulse at 0 h ET. This pressure pulse, occurring at 17:32 UT on 7 April 2001, is a mixed gradient event, where the PSD for electrons with $\mu = 50$ MeV/G increases, while the PSD for μ's higher than 200 MeV/G all decrease, which is evident in Figure 4.12 (bottom). This implies that the PSD radial gradient was positive for lower-energy electrons and negative for electrons with energies greater than a couple hundred keV prior to the event. This is evidence of two distinct populations. A potential explanation of this case is that an internal heating source, potentially whistler mode chorus and/or magnetosonic waves generated by substorm-injected electrons and ring current particles, respectively, was active somewhere inside of GEO for electrons with energy greater than a couple hundred keV in the 0-3 days leading up to the event. Meanwhile, the positive gradients observed for lower-energy electrons are explained by a source population at higher L^*, most likely plasma sheet electrons injected during substorms. From Figure 4.12 (top), it is evident that in the days leading up to the event, the electron sources dominated slightly over electron loss, since the flux for all four energy channels increases overall prior to the event. Finally, the third pressure pulse, which occurs at around 17.5 h ET, is also used in this study and is classified as an all-negative gradients event in which the PSD for the full-range of μ's decreases most likely due to enhanced loss to the magnetopause from the pressure pulse at 0 h ET.

4.3.6 Superposed Epoch Analysis

A superposed epoch analysis has been conducted to determine if there are any distinguishing characteristics in the statistical preconditions leading up to different types of events. We have gone through several different variations of this study, comparing different combinations of event types to one another, though here, we only discuss the results from one of these variations. For this analysis, all events are aligned by ET, which is once again defined as the pressure pulse impact times, and events are grouped to form two sets based on their type or PSD behavior for a particular

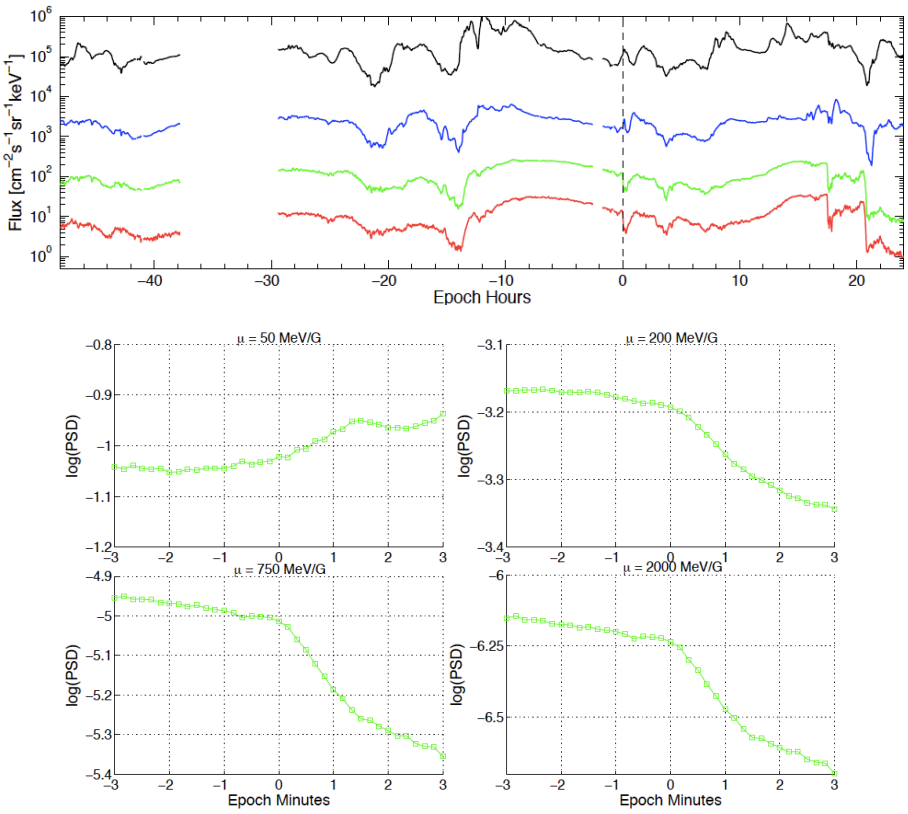

Figure 4.12: (top) Electron fluxes from LANL-01A for the 7 April 2001 event. Epoch time is the same as that for Figure 4.11. Colors correspond to the same four energy channels as in Figure 4.8. (bottom) Phase space density results from this event shown in same format as Figure 4.6.

μ. We compare 20 parameters in all, ten from the solar wind (dynamic pressure; total velocity; IMF magnitude; IMF B_x, B_y, and B_z in GSM coordinates; number density; VB_s; clock angle; and the Akasofu ε parameter), nine from geomagnetic index data (Dst, Dst_{min}, AU, AL, AE, AE^*, Kp, and plasmapause locations derived from Dst [*O'Brien and Moldwin*, 2003] and Kp [*Carpenter and Anderson*, 1992]), and LANL electron fluxes. We compare the upper and lower quartiles, medians, and means of each parameter from the two sets of events for 120 h before the ET and 24 h after it for the solar wind and geomagnetic parameters, and 48 h before the ET and 24 h after it for electron fluxes. The two events from 1996 are not included in the epoch analysis since there are no AE data available from that year.

The variation discussed here separates events into two groups based upon the sign of the gradient for electrons with μ = 2000 MeV/G: all those events in which a negative gradient is observed are grouped together to make one set, and all events in which a positive gradient is observed are grouped to make the second. The negative gradients set consists of 51 events since the all-negative gradient events in which loss to the magnetopause is suspected to be based on estimated magnetopause locations [*Petrinec and Russell*, 1996] in the days leading up to the event are not included. These are omitted because we understand, at least in part, why the gradients are all negative and also because they all have large events occurring in the days leading up to the actual event, which will skew the results. All-flat gradient events are not included since a wide range of preconditions can result in all-flat PSD gradients, which was discussed at the end of the section on event 1. Results from this variation are shown in Figure 4.13. Means of each set are displayed and differentiated by color, with black curves corresponding to the negative gradients set and red curves corresponding to the positive gradients set. Here, we only show means, since quartiles for the positive gradients set are insufficient because there are only four of these events. Other pressure enhancement events are evident in the positive gradients data at around -118, -88, -82, and -69 h ET, and the evidence of these events is also present in the geomagnetic activity indices, as can be seen in the AE^* enhancements and geomagnetic storm evident from the Dst curves. This activity is interesting, however, since only two of the four events see pressure enhancements and activity 3-5

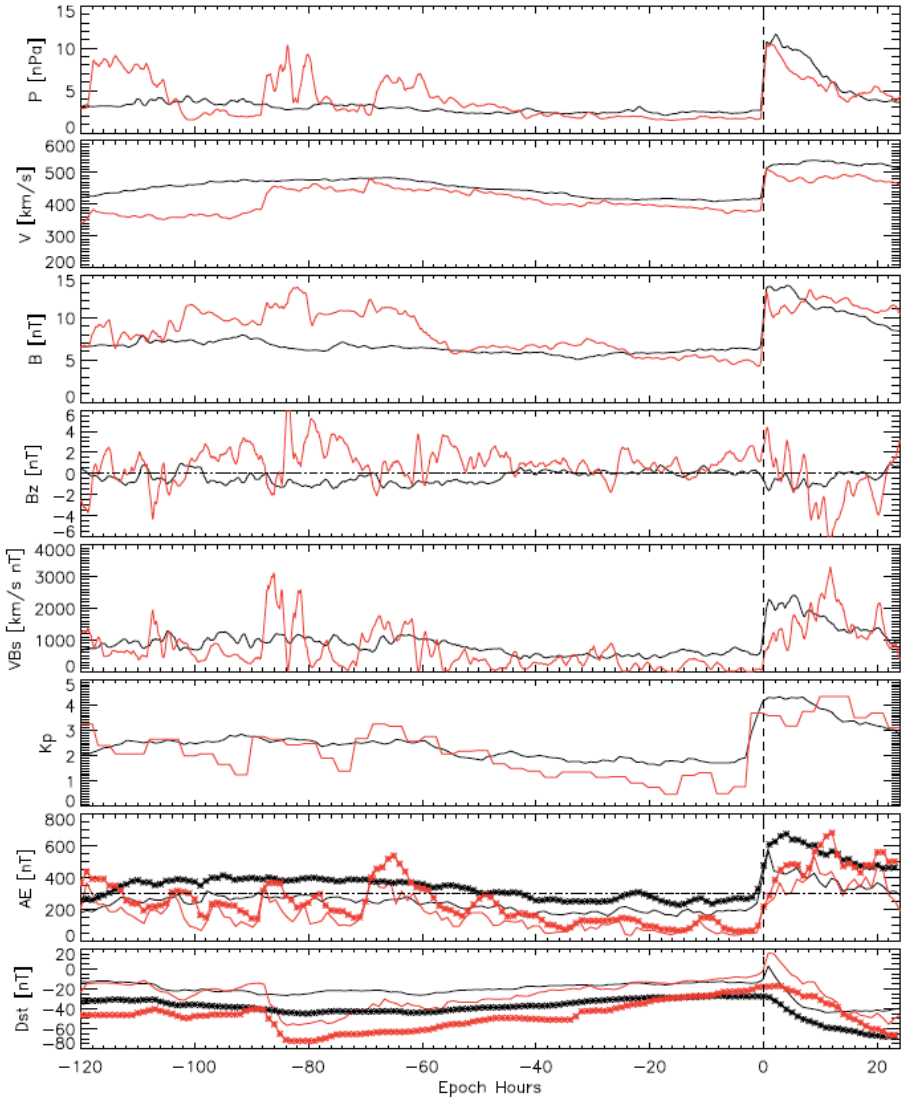

Figure 4.13: Solar wind and geomagnetic results from a superposed epoch analysis. Black curves represent the means from 2000 MeV/G negative gradient events, and red curves represent the means from 2000 MeV/G positive gradient events. For the AE and Dst plots, asterisks are used for AE^* and Dst_{min} means.

days prior to the ET, and both of these are followed by at least two days of very calm conditions that stay calm right up to the ETs. The other two positive gradient events exhibit very calm conditions for more than five days prior to the ETs, as is shown in the second example case. In this same two days of time leading up to the negative gradient events, notice how the means of Kp, AE, and AE^* all stay relatively high compared to the positive gradient events. Also, notice that the mean B_z is almost entirely southward from around -98 to -44 h ET for the negative gradient events, while it is most often northward for the five days leading up to the positive gradient events. From Figure 4.14, it is clear that the average fluxes for the full range of LANL energies, 50 keV-1.5 MeV, are significantly higher prior to the negative gradient events than they are prior to the positive gradient events, and the difference between the two sets increases with increasing energy.

4.3.7 Discussion of Results

4.3.7.1 Basic Scenario

The events discussed here can all be described using one basic scenario, in which radial diffusion redistributes outer-belt electron PSD from regions of high PSD to regions of lower PSD. In the radial direction, this redistribution is dependent on the radial gradient of the PSD between the two "sink" regions, the slot region between the inner and outer belts, and the magnetopause. We know some source of PSD is active because if it was not, then the outer belt would be empty due to the PSD diffusing to these two sinks. There are three potential sources of PSD for electrons near GEO: (1) radial transport from regions of higher PSD inside of GEO, (2) radial transport from regions of higher PSD outside of GEO, and (3) local acceleration of lower-energy electrons to higher energies near GEO. The effects from each of these source processes at GEO can be dependent upon electron energy, and the temporal history of the sources and sinks.

With this basic scenario in mind, we can now discuss the various combinations of sources and sinks that can lead to the types of gradients that we observe in this study beyond GEO. Negative gradients beyond GEO can be the result of: (1) PSD outside the trapping boundary (e.g., in the

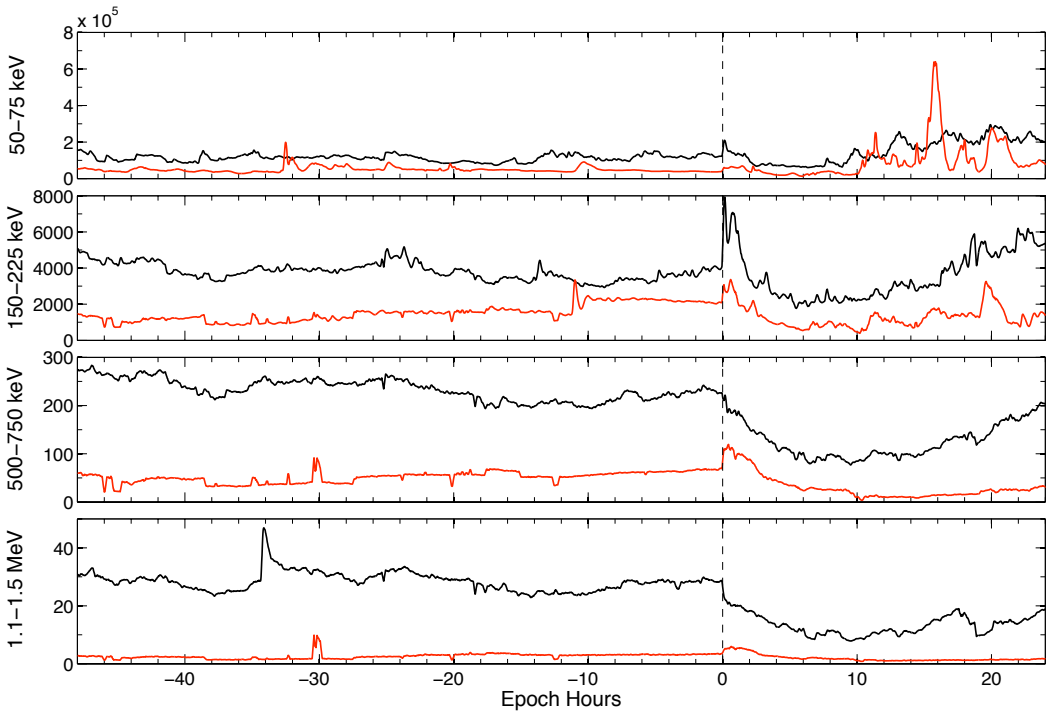

Figure 4.14: Electron flux results from a superposed epoch analysis. Results from four different energy channels are shown: 50-75 keV, 150-225 keV, 500-750 keV, and 1.1-1.5 MeV. Black and red curves correspond to mean fluxes from the same events used for the results in Figure 4.13.

plasma sheet) decreasing over time, (2) an earlier event increased the PSD inside of GEO and the electrons are still diffusing outward, (3) ongoing heating/acceleration of electrons inside of GEO, or (4) the PSD source not changing but an increased rate of diffusion at higher L^*. Positive gradients beyond GEO can be the result of the exact opposite situations occurring, i.e.: (1) PSD outside the trapping boundary increasing over time, (2) an earlier event decreased the PSD inside of GEO and electrons are still diffusing inward, (3) ongoing heating/acceleration occurring outside of GEO, and (4) the PSD source not changing but a decreased rate of diffusion at higher L^*. Flat gradients observed in this study can result from diffusion smoothing out any PSD gradients beyond GEO or because the gradient was not sharp enough to classify as either positive or negative. A mix of PSD gradients for different μ's can occur when the source and sink processes are different for different energies. Finally, a peak in the PSD gradient beyond GEO can occur if: (1) the PSD gradient is originally positive, then there is some loss at higher L^*, (2) there is an "on-off" source at higher L^*, or (3) there is local heating/acceleration beyond GEO. For discussions on scenarios resulting in PSD peaks, see *Green and Kivelson* [2004] and *Chen et al.* [2007b].

4.3.7.2 Discussion of the Example Cases

We now offer some speculation as to which of the aforementioned conditions may have resulted in some of the events discussed in this study. The events in which the PSD over the full range of μ's examined is negative can be the result of any of the four source/sink conditions for negative gradients. However, for 12 of these events (out of 23 total), including the event in the first example, we can say with some confidence that the negative gradients are at least partially the result of enhanced losses to the magnetopause in the days leading up to the events. For the remaining 11 events, since the magnetopause does not come inside the range from which we expect the electrons to be transported inward during the field compressions (based on previous test-particle simulations by *Li et al.* [2003]), we can speculate that an internal source, an increased rate of diffusion at high L^*, or a decrease in the plasma sheet PSD is likely the cause of the negative gradients observed.

Despite understanding the likely reason behind the all-negative gradients observed in the first

example event, the series of events that occurred in the days leading up to this event introduced a very interesting case study. The intriguing thing about these events, which occurred between 7 and 9 November 2004, is that in the time span of just 39 h between the pressure pulse shortly before -48 h ET (in Figure 4.7) and the pressure pulse at -9 h ET, the source populations for both low-energy (50-200 keV) and high-energy (200 keV to >1 MeV) electrons is replenished. This timescale of around 1-2 days is important and will be repeated throughout this discussion of results. Also note that this replenishing of the source occurs during the recovery phase of a very large storm (see *Dst* data in Figure 4.7) in which there is significantly enhanced substorm and magnetospheric activity (see *AE* and *Kp* data in Figure 4.7) that result in substorm injections of electrons over an abnormally large energy range (tens of keV to >1 MeV; starting at around -33 h ET in Figure 4.8).

The all-positive gradient events can be the result of any of the four aforementioned source/sink conditions for positive gradients, and thus, it is difficult to speculate the reason why these gradients are observed. PSD in the plasma sheet may have increased prior to these events, or losses at lower L due to an expanding plasmasphere (in more than 2 days of quiet conditions prior to these events) can decrease the PSD inside of GEO. Heating outside of GEO is possible, though if this was the case, we would expect to see some evidence of a peak in the results. Finally, diffusion rates may have decreased at higher L, which once again may be related to the 2+ days of quiet conditions. Again, these results are consistent with the results of *Onsager et al.* [2004], who found the gradient near GEO to be positive during quiet conditions.

We find 48 mixed gradient events in this study, which is indicative of two distinct populations. Of these, there are 41 in which the PSD gradient is negative for 2000 MeV/G electrons, while being positive or flat for 50 MeV/G electrons. This is consistent with the expected results of the theory of relativistic electron heating by wave-particle interactions. By this theory, electrons with energy greater than a couple hundred keV have a source somewhere outside of the plasmapause [*Meredith et al.*, 2001, 2003a] where local heating by whistler mode chorus [e.g. *Horne and Thorne*, 1998; *Summers et al.*, 1998] and/or magnetosonic waves [e.g. *Horne et al.*, 2007] occurs, and lower-

energy electrons (energy of tens of keV to a couple hundred keV) have a source at higher L^* due to substorm injections and convection [e.g. *Meredith et al.*, 2003a, and references therein]. The timescales for relativistic electron heating by wave-particle interactions are about the same for both whistler mode chorus and magnetosonic waves, around 1-2 days [*Horne et al.*, 2005a, 2007], and both whistler mode chorus and magnetosonic waves tend to be more intense with enhanced AE^*, which indicates a connection between these waves and substorm activity and/or periods of enhanced convection [*Meredith et al.*, 2001, 2008]. Finally, *Bortnik and Thorne* [2007] defined an "anchor point" energy of a couple of hundred keV at which electrons with greater energy tend to be accelerated by interactions with whistler mode chorus, while those with less energy tend to be scattered and lost by the interactions.

This is all consistent with the majority of the mixed gradient event results in that the gradient of electrons with μ greater than a couple hundred MeV per Gauss (equivalent to those with energy above a couple hundred keV at GEO) is negative beyond GEO, which may be the result of a PSD source inside of GEO prior to the event time. Meanwhile, for these same events, the gradient of electrons with μ less than a couple hundred MeV per Gauss is positive or relatively flat, indicating a source outside of GEO, and electrons with μ between around 100 and 300 MeV/G consistently mark the transition region between the two populations. Also, based on the example mixed gradient event and the superposed epoch analysis results, the AE and AE^* indices are typically high in the days leading up to those events that reveal a negative gradient for 2000 MeV/G electrons. Last, it is stressed that the opposite situation, in which the gradient of 2000 MeV/G electrons is either positive or flat while the gradient of 50 MeV/G electrons is negative, is not observed.

4.3.7.3 Discussion of the Superposed Epoch Analysis

The most significant features of the superposed epoch analysis are the differences in IMF B_z, Kp, AE, AE^*, and fluxes at different energies, as well as the vastly different conditions at greater than -50 h that can produce all-positive PSD gradient results. The AE and AE^* indices are consistently high, on average, for the negative gradient events, and there is considerable activity

in both indices during the active periods preceding two of the positive gradient events. However, after -48 h ET, the AE and AE^* levels drop significantly for the positive gradient events, while remaining high for the negative gradient events. On this, *Meredith et al.* [2003a] reported that the most significant electron enhancements, which they also relate to chorus-driven acceleration, are associated with prolonged substorm activity, where the AE index is greater than 100 nT for a total integrated time of more than two days. The AE index is, on average, around 200 nT for more than two days leading up to the negative gradient events, whereas for the positive gradient events, it drops to below 100 nT and remains almost consistently below this level in the two days leading up to the events. Finally, the differences in the two sets of fluxes prior to the events (see Figure 4.14) are also consistent with the results of *Meredith et al.* [2003a], who found that significant flux enhancements are also associated with enhanced fluxes of electrons at a couple hundred keV.

We believe that the weak statistics of the four all-positive gradient events provide further insight into an important time scale for the outer-belt electrons. First of all, the active periods are only seen at greater than 50 h for two of the four events, but all four events are classified as that in which the PSD gradients over the full range of μ is positive beyond GEO. Thus, either both active conditions and quiet conditions over five days can lead to positive PSD gradients beyond GEO or what happens more than two days before the event is not as important as what happens in the two days leading up to it. Based on previous studies, positive gradients beyond GEO have been observed during quiet times [e.g. *Onsager et al.*, 2004, and references therein], but during active conditions, particularly, geomagnetic storms, negative gradients have been observed beyond GEO for high-energy electrons [e.g. *Chen et al.*, 2007a]. Taking these previous results into account with our own, we propose that the outer-belt electrons may have an effective "memory" of approximately two days.

4.3.8 Conclusion and Further Work

Here, we have studied the radial gradients of outer-belt electron PSD prior to 86 sudden solar wind pressure enhancement events. Of these, the majority reveal that the gradient for electrons

with μ = 2000 MeV/G is negative, which is consistent with the results of *Chen et al.* [2007b], while the gradient for electrons with μ = 50 MeV/G is positive or relatively flat, and there is a transition between the two types of gradient normally for electrons with μ around 200 MeV/G. This is indicative of two different source populations for near-equatorially mirroring electrons with high and low energies. We have discussed how the results for 41 of the 86 cases can be explained directly by the current theory and understanding of relativistic electron acceleration by wave-particle interactions. Additionally, we have examined the preconditions for several examples of distinct types of PSD gradient results. One of the most notable features of these different examples is the geomagnetic activity in the 0-2 days leading up to the event times; the events in which a negative gradient is seen for 2000 MeV/G electrons have considerably higher Kp and AE levels than those for the events in which a positive gradient is seen for 2000 MeV/G electrons. A superposed epoch analysis has also been conducted, and it reveals similar differences.

Results here indicate that 1-2 days is a significantly important timescale to the outer-belt electrons, though this should not come as a surprise as other studies have repeatedly found this to be true [e.g. *Baker et al.*, 1994; *Horne et al.*, 2003, 2007; *Li et al.*, 2005; *Burin des Roziers et al.*, 2009]. Events that show at least two days of little to no geomagnetic activity tend to produce positive or flat gradients over the full range of μs examined, whereas geomagnetic activity (evident in the AE and Kp indices) in the 0-2 days prior to events tends to produce negative gradients for the higher-energy electrons. This is indicative of the great importance of substorms and/or enhanced convection to the gradient results, and thus, outer-belt electron acceleration. This is consistent with the findings of *Li et al.* [1998] and *Meredith et al.* [2002, 2003b], and is also additional evidence that approximately two days is an important timescale for the outer-belt electrons.

It is important to note that these conclusions are consistent with those of previous studies, though they are independent and come from the results of a new analysis technique. This study provides new observational evidence agreeing with the combined works of several, independent studies on the acceleration of outer-belt electrons by wav-particle interactions. Also, the results presented here extend our understanding of outer radiation belt dynamics and provide a broad context for

comparisons with previous PSD gradient studies since this study examines PSD gradients resulting from quiet, moderate, and active geomagnetic conditions for outer-belt electrons at and beyond GEO over a very broad range of energies (tens of keV to >1 MeV).

This paper introduces a great deal of additional studies that can be conducted. Test-particle simulations can be used for selected individual events to determine how far electrons are transported radially inward and to quantify the gradient. Also, the analysis technique can be applied to spacecraft measurements made in orbits outside of GEO. This study does not include ULF wave power, which would be interesting to analyze for these events in an attempt to establish any correlation with the different PSD gradients, since it has been established that ULF waves are critical to enhanced radial diffusion [e.g. *Elkington et al.*, 1999] and previous studies find that they may be important to electron acceleration beyond GEO [e.g. *O'Brien et al.*, 2003]. Finally, considering the apparent importance of substorm activity to how outer-belt electron radial gradients develop, a survey of relativistic electron responses to substorms, similar to either of those conducted for geomagnetic storms by *O'Brien et al.* [2001] or *Reeves et al.* [2003], should prove to be beneficial to the community.

Many questions remain concerning Earths outer-belt electrons, and as we become more dependent on satellites in this region of space, better understanding and models of the outer radiation belt become increasingly more important. As more evidence of local heating by wave-particle interactions is discovered, the question of electron acceleration appears to be getting clearer. However, the events examined for this study still display some of the complexity in the nature of the outer radiation belt electrons. Hopefully, future missions like NASAs Radiation Belt Storm Probes will provide the measurements needed to further resolve some of the outstanding issues.

4.4 Conclusions

From this study of outer belt PSD radial gradients for electrons from 50 keV to 1.5 MeV at GEO, we have produced results that reveal two distinct populations with different primary source regions. Electrons with μ from 50 MeV/G up to ~200 MeV/G, which correspond to energies of 50

to a few hundred keV at GEO, have a source at L-shells higher than GEO, which is most likely the plasma sheet. Relativistic electrons with μ above several hundred MeV/G, however, have a source that is most often inside of GEO. This is most consistent with the theory of relativistic electron acceleration by wave-particle interactions near the heart of the outer belt (L$\sim$5 R_E), which is discussed in Chapter 2. This study is the first to cover such a wide range of electrons μ's (and energy), and it explains many of the seemingly inconsistent results from earlier studies. Though the results reveal that acceleration by wave-particle interactions can explain the majority of the observed PSD gradients, there are still several cases for all-flat gradients and a few cases of all-positive gradients, which show that at other times under different conditions, other processes, like inward radial diffusion for example, may be important to relativistic electron acceleration.

Appendix A details three additional case studies that were not included in the JGR paper. One of the cases included represents those in which negative gradients were observed for the full range of μ examined when there is no evidence of magnetopause shadowing in the days leading up to the observation. Originally, we concluded that these cases may be the result of a source inside of GEO for both populations of electrons. However, this type of case may better be explained by off-equatorial B_{min} (i.e. minimum magnetic field strength) pockets at higher-L, which result in Shabansky orbits [*Shabansky and Antonova*, 1968]. Shabansky orbits describe electron drift shells that have become bifurcated on the dayside such that electrons bounce around B_{min} locations off the magnetic equator. These drift orbits are described in detail in *McCollough et al.* [2010]. Assuming near-90°-peaked pitch angle distributions at higher-L, if electrons are bouncing in Shabansky orbits on the dayside, then the near-equatorial flux measurements at those L-shells will be lower. Thus, for the study discussed in this chapter, Shabansky orbits at higher L-shells can explain how results of PSD for fixed μ could show a decrease for near equatorial measurements.

A good extension to this study would be to study the PSD radial gradients for a wide-range of fixed μ and K inside of GEO, similar to that of *Green and Kivelson* [2004]. Such a study is possible using CRRES data, though for a longer time range over different phases of the solar cycle, RBSP data will be ideal. Another extension is to study the electron population beyond GEO near

the outer boundary of the outer radiation belt. Just such a study is discussed in the following chapter.

Chapter 5

Identifying outer belt electron sources II: Energetic electrons near the last closed drift shell

5.1 Introduction

As discussed in Chapter 2, trapped energetic particles in Earth's magnetosphere drift azimuthally around the system on closed surfaces known as drift shells. The region near the outermost closed drift shell (i.e. the Alfven layer as defined in *Wolf et al.* [2007] and referred to throughout as L^*_{max}), which defines the boundary between the stable trapping region and the quasi-trapping or loss region, is important to Earth's trapped particle population and has not been thoroughly studied for low latitudes in the past. It is in this region that lower-energy source electrons can first become stably trapped after substorm injections or enhanced convection introduce them from the tail. It is here too that radiation belt electrons can become lost to the magnetopause by way of magnetopause shadowing. Also, the electron phase space density for fixed first and second adiabatic invariants at this outer boundary defines whether radial diffusion is radially inwards or outwards, and thus, it is crucial to understand the dynamics of this boundary to better understand the source, loss, and transport processes of Earth's radiation belt electrons.

In this study, I identify L^*_{max} crossing times for the THEMIS spacecraft using the Tsyganenko 2001-stormtime (Ts01S) [*Tsyganenko et al.*, 2003] magnetic field model, and then, THEMIS-SST electron flux data from 10's to >100 keV are used to identify the actual crossing times. With their highly eccentric orbits and apogees ranging from 10 to 30 R_E, the THEMIS spacecraft are ideal for studying this region near the last closed drift shell. Figure 5.1 shows THEMIS-A (TH-A) positions

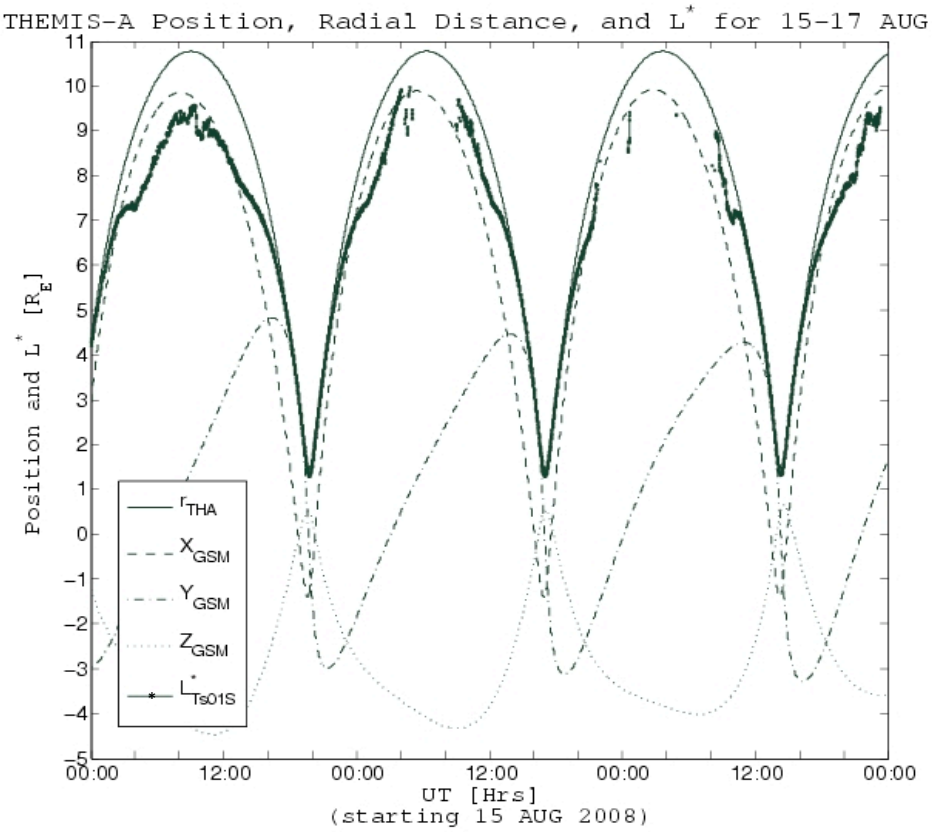

Figure 5.1: Plot showing TH-A orbits for 15-17 August 2008 with the calculated L^*'s for 90 degree equatorial pitch angle electrons from the Ts01S model.

and Ts01S L^* results for 15 - 17 August 2008. L^*_{max} here is the last defined L^* identified using the Ts01S model. For example: in Figure 5.1, TH-A does not cross the L^*_{max} boundary based on Ts01S on 15th August since L^* remains defined throughout the entire orbit; however, on 16th August, TH-A makes three L^*_{max} crossings: once just before 04:00 UT (going outward from defined to undefined L^*), then again coming back into the system at around 09:00 UT, and finally once more on another outward pass at around 22:00 UT.

Using the Ts01S model, there are nearly 2000 L^*_{max} crossings by the THEMIS-A, -D, and -E spacecraft between 16 Dec. 2007 and 15 Mar. 2009. The crossings for the year 2008 are shown in L^* and MLT in Figure 5.2. This chapter describes the analysis I performed using these crossings. I examine some interesting cases including substorms, sawtooth injections, instrument anomalies, and plasma sheet thinning. I also describe the development and results of a simple, analytic model that can be used to quickly approximate L^*_{max} and show how this model is actually more accurate than using the much more computationally intensive Ts01S model. Finally, I discuss how these crossings present additional evidence in support of the results from the previous chapter implying that low-energy (10's $\sim$ 100 keV), seed electrons have a source in Earth's magnetotail, while the relativistic population most often has a source in the inner magnetosphere.

5.2 Datasets and Observations

To determine the location of the last closed drift shell, I start by using the Ts01S model, which uses the Dst index and various solar wind conditions propagated to the magnetopause as inputs [*Tsyganenko et al.*, 2003]. In this study, I use AE, AL, AU, Dst, and Kp index data available from the World Data Center for Geomagnetism, Kyoto [See: $http://wdc.kugi.kyoto-u.ac.jp/wdc/Sec1.html$], and solar wind data from the OMNI dataset available on NASA's CDAWeb [See: $http://cdaweb.gsfc.nasa.gov/$]. With this data, the ONERA-DESP library [See: $http://craterre.onecert.fr/support/user\_guide.html$] is employed to use the Ts01S model for calculating L^* and MLT. Using TH-A, -D, and -E ephemeris data, L^*'s are calculated for particles with local pitch angles of 90 degrees. Since calculating L^* is computationally intensive, I use an algorithm that

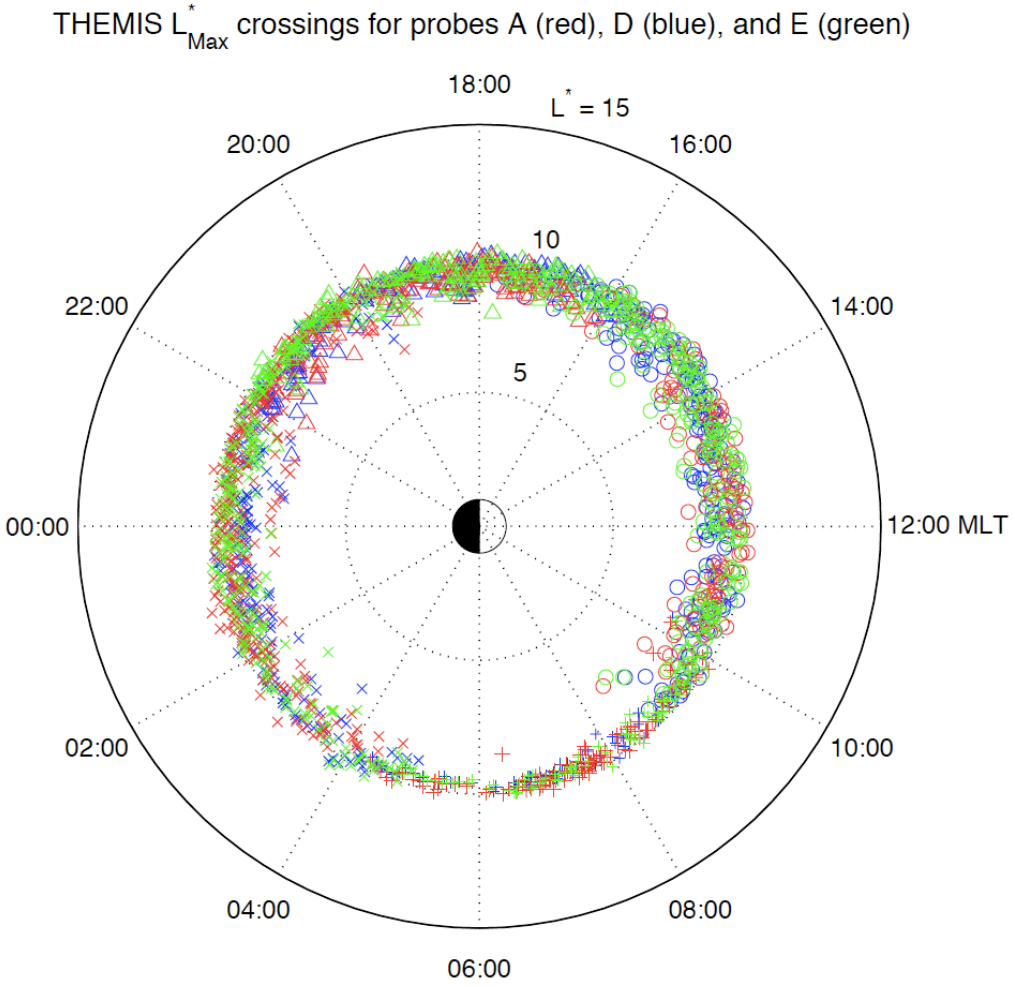

Figure 5.2: Plot showing all of the L^*_{max} crossings identified using the Ts01S magnetic field model for the THEMIS spacecraft orbits. Crossings are color coded by spacecraft as listed in the heading and symbol coded by orbit phase (dayside with circles, duskside with triangles, nightside with x's, and dawnside with pluses).

starts at the apogee of each orbit and calculates L^* for each time before and after apogee so long as L^* is undefined. When the algorithm encounters more than ten consecutive defined L^*'s, it marks the turning point from undefined to defined as a L^*_{max} crossing time. In this way, a large database of L^*_{max} crossing times for TH-A, -D, and -E was constructed for the period from December 2007 - March 2009.

Using these times when the Ts01S model indicates that each THEMIS spacecraft has crossed the last closed drift shell, I examine the corresponding THEMIS-Solid State Telescope (SST) data for two hours before and after for signs of the boundary in the energetic electron fluxes. THEMIS-SST data has some severe issues concerning its reliability within GEO based on inter-satellite calibrations. This is likely due to it's inadequate shielding, which consists of only a thin layer of aluminum (see discussion and instrument diagram in Chapter 2). However, here I am only using the data at higher L-shells and am not comparing the flux levels with other spacecraft measurements. I am simply studying relative changes in the flux levels, which should be generally unaffected by the instruments' shielding issues at these L-shells. For this study, I examine a time range around each of the Ts01S L^*_{max} times since Ts01S is only a model and not necessarily accurate at determining the true boundary. Figure 5.3 is an example of clear evidence of the boundary from a nightside crossing by TH-D. In this figure, TH-D is initially in the tail, where energetic electron fluxes are significantly lower. Crossing the L^*_{max} boundary, TH-D observes a large change in electron fluxes as it enters the trapping region. However, this is just one type of feature present in the dataset of energetic electron data near L^*_{max}.

Reviewing all of the crossings, I take note of any events and features that are evident in the data. One of the features that occurs regularly in the data consists of large spikes in the fluxes as can be seen in Figure 5.4. THEMIS-SST uses an attenuator to change the geometric factor and control the count rates on the detectors, which allows the instrument to operate in a large range of flux environments. The instrument opens the attenuator, increasing the geometric factor by a factor of around 64, when environmental fluxes are low. However, when the environmental flux goes up to a certain level, the instrument closes the attenuator, reducing the geometric factor and

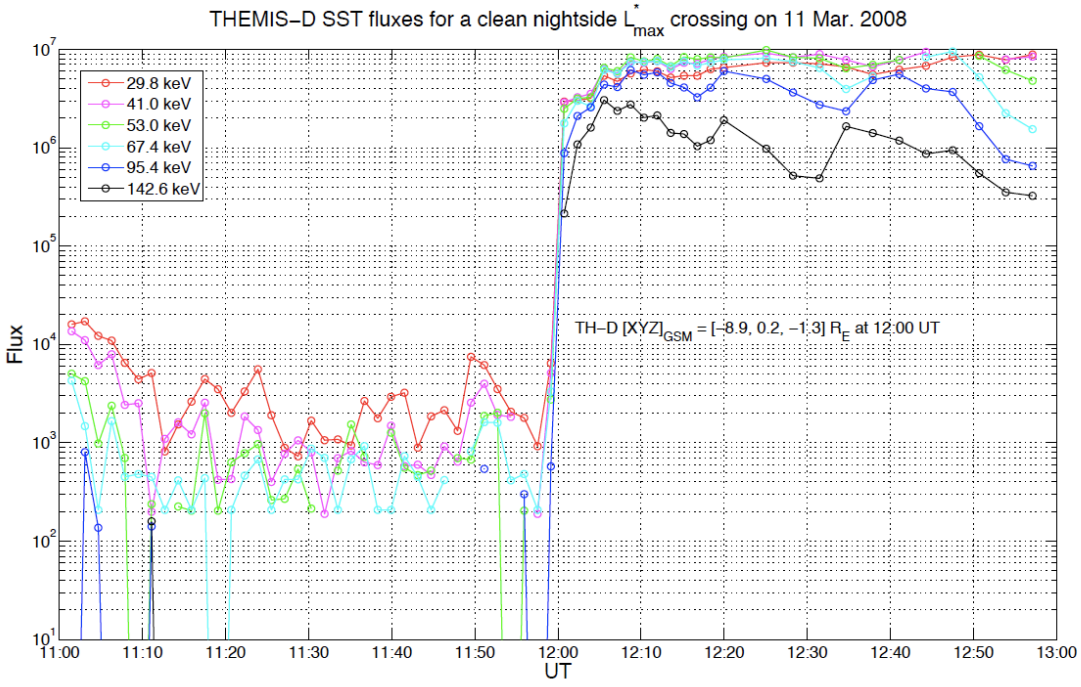

Figure 5.3: THEMIS-D SST fluxes for a clean nightside crossing of the L^*_{max} boundary on 11 March 2008. The X-axis shows the time in UT, and the Y-axis shows the SST energy fluxes (units $ev \cdot cm^{-2} \cdot s^{-1} \cdot sr^{-1} \cdot ev^{-1}$) for different energy channels. The equivalent energies for each channel are listed in the plot legend. TH-D's location is also included for 12:00 UT.

thus the total count rates on the detectors to prevent the instrument from saturating. If the change in geometric factor is applied to the count rates at the same time as the attenuator changes states (open or closed), then the flux level should not change since the count rate is equal to the flux times the geometric factor. Both the count rate and geometric factor should change by the factor of 64 simultaneously. However, if the timing is off, then there will be a factor of 64 difference in the flux, and the spikes in the flux data simply turn out to be a result of this. There is apparently a timing issue between the time when the SST attenuator actually opens or closes and the time when the correct geometric factor is applied when calculating the flux data . This results in large-amplitude (factor of ∼64), short-term fluctuations in the flux data as can be seen in Figure 5.4. When the attenuator closes, the instrument count rates go down, but if the open geometric factor is still applied, the fluxes will also reveal a strong decrease, which is totally artificial. The opposite will occur if the attenuator opens and there is a delay in when the correct geometric factor is applied to the data. The attenuator opens and closes based on its orbit position: it is closed in the inner magnetosphere and mostly open in the outer. However, the count rates on the detectors can trigger an electronic override and switch the current attenuator state.

Not all of the effects observed in the data are problems with the instrument, however. This THEMIS dataset has revealed many multipoint observations of substorm injections, a couple of which reveal sawtooth injection events. Figure 5.5 is an example of one of these sawtooth observations, and in Chapter 8, I discuss my future plans for using THEMIS data like this for studying substorms and their effects on the outer radiation belt electrons.

There are also many examples of very distinct boundary crossings, where the flux levels change drastically over a matter of minutes, and we interpret these as the result of the spacecraft having crossed the L^*_{max} boundary. Some of these result from plasma sheet thinning, as shown in Figure 5.6, while others are just clean crossings. Plasma sheet thinning events occur regularly in the dataset. These are identified by sudden and drastic flux dropouts as the fields in the tail become stretched and pinched, transporting the spacecraft into the lobes. Fluxes in the lobes are very low, as can be seen between around 11:20 and 11:45 UT in Figure 5.6. After the thinning

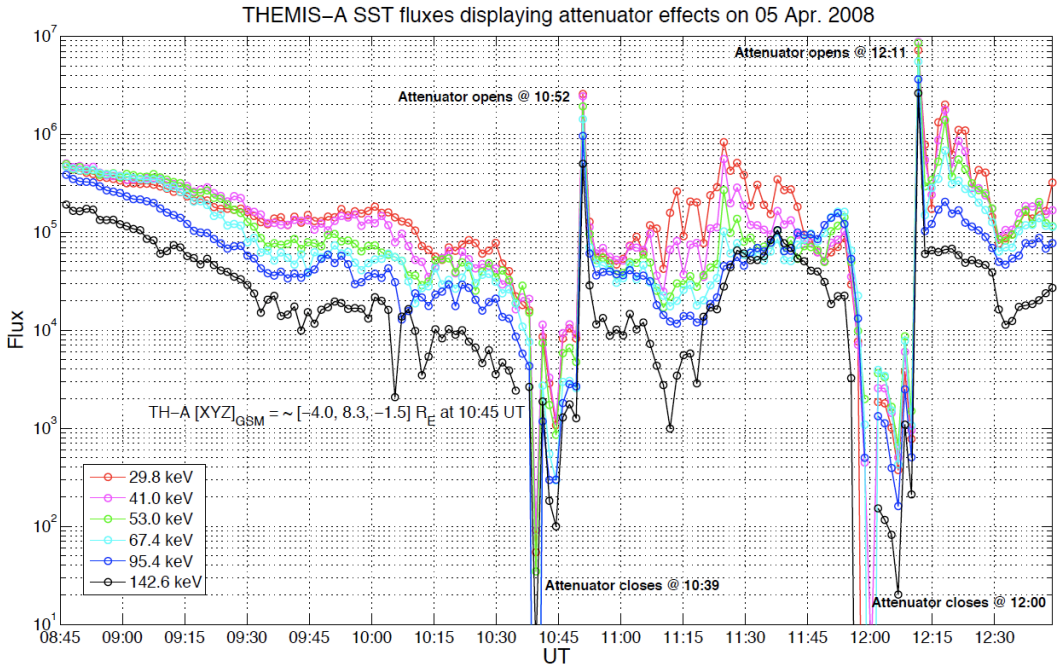

Figure 5.4: THEMIS-SST data showing examples of attenuator effects in the data. The SST design employs a mechanical attenuator to change the geometric factor of the instrument given different environmental fluxes. The attenuator is opened or closed based on large changes in the flux. However, there is a timing issue in when that change in geometric factor is applied for the flux calculation, which results in these seemingly anomalous spikes. Here, the attenuator opening and closing times are indicated next to their corresponding anomaly.

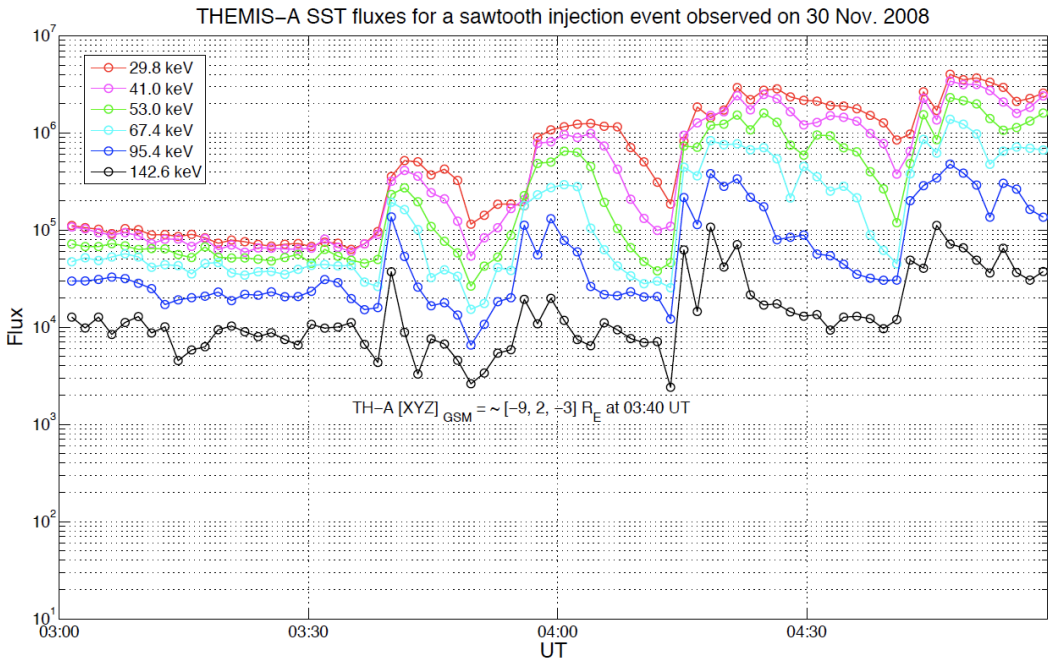

Figure 5.5: THEMIS-A SST fluxes for a sawtooth injection event on 30 November 2008. The X-axis shows the time in UT, and the Y-axis shows the SST energy fluxes (units $ev \cdot cm^{-2} \cdot s^{-1} \cdot sr^{-1} \cdot ev^{-1}$) for different energy channels. The equivalent energies for each channel are listed in the plot legend. TH-A's location is also included for 03:40 UT.

and stretching period, substorms occur, which dipolarize the field and inject particles from the plasmasheet into the trapping region. The dipolarization associated with these substorms also result in the THEMIS spacecraft coming back into the trapped particle region and thus crossing the L^*_{max} boundary, which is reflected in Figure 5.6 as the sudden enhancement of fluxes to levels consistent with those in the trapped region.

Clean L^*_{max} crossings occur on both the nightside (e.g. Fig. 5.3) and the dayside, as can be seen in Figure 5.7. Clean crossings on the dayside most often occur within a few minutes of magnetopause crossings. This is partially because the low-resolution, full-mode SST data is required so that the sunlight contamination can be removed from the data. If higher resolution data were available, it would be interesting to look for and quantify a quasi-trapped population of electrons along the dawnside on open drift shells that intersect the magnetopause near noon. This is not possible with the dataset as is, but in the next section, I discuss how the clean crossings on the nightside can be used to develop a model to approximate L^*_{max} given only solar wind dynamic pressure.

5.3 An Analytic Model to Approximate L^*_{max}

Using 263 identified L^*_{max} crossings from the nightside of the magnetosphere, we developed an analytic model to determine L_{max}, which is the McIlwaine-L corresponding to the observed L^*_{max} locations. We decided to train the model simply for McIlwaine-L since it is both versatile as a geomagnetic coordinate and easy to calculate compared to L^*. Additionally, the error in the model is often greater than the difference between McIlwaine-L and L^*, which is discussed later in this chapter. To determine which parameters to make the model a function of, I examined the correlations between the McIlwaine-L parameters corresponding to the Ts01S L^*_{max}'s from the observed crossing events and various solar wind parameters and geomagnetic indices. These correlations are listed in Table 5.1.

The method I use to develop this model follows closely that of *Shue et al.* [1997]. To determine which parameters to use in the model, the correlations between the L_{max} observations and the

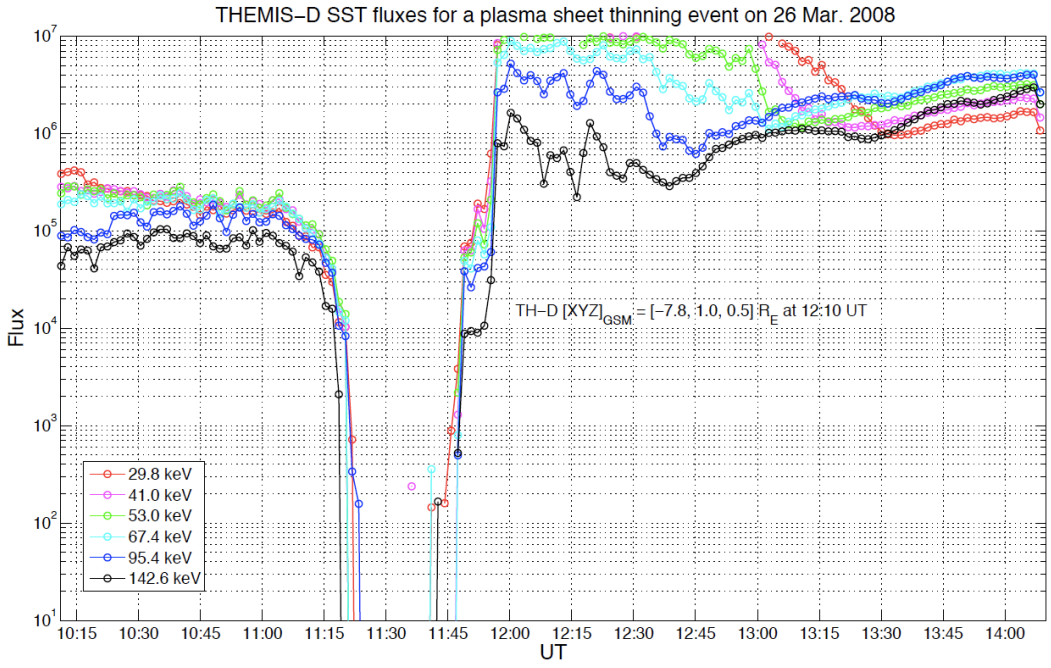

Figure 5.6: THEMIS-D SST fluxes during a plasma sheet thinning event. The X-axis shows the time in UT, and the Y-axis shows the SST energy fluxes (units $ev \cdot cm^{-2} \cdot s^{-1} \cdot sr^{-1} \cdot ev^{-1}$) for different energy channels. The equivalent energies for each channel are listed in the plot legend. TH-D's location is also included for 12:10 UT.

Table 5.1: Correlations between the identified Lmax's and various solar wind and geomagnetic parameters

Parameter	CorrCoef	Parameter	CorrCoef
$P_{dyn-1hr-avg}$	-0.21	Kp	-0.10
$P_{dyn-1.5hr-avg}$	-0.24	Dst	0.02
$Bz_{1hr-avg}$	-0.04	$AE_{1hr-avg}$	-0.11
$Bs_{1hr-avg}$	-0.06	$AL_{1hr-avg}$	0.13
$V_{1hr-avg}$	0.08	$AU_{1hr-avg}$	0.05
$(V \cdot Bs)_{1hr-avg}$	0.07	$\log(AL_{1hr-avg})$	-0.10
$\log(P_{dyn-1.5hr-avg})$	-0.28	$(AL \cdot P_{dyn})_{1hr-avg}$	0.18

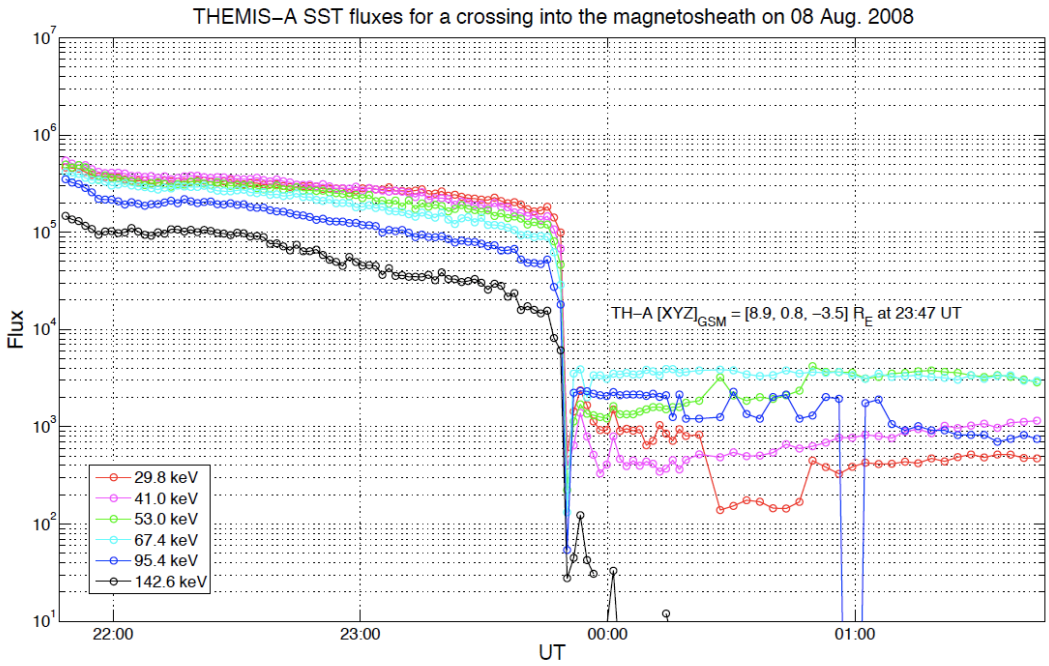

Figure 5.7: THEMIS-A SST fluxes for a clean dayside crossing of the L^*_{max} boundary close to the magnetopause on 08 August 2008. The X-axis shows the time in UT, and the Y-axis shows the SST energy fluxes (units $ev \cdot cm^{-2} \cdot s^{-1} \cdot sr^{-1} \cdot ev^{-1}$) for different energy channels. The equivalent energies for each channel are listed in the plot legend. TH-A's location is also included for 23:47 UT.

various solar wind and geomagnetic parameters are examined. Using all 263 crossings identified from the THEMIS-A, -D, and -E observations, the best correlations with L_{max} are the solar wind number density and dynamic pressure (both show same correlation coefficient, which is why n_{sw} is not included in Table 5.1) and the AL index. However, it is interesting to note that these correlations are significantly improved when the dataset is restricted to the 68 observations in which the THEMIS spacecraft are at $-2\,R_E \leq Y_{GSM} \leq 2\,R_E$. In this near-midnight sector, the best correlations are with Kp and dynamic pressure, at R = -0.42 and -0.39 respectively. Here, I only use P_{dyn} as input for the model, but in Appendix B, I discuss some additional work on a similar model using Kp as an additional input.

To determine the analytic form of the model, I plotted the L_{max} observations versus the corresponding 1.5 hour averaged solar wind dynamic pressure. Figure 5.8 shows the log-log fit between the two parameters. This linear fit and strongest correlation between L_{max} and $\log(P_{dyn-1hr-avg})$ implied that a power law form should be employed. This was confirmed by testing some of the different functional forms with both P_{dyn} and several of the other parameters. The power law form I use is:

$$L_{max} = AP_{dyn-avg}^{-\gamma} \tag{5.1}$$

The constants A and γ from Equation 5.1 are determined based on the least-squares linear fit shown in Figure 5.8: A is $e^{2.33\pm0.01}$ and γ is 0.05 ± 0.01. These values for the equation variables are determined by minimizing the standard deviation of the difference between the observed L_{max}'s and those from the model. In the next section, we discuss the results of this model compared to the observed crossings and other models that can be used to approximate the last closed drift shell.

5.4 Results and Comparison

To rate the performance of the model, I calculate the standard deviation (σ) of the difference between the model-determined L_{max}'s and those determined from the observed crossing locations. The results of this new L_{max} model are summarized in Figure 5.9. The Ts01S-determined L_{max}'s

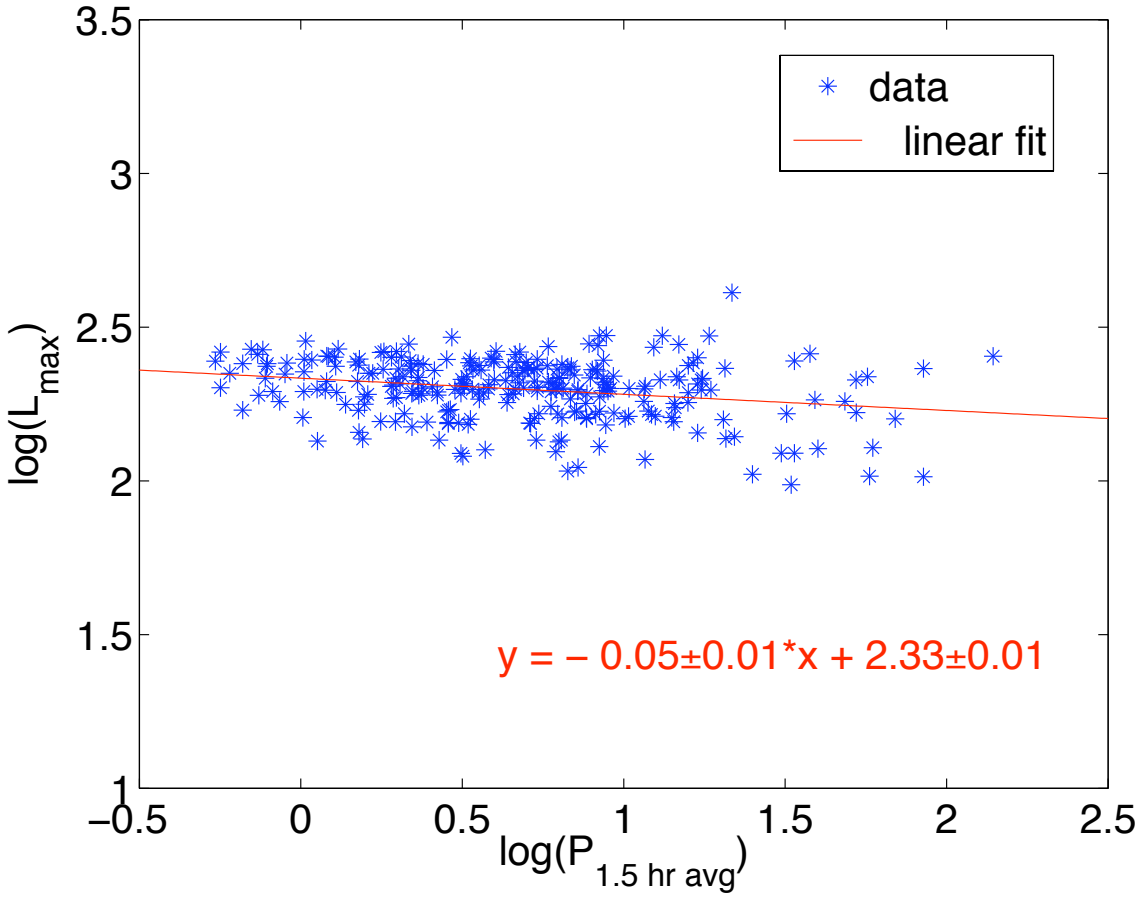

Figure 5.8: L_{max} correlation with $P_{dyn-avg}$

are also shown here for comparison. In Figure 5.9, the L_{max}'s corresponding to the THEMIS observed locations are marked with black stars. The new model L_{max}'s based on dynamic pressure are marked with blue circles, and the L_{max}'s corresponding to the locations where the Ts01S model predicts are shown with red triangles. The differences between the two models and the observations are shown with the colored curves around the 0 R_E dashed reference line.

As can be seen in Figure 5.9, the new, analytic model outperforms the Ts01S for determining the observed THEMIS L_{max}'s. This can be seen by the σ_{diff}'s for the results shown on the plot, and it is further confirmed by checking the prediction efficiency for the models. For a definition and summary of prediction efficiency (PE), see Equation 7.2 in Chapter 6. The PE for the new model is 0.05, while it is -0.21 for the Ts01S model. Since PE is positive for the new model, it outperforms the "average" model, in which the predicted value is simply the average of the observed data set used for training.

Another model I tested against is the *Shue et al.* [1997] model. The *Shue et al.* [1997] model is an analytic fit to observed magnetopause crossings, so at first it may seem inappropriate for a last closed drift shell model. However, based on the dayside crossings observed in this study, L^*_{max} is bunched up close to the magnetopause on the dayside. Thus, the subsolar magnetopause location might provide a good estimate of the last closed drift shell since it is here that magnetopause shadowing first occurs as one goes to higher and higher L. When this theory is tested, however, the *Shue et al.* [1997] model proves not to be a good estimate of the boundary. Using the *Shue et al.* [1997] subsolar locations for each observed crossing time, I calculated the McIlwaine L's for the locations. When these are compared to the L_{max}'s from the observed crossings, the fit is very poor. The σ_{diff} between the Shue approximations and the observed crossings is 4.85 R_E. This is discussed further in the Discussion section below.

To test the model outside of the training data set, I retrained it with 3/4 of the data to find new A and γ values and tested the resulting model on the remaining 1/4 of the data. For this sampling, the model performs comparably to the Ts01S results (both with $\sigma_{diff} = 0.80$ R_E) and much better than with mapping with the *Shue et al.* [1997] model (with $\sigma_{diff} = 2.57$ R_E). The

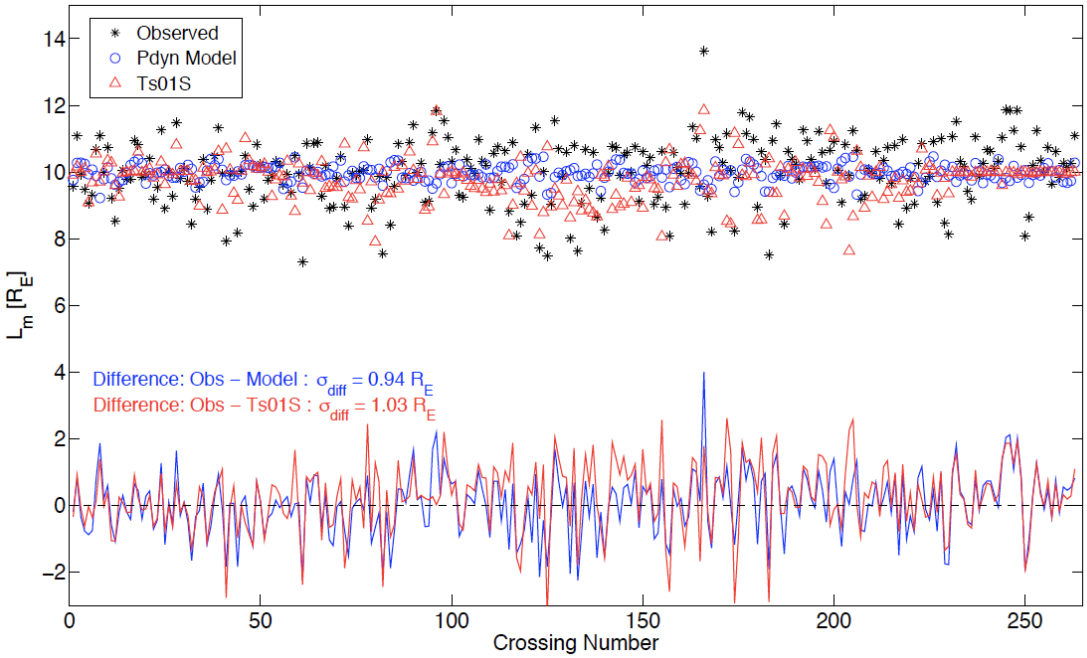

Figure 5.9: Top-most symbols: The results of the simple analytic L_{max} model compared to the actual crossings observed by THEMIS and the L_{max}'s predicted by the Ts01S model given the THEMIS orbits and conditions. Bottom-most curves around dashed-zero line: difference between the observed and modeled L_{max} locations, color-coded the same as above (new model in blue, Ts01S in red). The standard deviation of these curves is also provided. Note, the standard deviation (σ) in just the observed L_{max}'s is 0.96 R_E.

standard deviation in the quarter of the observed data outside the training set is 0.95 R_E.

5.5 Discussion

5.5.1 L^*_{max} Crossing Results

Overall, this study provides a glimpse into a region that is considered to be very important to the outer belt electron population. Electron sources from this region are often used in models of radiation belt electron dynamics, though actual data from this region has not been studied extensively in the past. Here, I have examined THEMIS-SST data from close to 2000 L^*_{max} crossings and have found some interesting results.

On the dayside, the L^*_{max} boundary seems bunched up near the magnetopause, as is evident in Figure 5.7. There is likely a finer structure to the boundary that includes a "quasi-trapped" region along the morning sector in which electrons can drift into the morning sector from the tail before being lost to magnetopause shadowing. Studying this "quasi-trapped" region and its variability would be interesting considering the implications to outward radial diffusion of higher-energy (i.e. greater than several 100's keV) electrons and outer belt loss to the magnetopause. However, I was unable to conduct such studies using the THEMIS-SST dataset since only "Full" resolution data is available (time resolution of ~3 mins) due to a sunlight contamination issue with the instrument.

On the nightside, clear boundary crossings are also evident, which are signatures of the THEMIS spacecraft crossing the L^*_{max} boundary (e.g. Fig. 5.3). However, there are many cases on the nightside where no clear boundary is evident. Figure 5.10 shows an example of this type of observation. These smooth flux transitions between ~7 and 12 R_E, in which no L^*_{max} boundary is visible, are of particular interest as they imply significantly high fluxes of high energy (10's keV ~ 100 keV) electrons in the plasma sheet. This implies a source for these electrons in the plasma sheet, which is consistent with the findings of *Turner et al.* [2010b] presented in the previous chapter. Also note that for the higher energy flux channels (e.g. gray and black curves shown in the top plot of Fig. 5.10), these smooth transitions do not occur, and there are large and seemingly random

dropouts present in the data. This further agrees with the results from *Turner et al.* [2010b], who found that the relativistic electrons in the outer belt most often have a source that is internal to the outer belt. However, these observations are simply implications based on the observed fluxes. The true PSD gradients can be confirmed with a study of phase space densities for fixed first and second adiabatic invariants using this data set.

Figure 5.10 also shows some additional interesting features. At the beginning of the plot, i.e. before 04:00 UT, note that the lowest energy fluxes (i.e. 29.8 keV) are actually at lower levels than the 207.4 keV fluxes. This feature occurs often in the data always inside of GEO, and it is likely the result of insufficient instrument performance in the presence of higher fluxes of relativistic electrons and energetic protons in the ring current. Note too the interesting feature at ~04:50 UT, in which there is an increase in the fluxes of the low-energy electrons but a decrease in the 95.4 and 207.4 keV channels. This is likely a substorm injection, and the disparity between the response to the fluxes from different energy channels may further imply insufficient source at higher L-shells for the higher-energy electrons. This is similar and possibly analogous to the flux responses to sudden solar wind dynamic pressure enhancements on the dayside and the corresponding PSD radial distributions discussed in the previous chapter.

This database of crossings can also be useful for looking at other space physics processes such as magnetic reconnection along the magnetopause, Kelvin-Helmholtz instabilities along the flanks, the near-Earth plasma sheet, substorms, and various magnetopause disturbance events (for an example, see Appendix C). However, when using the SST data, it should be noted that there is a timing issue for when the correct geometric factor is applied to the data when the instrument aperture opens or closes, which results in anomalous spikes in the flux data (e.g. Fig. 5.4).

In addition to the interesting observations discussed here and many others identified with this data set, I have also developed an analytic model to determine the McIlwain-L corresponding to the last closed drift shell, which is discussed in the following subsections.

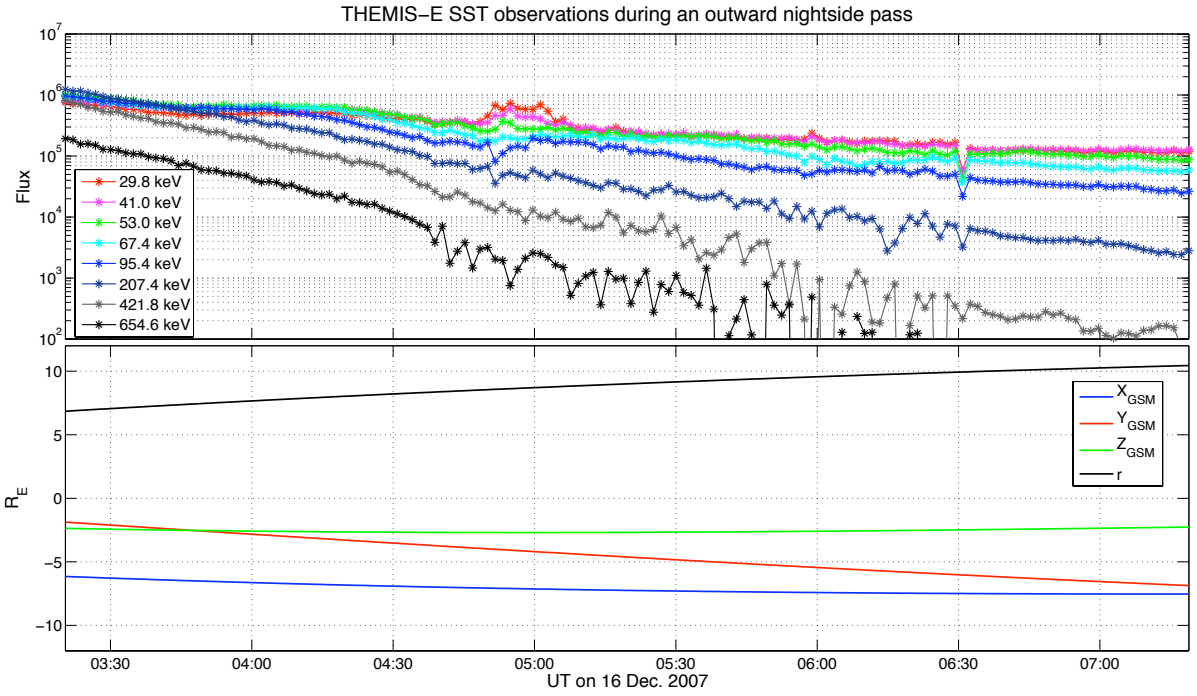

Figure 5.10: THEMIS-E SST fluxes for a nightside crossing in which there is no evidence of the L^*_{max} boundary on 16 December 2007. The X-axis shows the time in UT. The top plot shows the SST energy fluxes (units $ev \cdot cm^{-2} \cdot s^{-1} \cdot sr^{-1} \cdot ev^{-1}$) for different energy channels, and the bottom plot shows the corresponding TH-E locations. These smooth crossings are common on the nightside.

5.5.2 L^*_{max} Model and Limitations

The analytic model described in this chapter provides users with a quick and easy way to *approximate* the L^*_{max} location. This model can be useful to the any radiation belt researchers who require knowledge of the outer boundary location, and the observations from this study can be used to define the conditions of the particle population at that boundary. These are both critical to how many outer belt models operate, like radial diffusion models for example.

The model discussed here was trained using observed L^*_{max} boundary crossings by TH-A, -D, and -E, and it uses solar wind dynamic pressure to determine the McIlwaine-L corresponding to these crossing locations. McIlwaine-L was chosen over L^* since this is much less computationally intensive to solve for, and unlike a radial distance, an L-shell can be used for a variety of orbits with different apogees and inclinations. I have shown that the model generally outperforms the Ts01S model. For the test outside of the training period when the two models perform equally well, note that the test pertained to the last quarter of the data points shown in Figure 5.9. The Ts01S variability for this period is very low, reflecting the lack of activity in the solar wind and geomagnetic parameters used to drive the model during the first quarter of 2009. Ts01S predicts near the average L_{max} during this period, which is one of the reasons why it performs around as well as the simple model during the test. It does not perform nearly as well when the variability in its input parameters is higher. Both the new analytic model and the Ts01S model outperform an approximate L_{max} model using the *Shue et al.* [1997] subsolar magnetopause.

The new model is simply a function of the 1.5 hour averaged solar wind dynamic pressure:

$$L_{max} = e^{2.3341} P_{dyn-avg}^{-0.0525} \tag{5.2}$$

This model performs slightly better than using the average L_{max}. This is reflected by the low PE (0.05) achieved by the model. So, the simplest model one could use would just be the average L_{max} of $\sim$10 R_E. However, the variability provided by the P_{dyn} dependence does slightly improve upon the "average" model. As discussed in Appendix B, there are other variations of the model that perform significantly better than this one under particular conditions. One of the reasons for

the limitations on this unconditional model using only P_{dyn} may be that the training set includes plasma sheet thinning crossings. These crossings are related to substorms and are not necessarily well correlated with P_{dyn}. Also, the P_{dyn} model does not capture the large variation seen in the observations. This is likely a result of the generally weak correlation between P_{dyn} and L_{max}.

The weak correlations between L_{max} and the various solar wind and geomagnetic parameters are interesting to note. They are likely a reflection of the complexity and high-variability of the magnetic field at such high L-shells. Along the dayside, L_{max} is bunched up along the magnetopause, yet surprisingly, based on the comparison with the *Shue et al.* [1997] model, L_{max} obviously doesn't correspond well with the L-shell corresponding to the subsolar magnetopause. On the nightside, the variability in L_{max} is higher than the simple P_{dyn} model can account for. Considering this complexity, a neural network approach such as the LANL* toolset described in *Koller et al.* [2009] will likely be the best option once one is trained to specifically solve for L_{max}, or even directly for L^*_{max}, based on observed boundary crossings. Such a neural network could be trained using all the solar wind and geomagnetic parameters available to significantly improve the results.

5.6 Conclusion

I have constructed a data set of energetic electron observations from ~2000 L^*_{max} boundary crossings made by three of the THEMIS spacecraft between December 2007 and March 2009. Here, I have noted and discussed several interesting events, including anomalous spikes that prove to be a timing error resulting from the data processing. I have also introduced a new analytic model to solve for the approximate L^*_{max} L-shell using only solar wind dynamic pressure. This model provides a very simple and computationally inexpensive tool to identify this boundary, and it outperforms the *Tsyganenko et al.* [2003] model. Other variations of the model are discussed in Appendix C, and these analytic forms are apparently the best models available for approximating L^*_{max} until a neural network can be trained to incorporate additional parameters and account for the high variability in the L^*_{max} observations.

From the observations, I have also provided additional evidence in support of the results

from the previous chapter implying that low-energy (10's $\sim$ 100 keV), seed electrons have a source in Earth's magnetotail, while the relativistic population most often has a source in the inner magnetosphere. However, to confirm this, the SST flux data should be converted to PSD for fixed first and second adiabatic invariants. This study also reveals the potential for using THEMIS for radiation belt research, and in Chapter 8, I show how THEMIS-SST data can be used for studying substorm injections and quantifying their effects on outer belt electrons.

This chapter provides examples of how observed data can be used to both improve our understanding of the outer radiation belt electrons as well as to improve models of the system. In the next two chapters, I demonstrate how radiation belt data are used to develop forecast models for the system, which have practical applications by way of risk mitigation for spaceflight operations.

Chapter 6

Forecasting relativistic electrons at geosynchronous orbit without using solar wind data

6.1 Introduction

Now that I have discussed how relativistic electron data are acquired and analyzed for scientific understanding of the outer radiation belt, I will provide some examples of how such data can be used for practical applications, namely in the development of outer belt forecast models to mitigate the risk of these electrons to manned and unmanned spaceflight operations. This chapter consists of my first work on outer belt forecasting through the development of a model for electron fluxes at GEO that is independent of any solar wind quantities as input. This model is advantageous in that it is not single-point dependent on a spacecraft in the upstream or near-Earth solar wind. It relies only on flux measurements of both low- and high-energy electrons at GEO. The following is the Space Weather Journal publication that resulted from this study.

6.2 *Quantitative forecast of relativistic electron flux at geosynchronous orbit based on low-energy electron flux* by D. L. Turner and X. Li, published in Space Weather Journal in 2008

6.2.1 Abstract

A strong correlation between the behavior of low-energy (tens to hundreds of keV) and high-energy (>1 MeV) electron fluxes measured at geosynchronous orbit has been discussed, and this correlation is further enhanced when a time offset is taken into account. A model has been

developed incorporating this delay time between similar features in low- and high-energy electron fluxes to forecast the logarithm of daily averaged, 1.1-1.5 MeV electron flux at geosynchronous orbit several days in advance. The model uses only the current and previous days' daily averaged fluxes of low- and high-energy electrons as input. Parameters in the model are set by optimizing prediction efficiency (PE) for the years 1995-1996, and the optimized PE for these 2 years is 0.81. The model is run for more than one full solar cycle (1995-2006), and it consistently performs significantly better than a simple persistence model, where tomorrow's forecasted flux is simply today's value. Model results are also compared with an inward radial diffusion forecast model, in which the diffusion coefficient is a function of solar wind parameters. When the two models are combined, the resulting model performs better overall than each does individually.

6.2.2 Introduction

6.2.2.1 Background

Earths radiation belts make up a significant part of the environment for many high-use orbits, such as those for low-Earth orbiting, GPS, geotransfer, and geosynchronous spacecraft. The relativistic electrons in the outer belt can be especially hazardous to spacecraft systems [e.g. *Baker et al.*, 1998a; *Baker*, 2001], and thus, accurate forecasting of relativistic electron flux is important for mitigating the associated risk to spacecraft operations. This paper discusses a new, empirical model that forecasts the logarithm of daily averaged, 1.1-1.5 MeV electron flux at geosynchronous orbit (GEO).

Having a good understanding of a system's governing physical processes enables one to more accurately forecast the system. There are currently many theories concerning the mechanisms that accelerate electrons in the outer radiation belt to relativistic energies, but so far, none has proven to be the dominant factor for all cases when compared with observational data. Early research found that the outer belt flux is driven by changes in the solar wind [*Williams*, 1966; *Paulikas and Blake*, 1979]. *Williams* [1966] showed that there was a 27-d periodicity (the same

as the average solar spin period) in energetic electron intensities in the outer belt, and *Paulikas and Blake* [1979] found that MeV electron flux at GEO is enhanced 1-2 d after the passage of high-speed solar wind streams. However, changes in the solar wind alone do not account for the high variability of electron flux in the outer belt; relativistic electron flux can vary by up to 2 orders of magnitude over a timescale of hours to days. *Reeves et al.* [2003, p. 36-1] describe variability in electron flux resulting from geomagnetic storms as a "delicate and complicated balance between the effects of particle acceleration and loss." This "balance" of multiple magnetospheric source and loss processes, which often operate simultaneously, has been discussed in detail in reviews by *Li and Temerin* [2001], *Friedel et al.* [2002], and *Millan and Thorne* [2007].

6.2.2.2 Current Understanding

Most source terms can be categorized into one of two types of models: (1) energization by radial transport and (2) local acceleration. Early theoretical work on radial transport, particularly inward radial diffusion, was conducted by *Fälthammar* [1965] and *Schulz and Lanzerotti* [1974]. This process involves a source population of particles in the outer magnetosphere, with a greater phase space density than in the inner magnetosphere, breaking the third adiabatic invariant and diffusing inward. By conserving the first adiabatic invariant, μ, particles are energized to make up for the stronger magnetic fields encountered at lower L shells. Recent studies show that radial diffusion can be enhanced by ULF waves in the magnetospheric electric and magnetic fields [*Rostoker et al.*, 1998; *Hudson et al.*, 2000; *O'Brien et al.*, 2001, 2003; *Mann et al.*, 2004; *Sarris et al.*, 2006]. Another form of radial transport is that induced by impacts of interplanetary shocks with the magnetosphere, where the strong inductive electric fields transport a source population of particles, which also become energized in the process by conserving m, to lower L shells [*Li et al.*, 1993, 2003; *Gannon et al.*, 2005].

Electrons can also be accelerated to relativistic energies locally via wave-particle interactions, particularly whistler mode chorus [*Temerin et al.*, 1994; *Horne and Thorne*, 1998; *Summers et al.*, 1998; *Roth et al.*, 1999a; *Meredith et al.*, 2002]. *Horne and Thorne* [1998] showed that whistler

mode chorus could interact with electrons from a wide range of energy levels via Doppler-shifted cyclotron resonance and that it is theoretically possible to accelerate these seed populations up to relativistic (MeV) energies. *Bortnik and Thorne* [2007] provide a brief review of chorus' role in Earths outer radiation belt dynamics and also define an "anchor point" at a few hundred keV, above which chorus tends to accelerate electrons and below which it tends to cause electrons to precipitate and be lost to the atmosphere. This is in accordance with *Summers et al.* [1998] and *Meredith et al.* [2002], who find that a seed population of electrons with energies of a few hundred keV can be significantly energized by interactions with chorus waves.

A combination of both local acceleration and radial transport has also been used to explain the state of radiation belt energization, as mentioned by *O'Brien et al.* [2003] and *Onsager et al.* [2007]. *Brautigam and Albert* [2000] find that for the 9 October 1990 storm, radial diffusion is not enough to fully explain the observed increase in >1 MeV electron flux and suggest that wave-particle interaction with enhanced chorus waves may provide an explanation for the inconsistency. *Horne et al.* [2005a] conclude that whistler mode chorus is a viable explanation for electron flux increases around L = 4.5 during geomagnetically active periods, while *Loto'aniu et al.* [2006] and *Barker et al.* [2005] show that inward radial diffusion can explain most of the observations during magnetic storms. *Selesnick and Blake* [2000] find that a local source of relativistic electrons may exist around L = 4 on the basis of phase space density calculations. *Green and Kivelson* [2004] go on to explain how a peak in phase space density at L $\sim$ 5 could diffuse outward to account for the correspondence between flux enhancements at GEO and increased ULF wave power. Most recently, using a multisatellite study, *Chen et al.* [2007b] find that, on average, electron phase space density peaks inside of GEO during storm times and non-storm times alike, and they conclude that wave-particle interactions are the dominant source of relativistic electrons in the outer radiation belt. Therefore some local energization near the heart of the outer radiation belt may lead to a local peak in phase space density and radial diffusion. Those particles that diffuse inward gain energy but most likely interact with plasmaspheric hiss and are scattered into the loss cone [*Lyons et al.*, 1972; *Abel and Thorne*, 1998], while those particles that diffuse outward lose some energy

but may retain enough to be measured as relativistic by satellites at GEO.

Studies of electrons at various energies can provide some insight into acceleration and loss processes, which is crucial for better radiation belt models and forecasting abilities. *Li et al.* [2005] find that there is a good correlation between simultaneous electron flux measurements at various energy levels and that this correlation is enhanced when a time shift proportional to their energy difference is taken into account. They conclude that the time difference can be explained by either local energization, since it takes longer to energize electrons to higher levels, or radial diffusion, since lower-energy electrons diffuse faster than higher-energy electrons because there is more low-frequency ULF wave power available to drive lower-energy electrons through drift resonance. *Li et al.* [2005] also suggest that this time offset may be used as the basis for a forecast model.

6.2.2.3 Overview

This paper's discussion of the current research begins with the results of a study similar to that of *Li et al.* [2005], investigating the offset correlation between low- and high-energy electron fluxes at GEO. These results are compared to the *Li et al.* [2001b] predictive model, which solves the diffusion equation, calculating the diffusion coefficient as a function of solar wind parameters, to predict the logarithm of daily averaged relativistic electron flux at GEO. Recent improvements to the *Li et al.* [2001b] model are also discussed briefly in section 2. A discussion of a newly developed model, which incorporates the delay time between low- and high-energy electron fluxes to forecast relativistic electron flux at GEO, follows in section 3. This new forecast model is then compared in section 4 to the *Li* [2004] forecast model, which is currently running online in real time and uses solar wind data to solve the diffusion coefficient, like the *Li et al.* [2001b] model, to forecast daily averaged relativistic electron flux both 24 and 48 h in advance. A final model, which combines the new low- to high-energy model and the *Li* [2004] model, is then discussed and compared to the others individually. Section 5 provides a detailed discussion of the results and their implications, conclusions, and a brief note on proposed future work involving these models.

6.2.3 Data Handling and Fitting

This study was conducted using Los Alamos National Laboratory (LANL) electron flux measurements from the synchronous orbit particle analyzer (SOPA) instruments on the LANL satellites at GEO. Hourly flux data from all available LANL satellites during the years 1995-2006 are daily averaged to remove the variations observed at different local times in GEO. These variations arise from the spacecraft passing through different electron drift shells because of the asymmetry of Earth's magnetic field. At any given time, there were four to six point measurements from the LANL satellites, covering a wide range of local time. The local time flux dependence is discussed in detail by *Burin des Roziers and Li* [2006]. These daily averaged fluxes are used throughout the study as input for the models and also for comparison of model results to measured data. The LANL SOPA instrument measures differential electron flux on several channels covering different energy ranges. Figure 6.1 shows several of these channels for the first 2 months of 2005; the vertical dashed lines help display the time difference between similar features in the flux from various energy ranges. Notice how the 50-75 keV data often change more than a day before a similar change is seen in the 1.1-1.5 MeV data. *Li et al.* [2005] discuss this phenomenon in detail, and it is the basis for the forecast model discussed in this paper.

As discussed by *Li et al.* [2005], the correlation between low- and high-energy electron fluxes is enhanced when a delay time is taken into account. Figure 6.2 shows correlation coefficients for various offset times in hours for the 50-75 keV and 1.1-1.5 MeV energy channels. Note that the optimum correlation coefficient occurs when the 1.1-1.5 MeV data set is shifted back by 37 h. This agrees with both what *Li et al.* [2005] found and what can be seen in Figure 6.1. Table 6.1 shows the linear correlation coefficients for all lower-energy channels compared to the 1.1-1.5 MeV energy channel for the years 1995-1996. Optimum offset times (in hours) are given in the second column. These offset times correspond to the maximum in the respective correlation versus offset time curves, of which Figure 6.2 is an example, and they represent the amount of time the 1.1-1.5 MeV energy channel should be shifted to produce the maximum correlation coefficient when

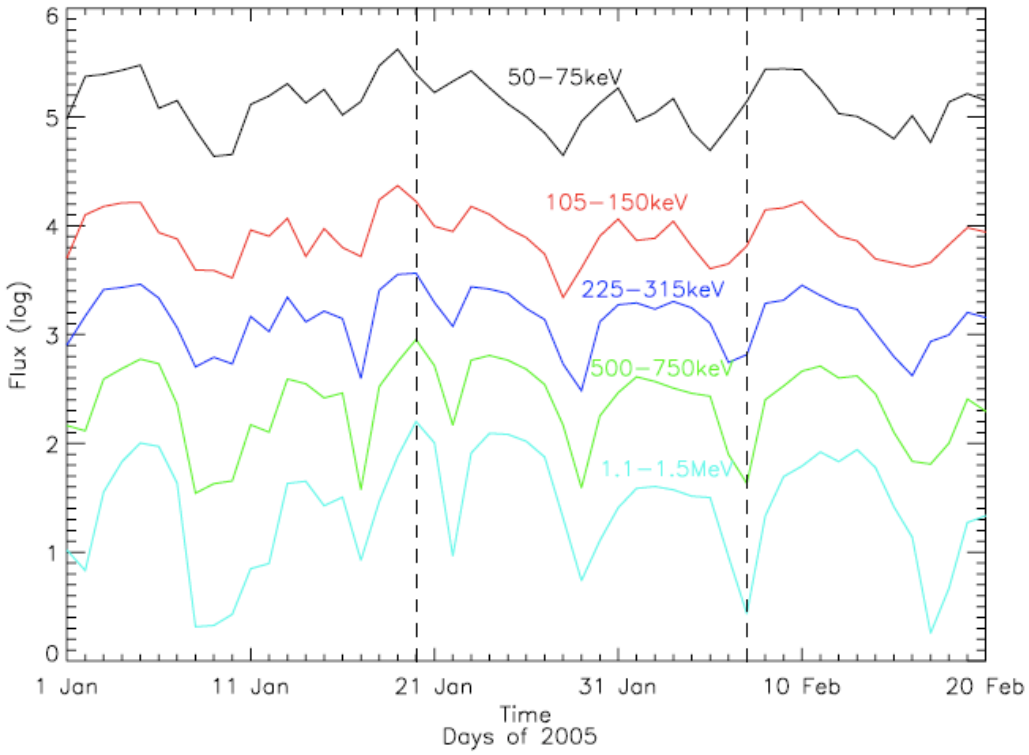

Figure 6.1: LANL logarithmic electron fluxes for various energy channels. Using dashed lines for constant time reference, it is noticeable how the lower-energy channels change before similar changes are seen in the higher-energy channels.

Table 6.1: Linear Correlations Between Low-Energy Channels and 1.1 - 1.5 MeV Channel for the Years 1995-1996

Low-Energy Chan. (keV)	Optimum Offset (h)	Linear Correlation w/o Offset	Linear Correlation w/ Offset
50-75	-37	0.64	0.80
75-105	-35	0.69	0.82
105-150	-34	0.70	0.81
150-225	-17	0.73	0.80
225-315	-14	0.77	0.82
315-500	-11	0.82	0.85
500-750	-7	0.90	0.92
750-1100	-2	0.97	0.97

compared to the lower-energy channels.

The *Li et al.* [2001b] predictive model uses solar wind parameters to compute the diffusion coefficient and to numerically solve the one-dimensional radial diffusion equation. Model parameters are optimized for the years 1995-1996. Recently, a magnetopause shadowing loss term was added. This new term results in the optimized prediction efficiency for 1995-1996 being improved from 0.81 to 0.82, which is a greater than 5% reduction in unpredicted variance. Linear correlation for both old and new forms of the model is 0.90. Prediction efficiency (PE) is defined as

$$PE = 1 - \frac{\sum_{i=1}^{N} (m_i - p_i)^2}{\sum_{i=1}^{N} (m_i - \langle m_i \rangle)^2} \tag{6.1}$$

where m_i is the measured quantity, p_i is the predicted quantity, and $\langle m_i \rangle$ is the mean of all m_i. A PE of 0 means that, on average, the predicted values are equal to the average of the measured data set, and a PE of 1 means that the predicted values are all the same as the corresponding measured ones.

On the basis of linear correlation, the potential for a model incorporating the time delay between low- and high-energy electron fluxes is good. From Table 6.1, one can see that with the 50-75 keV channel alone, a linear coefficient of 0.80 can be achieved when compared to the 1.1-1.5 MeV channel. This is not as good as the correlation of 0.90 achieved by the *Li et al.* [2001b] model,

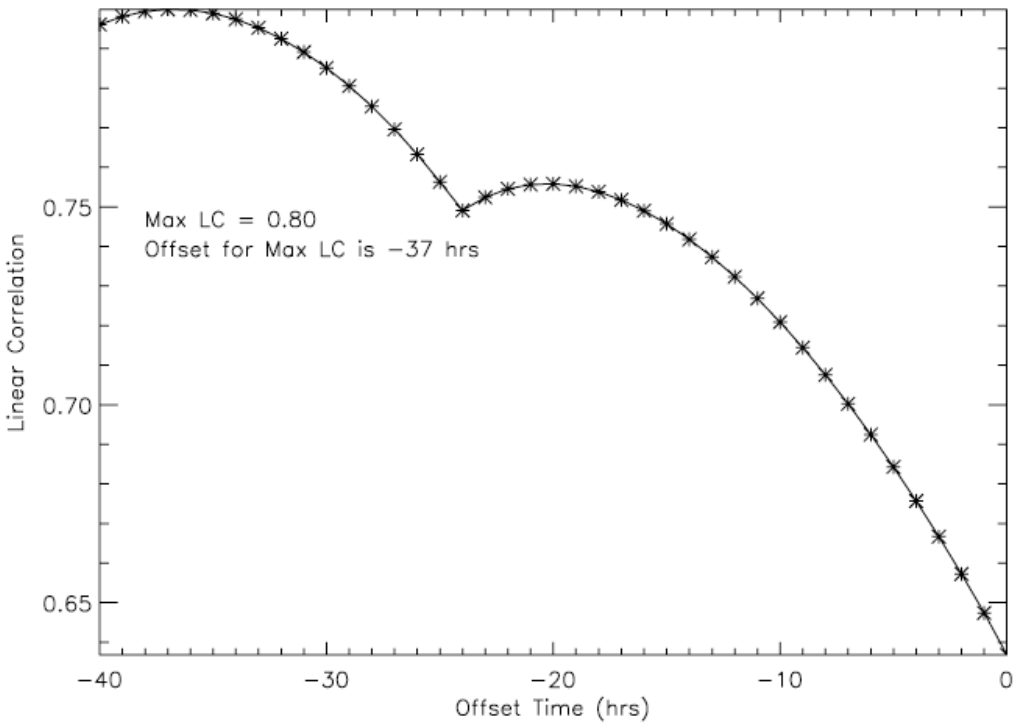

Figure 6.2: Linear correlation between 50-75 keV and 1.1-1.5 MeV energy channels for the years 1995-1996 for different offset times. Offset time is number of hours the 1.1-1.5 MeV data are shifted (back in time). Note that peak correlation, 0.80, occurs for a 37 h difference between the two channels. The kink at 24 h is an artifact of the daily averaged data.

but it demonstrates the potential effectiveness of using current lower-energy channel flux to predict flux at higher energies for some future time.

6.2.4 Forecast Model Description

The new forecast model, which incorporates the time delay between low- and high-energy electron fluxes, is referred to throughout the remainder of this paper as either the low- to high-energy model or the low-e model and takes on the form of a simple source and loss differential equation (equation 6.2), which physically implies that the flux variation depends on the balance of source and loss. This equation is numerically discretized (equation 6.3) in order to solve for "tomorrows" flux:

$$\frac{dj}{dt} = S + L \tag{6.2}$$

$$j\left(t + \Delta t\right)_{high} = j\left(t\right)_{high} + \Delta t\left(S + L\right) \tag{6.3}$$

where $j(t + \Delta t)_{high}$ is tomorrow's average, high-energy flux; $j(t)_{high}$ is "today's" average, high-energy flux; Δt is 1 d for a 24-h forecast; and S and L are the source and loss terms, respectively.

S and L are determined by optimizing PE for the model for the years 1995-1996. The source and loss terms are initially a function of the data from today's 50-75 keV, 75-105 keV, 105-150 keV, and 1.1-1.5 MeV energy channels as well as "yesterday's" 1.1– 1.5 MeV energy channel, and weighting parameters for each are then adjusted on the basis of optimization. In this manner, if the inclusion of an energy channel's data does not lead to a better optimization result, its weighting factor is set to zero so that it is no longer part of the equation. The three lowest-energy channels are used to optimize the source term since they all change more than 24 h before the 1.1-1.5 MeV channel, which can be seen in Table 6.1. Low-energy fluxes are mapped to 1.1-1.5 MeV flux levels (see Figure 6.1 for general flux ranges for different energy channels) by using a power function, the parameters for which are also optimized for the years 1995-1996. The power function takes the form seen in the first term on the right side of the final form of the source term equation (equation 6.4) where some constant ($C2$) is raised to the power of the low-energy flux ($j(t - t_o)_{low}$), which is

raised to some other constant (b):

$$S = C_1 C_2^{\left(\frac{j(t-t_o)_{low}}{j_o}\right)^b} + C_3 j\,(t-\Delta t)_{high} \tag{6.4}$$

where $j(t-t_o)_{low}$ is today's low-energy flux; j_o is units of flux to non-dimensionalize the exponent; $j(t-\Delta t)_{high}$ is yesterday's high-energy flux; and C_1, C_2, C_3, t_o, and b are optimized parameters. This form of energy level conversion is similar to that used by *Burin des Roziers and Li* [2006] for their flux conversion to compare LANL differential flux at 1.1-1.5 MeV to GOES integral flux at >2 MeV. The low-energy flux is also interpolated and time shifted forward by to to best represent the time delay observed in the data. Also, adding yesterday's high-energy flux slightly improves the results. As mentioned previously, the pre-optimized form of the source equation incorporated flux from the three lowest-energy channels, but after optimizing the parameters, PE is best when S is simply a function of todays lowest-energy flux channel, 50-75 keV, and yesterdays high-energy (1.1-1.5 MeV) flux (equation 6.4). In the final form of the loss equation, L is a function of todays high-energy flux:

$$L = -C_4 j(t)_{high} \tag{6.5}$$

where C4 is another optimized parameter. Equation 6.5 simply implies that the more high-energy flux is present, the more there is to be lost. The optimized model parameters are $C_1 = 7.870 \times 10^-4$, $C_2 = 2.533$, $C_3 = 1.940 \times 10^{-2}$, $C_4 = 0.508$, $t_o = 6$ (hours), and $b = 1.927 \times 10^{-1}$. On the basis of these equations and parameters, tomorrow's 1.1-1.5MeV forecasted flux is composed of todays 1.1– 1.5MeV flux (∼49%), yesterdays 1.1-1.5 MeV flux (∼2%), and today's 50-75 keV electron flux (∼49%).

One can see that this model includes persistence terms, $j(t)$ and $j(t-\Delta t)$, and this can make the results look as though there is sometimes a 1-d offset compared to the measured data. To help correct for the persistence offset, the gradient of today's and yesterday's high-energy logarithmic fluxes is used to either add to or subtract from tomorrow's forecast value. This employs the simple assumption that if the gradient between yesterday and today is positive, the flux is increasing and will continue to do so tomorrow, so a small amount, proportional to the gradient, is added to the

forecast value. Likewise, if the gradient is negative, it is assumed that the flux will continue to decrease into tomorrow, and a small amount is subtracted from the forecast value. The gradient is calculated using the log of flux because the flux can change very drastically from one day to the next, and ultimately, the forecast is for the logarithm of flux. One more parameter, f, is added for this step, and it is also optimized for the years 1995-1996 and is set for the remaining years. The form of this corrective term is seen in equations 6.6 and 6.7:

$$g = \log_{10}\left[j\left(t\right)_{high}\right] - \log_{10}\left[j\left(t-\Delta t\right)_{high}\right] \tag{6.6}$$

$$\log_{10}\left[j\left(t-\Delta t\right)_{high-correct}\right] = \log_{10}\left[j\left(t+\Delta t\right)_{high}\right]\left(1+fg\right) \tag{6.7}$$

where the left side of equation 6.7 is the final value for the forecast of the logarithm of the daily averaged 1.1-1.5 MeV flux; $j(t+\Delta t)_{high}$ is tomorrow's flux calculated from equation 6.3; g is the gradient term; and f is the optimized multiplicative factor, which, after optimization, has a value of $f = 0.0625$. This term slightly improves the PE, $\sim$1% for 1995-1996, by partially correcting for the persistence offset effect.

Model parameters are set on the basis of the 1995-1996 optimization, and the model is then run for the years up to 2006 at 2 year intervals to demonstrate the model's effectiveness at forecasting future results given parameters that are set for some past time. The model is compared to the *Li* [2004] forecast model, which has been modified to run using the LANL 1.1-1.5 MeV data. A third model is created by combining the two. The combination model is discussed in more detail in section 4.

6.2.5 Model Results

Using the parameters set for 1995-1996, the new model is run for 2 year periods from 1997 to 2006. Table 6.2 shows the results of the forecast model compared to a simple persistence model's results, where tomorrow's flux is simply the same as today's flux, as well as to the *Li* [2004] forecast model for both 24 and 48 h forecasts. Notice that both the new model's and the *Li* [2004] model's PEs are better than those of the simple persistence model for each 2 year period as well as for the

Table 6.2: New Model (Low-e) Results Compared to Simple Persistence, Li [2004] Radial Diffusion, and a Combination of Li [2004] and the New Model

	Run Years						
	1995-1996	1997-1998	1999-2000	2001-2002	2003-2004	2005-2006	1995-2006
Persistence 24-h PE	0.69	0.58	0.47	0.46	0.45	0.55	0.62
Low-e 24-h PE	0.81	0.73	0.63	0.54	0.66	0.74	0.73
Rad Diff 24-h PE	0.84	0.72	0.63	0.53	0.64	0.75	0.74
Combo 24-h PE	0.85	0.75	0.66	0.60	0.70	0.78	0.76
Persistence 48-h PE	0.34	0.07	-0.09	-0.12	-0.13	0.04	0.19
Low-e 48-h PE	0.59	0.39	0.24	0.27	0.29	0.36	0.46
Rad Diff 48-h PE	0.67	0.36	0.27	0.12	0.30	0.48	0.46
Combo 48-h PE	0.65	0.42	0.30	0.32	0.35	0.45	0.50

full 12 year run (last column). PE for all models changes with the solar cycle; maximum PE occurs around the declining phase of the solar cycle, when high-speed solar wind streams are dominant (1995-1996 and 2005-2006), while minimum PE occurs around solar maximum (2001-2002). The *Li* [2004] model achieves a higher PE for the solar minimum years, while the new model is better during the solar maximum years. Figure 6.3 shows the results from both models for the years 1995-1996.

The new low- to high-energy model has also proven effective at forecasting multiple days in advance. Another optimization was attempted to find new parameters for 48, 72, and 96 h forecasts, but PE turned out to be best when the 24 h forecast was simply projected forward to be compared with the measured values from each of these times. As expected, the PE gets worse as one forecasts further ahead in time, but the model forecast is consistently better than the simple persistence model using the measured data. Table 6.3 shows the results for the new models multiday forecasts compared to the simple persistence model's multiday forecasts.

A combination model has also been developed, which incorporates the *Li* [2004] forecasted flux into the low- to high-energy model by simply adding it, with its own weighting parameter, to the result from the new model. Using the same optimized forms of S and L seen in equations 6.4 and 6.5, parameters are optimized again for 1995 -1996, and it is interesting to note that, as expected, the persistence term drops out of the low to high model terms (C_4 from equation 6.5

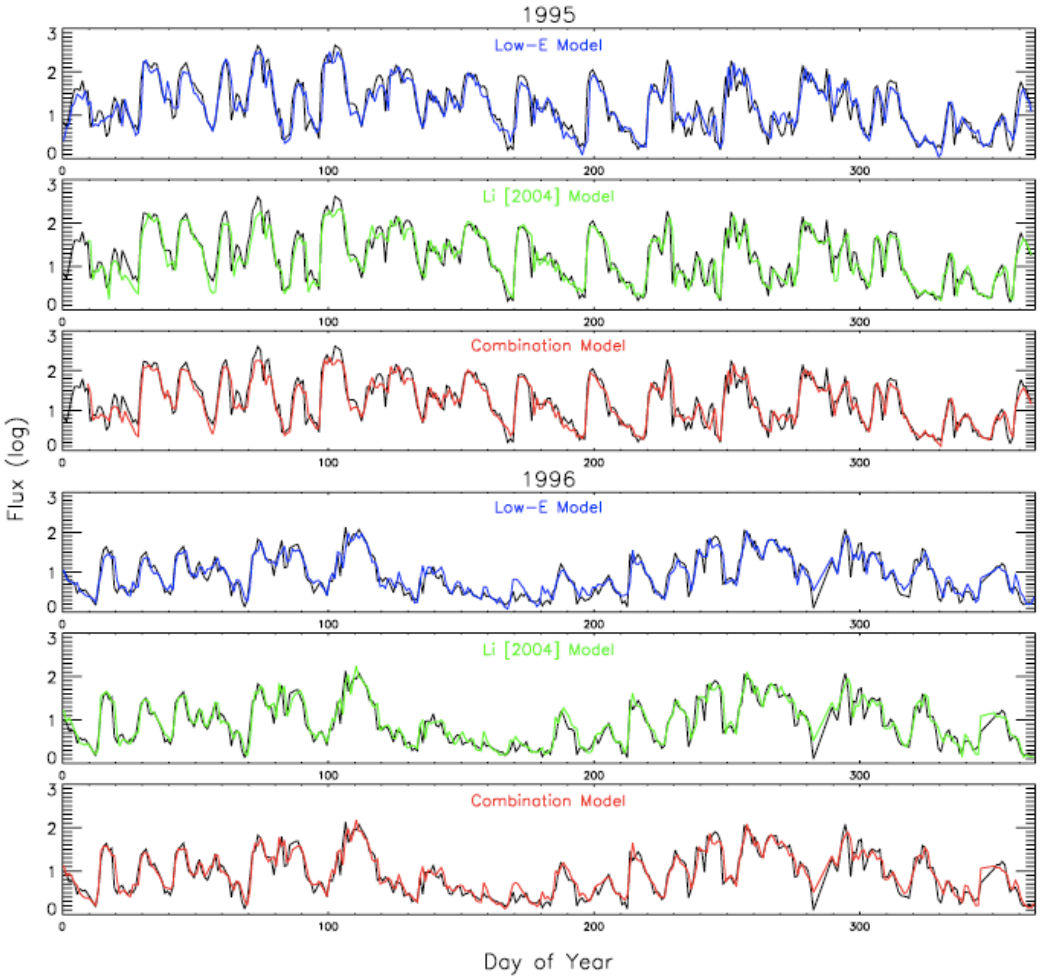

Figure 6.3: Various model results for the years 1995-1996. Top three plots are for 1995: daily averaged LANL 1.1 -1.5 MeV measured electron flux (black) new low- to high-energy model (low-e, blue), *Li* [2004] radial diffusion model (green), and the new model combining both the low to high and *Li* [2004] models (red). The bottom three plots are in the same format for 1996.

Table 6.3: Comparing Multiple-Day Forecast Results From the Simple Persistence Model to the New Model for 1995-1996

Forecast Time, h	Simple Persistence PE	Low-E Model PE
24	0.69	0.81
48	0.35	0.59
72	0.06	0.33
96	-0.17	0.09

becomes 1.0 so that it cancels totally with the$j(t)_{high}$ from equation 6.3). This was expected since the *Li* [2004] model already incorporates persistence. This new form is seen in equation 6.8:

$$j_{combo} = \hat{j}\,(t + \Delta t)_{high} + C_5 j_{Li} \tag{6.8}$$

where j_{combo} is the forecasted flux from the combined model, $\hat{j}(t + \Delta t)_{high}$ is the forecasted flux from the re-optimized low-e model, j_{Li} is the forecasted flux from the *Li* [2004] model, and C_5 is its weighting parameter. The new parameters for the combination model are $C_1 = 3.820 \times 10^{-4}$; $C_2 = 2.533$; $C_3 = 3.280 \times 10^{-2}$; $C_4 = 1.0$, $t_o = 6.0$; $b = 1.927 \times 10^{-1}$; and $C_5 = 0.703$, the new parameter multiplied by the *Li* [2004] forecasted flux. It is very interesting to note that this combination model performs better than both models individually for most years run, including the full 12 years run at once (Table 6.2). Figure 6.3 shows the results of this combination model, compared to the low- to high-energy and *Li* [2004] models, for the years 1995-1996.

6.2.6 Discussion and Conclusions

The results of this paper demonstrate the effectiveness of a new forecast model that uses a time delay between similar features in low- and high- energy electron fluxes to forecast the logarithm of daily averaged relativistic electron flux at GEO. However, it is not entirely clear what physical process this model represents, and determining the process responsible for the time delay between low- and high-energy electron fluxes is difficult because current theory of both radial diffusion and wave-particle interactions can be used to explain it. The most straightforward explanation for the observed delay is that low-energy electrons are being accelerated locally. However, lower-energy

electrons diffuse radially inward at rates higher than those of higher-energy electrons [*Schulz and Lanzerotti*, 1974; *Li et al.*, 2005], and this too can explain the delay observed in the data. The time for inward radial diffusion of MeV electrons to GEO is on the order of days [*Li et al.*, 2001b, 2005], and it also takes on the order of 1-2 d for whistler mode chorus to accelerate a seed population of electrons to MeV levels [*Summers and Ma*, 2000; *Horne et al.*, 2005a; *Shprits et al.*, 2006; *Bortnik and Thorne*, 2007].

Horne and Thorne [1998], *Summers et al.* [1998], and *Meredith et al.* [2002] all agree that the seed population needed for generating MeV electrons due to wave-particle interactions has energy on the order of a few hundred keV, and *Horne et al.* [2005a] and *Bortnik and Thorne* [2007] also agree upon a wave-particle interaction cutoff limit at ∼300 keV, above which particles are primarily accelerated by the mechanism and below which they are mostly lost by it. These energies correspond to the energies discussed in this paper, but the locations are different. Whistler mode chorus accelerates electrons primarily around L = 4.5 [*Horne et al.*, 2005a], but this paper looks at electrons at GEO, where the average L value is ∼6. Therefore, if this delay time between low- and high-energy electrons is indeed related to local acceleration by whistler mode chorus, then some outward radial diffusion must be taking place as well in order to explain the similar correlation at GEO.

Despite the ambiguity in determining the physical processes involved, this paper shows that a strong correlation exists between electrons at various energies in the tens of keV to MeV spectrum. This correlation is enhanced when a delay time between low- and high-energy electron fluctuations is incorporated, and, by incorporating this delay time, a new model that forecasts MeV electron flux at GEO has been developed. One of the strengths of this low- to high-energy model is that it relies only on satellites at GEO for input data. By comparison, the *Li* [2004] radial diffusion model needs electron flux data from GEO as well as solar wind measurements from spacecraft at the Sun-Earth L1 point. This L1, single-point reliance increases the risk to the reliability since, if the spacecraft at L1 fails or is shut down, the *Li* [2004] model is rendered inoperable. Thus, having a model that relies only on electron data taken at GEO lowers the risk to potential users because

of the multiple spacecraft at GEO that are capable of measuring electron flux.

Conclusions from this study are that a strong, time-dependent correlation exists between daily averaged electron fluxes at different energy levels in the tens of keV to MeV energy spectrum, and this correlation can be used as the basis for a model that accurately forecasts the logarithm of daily averaged MeV electron flux at GEO using only the previous 2 d of electron flux data as input. Such a model has been developed, is working, and can be used for a real-time forecast. Such a forecast can be an important tool for radiation environment risk mitigation for the many spacecraft at GEO. Future work will involve increasing the model's time resolution at GEO [*Burin des Roziers and Li*, 2006], expanding the forecast to other L shells and latitudes, and investigating further the physical processes this model best represents.

6.3 Conclusions

This chapter has described one type of radiation belt forecast model, yet many others exist. In the following chapter, I provide a review of these other models and discuss the many limitations that still exist in outer belt forecasting. For example, the model described in this chapter is only for daily averaged relativistic electrons at GEO, which is just one orbit that covers a very limited range in L near the outer edge of the outer radiation belt. Also, covering a range of L-shells, spacecraft in GEO observe a range of fluxes, which a daily average forecast does not account for. This model and many of the others are also limited in their forecasting range. Many models cannot perform better than persistence beyond 2∼3 days due to insufficient forecasts of solar wind quantities. In the following chapter, I address all of these limitations and introduce several new techniques to address them for improved radiation belt forecasting.

Chapter 7

An improved forecast system for relativistic electrons at geosynchronous orbit

7.1 Introduction

The following are two papers written for Space Weather Journal documenting my work on improvements to existing forecast models for relativistic electrons at GEO. The first describes an innovative technique to extend the forecast periods for solar wind based models (like the *Li* [2004] forecast). This technique relies on a solar wind monitor that is behind Earth in its orbit around the Sun, which is actually ahead of Earth in the solar wind due to the Sun's rotation. Using STEREO-B data as such a monitor, I show how its data can be employed to successfully extend the *Li* [2004] forecast to +6 days. In the second paper, I introduce a new forecast system of several models that can be used for outer belt electrons at GEO. This system incorporates a new model in which an internal source is added to the *Li* [2004] model and a statistical tool to improve the forecast resolution to account for the flux variations observed at different local times around GEO. Included in this second paper is a comprehensive review of existing outer radiation belt forecast models.

7.2 *Using spacecraft measurements ahead of Earth in the Parker spiral to improve terrestrial space weather forecasts* by D.L. Turner and X. Li, under review for Space Weather Journal

7.2.1 Abstract

Space weather forecasting is important for mitigating the risks that the effects of the near-Earth space environment have on manmade systems. Here, we investigate an innovative technique for extending the temporal range of solar wind based forecast models by using solar wind measurements made azimuthally ahead of Earth in the Parker spiral near 1 AU. Cross-correlations between STEREO (near 1 AU) and ACE (at L1) solar wind quantities are examined, and we show that data from STEREO-B, which is azimuthally behind Earth in its orbit but ahead of Earth in the Parker spiral, can be used as an input to a relativistic electron forecast model to extend its capability to +6 days from its original range of +2 days. We show that this extended forecast performs better than simple persistence or average models for all 6 forecast days. We also compare +1 day solar wind speed forecasts using offset STEREO-B data and the Wang-Sheeley-Arge model, and we find that the offset STEREO-B data performs significantly better for estimating the future solar wind at Earth. We conclude that this technique could be particularly beneficial to space weather forecasting and argue for a permanent solar wind monitor at the 5th Lagrange point in the Sun-Earth system.

7.2.2 Introduction

Since Richard C. Carrington noted the cause and effect of a large solar flare and subsequent geomagnetic storm in September of 1859, we have understood that there is a connection between solar events and Earth's magnetic field. In recognition of this, solar rotations, which occur on a ~27 day period as observed from Earth, are referred to as "Carrington" rotations. However, it wasn't until nearly a century later that L. Biermann proposed that there is a continuous outflow of plasma from the Sun, that is a continuum of charged particles and magnetic fields blowing outward

in some solar wind [see history in: *Gosling*, 2007]. *Parker* [1958] revolutionized our understanding of space weather and the solar-magnetospheric connection with his formulation of a model for the Sun's corona that included a continually expanding solar atmosphere. We now have developed a much better understanding of the solar wind from a multitude of in situ observations and improved modeling [*Gosling*, 2007]. The mean solar wind density, temperature, and velocity at 1 AU are 8.7 cm^{-3}, 12×10^5 K, and 468 km/s respectively, with the velocity primarily in the radial direction away from the Sun. Since the solar wind plasma is an excellent conductor, the Sun's magnetic field is "frozen" into it as it radiates outward. This combined with the solar rotation leads to a spiral configuration of the interplanetary magnetic field (IMF) when viewed in the solar equatorial plane [see Fig. 1 from *Gosling*, 2007], much like the spiral made by a person spinning and spraying a garden hose as viewed from above. In the solar wind, this IMF configuration is referred to as the Parker spiral. However, this is an idealized picture, as the solar wind is a turbulent plasma and highly variable. At any point, its conditions are the result of dynamics on the solar surface and in the corona when it originated as well as ongoing interactions with the solar wind around it.

Space weather at the Earth can seriously affect manmade systems, from power grids to spacecraft [*Baker*, 2001], and changes in this "weather" are largely driven by changes in the solar wind. Thus, solar wind quantities are important for various space weather forecast models, which are used to mitigate the risk of space weather effects on manmade systems. For example, trapped energetic particles in the radiation belts pose a threat to spacecraft electronic components and have been known to critically affect satellite operations [e.g. *Baker et al.*, 1998a]. Flux variations for these particles in the outer radiation belt are known to be correlated with the solar wind velocity [*Williams*, 1966; *Paulikas and Blake*, 1979; *Baker et al.*, 1979], and several radiation belt models are reliant on solar wind quantities as input [e.g. *Baker et al.*, 1990; *Li et al.*, 2001b; *Li*, 2004; *Fok et al.*, 2008]. However, these models are limited in their effective forecast range by accurate solar wind forecast capabilities.

Here, we investigate a new technique to estimate future solar wind conditions at Earth. This estimation simply relies on the nature of the solar wind, with its radial outward flow and

IMF Parker spiral. We test the hypothesis that a spacecraft measurement of the solar wind taken azimuthally behind Earth in its orbit around the Sun, which is actually ahead of Earth in the Parker spiral, can be used to estimate the solar wind at some later time at Earth taking into account the solar rotation and azimuthal difference between the spacecraft and Earth. We examine the cross-correlations between solar wind quantities observed at different azimuthal locations near 1 AU. The application to extending space weather forecasts is tested using a relativistic electron forecast model for Earth's outer radiation belt. Overall, we find this technique is applicable to extending some solar wind based space weather forecasts, and we note the technique and analysis limitations.

7.2.3 Data Description

The Advance Composition Explorer (ACE) mission was launched 25 August 1997, and since that time, it has provided measurements of the upstream solar wind from the first Lagrange (L1) point in the Sun-Earth system [*Stone et al.*, 1998]. Here, we use data from ACE's SWEPAM (solar wind plasma) and MAG (magnetic fields) instruments for solar wind velocity, density, and magnetic field quantities. Also currently active in the solar wind is the Solar TErrestrial RElations Observatory (STEREO) mission [*Kaiser*, 2005], which launched its twin spacecraft on 25 October 2006. The STEREO mission involves two identical spacecraft, one ahead and one behind Earth in its orbit around the Sun. Figure 7.1 shows the locations of the STEREO-A (ST-A; for 'Ahead') and -B (ST-B; for 'Behind') on 29 Aug. 2008 and 28 Aug. 2009, which mark the start and stop times for the period used for most of this study. In this fixed heliographic-Earth-ecliptic (HEE) reference frame, the STEREO spacecraft will continue to travel away from Earth in their respective orbits until they each cross the X-Z plane on the other side of the Sun sometime in early 2015. For this study, we employ STEREO solar wind plasma, magnetic field, and ephemeris data available from NASA's CDAWeb (courtesy of Natasha Papitashvili at NASA/GSFC). We use hourly merged data from STEREO as available from CDAWeb and 10-minute ACE data, which is hourly-averaged to align it with the STEREO data.

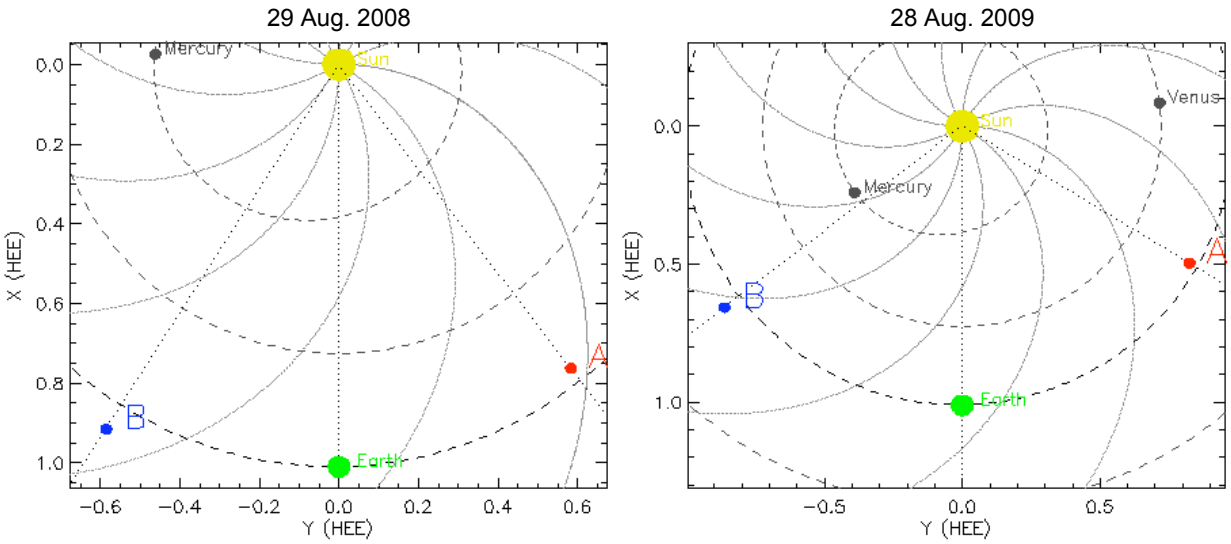

Figure 7.1: STEREO locations at 12:00 UT on 29 August 2008 (left) and 28 August 2009 (right). ST-A (A) and ST-B (B) are shown ahead and behind of Earth in its orbit around the Sun (planetary orbits are indicated with the dashed lines). The Parker spiral and the orbits of Venus and Mercury are also shown. Distances in the heliographic-Earth-ecliptic (HEE) X-Y plane are given in units of AU. Note that the scales are different on the two plots. STEREO orbit plots are generated by the online web tool at: $< http://stereo-ssc.nascom.nasa.gov/where/ >$.

For the outer radiation belt forecast model used to test the method described in this paper, we employ relativistic electron data from the GOES-11 spacecraft from NOAA's Geostationary Operational Environment Satellites series. GOES spacecraft have provided integral fluxes of relativistic electrons at geosynchronous orbit (GEO) for close to three decades. Until the latest generation, the GOES spacecraft since GOES-8 (including GOES-11) used the Energetic Particle Sensors (EPS) to measure electrons in three integral flux channels: >600 keV, >2 MeV and >4 MeV [*Onsager and et al.*, 1996]. Here, we use daily averaged >2 MeV electron flux data from GOES-11.

7.2.4 Correlating Solar Wind Measurements from Different Locations

Using the hourly, aligned ST-B and ACE data, we examine the cross-correlations for various solar wind quantities measured by each spacecraft. Cross-correlation (CC) is the measure of the similarity between two data sets given a time-lag applied to one of them, and it is analogous to the linear correlation. Table 7.1 shows the cross-correlations for the solar wind speed (V), density (n), and magnetic field components and magnitude as measured by the two spacecraft. The time-offsets shown correspond to the amount of hours that the ST-B data is shifted ahead to produce the correlations shown. For the magnetic fields, we have simply compared the ACE fields in the GSM frame to the ST-B fields in the radial-tangential-normal (RTN) frame. In the RTN frame, the radial component is along the vector from the center of the Sun through the center of ST-B, the normal component is along the projection of the solar north pole, and the tangential component completes the right-handed ortho-normal system. With this in mind, we only compare the field components from each spacecraft that best correspond between the two coordinate systems.

Table 7.1 reveals the strongest correlation (CC = 0.66) for the solar wind speed when the ST-B data is offset by 71 hours. The solar wind density is less correlated at CC = 0.21, and the offset to achieve this CC is slightly longer at 75 hours. The magnetic field components are very poorly correlated between the two spacecraft. This is expected considering they are in different reference frames and the variability in the IMF resulting from the solar wind's turbulent nature and ever-changing micro-scale conditions at the Sun (e.g. magnetic field loops and arcades). However,

Table 7.1: Cross-correlations for ST-B and ACE solar wind quantities from 29 Aug. 2008 - 28 Aug. 2009. Time offsets (T-off) corresponding to the cross-coefficients for each quantity are shown in hours.

Quantity	Cross-Corr.	T-off (hr)
V_{sw}:	0.66	71
n_{sw}:	0.21	75
B_{Tot}:	0.06	119
B_z-B_n:	0.04	94
B_y-B_t:	-0.09	0
B_x-B_r:	-0.16	1

the strong correlation in the speed is notable. Figure 7.2 shows the ST-B and ACE solar wind speed data for the period used in this study. Here, the full year of hourly data used to determine the cross-correlations is shown, and the time offset between similar features is clearly evident. This offset corresponds to features originating from approximately the same macro-scale features on the Sun (e.g. coronal holes) measured at different times by each spacecraft given the time it takes for the solar rotation to cover the angular distance between the two spacecraft. In this work, we focus primarily on the solar wind speed correlation.

As Figure 7.1 shows, the STEREO spacecraft are continually moving away from Earth in the HEE frame. Because of this, the time offset between similar features measured by ST-B and ACE are continually changing (i.e. getting longer) throughout the period used for this study. For example, if only two months from the beginning of this time period are used (29 Aug. - 28 Oct. 2008), the CC and offset time for solar wind speed are 0.87 and 53 hours respectively. When only the last two months of the period are used (29 Jun. - 28 Aug. 2009), the CC and offset time for the solar wind speed are 0.56 and 108 hours. So, for the solar wind speed, the correlation decreases and the time offset increases as the separation in the solar wind between the two spacecraft increases.

We also compare ST-B to ST-A data to determine how the correlations and offset times are affected by larger azimuthal separations. For the last two months of the period when the spacecraft are separated by around 110° in azimuth (see Fig. 7.1), the CC and offset for solar wind speed are 0.36 and 196 hours. Interestingly, the correlation for the B-normal component is still positive (CC

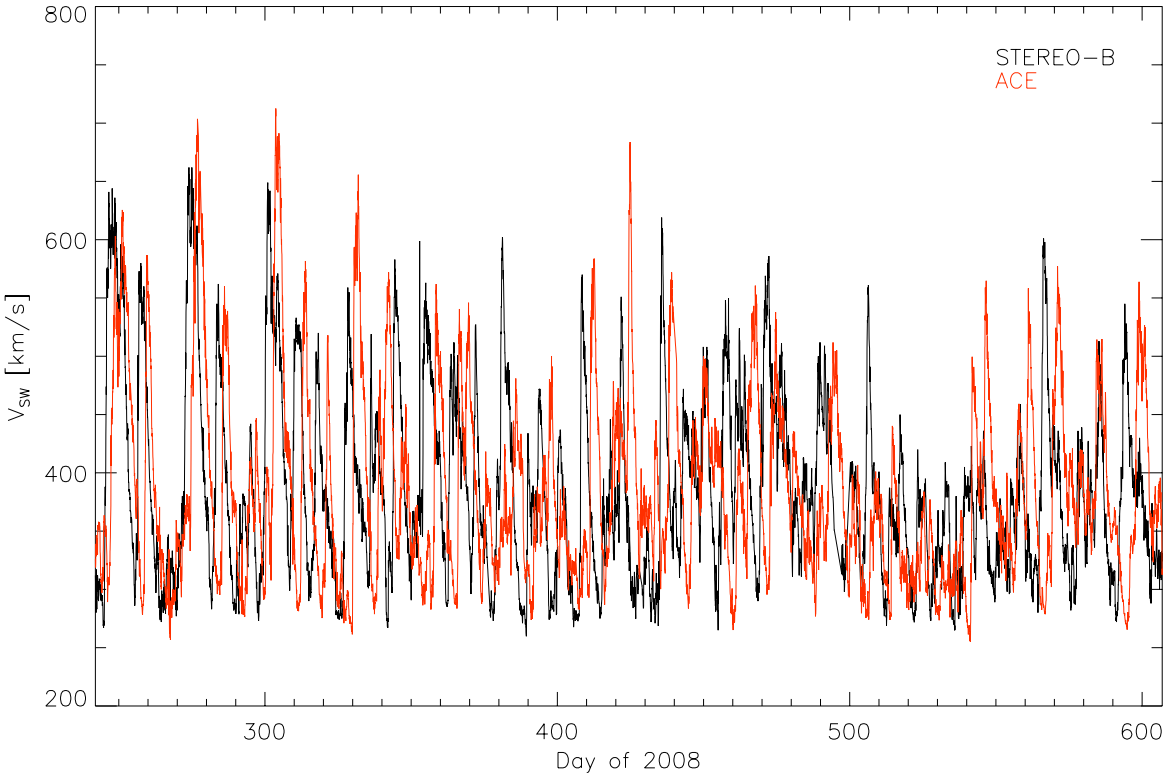

Figure 7.2: STEREO-B (black) and ACE (red) hourly solar wind speeds for 29 Aug. 2008 - 28 Aug. 2009.

= 0.11), and the density is actually more correlated than for the full period with the ST-B and ACE comparison (CC = 0.23). For the full time period comparing both ST-A and -B measurements, the CC and time offset for the solar wind speed are 0.46 and 138 hours respectively.

This analysis reveals that a cross correlation does exist for the solar wind velocity as measured by two spacecraft separated in azimuth in the Parker spiral. Thus, it should be possible to use measurements from a spacecraft ahead of Earth in the Parker spiral (i.e. behind Earth in its orbit around the Sun) to extend forecasts that rely on solar wind velocity as an input. In the next section, we test this concept using ST-B data with a time offset as input to a solar wind-based forecast model of relativistic electron fluxes at GEO.

7.2.5 Extending a Radiation Belt Forecast

To test this concept of using solar wind measurements from a spacecraft ahead of Earth in the Parker spiral to extend terrestrial space weather forecasts, we employ the *Li* [2004] model. *Li* [2004] described a forecast model for relativistic electron (>2 MeV) electron flux at GEO that uses solar wind speed and GOES >2 MeV daily averaged fluxes as inputs. The model has been shown to consistently outperform a simple persistence model (where tomorrow's flux is the same as today's) throughout the entire solar cycle for 1- and 2-day forecasts [*Turner and Li*, 2008a]. However, it is limited in its forecast range by accurate solar wind forecasting capabilities.

Taking advantage of the cross-correlation in solar wind speed between ST-B and ACE, we use offset ST-B data as solar wind input to the *Li* [2004] model to see how well it performs for 3-, 4-, 5-, and 6-day forecasts. Since the model already uses today's solar wind data from ACE to forecast 2 days into the future, it should be possible to use offset ST-B data, with its position ahead of Earth in the Parker spiral and temporal offset around 3 days ahead of ACE, to extend the forecast by several days. When the forecast model is run on its own using ACE and GOES-11 input data for 29 Aug. 2008 - 28 Aug. 2009, it achieves a prediction efficiency (PE) of 0.87 and 0.70 for the 1- and 2-day forecasts. For comparison, the PEs using the simple persistence model for 1- and 2- days are 0.81 and 0.56 respectively. PE is a measure of a forecast's performance, where PE =

1 represents a perfect forecast, PE = 0 represents an "average" model in which the forecast is the same as using the average value from the measured data, and PE < 0 means the model performs worse than the "average" model [see discussion on PE in: *Li*, 2004].

When ST-B velocity data are used as input to the model with no time shift applied, the PEs are 0.76 and 0.39 for the 1- and 2-day forecasts. However, when the ST-B data is shifted three and a half days (84 hrs) forward in time and used as input, the PEs are improved to 0.84 and 0.61, which is closer to those achieved using the ACE data and both better than the simple persistence model. The shifting time was chosen based on the forecast model performance (i.e. it resulted in the highest PE for the period of Aug. 2008 - Aug. 2009). Based on this, we use the ST-B data with a 1.5 day offset to extend the *Li* [2004] model for 3- and 4- day forecasts and the ST-B data with no offset for 5- and 6- day forecasts. Figures 7.3 and 7.4 show the model results for the day 1 through 6 forecasts. The model PEs are also displayed alongside the PEs from the simple persistence model for each day. Note that the model consistently outperforms simple persistence out to +6 days. In fact, by day six, the persistence model performs poorer than just using the average GOES-11 flux, while the *Li* [2004] model with ST-B data still has a positive PE.

7.2.6 Discussion

In this paper, we have addressed the following question: can solar wind measurements from a spacecraft that is azimuthally ahead of Earth in the Parker spiral be used to extend terrestrial space weather forecasts? We have examined the cross-correlations between the STEREO spacecraft, which are ahead and behind Earth in its orbit around the Sun, and ACE, which is upstream of Earth in the solar wind at the L1 point. Being behind the Earth, ST-B is actually ahead of Earth in the Parker spiral and thus observes similar features in the solar wind several days ahead of ACE and ST-A. The quantity with the strongest correlation of those examined during the period 29 Aug. 2008 - 28 Aug. 2009 is the solar wind speed, with CC = 0.66 for an offset of 71 hours applied to the ST-B data and compared with ACE. We have gone on to show that a space weather forecast, namely the *Li* [2004] relativistic electron forecast for GEO, can be successfully extended by using

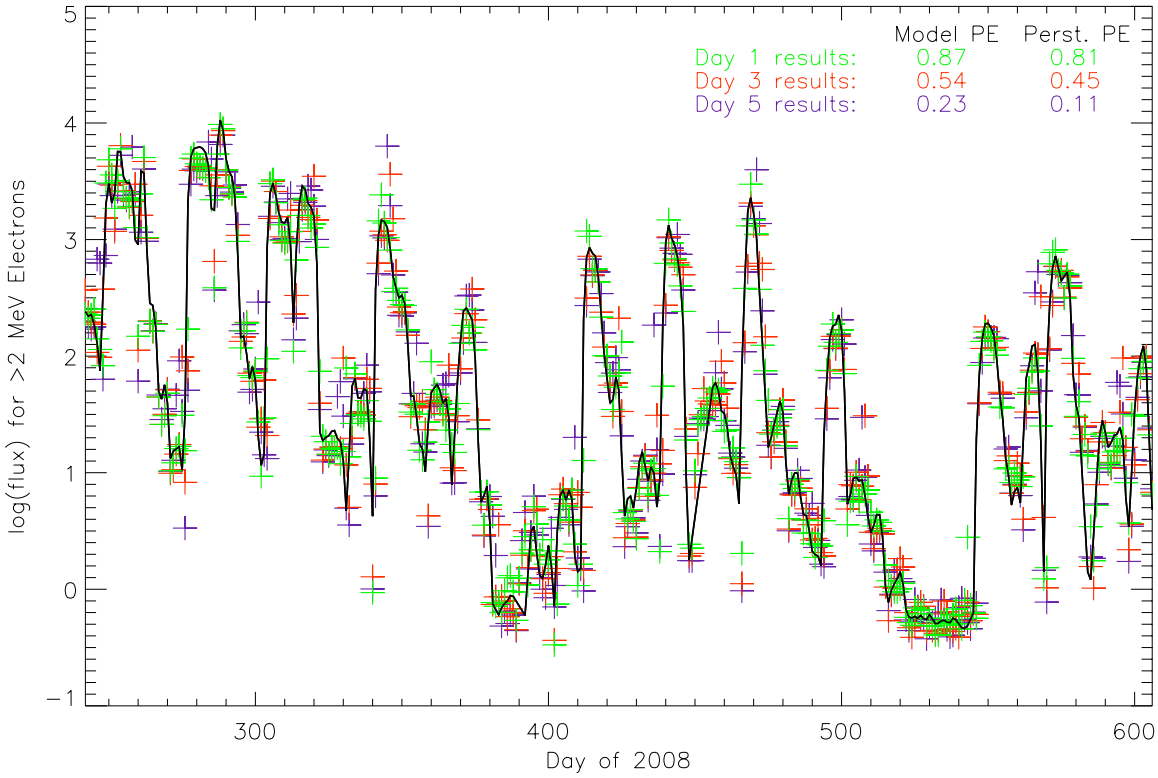

Figure 7.3: Results from the *Li* [2004] model for 1-, 3-, and 5-day forecasts using ACE and ST-B data as solar wind inputs. Model forecasts are shown with different color '+'s, and the observed GOES-11 daily average data is shown with the solid curve. Model and persistence PEs are also shown in the legend.

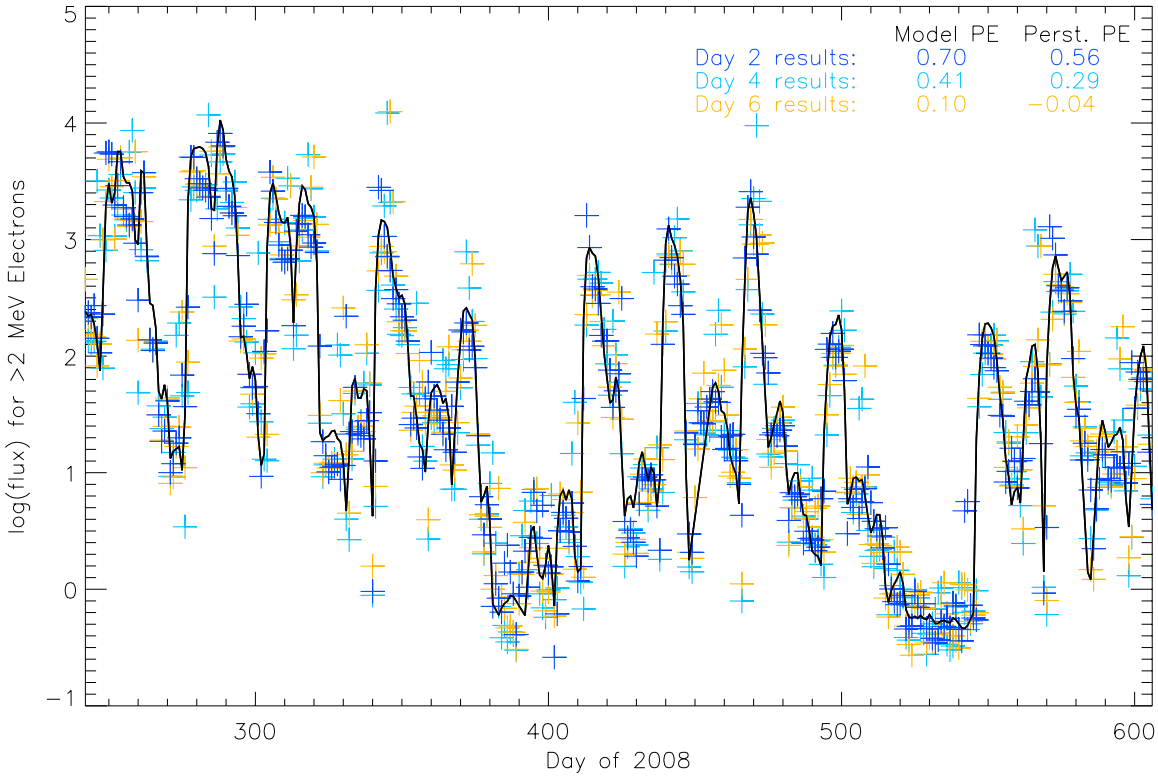

Figure 7.4: Results from the *Li* [2004] model for 2-, 4-, and 6-day forecasts using ACE and ST-B data as solar wind inputs. Model forecasts are shown with different color '+'s, and the observed GOES-11 daily average data is shown with the solid curve. Model and persistence PEs are also shown in the legend.

ST-B data as input. The model forecast range has been extended by a factor of three, from the original +2 day capability to +6 days. This is clear and simple proof of concept that solar wind data measured from ahead of Earth in the Parker spiral can indeed be used to extend terrestrial space weather forecasts that rely on solar wind data as input.

We have also performed a simple comparison between the forecasting capabilities of offset ST-B data to the Wang-Sheeley-Arge (WSA) model for 1-day solar wind speed forecasting. We used the period from 15 March - 15 September 2008 and evaluated the performance using the PE for each speed forecast compared to ACE data. During this period, we simply offset the ST-B data by 40 hours to serve as the forecast to compare with ACE. When compared to the 1-Day WSA solar wind speed forecast, the offset ST-B data performs much better, achieving a PE of 0.71 compared to the WSA PE of 0.23.

There are some limitations that should be noted. This technique is particularly useful for approximating when we will encounter high speed solar wind streams (HSSs) here at Earth. This is because of the nature of HSS origins from the Sun itself; they emanate from coronal holes, which are large-scale features that rotate with the Sun. Coronal mass ejections (CMEs), however, are explosive events whose arrivals at Earth cannot be approximated in the same manner (more on this below). Also, this study was conducted during a very quiet and extended solar minimum period. We expect that the correlations examined in this study will be weaker during solar maximum due to the increased activity in the solar wind and on the Sun itself.

Concerning any immediate application of this technique, there is an issue with the STEREO orbits. ST-B continues to drift in azimuth away from the Earth, as its orbital period is just slightly longer than that of the Earth. Thus, the performance of any model that uses ST-B data to extend its forecast time will continue to degrade as the correlation between the solar wind speed at ST-B and Earth decreases. If the spacecraft are still operational after early 2015, ST-A and -B will cross behind the Sun from Earth's perspective, and ST-A will then drift azimuthally towards Earth and ahead of it in the Parker spiral. However, there is a better solution to maintaining this solar wind forecasting capability: a solar wind monitor located at the 5th Lagrange point (L5). L5 is a stable

orbital point and is located 60° behind Earth in azimuth along its orbit [*Vallado*, 2001]. A spacecraft at the L5 point can provide a several day forecast extension capability for space weather models as well as provide a fixed stereoscopic view of the Sun when combined with another solar wind monitor at the L1 point. Such stereoscopic view is important, for example, for identifying whether halo CMEs are traveling towards or away from the Earth [e.g. *Kaiser*, 2005], so the space weather benefits of a solar wind monitor at L5 would go beyond the application to forecast extensions.

Given its current location, ST-B can still be used for solar wind forecasting. Based on the comparison with ST-A, the correlations with the solar wind velocity and density (to a lesser extent) persist over large azimuthal separations (the velocity CC was 0.36 with 196 hour offset for around 110° of separation). Also, if a model has only a weak dependence on the IMF, the ST-B IMF measurements should suffice as an estimate. For a real-time forecast, access to real-time ST-B data is necessary, and such data from the STEREO spacecraft are indeed available from the mission space weather beacon (see: $http://stereo-ssc.nascom.nasa.gov/beacon/beacon\_insitu.shtml$). Such data can be used to extend space weather forecasts or any other real-time models that rely on solar wind velocity, like electron flux mapping around GEO using statistical asynchronous regression for example [e.g. *Turner et al.*, 2010a].

7.2.7 Conclusions

We have shown how solar wind velocity measurements from spacecraft that are azimuthally ahead of Earth in the Parker spiral (behind it in its orbit around the Sun) can be used to accurately predict the solar wind speed at Earth several days later. This concept can be used for extending space weather forecasts that rely on solar wind data, as we have shown here by extending the *Li* [2004] relativistic electron forecast to +6 days. This presents a good argument for a devoted solar wind monitor at the stable L5 point in the Sun-Earth system. Such a monitor would be beneficial to solar and solar wind physics in general, as STEREO is currently proving. Concerning space weather, a solar wind monitor at L5 would provide several days warning for HSSs and be used alongside a monitor at the L1 point to identify halo CMEs that will impact Earth's magnetosphere.

7.3 *An improved forecast system for relativistic electrons at geosynchronous orbit* by D. L. Turner, X. Li, E. Burin des Roziers, and S. Monk, in preparation for Space Weather Journal

7.3.1 Abstract

As society becomes more dependent on satellite systems for navigation, communication, defense, and weather prediction, accurate forecasts of Earth's outer radiation belt electrons become ever more important to help mitigate risk to spacecraft in orbits that go through this hazardous region. Currently, outer radiation belt forecast models are only for daily-averaged fluxes (or fluence) at geosynchronous orbit (GEO), yet due to the nature of Earth's asymmetric magnetosphere, with its compressed dayside and stretched nightside, a spacecraft in GEO encounters a wide range of fluxes and field strengths at different local times, which are not reflected by a daily average. Here, we provide a review of existing forecast models, discuss some recent improvements to two of these models, and present a new and improved forecast system for relativistic electrons at GEO. For the first time, we can forecast at a local hour resolution around GEO using a statistical tool included in the system. This forecast system also includes several real-time forecast models, two previously existing and one that is a new development. This new model incorporates an internal electron source, simulating local acceleration by wave-particle interactions, and it proves to be the most accurate of the models in the system. For 2007-2008, it achieves +1 and +2 day prediction efficiencies of 0.90 and 0.63. We conclude this work with a discussion of how these models are currently operational and providing results to the community online in real-time, and we also speculate on future possibilities to allow for forecasts throughout the rest of the outer radiation belt.

7.3.2 Introduction

7.3.2.1 Background

Society has become extremely dependent on space-based assets for a variety of applications, including personal and commercial navigation, communication, entertainment, science, defense, and

weather prediction, and many of the spacecraft we rely upon for these applications are in orbits that exist in or pass through Earth's outer radiation belt. The outer radiation belt is an extremely dynamic system, consisting primarily of relativistic electrons that are stably trapped in Earth's magnetosphere. These electrons can be potentially hazardous to spacecraft [*Baker*, 2001], particularly any inadequately shielded electronic components onboard. Energetic electrons can penetrate into sensitive semi-conducting materials that make up these components, and if their incoming rate is faster than the rate that the material can naturally absorb them, strong electric fields can build up within a component and discharge, which can cause significant and potentially fatal damage to it. Recently, the Galaxy 15 satellite, a communications satellite in geosynchronous orbit (GEO) providing commercial media services and a payload used by the United States Federal Aviation Administration, suffered a critical system failure in which it stopped responding to operational commands [*Ferster*, 2010]. This event sparked fears concerning loss of commercial services, and the cause of the spacecraft failure was initially suspected to be the result of "unusually violent solar activity" [*de Selding*, 2010, page 1], which likely manifested itself in the form of enhanced energetic electron fluxes considering that Galaxy 15 was in the magnetosphere in GEO. As society becomes increasingly more dependent on spacecraft in the outer radiation belt, the ability to mitigate risk to these assets is critical, and the ability to accurately forecast outer belt electrons becomes increasingly more important. However, to develop a forecast of a system, it is first critical to understand the underlying physics of the system itself.

Earth's trapped radiation environment was first discovered by *Van Allen and Frank* [1959] with geiger counter measurements from the early Explorer series of spacecraft. They reported two distinct "belts" of radiation around the Earth. The three characteristic motions of the trapped energetic electrons that populate the outer radiation belt are 1) gyro-motion around field lines, 2) bounce motion along field lines, and 3) azimuthal drift perpendicular to field lines around the system. These motions define the outer radiation belt's torus-like shape around the Earth, with inner and outer equatorial bounds around 3 and 7 Earth radii (R_E) respectively and bounds at higher latitudes that follow magnetic field lines down into the atmosphere near the poles, where

the electrons can precipitate and be lost [e.g. *Abel and Thorne*, 1998]. *Roederer* [1970] handled the dynamics of energetic electrons in the outer belt using adiabatic theory, in which three adiabatic invariants, which are related to the electrons three characteristic motions in the magnetic field, can be derived. These invariants are conserved so long as the magnetic field is not changing faster than the time scales of their respective characteristic motion. Following the convenience of adiabatic theory for describing outer belt dynamics, *Schulz and Lanzerotti* [1974] established the theory of electron diffusion in the outer radiation belt, which provided an explanation for how the electrons could be accelerated to relativistic energies. By this theory, if the third adiabatic invariant, which is associated with electrons' drift motion around the Earth, is broken, then electrons can diffuse radially towards or away from the Earth depending on the radial gradient of their phase space density (PSD). *Schulz and Lanzerotti* [1974] proposed that this gradient promoted inward radial diffusion, such that the electrons gain energy by conserving their first adiabatic invariant, which is associated with electrons' gyro-motion around field lines, as they diffuse inwards to regions of higher magnetic field strength. This radial diffusion is summed up mathematically in Equation 7.1:

$$\frac{\partial f}{\partial t} = L^{*2}\frac{\partial}{\partial L^*}\left(\frac{D_{LL}}{L^{*2}}\frac{\partial f}{\partial L^*}\right) - \frac{f}{\tau} + S \tag{7.1}$$

where f is PSD for fixed values of the first and second adiabatic invariants, L^* describes an electron's drift shell in R_E and is directly related to the third adiabatic invariant [*Roederer*, 1970], and D_{LL} is the diffusion coefficient, which regulates the rate at which diffusion occurs. Here, we also include a loss term (τ) and a source term (S), both of which can be functions of L^*.

Recent studies based on more sophisticated observations of the outer belt have indicated that inward radial diffusion is not entirely adequate to describe the extreme variations observed. *Temerin et al.* [1994] followed by *Summers et al.* [1998] and *Horne and Thorne* [1998] were the first to discuss how plasma waves, VLF chorus in particular, could interact with energetic electrons to preferentially accelerate them to relativistic energies. *Horne et al.* [2007] showed how fast magnetosonic waves, which are produced by ring current protons, can also preferentially accelerate electrons to relativistic energies. Evidence for this internal acceleration by wave-particle interac-

tions has since been presented in a multitude of studies [e.g. *Brautigam and Albert*, 2000; *Green and Kivelson*, 2004; *Koller et al.*, 2007; *Shprits et al.*, 2007a; *Chen et al.*, 2007b; *Turner et al.*, 2010b]. These (and several other) studies indicated that wave-particle interactions with chorus and fast magnetosonic waves are the dominant acceleration mechanism for outer belt electrons. In this picture, substorms inject 1∼300 keV electrons and ∼10's keV protons into the inner magnetosphere, and these electrons and protons are responsible for generating chorus and fast magnetosonic waves respectively. These waves then interact with radiation belt electrons and accelerate them to relativistic energies, resulting in peaks in the PSD radial distributions and intense fluxes near the heart of outer belt (∼5 R_E) [*Green and Kivelson*, 2004; *Koller et al.*, 2007; *Chen et al.*, 2007b]. This theory is complemented by the findings of *Meredith et al.* [2002], who presented a case study that showed prolonged substorm activity is more important to outer belt electron enhancements than geomagnetic storms. This dependence on substorm activity can also explain the intriguing results of *Reeves et al.* [2003], who found that only 53% of a set of 276 moderate and intense geomagnetic storms resulted in an increase in outer belt electron fluxes.

It has long been established that variations in the outer radiation belt electrons are correlated to variations in the solar wind [e.g. *Williams*, 1966]. For example, enhancements in outer belt electron fluxes are known to regularly follow around one to two days after the passage of high speed solar wind streams [*Paulikas and Blake*, 1979]. Many studies focus primarily on solar wind velocity when considering how the solar wind affects outer radiation belt electron fluxes, but more recently, *Lyatsky and Khazanov* [2008b, c] studied the effects from solar wind number density (n_{sw}). They found that relativistic electron flux is negatively correlated to n_{sw}, with the best correlation with the electrons occurring about 15 hours after a change in the density [*Lyatsky and Khazanov*, 2008b], and that for most cases examined, relativistic electron flux enhancements are precluded 1-2 days in advance by geomagnetic activity with low n_{sw} for the same 1-2 days prior [*Lyatsky and Khazanov*, 2008c]. Correlations like those with the solar wind have been critical to the development of accurate forecasts of relativistic electrons in the outer radiation belt, and next, we provide a brief review of several of those models.

7.3.2.2 Existing Forecast Models

In this section, we discuss several of the existing models used to forecast relativistic electrons in the outer belt, but before that discussion can begin, a brief explanation of two of the techniques commonly used to evaluate these models is needed. Linear correlation (LC) is one way to compare a set of forecast values with a corresponding set of actual measured values, but LC is technically intended to determine the correlation between two *different* data sets that are not supposed to have the same value (e.g. solar wind velocity and relativistic electron flux). For two sets of data that should ideally be identical (i.e. the results of a perfect forecast model and the data set it is forecasting), prediction efficiency (PE) can be used to better quantify model accuracy. PE is mathematically defined as:

$$PE = 1 - \frac{\sum_{i=1}^{N} (x_i - \hat{x}_i)^2}{\sum_{i=1}^{N} (x_i - \langle x_i \rangle)^2} \tag{7.2}$$

where N is the number of points in a sample set, $\hat{x_i}$ is the model data set, and x_i is the actual measured data set with $\langle x_i \rangle$ its average. The resulting values of a PE calculation are in the range of $(-\infty,\ 1)$, with a PE of 1 implying a "perfect" model, in which the predicted values are all the same as the corresponding measured ones, and a PE of 0 indicates that the average of the predicted values are equal to the average of the measured data set (i.e. an "average" model). A negative PE means that the model results are worse than the "average" model. Forecast models should ultimately outperform (i.e. their PE should be closer to 1 than) a simple persistence model in which "tomorrow's" forecasted value is simply the same as "today's" value. We use this test to establish the effectiveness of the models developed for this paper.

One of the earlier outer belt electron forecasts is based on the work of *Baker et al.* [1990] and uses a linear prediction filter to forecast relativistic electron fluence (i.e. time-integrated flux) at GEO. Linear prediction filters employ historic data to create correlation coefficients, which can then be applied to real-time data to calculate forecast values. The filter of *Baker et al.* [1990] used only average solar wind speed as input. This filter model has been adapted

and is currently used by the National Oceanic and Atmospheric Administration's Space Weather Prediction Center (NOAA-SWPC) for their Relativistic Electron Forecast Model (REFM; see $< http://www.swpc.noaa.gov/refm/index.html >$).

Li et al. [2001b] described a prediction model for the daily averaged relativistic electron flux at GEO. This model numerically solves the one dimensional radial diffusion equation (Equation 7.1) using solar wind parameters to define a diffusion multiplier for a diffusion coefficient in the form:

$$D_{LL} = D_0 \left(\frac{L^*}{6.6} \right)^{10} \tag{7.3}$$

where D_0 is the diffusion multiplier that is a function of solar wind parameters (see Equation 7.5 below for the form of this term), and L^* is the invariant L-parameter from Equation 7.1. *Li et al.* [2001b] determined the model parameters empirically by best fitting (based on PE) the model results to the measured data from 1995-1996, and with this model, they achieved a PE of 0.81 and LC of 0.90 for the training years (1995-1996) and a corresponding PE and LC of 0.59 and 0.80 respectively when the model was extended to predict the years 1995-1999, using the parameters determined by optimizing for the training years.

Li [2004] used the *Li et al.* [2001b] prediction model to develop a forecast model for 24- and 48-hour forecasts of the logarithm of daily averaged, relativistic electron flux at GEO. This model incorporates several other features in addition to the solar wind based diffusion multiplier. Seasonal and solar cycle factors for the diffusion coefficients and a loss term were added, which reflect the results of *Li and Temerin* [2001] that show how relativistic electron flux intensities peak during the declining phase of the solar cycle as well as near the equinoxes of each year. Dst effect and dynamic pressure terms are also included in the model. The Dst effect simply accounts for the adiabatic response of electrons due to changes in the magnetic field [e.g. *Kim and Chan*, 1997], while the dynamic pressure term reflects the loss of electrons to the magnetopause during times of high solar wind dynamic pressure, known as magnetopause shadowing. Real-time results from this model are currently displayed online (see: $< http://lasp.colorado.edu/space\_weather/xlf3/xlf3.html >$),

and this model serves as one of the two baseline models that will be improved and expanded upon as discussed later in this paper.

Turner and Li [2008a] created a forecast model that used low-energy electron flux to forecast relativistic flux at GEO. They did this by taking advantage of a time delay between similar changes in low and high energy, daily averaged electron fluxes discussed in *Li et al.* [2005]. Their model used daily averaged, differential flux measurements from geosynchronous LANL spacecraft to forecast the logarithm of daily averaged, 1.1-1.5 MeV electron flux at GEO. This new forecast model is advantageous in that it only uses daily averaged flux measurements from GEO as input and is not reliant upon a single spacecraft for solar wind measurements (e.g. ACE). The model uses a simple source and loss differential equation for electron flux (see Equation 7.4; j is relativistic electron flux), which is numerically discretized, and empirical forms are determined for the source and loss terms (S and Λ, respectively in Equation 7.4; note that Λ is used here instead of L from *Turner and Li* [2008a] so as not to be confused with L, the drift-shell parameter) to solve for "tomorrow's" flux.

$$\frac{dj}{dt} = S + \Lambda \tag{7.4}$$

S and Λ are functions of "today's" electron flux from both low and high energy channels, and the parameters for these terms were determined by *Turner and Li* [2008a] by optimizing the PE for the years 1995-1996 using flux data from several LANL energy channels. They found that the PE for the training years is best when S is a function of the fluxes from the lowest and highest LANL energy channel, 50-75 keV and 1.1-1.5 MeV respectively, and when Λ is a function of the highest channel's flux, which is the same as that being forecasted. *Turner and Li* [2008a] also introduced a simple combination model put together using a linear combination of both their new model and the *Li* [2004] forecast model. They showed how this combination model consistently outperformed both models individually. The PEs and LCs for the models run for 2005-2006 are: 0.74 and 0.90 (PE and LC respectively) for the *Turner and Li* [2008a] forecast, 0.75 and 0.90 for the *Li* [2004] forecast, and 0.78 and 0.91 for the combination forecast.

Several other models exist as well. *Ukhorskiy et al.* [2004] derived a data-based model to produce a one day forecast for the daily maxima of electron flux at GEO. The model uses multiple input parameters and combines conditional probability with nonlinear time series analysis techniques. By incorporating conditional probability, the model is also able to estimate error in the predicted value. *Ukhorskiy et al.* [2004] tested this model for the years 1995-2000, and they achieved a PE and LC of 0.77 and 0.89 respectively. *Fok et al.* [2008] developed the physics-based Radiation Belt Environment (RBE) model to study Earth's outer radiation belt and to provide real-time nowcasting of the outer belt electron population. They included realistic electric and magnetic field models, plasma sheet and plasmasphere models, and wave-particle interactions. When the RBE model results were compared to measurements from SAMPEX and LANL-GEO spacecraft, they found a good qualitative agreement between them. The RBE model is currently running online in real-time providing the community with a full radiation belt nowcast. The RBE is one of the most comprehensive outer belt models currently available, yet it is limited in its forecasting ability by a lack of accurate solar wind forecasting capabilities.

Lyatsky and Khazanov [2008a] introduced another forecast model, which forecasts the cube root of daily averaged, >2 MeV electron flux at GEO. Their method uses two source and loss equations, one for low energy electrons representing the "seed" population to be accelerated, and the other representing relativistic electrons. The source term for the low energy electrons is proportional to a solar wind coupling function, and the source term for the relativistic electrons is only proportional to the low energy electron flux from the first equation. The loss terms for both equations are only proportional to the low and high electron flux respectively, and the proportionality constants are solved by fitting to the data. The only inputs to the model are the solar wind parameters needed to solve the coupling function. With this model run for four years, 2004-2007, the LC of the results to the actual data is 0.90 (the forecast PE is not published). This model assumes no particular acceleration method but only recognizes that the solar wind is the ultimate driver of relativistic electron flux variations.

Perry et al. [2010] conducted a comparative study of three different outer belt forecasts:

NOAA's REFM, *Li* [2004], and the Air Force's FluxPred model. FluxPred is a neural network model using 17 inputs consisting of the past 10 days of GEO flux data and 7 days of Kp. The output of the neural network were 24-, 48-, and 72-hour forecasts of >2 MeV, daily averaged flux at GEO. They found that all three models performed comparably, with some performing better than others at different points in the solar cycle. Like *Turner and Li* [2008a], they note a solar cycle dependence on the models' performance, with improved results around solar minimum and poorer results around solar maximum.

Note that for most of these models, only the daily averaged flux at GEO is forecast. This does not capture the true range of fluxes seen around GEO, and more importantly for an energetic particle forecast, it does not reveal the maximum flux encountered by spacecraft in GEO throughout a day. Due to the asymmetry of Earth's magnetosphere, with its compressed dayside and stretched nightside, energetic electrons trapped in this field drift around the system along asymmetric paths; the energetic particles drift farther from the Earth on the dayside portion of their drift orbit and closer to the Earth on the nightside portion. Figure 7.5 is a cartoon demonstrating this for two electron drift paths that intercept GEO at noon and midnight. From Figure 7.5, note that the drift path (blue dash-dot lines) that intercepts GEO (black dashed line) at noon local time (LT) lies inside of GEO and thus closer to the heart of the outer radiation belt than the drift path that intercepts GEO at midnight LT. Thus, a spacecraft measuring electron flux should measure higher fluxes near local noon than it measures near local midnight. This is confirmed by the results shown in Figure 7.6, which shows GOES >2 MeV electron fluxes averaged by local hour around GEO from 1995-2009. The flux distribution in local time peaks near noon (between 1100 and 1200 LT) and sees its minimum near midnight (between 2300 and 0000 LT). The average value of this flux distribution, which is synonymous with the daily average value, is shown with the horizontal dashed line in Figure 7.6, and from this it is clear that the daily average can be significantly less than the maximum flux encountered around GEO.

Since many of the existing forecasts rely on solar wind measurements, being able to accurately forecast solar wind parameters is important if one wishes to extend the relativistic electron forecasts

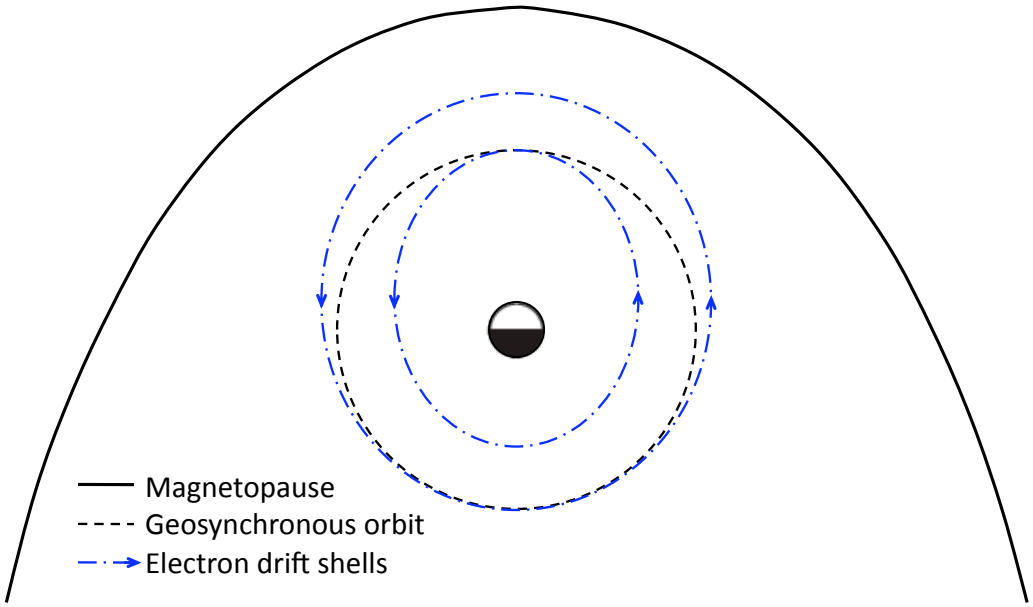

Figure 7.5: Cartoon depicting asymmetric electron drift shells intersecting GEO at noon and midnight. Drift shells are shown with the blue dash-dot lines, while GEO is shown with the black dashed line. Note that this is a cartoon, and the drift shells' asymmetry has been exaggerated for conceptual clarity.

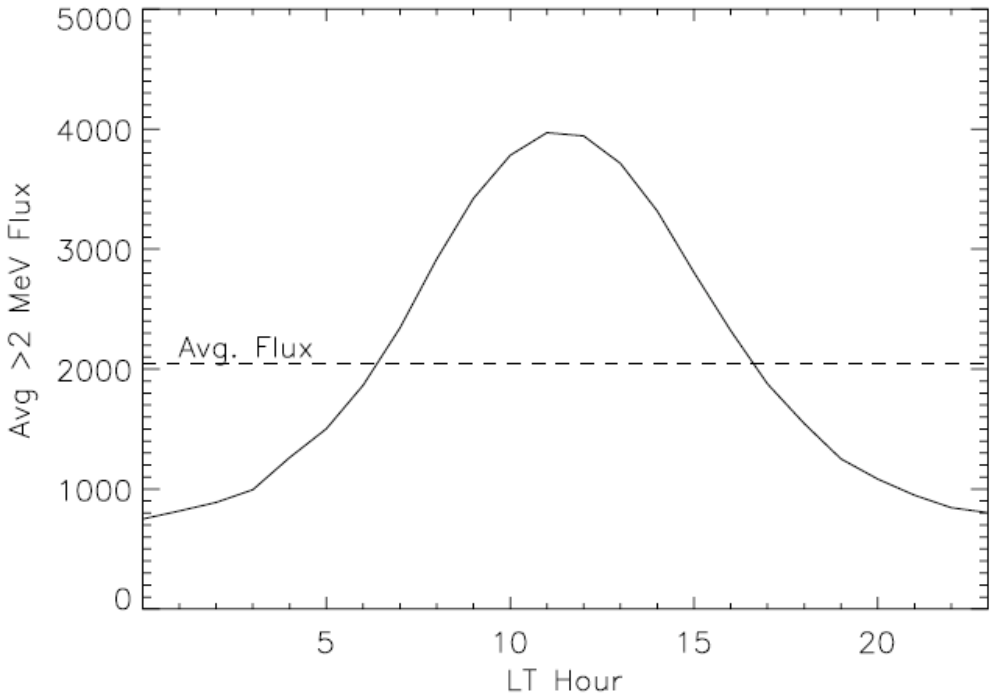

Figure 7.6: GOES >2 MeV electron fluxes combined and averaged by local hour for 1995-2009. The total average value of this data set is displayed with the horizontal dashed line marked "Avg. Flux".

forward in time (i.e. to forecast several days more into the future than the models were originally designed to do). *Fry et al.* [2004, 2007] discussed the HAFv.2 model, which forecasts solar wind parameters, and according to [*Fry et al.*, 2007, p. 114], "should serve as a baseline metric for future operational solar wind models to meet or beat." Another solar wind forecast is the Wang-Sheeley-Arge model (see details at NOAA's website, <http://www.swpc.noaa.gov/ws/index.html>); this model is used by NOAA-SWPC to forecast solar wind velocity and IMF polarity for one to seven days in advance. The *Baker et al.* [1990] forecast used by NOAA employs the Wang-Sheeley-Arge model to extend its forecast time. In addition to extending forecast times, solar wind forecasts can also be useful for other applications, like employing statistical asynchronous regression to determine the flux distribution at different local times around GEO.

7.3.2.3 Statistical Asynchronous Regression

Statistical asynchronous regression (SAR) is, as its name implies, a statistical technique, which specifies a relationship between two quantities, both of which vary in time, that are not simultaneously measured. This technique is described in detail with several examples provided in *O'Brien et al.* [2001], and here we will only provide a brief introduction. SAR provides a mapping function to determine one variable given a measurement of the other. Thus, it can be used to determine the electron fluxes at different local times around GEO given a flux measurement at one local time. For this application, SAR uses complementary cumulative distribution functions (CCDFs) compiled from measurements during specific input conditions (e.g. electron flux at a given local time for a corresponding Kp index or solar wind velocity range). Figure 7.7 graphically demonstrates the implementation of this technique given two CCDFs, *F(X)* at dawn and *G(Y)* at noon. With a measurement of X at dawn, one can find the CCDF value, ~0.07 in this example, from *F(X)*, and the CCDF value for noon will be the same due to a fundamental principle of statistics that states that probability is conserved under a change of variables. This CCDF value can then be used for *G(Y)* to find the approximate value of Y at noon based on the empirically developed statistics. So with a library of these CCDFs compiled for electron fluxes at each local

time given specific input conditions, it is possible to use a flux measurement from one local time to determine an accurate value of the flux at any other local time.

SAR was first introduced to the radiation belt community by *O'Brien et al.* [2001], in which GOES 8 flux measurements near dawn were mapped to local noon using SAR with CCDFs generated for each local hour around GEO using the Kp index. Their results, when compared to actual corresponding electron flux measurements at GEO noon, revealed that the SAR technique is valid for this application and could accurately map fluxes from one local time to another. *Burin des Roziers and Li* [2006] used SAR to map electron measurements made by GOES 10 to other local times around GEO, using LANL flux measurements to check their results. They used solar wind velocity as the training condition to develop their CCDFs. When compared to the LANL flux measurements at all 24 local time hours around GEO, their results yield PEs ranging from ~0.68 to 0.85, with the lowest PE at midnight and the highest near dawn and dusk.

7.3.2.4 Overview

In this paper, we first introduce the data and baseline models used for this study. We then begin discussions of the various additions that have been made to these baseline models including adding the solar wind number density and an internal source to the *Li* [2004] model, updating the *Turner and Li* [2008a] model to be able to run in real-time, and investigating the use of SAR with forecast models to be able to forecast at a local hour resolution around GEO. Following these investigation descriptions, we discuss the results of these additions and their implications for radiation belt forecasting and provide the model parameters necessary to implement the improvements to the baseline models. We conclude with 1) a discussion on how these improvements have been implemented to models running in real-time with their results posted online for the benefit of the community and 2) some thoughts on how outer belt forecasts can be extended beyond GEO.

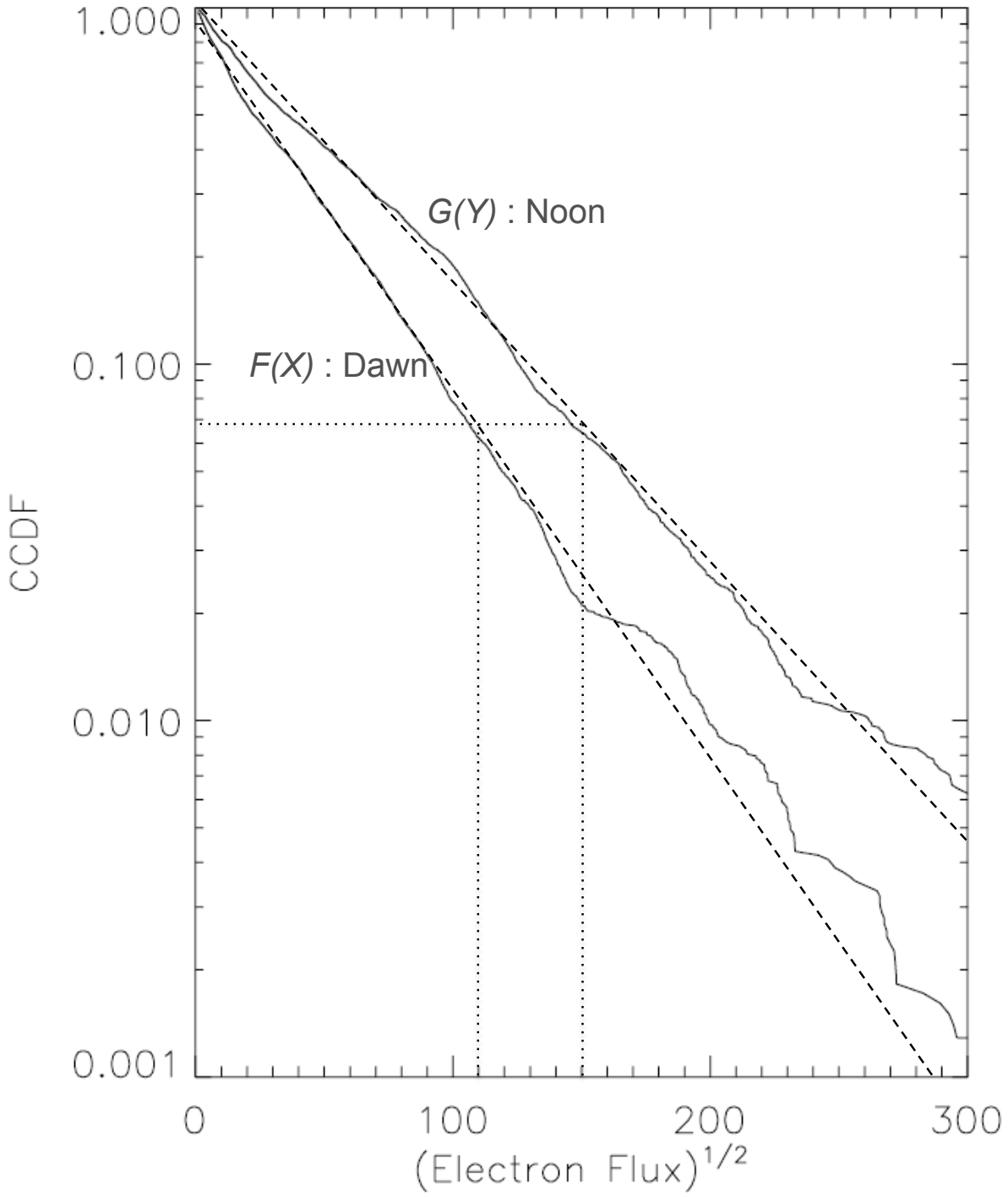

Figure 7.7: Example of SAR mapping using complementary cumulative distribution functions (CCDFs). The CCDFs here are compiled from GOES >2 MeV electron fluxes from 1995-2009 during solar wind conditions when 500 km/s $\leq V_x <$ 600 km/s.

7.3.3 Data and Baseline Models

For this study, we use integral electron fluxes from the >2 MeV channels of the Energetic Particle Sensors (EPS) from the GOES spacecraft in GEO [For EPS details, see *Onsager and et al.*, 1996]. For our data set, these fluxes are daily averaged from all available GOES spacecraft to get a total average value around GEO as well as 24 values for the daily average from each local hour around GEO. The data set covers 1 Dec. 1995 - 31 Dec. 2009, and is used for both input and validation of the two baseline models used in this study, the *Li* [2004] and *Turner and Li* [2008a] forecast models. These baseline models serve as the testing platforms for investigating the various additions to the electron forecasts discussed in this paper. For the *Li* [2004] forecast, we adjust only the diffusion multiplier parameters, the loss term, and the seasonal and solar cycle terms in addition to the potential improvement terms discussed below. The solar wind data set required by this model is a combination of WIND and ACE data. For the *Turner and Li* [2008a] model, we employ the same forms for source and loss as the original model, i.e. using low and high energy electron fluxes, and simply update the input data set to use daily averaged GOES >600 keV and >2 MeV fluxes since these are available in real-time. The various new additions to both baseline models are introduced in the following section.

7.3.4 Investigating Additions to the Baseline Models

7.3.4.1 Including Solar Wind Density

Based on the results of *Lyatsky and Khazanov* [2008b, c], we have investigated the potential improvements of including n_{sw} in the *Li* [2004] model, which previously did not include solar wind density. Since *Lyatsky and Khazanov* [2008b] found that n_{sw} is inversely related to enhancements in electron flux, we have modified the diffusion multiplier from *Li* [2004] as follows:

$$D_0 = C\left(\frac{v}{v_0}\right)^{\gamma_1}\left[1+\left(\frac{(v_xB_z+|v_xB_z|)}{\alpha}\right)^2\right]^{\gamma_2}\left[\left(\frac{\Delta v^2}{\Delta t}\right)^2\beta^{-1}\right]^{\gamma_3}\left(\frac{\varepsilon}{n_{sw}}\right)^{\gamma_4} \tag{7.5}$$

where D_0 is the diffusion multiplier term that regulates the rate of radial diffusion in the *Li* [2004] model, v is the solar wind velocity with v_0 its long-term average and v_x its GSE X-component, B_z

is the GSE Z-component of the IMF, α and β are the long-term average values of the terms in their respective numerators, n_{sw} is the solar wind number density with ε its long-term average, and C, γ_1, γ_2, γ_3, and γ_4 are adjustable parameters. In Equation 7.5, everything until the last term (in parentheses raised to the power of γ_4) is the same as in the original *Li* [2004] model, and the last term is the new term incorporating n_{sw}.

Following *Li* [2004], we tuned the model parameters to optimize PE using GEO electron flux data from 1995-1996. We also investigated two different ways of applying this new term. The first is unconditional, where the term was applied for all model run times, while the second takes the results of *Lyatsky and Khazanov* [2008c] into account and applies conditions to the application of the n_{sw} term in Equation 7.5 based on previous days geomagnetic activity and density magnitudes. With this conditional case, the density term is included in the diffusion term only when there was low density and high geomagnetic activity for the previous two days. We investigated using both AL (since it can be predicted in real time [*Li et al.*, 2007], which makes it ideal for a real-time forecast model) and Kp indices to determine geomagnetic activity and adjusted the condition limits for both density and geomagnetic activity. However, neither of these methods, conditional or unconditional, resulted in an improvement to the PE of the model for 1995-1996. For this time period, the training reveals that the PE is highest when γ_4 is zero, rendering the term unchanging regardless of the value of n_{sw}. We discuss the reason why this term seemingly doesn't help the forecast in the Discussion of Results section.

7.3.4.2 Including an Internal Source

Given the results of recent studies that indicate the importance of internal acceleration as a source for relativistic electrons [e.g. *Shprits et al.*, 2007a; *Koller et al.*, 2007; *Chen et al.*, 2007b; *Turner et al.*, 2010b], we have investigated adding an internal source term to the *Li* [2004] model. To implement this source, we looked at different forms for S in Equation 7.1 as well as different

PSD distributions. The first form for S that we investigated was:

$$S = \begin{cases} S_0 \times 10^{S_1 \ AL^*} & : \quad L^*_{pp} < L^* < L^*_{pp} + \Delta L^* \\ 0 & : \quad \text{elsewhere} \end{cases} \tag{7.6}$$

where S_0 adjusts the source amplitude, AL^* is the maximum of the absolute value of the AL index from the previous three hours, S_1 adjusts the level of influence of the AL^* index, L^*_{pp} is the plasmapause location in L^*, and $\Delta\ L^*$ defines a finite heating region. Here, S_0, S_1, and $\Delta\ L^*$ are adjustable parameters, and we approximate L^*_{pp} using the Dst-dependent empirical model of *O'Brien and Moldwin* [2003]. This form is based on the source term used by *Tu et al.* [2008] and relies on the correlation between chorus and magnetosonic wave amplitudes with the AE index [*Shprits et al.*, 2007b; *Meredith et al.*, 2008]. Since AE is not available in real-time, the AL index is employed instead since this index is highly correlated with the AE index and can be forecast in real-time based on solar wind measurements [*Li et al.*, 2007].

The red dashed line in Figure 7.8 shows the effect of this source added into the radial PSD distribution used by the *Li* [2004] model. As can be seen, the source form from Equation 7.6 creates a discontinuous PSD distribution. To make a more realistic form, we next investigated replacing this discontinuous function with a continuous one by adding S in the form of a gaussian. For this second source form, the gaussian amplitude and width are adjustable model parameters, and its center location in L^* is based on the empirical plasmapause location and the width of the heating region (i.e. halfway between L^*_{pp} and $L^*_{pp} + \Delta L^*$. The effect of this source on the PSD distribution is shown with the green line in Figure 7.8, and this form resulted in the highest PE when compared with the first form and the model without source for the years 2007-2008.

These two forms, however, do not account for observations [e.g. *Chen et al.*, 2007b; *Turner et al.*, 2010b] and model results [e.g. *Koller et al.*, 2007; *Shprits et al.*, 2007a] that indicate that the PSD radial gradient beyond GEO is most often negative, i.e. decreasing with increasing L^*. Thus, we have changed the PSD distribution used by the *Li* [2004] model, as is seen in the blue curve in Figure 7.8. This distribution is based primarily on results of *Koller et al.* [2007], and its functional

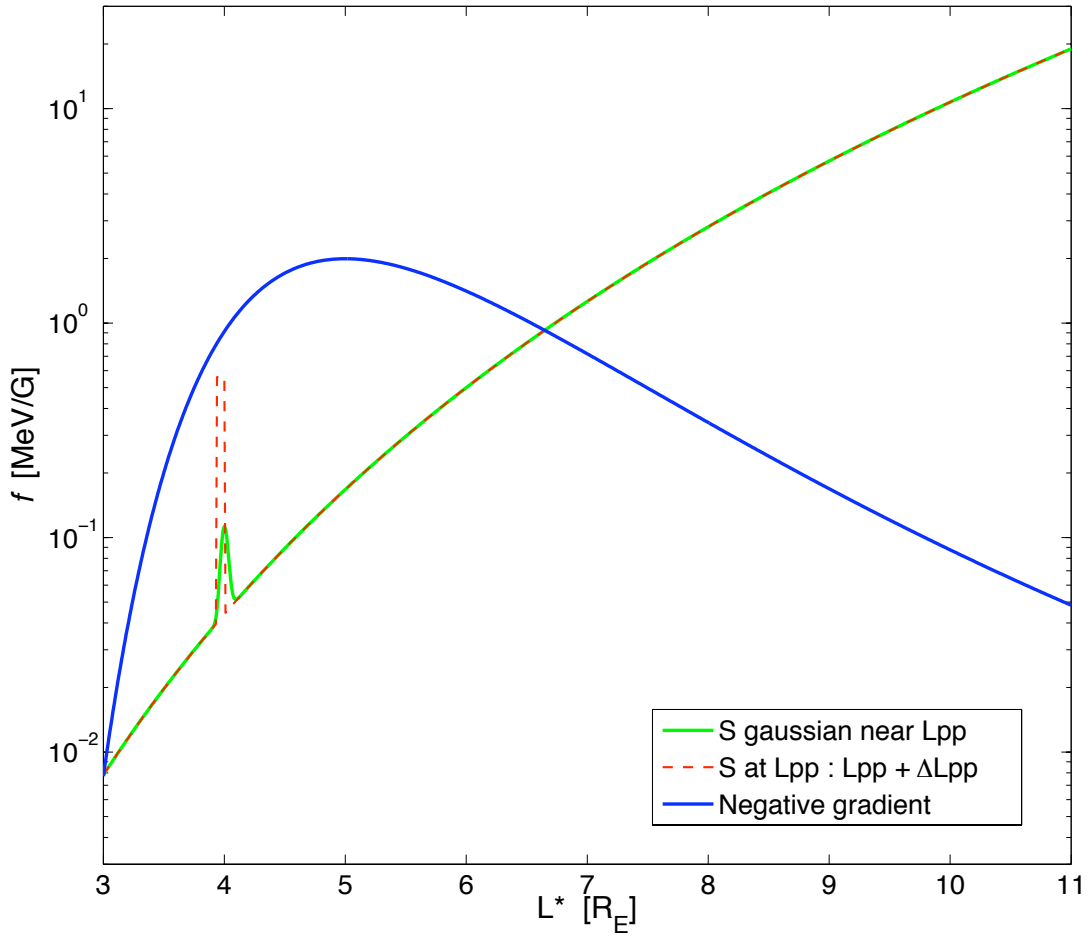

Figure 7.8: Different PSD distributions used to simulate an internal source of relativistic electrons. Each of these distributions was used to investigate the benefit of incorporating internal source into the *Li* [2004] forecast model. The green and red-dashed curves represent sources added onto the original distribution used by *Li* [2004], while the blue curve represents a distribution with a central peak and negative gradient beyond GEO.

form is:

$$f(L^*) = \frac{1}{\sqrt{2\pi\sigma^2}} e^{\frac{-(L^* - L_s^*)^2}{2\sigma^2 (L^*)^2}} \tag{7.7}$$

where $f(L^*)$ is the PSD distribution in invariant L^*, σ controls the width of the distribution, and L_s^* is the peak location. These last two terms are set to 0.2 and 5.0 respectively for Figure 7.8, which generates a distribution that agrees well with the non-stormtime PSD distributions from *Koller et al.* [2007]. Though this distribution is likely more realistic for the majority of times in the outer radiation belt, using it with the *Li* [2004] model does not improve the forecast performance. We discuss the reason for this and more on the results from the forecast with internal source in the Discussion of Results section.

7.3.4.3 Low-E Model in Real-Time

The *Turner and Li* [2008a] forecast model (referred to in that work as the "low-E model") was developed using differential flux measurements from LANL spacecraft in GEO. However, the LANL data set is not available in real-time, so the model must be adapted to be useful as a real-time forecast tool. To do this, we have investigated using GOES >600 keV flux measurements to forecast >2 MeV fluxes at GEO, since GOES flux data is available in real-time. *Li et al.* [2005] and *Turner and Li* [2008a] showed that there is a time delay between similar features in the daily average fluxes of lower energy (i.e. ~10's keV) and higher energy (i.e. >1 MeV) electron fluxes measured by LANL spacecraft in GEO; that is, changes in the low-energy electron population are followed at a later time by similar changes in the high-energy electron population. When daily averaged GOES electron fluxes from the >600 keV and >2 MeV integral channels are compared, this cross-correlation also exists. Thus, based on the work of *Turner and Li* [2008a], it should be possible to use today's >600 keV GOES flux to forecast tomorrow's >2 MeV flux.

We have re-trained the *Turner and Li* [2008a] model parameters to maximize PE for 2008-2009 using only daily averaged GOES >600 keV and >2 MeV fluxes. This adaptation to the model proves effective by consistently outperforming a simple persistence model. The results from this new form of the *Turner and Li* [2008a] forecast model are discussed and compared to the other

models in the Discussion of Results section.

7.3.4.4 Local Time Resolution

SAR can be applied to improve the resolution of forecast model results so that electron fluxes can be forecast at each local hour around GEO. To implement this, we employ the method of *Burin des Roziers and Li* [2006], which used solar wind velocity to determine electron flux CCDFs for different local times around GEO. We have developed the CCDFs from an extensive set of GOES flux data and solar wind velocities from 1995-2009. CCDFs were compiled using solar wind velocity bin widths of 100 km/s and a range from 200 km/s to 900 km/s. If in the unusual occurrence the solar wind velocity is outside of this range, the highest or lowest bin is used (depending on if the velocity was greater than 900 km/s or less than 200 km/s). For the 1995-2009 data set, this produces CCDFs with sufficient statistics; for example, the CCDFs shown in Figure 7.7 each consist of ∼9000 data points.

To apply SAR, we needed to determine which local time is best to forecast to (i.e. to use as "tomorrow's observation" at a particular local time). We compared the results of the *Li* [2004] forecast model to GOES fluxes daily averaged by local hour around GEO. Figure 7.9 shows the results of this study. The PEs of the forecast for different local hours exhibit a double-peaked characteristic, with local maxima at ∼07:00 and ∼16:00 LT. However, taking the local time flux distribution shown in Figure 7.6 into account, this makes sense considering that the daily average flux is closest to the average flux values at ∼06:30 and ∼16:30 LT (i.e. where the dashed, average flux line intersects the flux distribution curve). When this curve is examined for model runs over different time periods, the PE peak at 16:00 LT is consistently the global maximum value, so we use this local hour as the best local time for "tomorrow's observation" for SAR mapping.

We have re-trained the *Li* [2004] forecast model to maximize PE when the forecasted flux is compared with the daily average flux at 16:00 LT at GEO. We use the years 1995-1996 for this since these are the years originally used for the *Li* [2004] model, and this allows for a direct comparison between the SAR results with the original parameters and those with the re-trained parameters for

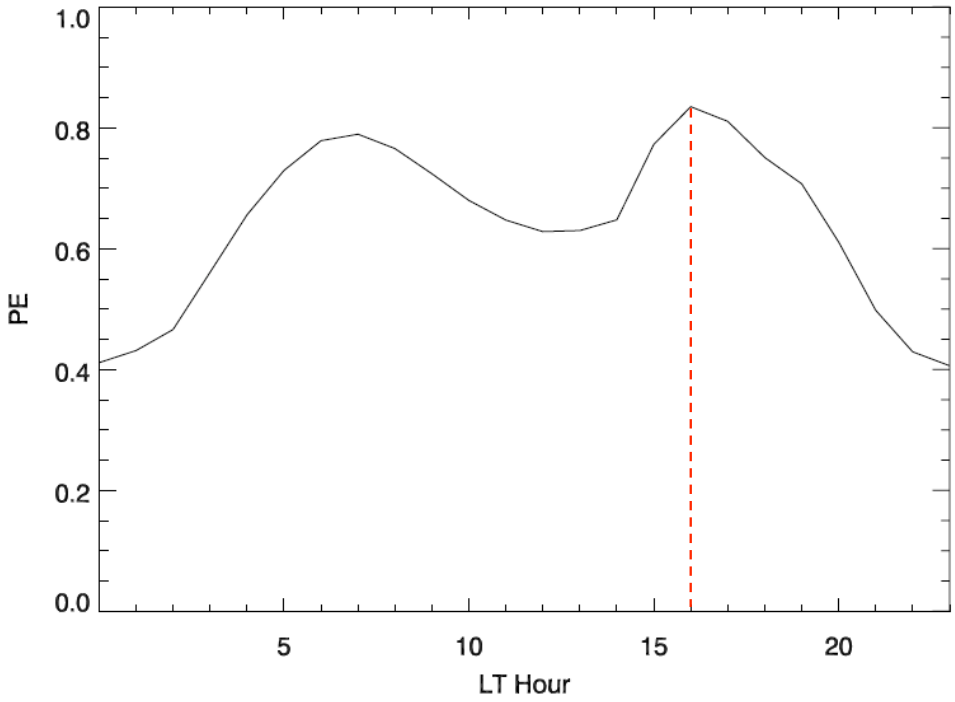

Figure 7.9: Prediction efficiencies when the *Li* [2004] model's daily average results are compared with GOES >2 MeV electron fluxes daily averaged by local hour around GEO.

1600 LT average fluxes. As expected, the technique works better using the parameters tuned for 1600 LT. This provides the flux measurement at one local time required for implementing the SAR technique. However, "tomorrow's" solar wind velocity is also required, so a solar wind forecast must be included. We have investigated the effect of the Wang-Sheeley-Arge model compared to simple persistence when used for "tomorrow's" solar wind velocity for the SAR technique. We find that for this application, the forecast PEs for electron flux are consistently better when simple persistence is used to forecast the solar wind velocity.

7.3.5 Discussion of Results

Three of the four model additions we have investigated have proven to be beneficial to their respective baseline models. Adding a source term to the PSD distribution in the form of a gaussian in the *Li* [2004] forecast model results in PEs that are higher than the model without source. Adapting the *Turner and Li* [2008a] model to run with GOES electron fluxes allows the model to be run in real time, and SAR proves to be effective for forecasting electron fluxes at a local hour resolution around GEO to account for variations in the fluxes encountered throughout a day. However, adding a solar wind number density term to the diffusion multiplier in the *Li* [2004] model does not improve the model's PE. This is probably because of the underlying meaning of the correlation between n_{sw} and relativistic electron fluxes at GEO. The correlation between the two parameters is negative and most likely related to magnetopause shadowing. This is discussed in *Lyatsky and Khazanov* [2008b]. Considering this, the *Li* [2004] forecast model already has a magnetopause shadowing term incorporated to account for loss to the magnetopause due to changes in solar wind dynamic pressure, which is highly correlated to n_{sw}. Thus, adding a n_{sw} term into the diffusion multiplier probably did not help the model PE because the underlying effect of this term was already included in the model.

A source term, which represents internal heating mechanisms like wave-particle interactions, improves the PE of the *Li* [2004] model. It is added to the PSD distribution in the form of a gaussian to maintain a continuous distribution, and its amplitude is a function of the AL index,

which can be forecast in real-time and is very well correlated to the AE index that is an indicator of potential electron acceleration by wave-particle interactions [i.e. *Meredith et al.*, 2001, 2008]. When a PSD distribution with an internal peak and a negative gradient beyond GEO is included, it does not perform well. Upon close examination of the behavior of this model, the PSD distribution rapidly changes due to diffusion, with the PSD in the central peak quickly being lost from the system by transport into the sinks at the inner and outer boundaries. Thus, the poor results of this form of the model are likely because of insufficient source and loss terms to compensate for the rapid diffusion of the central peak.

To compare the results of these models with each other, it is necessary to define a relative scale to do so since PE can vary significantly when different data sets are used. For example, using the full GOES data set with the *Li* [2004] forecast for 1995-1996, the forecast PE for the model data set when gaps are accounted for is 0.882 with a persistence PE of 0.841, but when the exact same data sets are used with only the first ten days excluded from the PE calculation, the forecast PE is 0.918 with a persistence PE of 0.844. So, for comparing results from different forecast models, which potentially have different data gaps due to different input data sets, a more impartial method should be employed. For this reason, we introduce a simple forecast score (FS):

$$FS = \frac{PE_{Model}}{PE_{Persist.}} \tag{7.8}$$

where PE_{Model} is the PE of the forecast model and $PE_{Persist.}$ its corresponding PE from the simple persistence model from the same data set. Thus, the forecast model's PE is normalized by its corresponding persistence model so that the forecast score is a measure of how well the forecast model performs compared to simple persistence. Thus, a FS of >1 means the forecast performed better than simple persistence, while a FS of 1 or less means the forecast performed the same or worse than simple persistence. Figure 7.10 shows the forecast scores of the three models from this work that showed an improvement over their baseline versions. Each model was run for one year periods from 1998-2009. The black dashed line at FS = 1 marks the persistence model level, which is the "score to beat" for each model. Note that all three models consistently outperform the simple

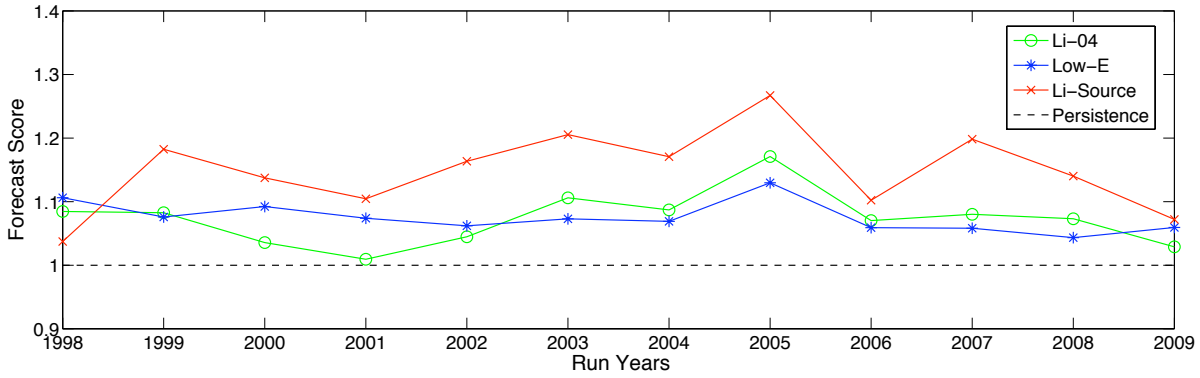

Figure 7.10: Comparison of forecast scores from three different models: the updated *Turner and Li* [2008a] (Low-E), the original *Li* [2004] (Li-04), and the *Li* [2004] with source (Li-source) forecasts. For ease of comparison, simple persistence is also displayed with the dashed black line at FS = 1.

persistence; their FSs are >1 for all comparison years. The *Li* [2004] forecast including an internal source is the highest performing of the models, with an average forecast score of 1.15. Interestingly, this model outperforms the other two for every year it is run except 1998. The *Li* [2004] model results shown here are using the model parameters trained for 1600 LT (from use with SAR), and its average forecast score is 1.07. The *Turner and Li* [2008a] results (low-E) are using the model parameters trained for 2008-2009. Its average forecast score is 1.08, and it is interesting to note that overall it performs better than the *Li* [2004] model during several of the more solar active years (i.e. 2000-2002) but worse during most of the more quiet years. This is consistent with the original results of *Turner and Li* [2008a].

The optimized model parameters used for the results shown in Figure 7.10 are: 1) for the *Li* [2004] model with source term (i.e. Eq. 7.6): C = 0.017, γ_1 = 2.530, γ_2 = 0.330, γ_3 = -0.068, τ = 2.660 (days), F_{sol} = -0.085, F_{sea} = 0.320, E_{sol} = -0.770, E_{sol} = -0.020 (the last four terms are the solar and seasonal cycle terms), $S_0 = 1.197 \times 10^{-5}$, $S_1 = 2.050 \times 10^{-3}$, and $\Delta L^* = 3.510$; and 2) for the *Turner and Li* [2008a] model updated for GOES data: $C_1 = 1.050 \times 10^{-3}$, $C_2 = 2.863$, $C_3 = 1.700 \times 10^{-2}$, $C_4 = 0.126$, $t_0 = 0$ (hours), $b = 1.773 \times 10^{-1}$, and $f = 0.146$. Note, the forms of the equations and the parameter names for the updated *Turner and Li* [2008a] forecast model are

the same as those used in that reference. With these parameters, the new source model achieves +1 and +2 day PEs of 0.90 and 0.63 for 2007-2008, and the *Turner and Li* [2008a] model achieves +1 and +2 day PEs of 0.82 and 0.44 for the same period.

Finally, statistical asynchronous regression, SAR, has been used to demonstrate its capability for forecasting relativistic electron fluxes for each local hour around GEO. This is an improvement in that it can capture the local time dependency of the electron fluxes due to the asymmetry of the magnetosphere. Figure 7.11 shows the results of this technique applied to the *Li* [2004] model. Here, different local hour forecasts (dashed lines with □ symbols) are shown compared to their respective local hour average measurements (solid lines with × symbols) in different colors for the entire year of 2009. The results for 1200, 0800, and 0000 LTs have been offset for clarity. Note that the forecast performs best at 1600 LT, which corresponds best to the total daily average and is the local hour used to train the model parameters. The results shown in Figure 7.11 use simple persistence to estimate "tomorrow's" solar wind velocity, and as can be seen, SAR can accurately estimate the flux distribution around GEO for most times. The SAR mapping performs poorly when the fluxes are low, which was quite frequent during 2009 due to the very quiet Sun. During times of low flux, SAR overestimates the flux near noon and underestimates it near midnight; this poor performance is due to poor statistics at such low flux levels, which occurred primarily during periods of particularly slow solar wind. However, the performance when the fluxes are high is not affected in this way, and it is during these times that the forecast accuracy is most critical since high flux levels can be potentially fatal to on-orbit spacecraft. SAR can easily be applied to any forecast model in the way we have demonstrated here so that a forecaster can accurately estimate the future flux distribution around GEO.

By combining the various models and techniques described in this paper, an improved system of forecasts has been developed. This system, maintained at the University of Colorado's Laboratory for Atmospheric and Space Physics (LASP), consists of the three primary forecast models (i.e. the *Li* [2004] model with and without an internal source term and the adapted *Turner and Li* [2008a] model), a combination forecast similar to that discussed in *Turner and Li* [2008a], and the SAR tool

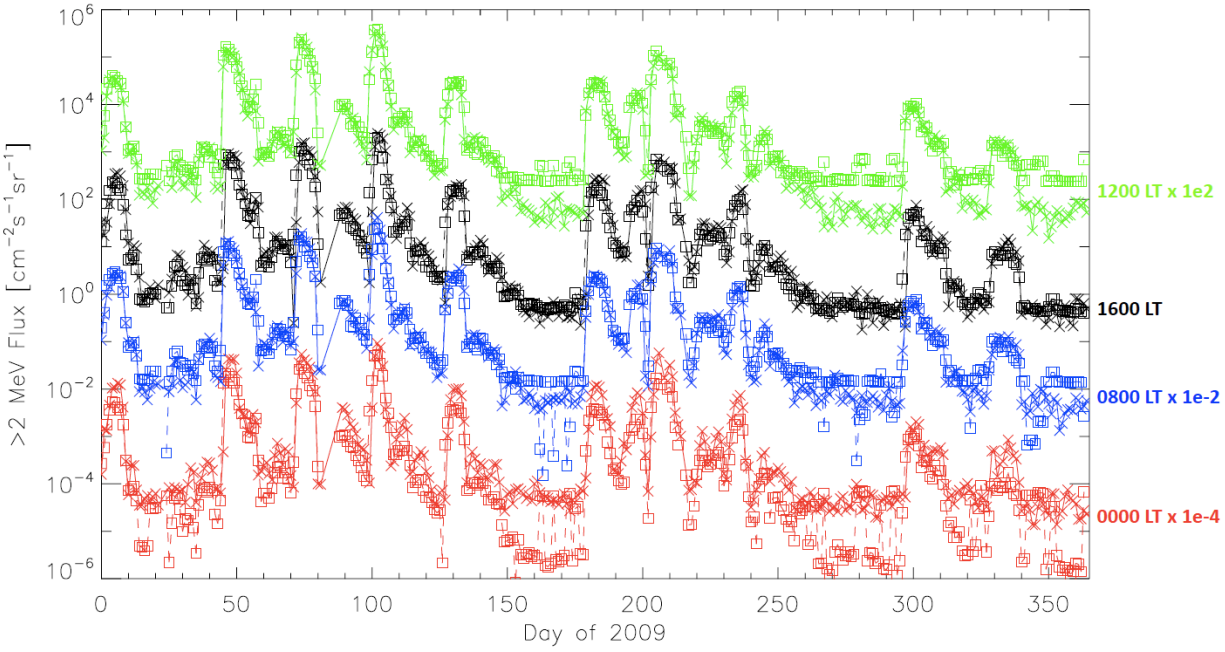

Figure 7.11: Results of the *Li* [2004] forecast when SAR is applied for 2009. '×' symbols connected by solid lines mark the actual measured fluxes, while '□' symbols connected by dashed lines mark the forecasted values. Different local hours (0000, 0800, 1200, and 1600 LT) are displayed in different colors. Note that the results for all local hours shown except for 1600 LT are offset by the amounts displayed in their respective labels to the right of the plot.

to provide a forecast of relativistic fluxes at all 24 hours around GEO, essentially covering a small range of L-shells in the outer belt around GEO. Also, this system incorporates a model that is not single-point dependent (i.e. on a solar wind measurement from ACE), which provides versatility for times when solar wind data is not available in real-time. In the next, and final, section, we discuss how this new system has been implemented to provide these forecasts in real-time online and provide some thoughts on how our relativistic electron forecasting capabilities can be extended to cover the full extent of Earth's outer radiation belt.

7.3.6 Conclusion

7.3.6.1 Implementing the New Forecast System

Using current GOES and ACE data, the real-time forecast results from the new *Li* [2004] model with source and the updated *Turner and Li* [2008a] model are available online at *http* : *//lasp.colorado.edu/space_weather/xlf3/xlf3.html*. Additionally, a combination forecast consisting of a weighted summation of the results from each of the three primary models (i.e. the *Li* [2004] with and without source and *Turner and Li* [2008a] models) is also included. Equation 7.9 shows the form of this combination:

$$J_{combo} = W_1 J_{Low-E} + W_2 J_{Li-04} + W_3 J_{Li-Source}, \text{ where: } W_1 + W_2 + W_3 = 1 \tag{7.9}$$

where W_i's are the weighting factors for the respective models. This combination model compares all the weighted combinations (with a weighting resolution of 0.01) of the three input model results and determines the combination with the maximum PE based on the previous 30 days of data. As can be seen from the operational results online, this ensemble of models most often outperforms the individual input models. Also available are the results from each of the forecasts mapped to other local hours around GEO using SAR with the current day's solar wind velocity. Thus, this new, online forecast system is operational and running in real-time to provide a range of forecast values for all 24 local hours around GEO. The up-to-date performance of each of the models (PE and FS) are also provided there. This system ultimately provides the spaceflight community with a

real-time warning source for when relativistic electron flux at GEO may reach potentially hazardous levels as well as a comparison and verification for other radiation belt forecasts.

7.3.6.2 Future Work: Extending Forecasts' Temporal and Spatial Ranges

Most forecast models are limited in their temporal range based on the highly dynamic nature of their various input parameters. For example, many of the forecast models discussed in the introduction rely on solar wind parameters, but current solar wind models can be limited and inaccurate (e.g. the comparison between the WSA model and simple persistence for the SAR technique described in this work). However, we have investigated extending the *Li* [2004] forecast to up to +6 days using solar wind measurements from the STEREO-B spacecraft, which is ahead of Earth in the Parker spiral. In *Turner and Li* [2010], we show that this application can be used to extend forecast times for solar wind based models to multiple days (at least +6), while consistently outperforming simple persistence.

As stated in the introduction, all of the existing forecasts discussed in detail here only provide models for relativistic electrons at GEO, yet the outer belt encompasses a much larger region of space than just near GEO. To extend forecasting capabilities to the rest of the outer belt, there are two methods that may be particularly useful as alternatives to the physics-based approach of *Fok et al.* [2008]. First, SAR can be used with a set of CCDFs trained to map electron fluxes from one L-shell to a variety of other L-shells given sufficient statistics of fluxes at different L-shells throughout the outer belt during different solar wind or geomagnetic conditions. Some potentially useful datasets for this application may be CRRES, LANL-GEO, GPS, Polar, GOES, and NASA's Radiation Belt Storm Probes, when it becomes available in 2012. Second, data assimilation techniques can be employed to extend forecast capabilities. Kalman filters with parameter estimation [e.g. *Kondrashov et al.*, 2007; *Koller et al.*, 2007] use a numerical algorithm (i.e. a Kalman filter) to produce model results that fit a set of system observations in such a way that the error between the observations and their corresponding model data points is minimized. Such a tool can be coupled with a forecast model to use the most up-to-date observational data (i.e. a real-time data sets of

electron fluxes) to adjust the parameters in a system model (e.g. a radial diffusion model of the outer radiation belt) to best fit the most current observations. This updated system model can then be run forward in time to establish a full system forecast for future times.

7.4 Conclusions

In this chapter, I've discussed several improvements to our forecasting capabilities at GEO. Extending forecast times using ST-B data proved very effective for out to +6 days. Theoretically, as ST-B continues to drift away from Earth, this can continue to be extended, but I expect that the PEs will also degrade as the cross-correlation decreases with the increasing distance and corresponding time offset. However, I have shown that simply offsetting the ST-B data is much more effective as a solar wind speed forecast than the popular Wang-Sheeley-Arge forecast. I believe a mission dedicated to putting a solar wind monitor at the L5 point would prove very beneficial to both our space weather capabilities as well as our physical understanding of solar and solar wind dynamics. Analogous to multi-point measurements in the radiation belt, with more measurements in the solar wind, we should be able to develop a better picture of the system overall.

Concerning the improved forecast system, I have developed a new model that includes an internal source term in the *Li* [2004] forecast model. This source term is a function of the AL index and is activated outside the plasmapause to simulate the effect of local acceleration. It is interesting to note that this source model most often outperforms the other two models. Using the three models (i.e. *Li* [2004], *Turner and Li* [2008a], and the new source model), a combination model consisting of a weighted average of the three input models can be used. This model consistently outperforms the three input models and is discussed further in Appendix D. Finally, I have shown how SAR can be employed to improve the local time resolution of forecasts to account for the range of fluxes encountered around GEO. I have investigated using different solar wind quantities to train the CCDF libraries needed for the SAR technique, and the results of this study are also discussed in Appendix D. These models are being implemented to run in real-time with their results posted online for the benefit of any spaceflight users that are concerned with relativistic electron fluxes

at GEO. In the next, and final, chapter of this work, I discuss how this work can be continued to extend our forecasting capabilities beyond GEO to the rest of the outer belt.

Chapter 8

Conclusion

8.1 Summary and Conclusions

Here, I have covered my work on Earth's outer radiation belt electrons. I have followed the data process from acquisition to analysis and finished with practical use in the form of an improved forecast system. All of this work is focused around outer belt electrons, and there are several recurring key points that I will use to develop the joint conclusions from the different sections of this work. First, multi-point measurements are critical to developing our understanding of the radiation belts and space physics in general. Considering the massive system size and the rates at which the relativistic electron population can vary, in situ measurements from a variety of locations are critical to identifying the underlying acceleration, loss, and transport mechanisms. The CSSWE mission with the REPTile instrument will provide measurements of radiation belt electrons and solar energetic protons from its low-Earth orbit. This data will prove particularly beneficial when included with RBSP data, since REPTile will provide outer belt electron data from the loss cone, which RBSP is unable to resolve. Overall, CSSWE is a prime example of how small, relatively simple and inexpensive space missions can be used to scientifically complement larger, complex and much more expensive missions.

Next, based on the results from the PSD radial gradients study in Chapter 4, electron acceleration via wave-particle interactions within the outer belt itself is most frequently the dominant mechanism for electron energization. Three quarters of the cases examined reveal negative gradients for 2000 MeV/G electrons (i.e. those with energy ~1 MeV at GEO), while nearly that same

amount of cases show positive or relatively flat gradients for 50 MeV/G electrons (i.e. those with energy ~50 keV at GEO). There is regularly a difference between the gradients for electrons with μ less than a couple hundred MeV/G and those with μ greater than this, and the majority of cases examined reveal positive or flat PSD gradients for the lower-μ electrons with negative gradients for the relativistic electrons. This is clear evidence that there are two distinct populations of electrons in the outer belt, each with a different source region at most times. The low-energy population has a source at higher L-shells in the plasma sheet, and these are transported into the belt via radial diffusion, substorm injections, and enhanced convection. These electrons then serve as both the seed population and the generator for the plasma waves responsible for accelerating a portion of the population up to relativistic energies, which result in a peak in PSD somewhere inside of GEO and the primarily negative gradients beyond GEO observed for the high-energy population. Qualitatively, THEMIS-SST observations from near the last closed drift shell are consistent with this picture of two distinct populations, and this is apparently the way the system works most often but definitely not at all times. During periods consisting of several days of very little solar wind and geomagnetic activity, the source of relativistic electrons shifts to L-shells beyond GEO.

This work reveals the importance of substorms and periods of enhanced convection to Earth's relativistic electron population. It is from these events that the seed population and the plasma waves it generates are enhanced. Once again, multi-point measurements are truly necessary to further confirm this, and in 2012 when RBSP and CSSWE are launched, there should exist a near-ideal system of spacecraft to do so. With THEMIS covering the plasma sheet and the L-shells near the outer boundary, the array of spacecraft at GEO (i.e. LANL and GOES), the two RBSP spacecraft as well in their GEO-transfer-like orbits, and SAMPEX and CSSWE covering the horns of the outer belt and the loss cone, we will have excellent coverage of the different regions important to the outer radiation belt. This picture should significantly improve by 2014 as well with the addition of the Russian RESONANCE, Canadian ORBITALS, and Japanese ERG missions.

Finally, I have introduced an improved forecast system for relativistic electrons at GEO. This system includes a technique to extend forecasts out to +6 days, a tool to forecast fluxes at

all 24 local hours around GEO, and several new and improved models, all of which operate in real time. The importance of the seed population is reflected in the *Turner and Li* [2008a] model performance, while the importance of internal acceleration, substorms, and enhanced convection is reflected by the success of the *Li* [2004] forecast model that includes an internal source of electron PSD. In this model, the source amplitude is a function of the AL index, which is an indicator of substorm and enhanced convection activity, and the source is activated in a finite region outside of the plasmapause, which is in agreement with the current theories and observations on where chorus is most prevalent. This forecast model performs the best overall compared to the others in the system. The forecast system represents a comprehensive tool set for forecasting relativistic electrons at GEO, which is useful for spaceflight operations in this popular orbit, however there are several extensions that could allow for forecasting capabilities throughout the entire outer radiation belt.

8.2 Potential Extensions

All of the current forecast models rely on the most up-to-date data available. Data-assimilative techniques, such as the various Kalman filter algorithms, are already being used for radiation belt studies (see Chap. 2), and it is also possible to use a Kalman filter as a forecast tool to use the most current data more effectively. Since the *Li* [2004] model solves the radial diffusion equation for all L between 4 and 11 and with SAR we can solve for this range at each local time, a Kalman filter can be used to automatically tune and update the model parameters based on fitting the model to a variety of real-time data sources in that region (e.g. flux measurements from GOES, THEMIS, and/or RBSP when available) up to the current time ("now"). Then, running the model forward in time with the most up-to-date parameters, forecast values can be used for future "observations" to which the Kalman filter can fit model output. This technique could produce a more accurate and robust 2-D forecast (i.e. L-shell and local time in the equatorial plane) throughout the full range of the outer belt. An extended Kalman filter (EKF), like that used by *Kondrashov et al.* [2007], can be used for parameter estimation in a linear physical model, but if we wish to extend the model

into the nonlinear realm by including the nonlinear model parameters in the state vector, a sigma point filter by *Julier et al.* [1995] can be used. This sigma point filter is proven to be more accurate than the EKF for nonlinear systems in that it does not require linearization of the system and there is no need to calculate Jacobian matrices [*Julier et al.*, 1995]. Also, this sigma point filter has not yet been used for radiation belt reanalysis studies, and it will be of interest to the community to compare the results of this new filter with those of *Shprits et al.* [2007a], who use a basic Kalman filter, *Koller et al.* [2007], who used an ensemble Kalman filter, and *Kondrashov et al.* [2007].

Another way to fill in forecasts for the rest of the L-shells in the outer belt is to employ SAR. CCDF libraries can be developed using CRRES or GPS data from different L-shells during specific solar wind conditions in much the same way that I used GOES data from different local times to develop the CCDF libraries to map from one local time to the other 23 around GEO (see Chap. 7). With such a system trained using solar wind velocities for example, one could take a single flux measurement from one L-shell somewhere in the outer belt, say L$\sim$6 near GEO from an observation or a forecast, and with a concurrent solar wind speed measurement use SAR to map the flux to the other L-shells throughout the belt. This is another, very straightforward way that we can "fill in" the forecast results to other L-shells in the outer belt.

Concerning the PSD gradients study, this can be extended and validated using THEMIS data beyond GEO. SST and ESA data can be used to fit the flux with a power law such that PSD for fixed μ can be calculated as in Chapter 4. Then, taking advantage of the THEMIS orbits, it is straightforward to examine the near equatorial PSD radial gradients beyond GEO and into the tail. Since such a study would only involve relative changes in the PSD for fixed μ as measured by individual spacecraft, the problems with the SST magnitudes (i.e. those discussed in Chapters 2 and 5) would not be an issue. It would be interesting to compare statistics from such a study for a range of μ from THEMIS when the spacecraft are on the nightside, and thus going towards or into the plasmasheet, with those from the study discussed here.

8.3 Future Work

Some future work that I am looking forward to will involve comparing the PSD gradients from our study to those from the reanalyzed data produced using UCLA's Kalman filter and model toolset [see: *Shprits et al.*, 2007a; *Kondrashov et al.*, 2007]. Such a study will prove useful for validation of and improved confidence in both analysis techniques and may provide some insight into some of the more interesting events from Chapter 4.

I also want to conduct a statistical study of substorms and their effects on the outer radiation belt electrons similar to the studies on the effects from geomagnetic storms by *O'Brien et al.* [2001] and *Reeves et al.* [2003]. Based on my work on the PSD gradients, I expect that substorm activity plays a very important role in outer belt dynamics, and I want to quantify this with a statistical study. Superposed epoch analysis can be employed using the injection time observed near midnight at GEO as 0 ET, and I can develop statistics of what conditions or types of events result in net radiation belt enhancements or losses or in no net change. I will convert fluxes to PSD for fixed μ to remove any ambiguity from adiabatic effects. I am particularly interested in the cases exhibiting periods of prolonged substorm activity that result in substorm injections of relativistic electrons as was shown in *Ingraham et al.* [2001] and the all-negative gradient example case discussed here in Chapter 4. Observations from multiple spacecraft can be used to study substorm injection fronts, injected particle penetration depths in L, and azimuthal ranges. Figure 8.1 shows an example using THEMIS and LANL-GEO flux observations. Here TH-D and -E are in the tail at around 03:00 LT when they observe a particle injection just before 11:00 UT. 1989-046 observes the injection just a few minutes later, though interestingly, it does not observe the additional enhancements that TH-D and -E observe in the hour and a half leading up to the injection at 11:00 UT. Note too that the 225-315 keV channel on 1989-046 actually observes a brief dropout in flux corresponding to the injection, which infers a negative PSD gradient for μ ~300 MeV/G and is fully consistent with the results from our PSD gradient study. The other LANL spacecraft around GEO observe the injection at later times as the electrons drift eastward around the system. Multi-point observations

like this can be used to study the characteristics of substorm injections and quantify their effects on the outer belt electron populations. I'm looking forward to conducting a very comprehensive study of substorms' effects on the outer radiation belt electrons that includes all of the above-mentioned work.

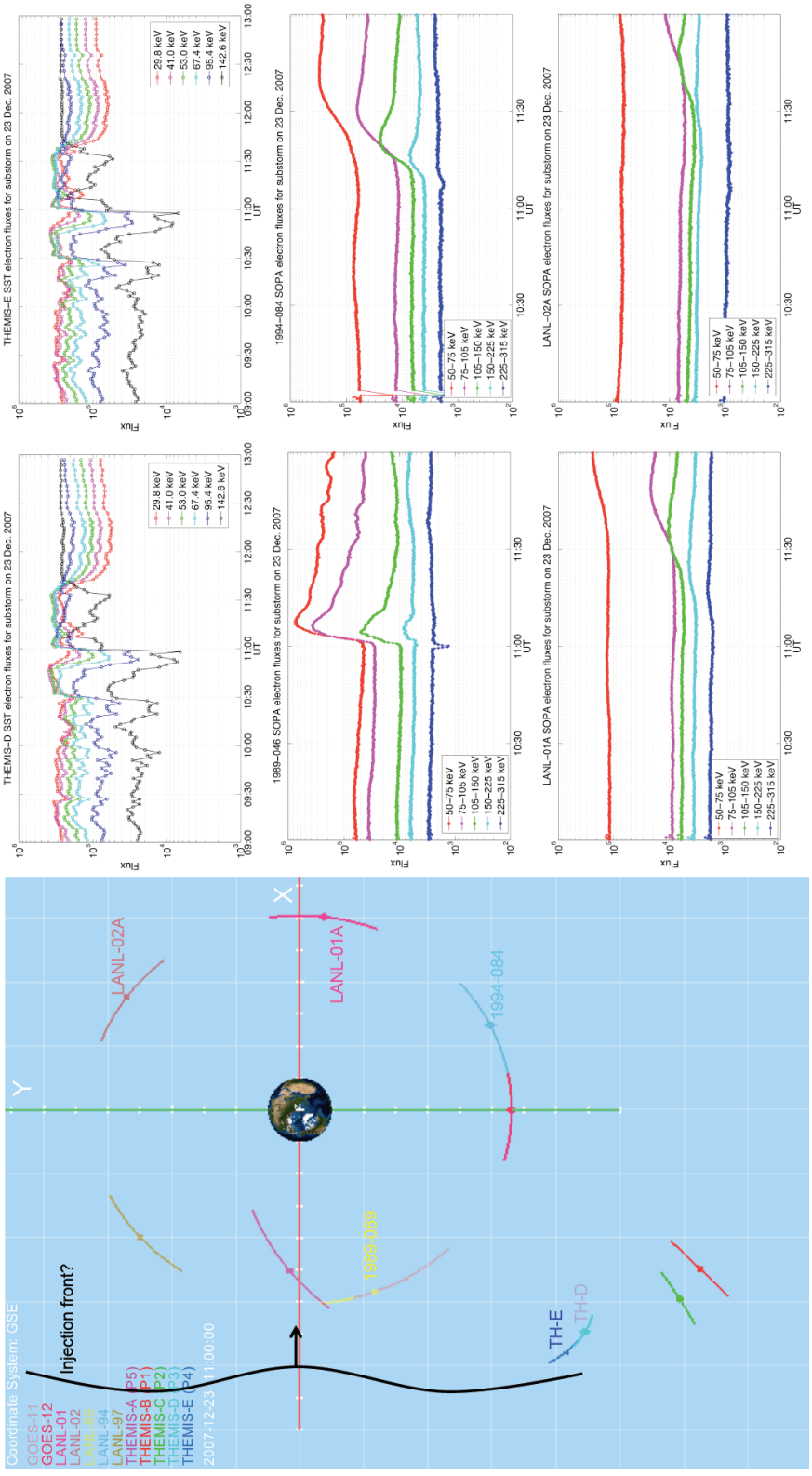

Figure 8.1: THEMIS SST and LANL-GEO SOPA multipoint measurements of a substorm injection on 23 December 2007.

Bibliography

Abel, B., and R. M. Thorne, Electron scattering loss in Earth's inner magnetosphere 1. Dominant physical processes, *J. Geophys. Res.*, *103*(A2), 2385, doi:10.1029/97JA02919, 1998.

Angelopoulos, V., The THEMIS Mission, *Space Sci. Rev.*, doi:10.1007/s11214-008-9336-1, 2008.

Auster, H. U., et al., The THEMIS fluxgate magnetometer, *Space Sci. Rev.*, doi:10.1007/s11214-008-9365-9, 2008.

Bailey, D. K., Some quantitative aspects of electron precipitation in and near the auroral zone, *Reviews of Geophysics and Space Physics*, *6*, 289, 1968.

Baker, D. N., Solar wind-magnetosphere drivers of space weather, *J. Atmos. Solar Terr. Phys.*, *58*, 1509, 1996.

Baker, D. N., Satellite anomalies due to space storms, in *Space Storms and Space Weather Hazards*, edited by I. A. Daglis, chap. 10, pp. 251–284, Springer, New York, 2001.

Baker, D. N., How to cope with space weather, *Science*, *297*, 1486, 2002.

Baker, D. N., R. D. Belian, P. R. Higbie, and E. W. Hones, High-energy magnetospheric protons and their dependence on geomagnetic and interplanetary conditions, *J. Geophys. Res.*, *84*(A12), 71387154, 1979.

Baker, D. N., R. L. McPherron, T. E. Cayton, and R. W. Kebesadel, Linear prediction filter analysis of relativistic electron properties at 6.6 RE, *J. Geophys. Res.*, *95*, 15,133–15,140, 1990.

Baker, D. N., G. M. Mason, O. Figueroa, G. Colon, J. G. Watzin, and R. M. Aleman, An overview of the solar, anomalous, and magnetospheric particle explorer (SAMPEX) mission, *IEEE Trans. Geosci. Rem. Sensing*, *31*(3), 531, 1993.

Baker, D. N., J. B. Blake, L. B. Callis, J. R. Cummings, D. Hovestadt, S. Kanekal, B. Klecker, R. A. Mewaldt, and R. D. Zwickl, Relativistic electron acceleration and decay time scales in the inner and outer radiation belts: SAMPEX, *Geophys. Res. Lett.*, *21*(6), 409, 1994.

Baker, D. N., J. H. Allen, S. G. Kanekal, and G. D. Reeves, Disturbed space environment may have been related to pager satellite failure, *Eos Trans. AGU*, *79*, 477, 1998a.

Baker, D. N., et al., A strong CME-related magnetic cloud interaction with the Earth's magnetosphere: ISTP observations of rapid relativistic electron acceleration on May 15, 1997, *Geophys. Res. Lett.*, *25*, 2975, 1998b.

Baker, D. N., et al., Coronal mass ejections, magnetic clouds, and relativistic magnetospheric electron events: ISTP, *J. Geophys. Res.*, *103*, 17,279, 1998c.

Barker, A. B., X. Li, and R. S. Selesnick, Modeling the radiation belt electrons with radial diffusion driven by the solar wind, *J. Geophys. Res.*, (in review), 2005.

Billingham, L., S. J. Schwartz, and D. G. Sibeck, The statistics of foreshock cavities: results of a Cluster survey, *Ann. Geophys.*, *26*, 3653–3667, 2008.

Blake, J. B., M. D. Looper, D. N. Baker, R. Nakamura, B. Klecker, and D. Hovestadt, New high temporal and spatial resolution measurements by sampex of the precipitation of relativistic electrons, *Adv. Space Res.*, *18*(8), 171–186, 1996.

Bortnik, J., and R. M. Thorne, The dual role of ELF/VLF chorus waves in the acceleration and precipitation of radiation belt electrons, *J. Atmos. Solar Terr. Phys.*, *69*, 378–386, 2007.

Bortnik, J., R. M. Thorne, T. P. O'Brien, J. C. Green, R. J. Strangeway, Y. Y. Shprits, and D. N. Baker, Observation of two distinct rapid loss-mechanisms during the November 20^{th}, 2003 radiation belt dropout event, *J. Geophys. Res.*, *111*, A12216, doi:10.1029/2006JA011802, 2006.

Bortnik, J., R. M. Thorne, and N. P. Meredith, The unexpected origin of plasmaspheric hiss from discrete chorus emissions, *Nature*, *452*, doi:10.1038/nature06741, 2008.

Boscher, D., S. Bourdarie, R. M. Thorne, and B. Abel, Influence of the wave characteristics on the electron radiation belt distribution, *Adv. Space Res.*, *26*, 163, 2000.

Brautigam, D. H., Crres in review: space weather and its effects on technology, *J. Atmos. Solar Terr. Phys.*, *64*(16), 1709–1721, 2002.

Brautigam, D. H., and J. M. Albert, Radial diffusion analysis of outer radiation belt electrons during the October 9, 1990, magnetic storm, *J. Geophys. Res.*, *105*(A1), 291, 2000.

Burin des Roziers, E., and X. Li, Specification of >2 MeV geosynchronous electrons based on solar wind measurements, *Space Weather*, *4*, S06007, doi:10.1029/2005SW000177, 2006.

Burin des Roziers, E., X. Li, D. N. Baker, T. A. Fritz, R. Friedel, T. G. Onsager, and I. Dandouras, Energetic plasma sheet electrons and their relationship with the solar wind: A Cluster and Geotail study, *J. Geophys. Res.*, *114*, A02220, doi:10.1029/2008JA013696, 2009.

Carpenter, D. L., and R. R. Anderson, An isee/whistler model of equatorial electron density in the magnetosphere, *J. Geophys. Res.*, *97*, 10971108, doi:10.1029/91JA01548, 1992.

Chen, Y., R. H. W. Friedel, G. D. Reeves, T. G. Onsager, and M. F. Thomsen, Multisatellite determination of the relativistic electron phase space density at geosynchronous orbit: Methodology and results during geomagnetically quiet times, *J. Geophys. Res.*, *110*, A10210, doi: 10.1029/2004JA010895, 2005.

Chen, Y., R. H. W. Friedel, and G. D. Reeves, Phase space density distributions of energetic electrons in the outer radiation belt during two Geospace Environment Modeling Inner Magnetosphere Storms selected storms, *J. Geophys. Res.*, *111*, A11S04, doi:10.1029/2006JA011703, 2006.

Chen, Y., R. H. W. Friedel, G. D. Reeves, T. E. Cayton, and R. Christensen, Multisatellite determination of the relativistic electron phase space density at geosynchronous orbit: An integrated investigation during geomagnetic storm times, *J. Geophys. Res.*, *112*, A11214, doi: 10.1029/2007JA012314, 2007a.

Chen, Y., G. D. Reeves, and R. H. W. Friedel, The energization of relativistic electrons in the Van Allen radiation belt, *Nature*, *3*, 614–617, doi:10.1038/nphys655, 2007b.

Cook, W. R., et al., PET: A proton/electron telescope for studies of magnetospheric, solar, and galactic particles, *IEEE Transactions on Geoscience and Remote Sensing*, *31*(1), 1993.

de Selding, P. B., Orbital blames Galaxy 15 failure on solar storm, *Space News (online)*, Available from: <http://www.spacenews.com/satellite_telecom/orbital-blames-galaxy-failure-solar-storm-discloses-further-taurus-delay.html>, published: 20 April, 2010.

Elkington, S. R., M. K. Hudson, and A. A. Chan, Acceleration of relativistic electrons via drift-resonant interaction with toroidal-mode Pc-5 ULF oscillations, *Geophys. Res. Lett.*, *26*(21), 3273, 1999.

Elkington, S. R., M. K. Hudson, M. J. Wiltberger, and J. G. Lyon, MHD/Particle simulations of radiation belt dynamics, *J. Atmos. Solar Terr. Phys.*, *64*, 607, 2002.

Elkington, S. R., M. K. Hudson, and A. A. Chan, Resonant acceleration and diffusion of outer zone electrons in an asymmetric geomagnetic field, *J. Geophys. Res.*, *108*(A3), 1116, doi: 10.1029/2001JA009202, 2003.

Elkington, S. R., M. Wiltberger, A. A. Chan, and D. N. Baker, Physical models of the geospace radiation environment, *J. Atmos. Solar Terr. Phys.*, *66*, 1371, doi:10.1016/j.jastp.2004.03.023, 2004.

Erlandson, R. E., and A. J. Ukhorskiy, Observations of electromagnetic ion cyclotron waves during geomagnetic storms: Wave occurrence and pitch angle scattering, *J. Geophys. Res.*, *106*(A3), 3883–3895, 2001.

Facsko, G., K. Kecskemety, G. Erdos, M. Tatrallyay, P. W. Daly, and I. Dandouras, A statistical study of hot flow anomalies using Cluster data, *Adv. Space Res.*, *41(8)*, 1286–1291, doi: 10.1016/j.asr2008.02.005, 2008.

Fairfield, D. H., W. Baumjohann, G. Paschmann, H. Luhr, and D. G. Sibeck, Upstream pressure variations associated with the bow shock and their effects on the magnetosphere, *J. Geophys. Res.*, *95*(A4), 3773–3786, 1990.

Fälthammar, C.-G., Effects of time-dependent electric fields on geomagnetically trapped radiation, *J. Geophys. Res.*, *70*(11), 2503, 1965.

Fear, R. C., S. E. Milan, A. N. Fazakerley, E. A. Lucek, S. W. H. Cowley, and I. Dandouras, The azimuthal extent of three flux transfer events, *Ann. Geophys.*, *26*, 2353–2369, 2008.

Ferster, W., Intelsat loses contact with Galaxy 15 satellite, *Space News (online)*, Available from: <http://www.spacenews.com/satellite_telecom/100408-intelsat-loses-contact-galaxy-satellite.html>, published: 08 April, 2010.

Fok, M.-C., R. B. Horne, N. P. Meredith, and S. A. Glauert, Radiation Belt Environment model: Application to space weather nowcasting, *J. Geophys. Res.*, *113*, A03S08, doi: 10.1029/2007JA012558, 2008.

Friedel, R. H. W., G. D. Reeves, and T. Obara, Relativistic electron dynamics in the inner magnetosphere – a review, *J. Atmos. Solar Terr. Phys.*, *64*(2), 265, 2002.

Fry, C. D., M. Dryer, W. Sun, T. R. Detman, Z. K. Smith, C. S. Deehr, C.-C. Wu, S.-I. Akasofu, and D. B. Berdichevsky, Solar observation-based model for multiday predictions of interplanetary shock and CME arrivals at Earth, *IEEE Transactions on Plasma Science*, *32*(4), 2004.

Fry, C. D., T. R. Detman, M. Dryer, Z. Smith, W. Sun, C. S. Deehr, S.-I. Akasofu, C.-C. Wu, and S. McKenna-Lawlor, Real-time solar wind forecasting: Capabilities and challenges, *J. Atmos. Solar Terr. Phys.*, *69*, 109–115, 2007.

Gannon, J. L., X. Li, and M. Temerin, Parametric study of shock-induced transport and energization of relativistic electrons in the magnetosphere, *J. Geophys. Res.*, *110*, A12206, doi: 10.1029/2004JA010679, 2005.

Gannon, J. L., X. Li, and D. Heynderickx, Pitch angle distribution analysis of radiation belt electrons based on combined release and radiation effects satellite medium electrons a data,, *J. Geophys. Res.*, *112*, A05212, doi:10.1029/2005JA011565, 2007.

Glassmeier, K. H., Traveling magnetospheric convection twin verticesObservations and theory, *Ann. Geophys.*, *10*, 547 565, 1992.

Gosling, J. T., The solar wind, in *Encyclopedia of the Solar System 2nd Ed.*, edited by L.-A. McFadden, P. R. Weissman, and T. V. Johnson, pp. 99–116, Academic Press, San Diego, CA, 2007.

Green, J. C., and M. G. Kivelson, Relativistic electrons in the outer radiation belt: Differentiating between acceleration mechanisms, *J. Geophys. Res.*, *109*(A3), A03213, doi: 10.1029/2003JA010153, 2004.

Hargreaves, J. K. (Ed.), *The Solar-Terrestrial Environment*, Cambridge Univ. Press, New York, 1992.

Hasegawa, H., B. U. . Sonnerup, C. J. Owen, B. Klecker, G. Paschmann, A. Balogh, and H. Rme, Flux transfer events recovered from Cluster data, *Ann. Geophys.*, *24*, 603–618, 2006.

Hilmer, R. V., G. P. Ginet, and T. E. Cayton, Enhancement of equatorial energetic electron fluxes near l=4.2 as a result of high speed solar wind streams, *J. Geophys. Res.*, *105*(A10), 23,311, doi:10.1029/1999JA000380, 2000.

Horne, R. B., Acceleration of killer electrons, *Nature Physics*, *3*, 2007.

Horne, R. B., and R. M. Thorne, Potential waves for relativistic electron scattering and stochastic acceleration during magnetic storms, *Geophys. Res. Lett.*, *25*(15), 1231, doi:10.1029/98GL01002, 1998.

Horne, R. B., S. A. Glauert, and R. M. Thorne, Resonant diffusion of radiation belt electrons by whistler-mode chorus, *Geophys. Res. Lett.*, *30*(9), 1493, doi:10.1029/2003GL016963, 2003.

Horne, R. B., R. M. Thorne, S. A. Glauert, J. M. Albert, N. P. Meredith, and R. R. Anderson, Timescale for radiation belt electron acceleration by whistler mode chorus waves, *J. Geophys. Res.*, *110*, A03225, doi:10.1029/2004JA010811, 2005a.

Horne, R. B., R. M. Thorne, S. A. Glauert, N. P. Meredith, D. Pokhotelov, and O. Santolík, Electron acceleration in the van allen radiation belts by fast magnetosonic waves, *J. Geophys. Res.*, *34*, L17,107, 2007.

Horne, R. B., et al., Wave acceleration of electrons in the Van Allen radiation belts, *Nature*, *437*(7056), 227, doi:10.1038/nature03939, 2005b.

Hudson, M. K., S. R. Elkington, J. G. Lyon, and C. C. Goodrich, Increase in relativistic electron flux in the inner magnetosphere: ULF wave mode structure, *Adv. Space Res.*, *25*(12), 2327, 2000.

Iles, R. H. A., N. P. Meredith, A. N. Fazakerley, and R. B. Horne, Phase space density analysis of the outer radiation belt energetic electron dynamics, *J. Geophys. Res.*, *111*, A03204, doi: 10.1029/2005JA011206, 2006.

Imhof, W. L., H. D. Voss, J. Mobilia, D. W. Datlowe, and E. E. Gaines, The precipitation of relativistic electrons near the trapping boundary, *J. Geophys. Res.*, *96*, 5619, 1991.

Ingraham, J. C., T. E. Cayton, R. D. Belian, R. A. Christensen, R. H. W. Friedel, M. M. Meier, G. D. Reeves, and M. Tuszewski, Substorm injection of relativistic electrons to geosynchronous orbit during the great magnetic storm of March 24, 1991, *J. Geophys. Res.*, *106*, 25,759, doi: 10.1029/2000JA000458, 2001.

Jacob, J. D., and C. Cattell, High-time resolution measurements of upstream magnetic field and plasma conditions during flux transfer events at the Earth's dayside magnetopause, *Geophys. Res. Lett.*, *20*(18), 2007–2010, 1993.

Jacobsen, K. S., et al., THEMIS observation of extreme magnetopause motion caused by a hot flow anomaly, *J. Geophys. Res.*, *114*, A08210, 2009.

Jordanova, V. K., C. J. Farrugia, R. M. Thorne, G. V. Khazanov, G. D. Reeves, and M. F. Thomsen, Modeling ring current proton precipitation by electromagnetic ion cyclotron waves during the May 14-16, 1997 storm, *J. Geophys. Res.*, *106*, 7–22, 2001a.

Jordanova, V. K., R. M. Thorne, C. J. Farrugia, Y. Dotan, J. F. Fennell, M. F. Thomsen, G. D. Reeves, and D. J. McComas, Ring current dynamics during the 13-18 july 2000 storm period, *Storm Physics*, *204*, 361–375, 2001b.

Julier, S. J., J. K. Uhlmann, and H. F. Durrant-Whyte, A new approach for filtering nonlinear systems, *IEEE: Proceedings of the American Control Conference*, *3*, 1628–1632, 1995.

Kaiser, M. L., The STEREO mission: an overview, *Adv. Space Res.*, *36*, 1483–1488, 2005.

Kawano, H., and C. T. Russell, Survey of flux transfer events with the ISEE 1 spacecraft: dependence on the interplanetary magnetic field, *J. Geophys. Res.*, *102*(A6), 11,307–11,313, 1997.

Kennel, C. F., and H. E. Petschek, Limit on stably trapped particle fluxes, *J. Geophys. Res.*, *71*(1), 1, 1966.

Kim, H.-J., and A. A. Chan, Fully adiabatic changes in storm-time relativistic electron fluxes, *J. Geophys. Res.*, *102*, 22,107, 1997.

Kivelson, M. G., and C. T. Russell (Eds.), *Introduction to Space Physics*, Cambridge Univ. Press, New York, 1995.

Koller, J., Y. Chen, G. D. Reeves, R. H. W. Friedel, T. E. Cayton, and J. A. Vrugt, Identifying the radiation belt source region by data assimilation, *J. Geophys. Res.*, *112*, A06244, doi:10.1029/2006JA012196, 2007.

Koller, J., G. D. Reeves, and R. H. W. Friedel, LANL* V1.0: a radiation belt drift shell model suitable for real-time and reanalysis applications, *Geoscientific Model Development*, *2*, 113–122, 2009.

Kondrashov, D., Y. Shprits, M. Ghil, and R. Thorne, A Kalman filter technique to estimate relativistic electron lifetimes in the outer radiation belt, *J. Geophys. Res.*, *112*, A10227, doi: 10.1029/2007JA012583, 2007.

Korotova, G. I., D. G. Sibeck, and T. Rosenberg, Geotail observations of FTE velocities, *Ann. Geophys.*, *27*, 83–92, 2009.

Lee, D.-Y., L. R. Lyons, and G. D. Reeves, Comparison of geosynchronous energetic particle flux responses to solar wind dynamic pressure enhancements and substorms, *J. Geophys. Res.*, *110*, A09213, doi:10.1029/2005JA011091, 2005.

Lee, L. C., and Z. F. Fu, A theory of magnetic flux transfer at the Earth's magnetopause, *Geophys. Res. Lett.*, *12*, 105–108, 1985.

Leo, W. R., *Techniques for Nuclear and Particle Physics Experiments*, Springer-Verlag, New York, 1987.

Li, W., et al., Global distribution of whistler-mode chorus waves observed on the THEMIS spacecraft, *Geophys. Res. Lett.*, *36*, L09104, doi:10.1029/2009GL037595, 2009.

Li, X., Variations of 0.7-6.0 MeV electrons at geosynchronous orbit as a function of solar wind, *Space Weather*, *2*(3), S03006, doi:10.1029/2003SW000017, (for real-time forecast, please see website: http://lasp.colorado.edu/∼lix/), 2004.

Li, X., and M. A. Temerin, The electron radiation belt, *Space Sci. Rev.*, *95*, 569, 2001.

Li, X., I. Roth, M. Temerin, J. R. Wygant, M. K. Hudson, and J. B. Blake, Simulation of the prompt energization and transport of radiation belt particles during the March 24, 1991 SSC, *Geophys. Res. Lett.*, *20*, 2423, 1993.

Li, X., D. N. Baker, M. Temerin, D. Larson, R. P. Lin, G. D. Reeves, M. Looper, S. G. Kanekal, and R. A. Mewaldt, Are energetic electrons in the solar wind the source of the outer radiation belt?, *Geophys. Res. Lett.*, *24*, 923, 1997.

Li, X., D. N. Baker, M. Temerin, G. D. Reeves, and R. D. Belian, Simulation of dispersionless injections and drift echoes of energetic electrons associated with substorms, *Geophys. Res. Lett.*, *25*, 3763, doi:10.1029/1998GL900001, 1998.

Li, X., D. N. Baker, S. G. Kanekal, M. Looper, and M. A. Temerin, Sampex long-term observations of MeV electrons, *Geophys. Res. Lett.*, *28*, 3827, 2001a.

Li, X., M. Temerin, D. N. Baker, G. D. Reeves, and D. Larson, Quantitative prediction of radiation belt electrons at geostationary orbit based on solar wind measurements, *Geophys. Res. Lett.*, *28*(9), 1887, 2001b.

Li, X., D. N. Baker, M. Temerin, G. D. Reeves, R. Friedel, and C. Shen, Energetic electrons, 50 keV - 6 MeV, at geosynchronous orbit: their responses to solar wind variations, *Space Weather*, *3*, S04001, doi:10.1029/2004SW000105, 2005.

Li, X., D. N. Baker, T. P. O'Brien, L. Xie, and Q. G. Zong, Correlation between the inner edge of outer radiation belt electrons and the innermost plasmapause location, *Geophys. Res. Lett.*, *33*, L14107, doi:10.1029/2006GL026294, 2006.

Li, X., K. S. Oh, and M. Temerin, Prediction of the AL index using solar wind parameters, *J. Geophys. Res.*, *112*, A06224, doi:10.1029/2006JA011918, 2007.

Li, X., A. B. Barker, D. N. Baker, W. C. Tu, T. E. Sarris, R. S. Selesnick, R. Friedel, and C. Shen, Modeling the deep penetration of outer belt electrons during the Halloween magnetic storm in 2003, *Space Weather*, *7*, S02004, doi:10.1029/2008SW000418, 2008.

Li, X., et al., Rapid enhancements of relativistic electrons deep in the magnetosphere during the may 15, 1997, magnetic storm, *J. Geophys. Res.*, *104*, 44674476, doi:10.1029/1998JA900092, 1999.

Li, X., et al., Energetic particle injection in the inner magnetosphere as a response to an interplanetary shock, *J. Atmos. Solar Terr. Phys.*, *65*, 233, 2003.

Loto'aniu, T. M., I. R. Mann, L. G. Ozeke, A. A. Chan, Z. C. Dent, and D. K. Milling, Radial diffusion of relativistic electrons into the radiation belt slot region during the 2003 Halloween geomagnetic storms, *J. Geophys. Res.*, in press, 2006.

Lui, A. T. Y., D. G. Sibeck, T. Phan, J. P. McFadden, V. Angelopoulos, and K. H. Glassmeier, Reconstruction of a flux transfer event based on observations from THEMIS satellites, *J. Geophys. Res.*, *113*, A00C01, 2008.

Lyatsky, W., and G. V. Khazanov, A predictive model for relativistic electrons at geostationary orbit, *Geophys. Res. Lett.*, *35*, L15108, doi:10.1029/2008GL034688, 2008a.

Lyatsky, W., and G. V. Khazanov, Effect of solar wind density on relativistic electrons at geosynchronous orbit, *Geophys. Res. Lett.*, *L03109*, doi:10.1029/2007GL032524, 2008b.

Lyatsky, W., and G. V. Khazanov, Effect of geomagnetic disturbances and solar wind density on relativistic electrons at geostationary orbit, *J. Geophys. Res.*, *113*, A08224, doi:10.1029/2008JA013048, 2008c.

Lyons, L. R., and R. M. Thorne, Equilibrium structure of radiation belt electrons, *J. Geophys. Res.*, *78*, 2142, 1973.

Lyons, L. R., R. M. Thorne, and C. F. Kennel, Pitch-angle diffusion of radiation belt electrons within the plasmasphere, *J. Geophys. Res.*, *77*, 3455, 1972.

Mann, I. R., T. P. O'Brien, and D. K. Milling, Correlations between ULF wave power, solar wind speed, and relativistic electron flux in the magnetosphere: solar cycle dependence, *J. Atmos. Solar Terr. Phys.*, *66*, 187, doi:10.1016/j.jastp.2003.10.002, 2004.

McAdams, K. L., and G. D. Reeves, Non-adiabatic response of relativistic radiation belt electrons to GEM magnetic storms, *Geophys. Res. Lett.*, *28*(9), 1879, 2001.

McCollough, J. P., J. L. Gannon, D. N. Baker, and M. Gehmeyr, A statistical comparison of commonly used external magnetic field models, *Space Weather*, *6*, S10001, doi: 10.1029/2008SW000391, 2008.

McCollough, J. P., S. R. Elkington, and D. N. Baker, Modeling EMIC wave growth during the compression event of 29 june 2007, *Geophys. Res. Lett.*, *36*, L18108, doi:10.1029/2009GL039985, 2009.

McCollough, J. P., S. Elkington, and D. Baker, The role of shabansky orbits in compression-related emic wave growth, *J. Geophys. Res.*, in review, 2010.

McFadden, J. P., C. W. Carlson, D. Larson, V. Angelopoulos, M. Ludlam, R. Abiad, B. Elliott, P. Turin, and M. Marckwordt, The THEMIS ESA plasma instrument and in-flight calibration, *Space Sci. Rev.*, doi:10.1107/s11214-008-9440-2, 2008.

McGuire, R. E., R. J. Burley, R. M. Candey, R. L. Kessel, and T. J. Kovalick, CDAWeb and SSCWeb: Enabling correlative international Sun-Earth-connections science entering the era of IMAGE and Cluster, *Eos Trans. AGU*, *81*, Abstract SM32A-14, 2000.

McIlwain, C. E., Coordinates for mapping the distribution of magnetically trapped particles, *J. Geophys. Res.*, *66*, 3681, 1961.

McIlwain, C. E., Ring current effects on trapped particles, *J. Geophys. Res.*, *71*, 3623, 1966.

Meredith, N. P., R. B. Horne, and R. R. Anderson, Substorm dependence of chorus amplitudes: implications for the acceleration of electrons to relativistic energies, *J. Geophys. Res.*, *106*, 13,165–13,178, 2001.

Meredith, N. P., R. B. Horne, R. H. A. Iles, R. M. Thorne, D. Heynderikx, and R. R. Anderson, Outer zone relativistic electron acceleration associated with substorm-enhanced whistler mode chorus, *J. Geophys. Res.*, *107*(A7), 1144, 2002.

Meredith, N. P., M. Cain, R. B. Horne, R. M. Thorne, D. Summers, and R. R. Anderson, Evidence for chorus-driven electron acceleration to relativistic energies from a survey of geomagnetically disturbed periods, *J. Geophys. Res.*, *108*(A6), 1248, doi:10.1029/2002JA009764, 2003a.

Meredith, N. P., R. B. Horne, R. M. Thorne, and R. R. Anderson, Favored regions for chorus-driven electron acceleration to relativistic energies in the earth's outer radiation belt, *Geophys. Res. Lett.*, *30*(16), 1871, doi:10.1029/2003GL017698, 2003b.

Meredith, N. P., R. B. Horne, and R. R. Anderson, Survey of magnetosonic waves and proton distributions in the earth's inner magnetosphere, *J. Geophys. Res.*, *113*, A06213, doi: 10.1029/2007JA012975, 2008.

Mewaldt, R. A., et al., Proton, helium, and electron spectra during the large solar particle events of October-November 2003, *J. Geophys. Res.*, *110*, 2005.

Millan, R., and R. Thorne, Review of radiation belt relativistic electron losses, *Journal of Atmospheric and Solar-Terrestrial Physics*, *69*(3), 362 – 377, doi:DOI: 10.1016/j.jastp.2006.06.019, global Aspects of Magnetosphere-Ionosphere Coupling, Global Aspects of Magnetosphere-Ionosphere Coupling, 2007.

Ni, B., Y. Shprits, T. Nagai, R. Thorne, Y. Chen, D. Kondrashov, and H.-J. Kim, Reanalyses of the radiation belt electron phase space density using nearly equatorial CRRES and polar-orbiting Akebono satellite observations, *J. Geophys. Res.*, *114*, A05208, doi:10.1029/2008JA013933, 2009.

O'Brien, B. J., High-latitude geophysical studies with satellite Injun 3: 3. Precipitation of electrons in the atmosphere, *J. Geophys. Res.*, *69*, 13–43, 1964.

O'Brien, T. P., and M. B. Moldwin, Empirical plasmapause models from magnetic indices, *Geophys. Res. Lett.*, *30*(4), 1152, doi:10.1029/2002GL016007, 2003.

O'Brien, T. P., R. L. McPherron, D. Sornette, G. D. Reeves, R. Friedel, and H. J. Singer, Which magnetic storms produce relativistic electrons at geosynchronous orbit?, *J. Geophys. Res.*, *106*(A8), 15,533, 2001.

O'Brien, T. P., D. Sornette, and R. McPherron, Statistical asynchronous regression: Determining the relationship between two quantities that are not measured simultaneously, *J. Geophys. Res.*, *106*(A7), 13,247–13,259, 2001.

O'Brien, T. P., K. R. Lorentzen, I. R. Mann, N. P. Meredith, J. B. Blake, J. F. Fennel, M. D. Looper, D. K. Milling, and R. R. Anderson, Energization of relativistic electrons in the presence of ULF power and MeV microbursts: Evidence for dual ULF and VLF acceleration, *J. Geophys. Res.*, *106*(A8), 15,533, 2003.

Omidi, N., and D. G. Sibeck, Flux transfer events in the cusp, *Geophys. Res. Lett.*, *34*, L04106, 2007.

Onsager, T. G., and et al., Operational uses of the GOES energetic particle detectors, in *GOES-8 and Beyond*, *Proc. SPIE*, vol. 2812, edited by E. R. Washwell, pp. 281–290, SPIE, Bellingham, WA, doi:10.1117/12.254075, 1996.

Onsager, T. G., G. Rostoker, H. J. Kim, G. D. Reeves, T. Obara, and C. Smithro, Radiation belt electron flux dropouts: local time, radial, and particle-energy, *J. Geophys. Res.*, *107*, A111382, 2002.

Onsager, T. G., A. A. Chan, Y. Fei, S. R. Elkington, J. C. Green, and H. J. Singer, The radial gradient of relativistic electrons at geosynchronous orbit, *J. Geophys. Res.*, *109*(A5), A05221, doi:10.1029/2003JA010368, 2004.

Onsager, T. G., J. C. Green, G. D. Reeves, and H. J. Singer, Solar wind and magnetospheric conditions leading to the abrupt loss of outer radiation belt electrons, *J. Geophys. Res.*, *112*, A01202, doi:10.1029/2006JA011708, 2007.

Owen, C. J., et al., Cluster observations of "crater" flux transfer events at the dayside high-latitude magnetopause, *J. Geophys. Res.*, *113*, A07S04, 2008.

Parker, E. N., Dynamics of the interplanetary gas and magnetic fields, *Astrophys. J.*, *128*, 664–676, 1958.

Paulikas, G. A., and J. B. Blake, Effects of the solar wind on magnetospheric dynamics: Energetic electrons at the synchronous orbit, in *Quantitative Modeling of Magnetospheric Processes*, vol. 21, edited by W. P. Olsen, p. 180, AGU, Washington, D. C., 1979.

Perry, K. L., G. P. Ginet, A. G. Ling, and R. V. Hilmer, Comparing geosynchronous relativistic electron prediction models, *Space Weather*, *In Press*, 2010.

Petrinec, S. M., and C. T. Russell, Near-earth magnetotail shape and size as determined from the magnetopause flaring angle, *J. Geophys. Res.*, *101*, 137 152, doi:10.1029/95JA02834, 1996.

Phan, T. D., and G. Paschmann, Low-latitude dayside magnetopause and boundary layer for high magnetic shear: 1. Structure and motion, *J. Geophys. Res.*, *101*(A4), 7801–7815, 1996.

Raeder, J., Flux transfer events: 1. generation mechanism for strong southward IMF, *Ann. Geophys.*, *24*, 381–392, 2006.

Reeves, G. D., Relativistic electrons and magnetic storms: 1992–1995, *Geophys. Res. Lett.*, *25*(11), 1817, 1998.

Reeves, G. D., K. L. McAdams, R. H. W. Friedel, and T. P. O'Brien, Acceleration and loss of relativistic electrons during geomagnetic storms, *Geophys. Res. Lett.*, *30*(10), 36–1, doi: 10.1029/2002GL016513, 2003.

Reeves, G. D., et al., The global response of relativistic radiation belt electrons to the January 1997 magnetic cloud, *Geophys. Res. Lett.*, *25*, 3265, 1998.

Rigler, E. J., D. N. Baker, R. S. Weigel, D. Vassiliadis, and A. J. Klimas, Adaptive linear prediction of radiation belt electrons using the Kalman filter, *Space Weather*, *2*, S03003, doi: 10.1029/2003SW000036, 2004.

Roederer, J. G., *Dynamics of Geomagnetically Trapped Radiation*, 166 pp., Springer-Verlag, New York, 1970.

Rosenberg, T. J., L. J. Lanzerotti, D. K. Bailey, and J. D. Pierson, Energy spectra in relativistic electron precipitation events, *J. Atmos. Solar Terr. Phys.*, *34*, 1977–1990, 1972.

Rostoker, G., S. Skone, and D. N. Baker, On the origin of relativistic electrons in the magnetosphere associated with some geomagnetic storms, *Geophys. Res. Lett.*, *25*, 3701, 1998.

Roth, I., M. Temerin, and M. K. Hudson, Resonant enhancement of relativistic electron fluxes during geomagnetically active periods, *Ann. Geophys.*, *17*, 631– 638, doi:10.1007/s00585-999-0631-2, 1999a.

Roth, I., M. Temerin, M. K. Hudson, G. Reeves, J. B. Blake, and R. S. Selesnick, Resonant heating of energetic storm-time electrons due to substorm-time excited whistler waves, in *International Conference on Substorms 4*, vol. 238, edited by S. Kokubun and Y. Kamide, p. 593, Klewer Academic Publishers, Astrophysics and Space Science Library, London, 1999b.

Russell, C. T., and R. C. Elphic, Initial ISEE magnetometer results: Magnetopause observations, *Space Sci. Rev.*, *22*, 681–715, 1978.

Russell, C. T., and Hoppe, Upstream waves and particles, *Space Sci. Rev.*, *34*, 155, 1983.

Sarris, T., X. Li, and M. Temerin, Simulating radial diffusion of energetic (MeV) electrons through a model of fluctuating electric and magnetic fields, *Ann. Geophys.*, *24*(10), 2583, 2006.

Sauvaud, J.-A., et al., Intermittent thermal plasma acceleration linked to sporadic motions of the magnetopause, first Cluster results, *Ann. Geophys.*, *19*, 1523–1532, 2001.

Scholer, M., Magnetic flux transfer at the magnetopause based on single X-line bursty reconnection, *Geophys. Res. Lett.*, *15*, 291–294, 1988a.

Scholer, M., Strong core magnetic fields in magnetopause flux transfer events, *Geophys. Res. Lett.*, *15*, 748–751, 1988b.

Schulz, M., and L. J. Lanzerotti, *Particle Diffusion in the Radiation Belts*, *Physics and Chemistry in Space*, vol. 7, 215 pp., Springer-Verlag, New York, 1974.

Schwartz, S. J., D. Sibeck, M. Wilber, and K. Meziane, Kinetic aspects of foreshock cavities, *Geophys. Res. Lett.*, *33*, L12103, doi:10.1029/2005GL025612, 2006.

Schwartz, S. J., et al., An active current sheet in the solar wind, *Nature*, *318*, 269–271, 1985.

Selesnick, R. S., and J. B. Blake, On the source location of radiation belt relativistic electrons, *J. Geophys. Res.*, *105*(A2), 2607, 2000.

Selesnick, R. S., and J. B. Blake, Relativistic electron drift shell splitting, *J. Geophys. Res.*, *107*(A9), 1265, doi:10.1029/2001JA009179, 2002.

Selesnick, R. S., J. B. Blake, W. A. Kolasinski, and T. A. Fritz, A quiescent state of 3 to 8 MeV radiation belt electrons, *Geophys. Res. Lett.*, *24*(11), 1343, 1997.

Shabansky, V. P., Some processes in the magnetosphere, *Space Sci. Rev.*, *12*(3), 299–418, 1971.

Shabansky, V. P., and A. E. Antonova, Topology of particle drift shells in the Earth's magnetosphere (English translation), *Geomagn. Aeron.*, *8*, 844, 1968.

Shi, Y., E. Zesta, and L. R. Lyons, Features of energetic particle radial profiles inferred from geosynchronous responses to solar wind dynamic pressure enhancements, *Ann. Geophys.*, *27*, 851 859, 2009.

Shprits, Y., D. Kondrashov, Y. Chen, R. Thorne, M. Ghil, R. Friedel, and G. Reeves, Reanalysis of relativistic radiation belt electron fluxes using CRRES satellite data, a radial diffusion model, and a Kalman filter, *J. Geophys. Res.*, *112*, A12216, doi:10.1029/2007JA012579, 2007a.

Shprits, Y. Y., and R. M. Thorne, Time dependent radial diffusion modeling of relativistic electrons with realistic loss rates, *Geophys. Res. Lett.*, *31*, L08805, doi:10.1029/2004GL019591, 2004.

Shprits, Y. Y., R. M. Thorne, R. B. Horne, and D. Summers, Bounce-averaged diffusion coefficients for field-aligned chorus waves, *J. Geophys. Res.*, *111*, A10225, doi:10.1029/2006JA011725, 2006.

Shprits, Y. Y., N. P. Meredith, and R. M. Thorne, Parameterization of radiation belt electron loss timescales due to interactions with chorus waves, *Geophys. Res. Lett.*, *34*, L11110, doi: 10.1029/2006GL029050, 2007b.

Shue, J. H., J. K. Chao, H. C. Fu, C. T. Russel, P. Song, K. K. Khurana, and H. J. Singer, A new functional form to study the solar wind control of the magnetopause size and shape, *J. Geophys. Res.*, *102*(A5), doi:10.1029/97JA00196, 1997.

Shue, J. H., et al., Magnetopause location under extreme solar wind conditions, *J. Geophys. Res.*, *103*(A8), 17,691–17,700, 1998.

Sibeck, D. G., A model for the transient magnetospheric response to sudden solar wind dynamic pressure variations, *J. Geophys. Res.*, *95*, 3755–3771, doi:10.1029/JA095iA04p03755, 1990.

Sibeck, D. G., Transient events in the outer magnetosphere - boundary waves or flux transfer events?, *J. Geophys. Res.*, *97*, 4009–4026, 1992.

Sibeck, D. G., and R. Q. Lin, Concerning the motion of flux transfer events generated by component reconnection across the dayside magnetopause, *J. Geophys. Res.*, *115*, A04209, doi: 10.1029/2009JA014677, 2010.

Sibeck, D. G., and M. F. Smith, Magnetospheric plasma flows associated with boundary waves and flux transfer events, *Geophys. Res. Lett.*, *19*, 1903–1906, doi:10.1029/92GL01614, 1992.

Sibeck, D. G., R. B. Decker, D. G. Mitchell, A. J. Lazarus, R. P. Lepping, and A. Szabo, Solar wind preconditioning in the flank foreshock: IMP 8 observations, *J. Geophys. Res.*, *106*(A10), 21,675–21,688, 2001.

Sibeck, D. G., T.-D. Phan, R. Lin, R. P. Lepping, and A. Szabo, Wind observations of foreshock cavities: A case study, *J. Geophys. Res.*, *107*(A10), doi:10.1029/2001JA007539, 2002.

Sibeck, D. G., N. B. Trivedi, E. Zesta, R. B. Decker, H. J. Singer, A. Szabo, H. Tachihara, and J. Watermann, Pressure pulse interaction with the magnetosphere and ionosphere, *J. Geophys. Res.*, *108*(A2), 1095, doi:10.1029/2002JA009675, 2003.

Sibeck, D. G., K. Kudela, T. Mukai, Z. Nemecek, and J. Safrankova, Radial dependence of foreshock cavities: a case study, *Ann. Geophys.*, *22*, 4143–4151, 2004.

Sibeck, D. G., M. Kuznetsova, V. Angelopoulos, K. Glassmeier, and J. P. McFadden, Crater FTEs: Simulation results and THEMIS observations, *Geophys. Res. Lett.*, *35*, L17S06, 2008.

Sibeck, D. G., et al., The magnetospheric response to 8-minute period strong-amplitude upstream pressure variations, *J. Geophys. Res.*, *94*(A3), 2505–2519, 1989.

Sibeck, D. G., et al., Magnetopause motion driven by interplanetary magnetic field variations, *J. Geophys. Res.*, *105*(A11), 25,155–25,169, 2000.

Smith, A. J., M. P. Freeman, and G. D. Reeves, Postmidnight VLF chorus events, a substorm signature observed at the ground near L = 4, *J. Geophys. Res.*, *101*(A11), 24,641, 1996.

Sonnerup, B. U. O., and M. Scheible, Minimum and maximum variance analysis, in *Analysis Methods for Multi-Spacecraft Data*, edited by G. Paschmann and P. W. Daly, ISSI Sci. Rep. SR-001, pp. 185–220, Eur. Space Agency Publ. Div., Noordwijk, Netherlands, 1998.

Southwood, D. J., C. J. Farrugia, and M. A. Saunders, What are flux transfer events?, *Planet. Space Sci.*, *36*, 503508, 1988.

Spreiter, J. R., A. L. Summers, and A. Y. Alksne, Hydromagnetic flow around the magnetosphere, *Planet. Space Sci.*, *14*, 223–253, 1966.

Stern, A. P., and N. F. Ness, Planetary Magnetospheres, *Tech. Rep. NASA Technical Memorandum 83841*, NASA Goddard Space Flight Center, Greenbelt, MD, 1981.

Stone, E. C., A. M. Frandsen, R. A. Mewaldt, E. Christian, L. Margolies, J. Ormes, and F. Snow, The advanced composition explorer, *Space Sci. Rev.*, *86*, 1, 1998.

Subbotin, D., Y. Shprits, and B. Ni, Three-dimensional VERB radiation belt simulations including mixed diffusion, *J. Geophys. Res.*, *115*, A03205, doi:10.1029/2009JA015070, 2010.

Subbotin, D. A., and Y. Y. Shprits, Three-dimensional modeling of the radiation belts using the Versatile Electron Radiation Belt (VERB) code, *Space Weather*, *7*, S10001, doi: 10.1029/2008SW000452, 2009.

Summers, D., and C.-Y. Ma, Rapid acceleration of electrons in the magnetosphere by fast-mode MHD waves, *J. Geophys. Res.*, *105*(A7), 15,887, 2000.

Summers, D., R. M. Thorne, and F. L. Xiao, Relativistic theory of wave-particle resonant diffusion with application to electron acceleration in the magnetosphere, *J. Geophys. Res.*, *103*(A9), 20,487, 1998.

Tascione, T. F., *Introduction to the Space Environment*, 116 pp., Orbit Book Company, Malabar, Florida, 1988.

Taylor, M. G. G. T., R. H. W. Friedel, G. D. Reeves, M. W. Dunlop, T. A. Fritz, P. W. Daly, and A. Balogh, Multisatellite measurements of electron phase space density gradients in the Earth's inner and outer magnetosphere, *J. Geophys. Res.*, *109*, A05,220, doi:10.1029/2003JA010294, 2004.

Temerin, M., I. Roth, M. K. Hudson, and J. R. Wygant, New paradigm for the transport and energization of radiation belt particles, *Eos Trans. AGU*, *75*, F538, 1994.

Thomas, V. A., and S. H. Brecht, Evolution of diamagnetic cavities in the solar wind, *J. Geophys. Res.*, *93*, 11,34111,353, 1988.

Thomsen, M. F., J. T. Gosling, S. A. Fuselier, S. J. Bame, and C. T. Russell, Hot, diamagnetic cavities upstream from the Earths bow shock, *J. Geophys. Res.*, *91*, 2961 2973, 1986.

Thomsen, M. F., V. A. Thomas, D. Winske, J. T. Gosling, M. H. Farris, and C. T. Russell, Observational test of hot flow anomaly formation by the interaction of a magnetic discontinuity with the bow shock, *J. Geophys. Res.*, *98*, 15,319–15,330, 1993.

Thorne, R. M., and L. J. Andreoli, Mechanism for intense relativistic electron precipitation, in *Exploration of the Polar Atmosphere*, pp. 381–394, Reidell Publishing Co., 1980.

Tsyganenko, N. A., H. J. Singer, and J. C. Kasper, Storm-time distortion of the inner magnetosphere: How severe can it get?, *J. Geophys. Res.*, *108*(A5), 1209, doi:10.1029/2002JA009808, 2003.

Tu, W., X. Li, Y. Chen, G. D. Reeves, and M. Temerin, Storm-dependent radiation belt electron dynamics, *J. Geophys. Res.*, *114*, A02217, doi:10.1029/2008JA013480, 2008.

Tu, W., X. Li, Y. Chen, G. D. Reeves, and M. Temerin, Storm-dependent radiation belt electron dynamics, *J. Geophys. Res.*, *114*, A02217, doi:10.1029/2008JA013480, 2009.

Turner, D. L., and X. Li, Quantitative forecast of relativistic electron flux at geosynchronous orbit based on low-energy electron flux, *Space Weather*, *6*, S05005, doi:10.1029/2007SW000354, 2008a.

Turner, D. L., and X. Li, Radial gradients of phase space density of the outer radiation belt electrons prior to sudden solar wind pressure enhancements, *Geophys. Res. Lett.*, *35*, L18101, doi:10.1029/2008GL034866, 2008b.

Turner, D. L., and X. Li, Using spacecraft measurements ahead of Earth in the Parker spiral to improve terrestrial space weather forecasts, *Space Weather*, under review, 2010.

Turner, D. L., X. Li, E. Burin des Roziers, and S. Monk, An improved forecast system for relativistic electrons at geosynchronous orbit, *Space Weather*, in preparation, 2010a.

Turner, D. L., X. Li, G. D. Reeves, and H. J. Singer, On phase space density radial gradients of Earth's outer-belt electrons prior to sudden solar wind pressure enhancements: Results from distinctive events and a superposed epoch analysis, *J. Geophys. Res.*, *115*, A01205, doi: 10.1029/2009JA014423, 2010b.

Ukhorskiy, A. Y., M. I. Sitnov, A. S. Sharma, B. J. Anderson, S. Ohtani, and A. T. Y. Lui, Data-derived forecasting model for relativistic electron intensity at geosynchronous orbit, *Geophys. Res. Lett.*, *31*, L09806, doi:10.1029/2004GL019616, 2004.

Vallado, D. A., *Fundamentals of Astrodynamics and Applications 2nd Ed.*, Published jointly by Microcosm Press and Kluwer Academic Publishers, El Segundo, CA and Dordrecht, The Netherlands, 2001.

Vampola, A. L., Measuring energetic electrons, in *Measurement Techniques in Space Plasmas: Particles*, edited by R. F. Pfaff, J. E. Borovsky, and D. T. Young, Geophysical Monograph, p. 102, American Geophysical Union, 1998.

Van Allen, J. A., and L. A. Frank, Radiation around the Earth to a radial distance of 107,400 km, *Nature*, *183*, 430, 1959.

Williams, D. J., A 27-day periodicity in outer zone trapped electron intensities, *J. Geophys. Res.*, *71*(7), 1815–1826, 1966.

Wolf, R. A., R. W. Spiro, S. Sazykin, and F. R. Toffoletto, How the earth's inner magnetosphere works: An evolving picture, *J. Atmos. Solar Terr. Phys.*, *69*, 288–302, 2007.

Zhang, H., et al., Evidence that crater FTEs are initial stages of typical FTEs, *J. Geophys. Res.*, *115*, A08229, doi:10.1029/2009JA015013., 2010.

Appendix A

Additional Details from the PSD Gradient Study

A.1 Introduction

This appendix describes three additional distinctive events from the study described in Chapter 4. These were originally included in the JGR paper, but were removed before submission due to excessive length and detail. I have included them here since they do show some very interesting features that are beneficial to the study in a broader context of overall understanding. The three events discussed include 1) an example of those events that reveal negative gradients beyond GEO for the full range of μ studied but no prior evidence of loss at higher-L due to magnetopause shadowing; 2) an example of an event that reveals all flat gradients for the full range of μ in which the preconditions in the solar wind and magnetosphere were very calm; 3) an event that reveals peaks in the PSD radial profile beyond GEO for the electrons with μ greater than a couple hundred MeV/G, but no such peak in the profiles for electrons with μ lower than this. Note that the naming convention for these events uses Types 1-6, which was not carried over into the JGR publication. Types 1, 4, and 6 are described in this appendix, while Types 2, 3, and 5 are those cases detailed in the JGR work.

A.2 Additional Distinctive Events

A.2.1 Event Type-1: PSD Full-Range Dropout with No Evidence of Magnetopause Shadowing

The first type of distinct event is that in which there is a decrease in PSD over a full range of μ's immediately following the shock impact with no indication of magnetopause shadowing prior to the event. We use the *Petrinec and Russell* [1996] magnetopause model as an indicator of magnetopause shadowing beyond GEO to distinguish between this type of event and the second type (discussed following this). We classify an event as a Type-1 event if the magnetopause does not come inside of 8.5 R_E at any point in the two days leading up to the event. We have chosen 8.5 R_E because of results from test-particle simulations by *Li et al.* [2003], which show approximately how far outer belt electrons are transported radially inwards during a shock event. Figure A.1 shows the solar wind parameters and geomagnetic indices for five days leading up to the event and one day after it. Note for this event that in the days leading up to the shock, the solar wind is significantly calm, with velocity no higher than 500 km/s, but there are strong southward turnings of the IMF at around -54 and -15 hours epoch time (ET). These correspond to enhancements in the AE and KP indices. From the Dst index plot, there were no significant storms in the days leading up to the shock. However, there is some intermittent geomagnetic activity before the event (apparent in the AE and Kp indices), particularly at >80 hours, ~60-68 hours, ~36-52 hours, and ~0-14 hours before the event time, which correspond to a couple small dynamic pressure enhancements and periods of southward IMF.

Figure A.2 shows GEO electron fluxes for this event measured by LANL spacecraft 1991-080, which is at 17:13 LT at the time of the shock. Notice here that when the shock impacts the magnetosphere the flux increases for the lower energy channels and decreases for the higher energy channels, but as is evident in Figure A.2, when the magnetic field compression is used to calculate the PSD for fixed μ's for this event (black curves with '+' marks), it is apparent that the PSD for μ's = 50, 200, 750, and 2000 MeV/G all drop significantly after the shock impact, which is direct

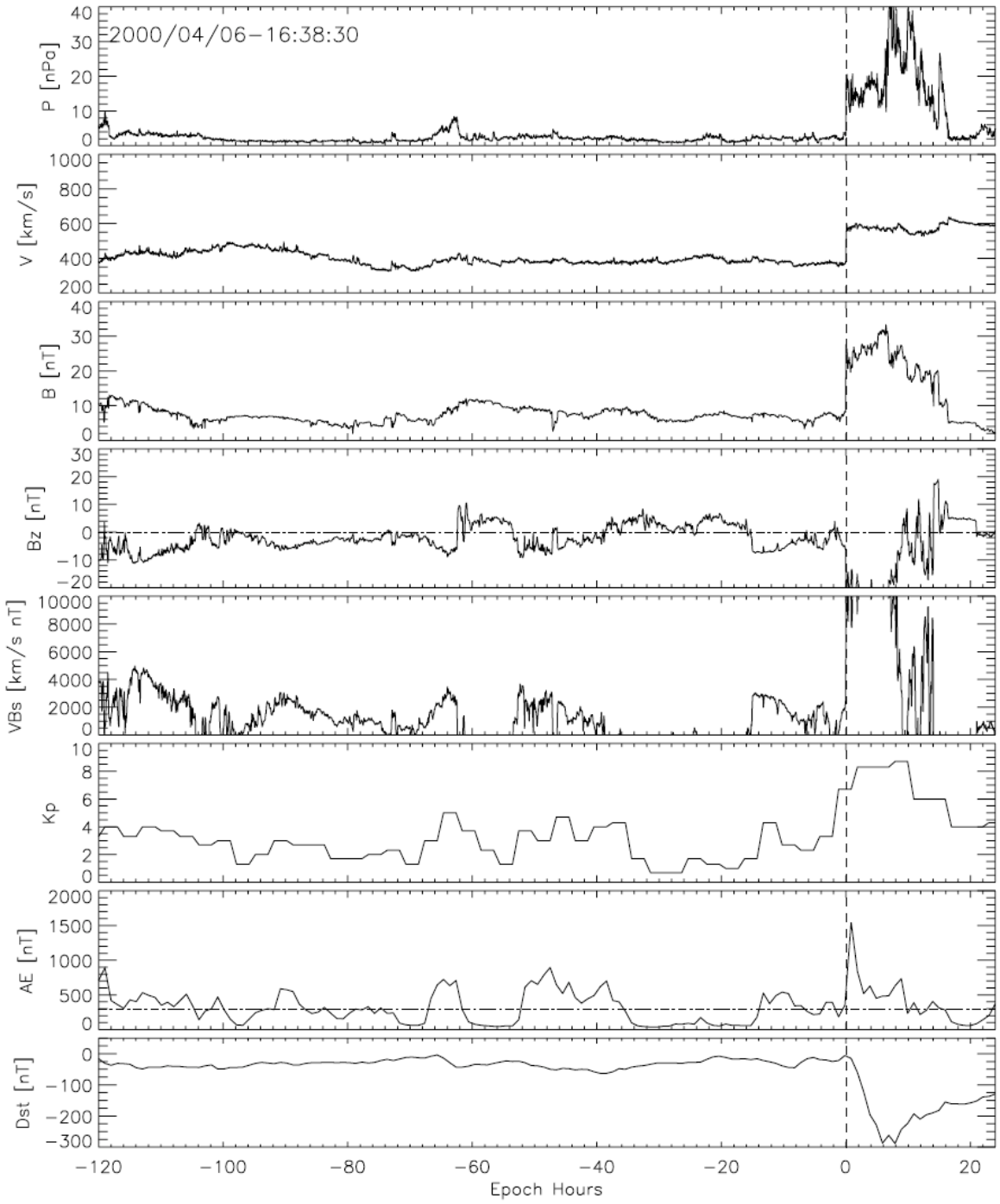

Figure A.1: Solar wind and geomagnetic conditions for five days before and one day after an event on 6 April 2000. Epoch time is given in the top left.

evidence that the PSD gradient beyond GEO is negative over this broad range of μ. There is no evidence in the flux data from the two days leading up to the shock of any loss. In fact, the fluxes from all four energy channels are higher right before the shock than they were at -48 hrs ET. This implies that there was some source active during this time and also that this source was overcoming electron loss over a broad range of energies (10's keV to>1 MeV). In addition to this, since there was no magnetopause shadowing to cause loss at higher L^* and the PSD results show that there is insufficient source at higher L^*, we must conclude that the source was located somewhere inside of GEO in the days leading up to this event.

A.2.2 Event Type-4: PSD Full-Range Flat

Type-4 events are those in which the PSD for a wide range of μ's remains relatively flat after the event. Figures A.3 and A.4 show the solar wind, geomagnetic indices, and fluxes prior to an all-flat gradient event on 27 March 2001. Similar to the example of the all-positive gradient event in Chapter 4, the solar wind and geomagnetic conditions are quite calm for more than two days before the event. However, starting at around -110 hours ET, solar wind pressure and IMF activity correspond well to a couple days of magnetospheric activity, evident in the Kp and AE indices. As with the previous example, we show fluxes from two LANL satellites since the one used to calculate the PSD (1991-080 at 14:51 LT at the time of the shock) has data gaps in the days leading up to the event. From the fluxes measured by1994-084, which is at 08:36 LT at the time of the shock, note how the 1.1-1.5 MeV flux steadily increases from around -39 hours ET up to the time of the shock. Since at the time of the shock the PSD gradient is relatively flat, this could be the result of two different acceleration scenarios: 1) a PSD peak formed from a source inside of GEO during the active period from around -60 hrs to -110 hrs epoch time, which then diffused outwards, increasing the flux at GEO and smoothing the PSD radial profile over the next two and a half days, or 2) PSD was high at higher L^* several days prior to the event and diffused inwards resulting in the flux increase and flat profile. However, for the second scenario to be relevant, the source at higher L^* must have turned off at some time prior to the event to allow the PSD profile to come to a steady

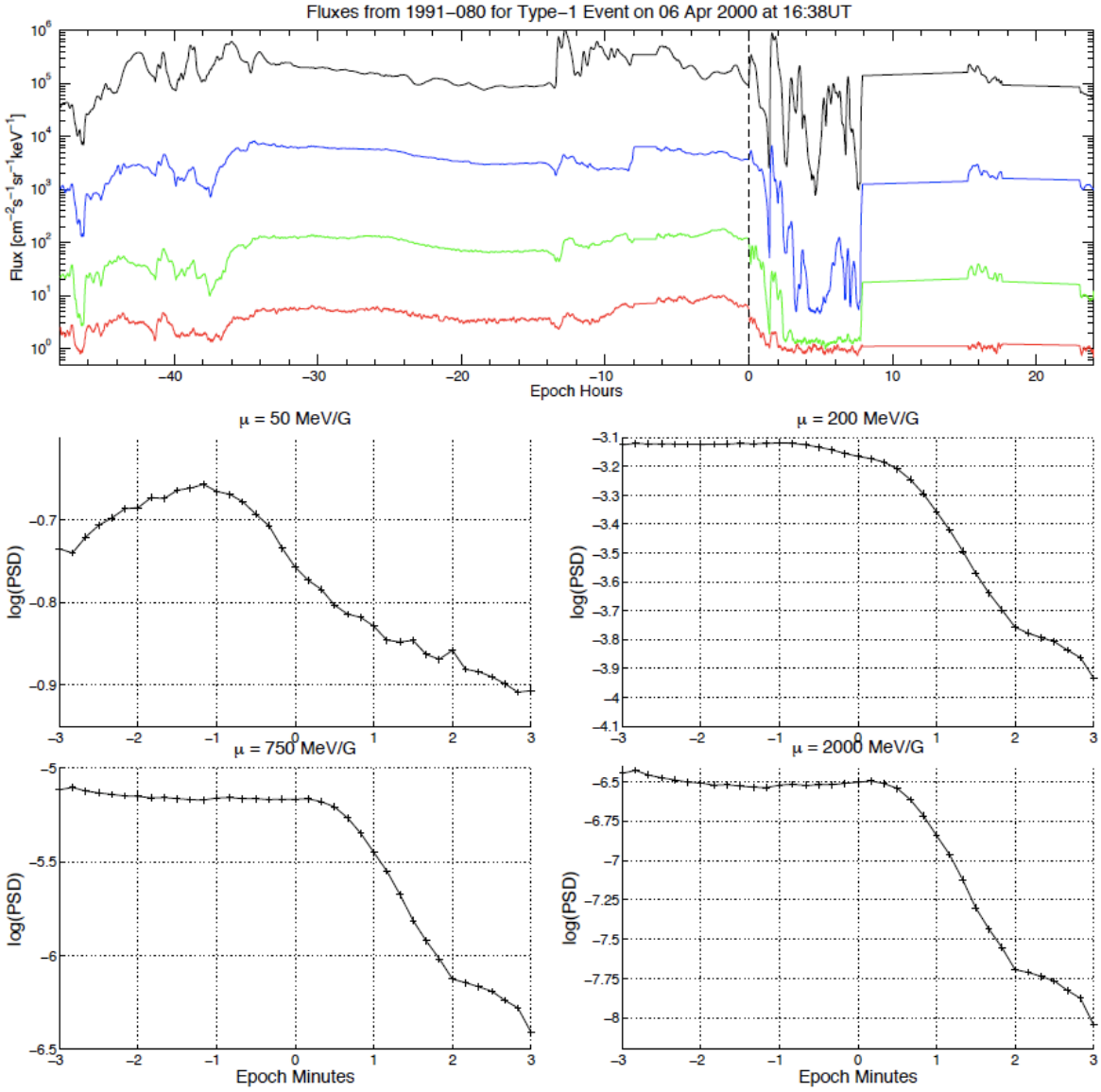

Figure A.2: (top) Electron fluxes from LANL satellite 1991-080 for the 6 April 2000 event. Epoch time is the same as that for Figure 4.7. Fluxes are shown from four different energy channels: 50-75 keV (black), 150-225 keV (blue), 500-750 keV (green), 1.1-1.5 MeV (red). For further details, see discussion in text. (bottom) Phase space density results from this event shown in the same format as Figure 4.6.

(flat) state, which could be explained by the period of enhanced substorm activity between around -107 hrs to -38 hrs ET that is evident in both the AE data (Figure A.3) and flux data (not fully shown; for further evidence look at 23-24 March 2001 flux plots available on the LANL website) and is followed by a period of relatively little activity for the last day and a half leading up to the event.

Very different conditions seem to be able to result in these flat PSD gradients, which is probably partially due to other types of events being misclassified as all-flat if their PSD doesnt change by more than 10% of the pre-shock average. The examples from the all-negative event with magnetopause shadowing (from Chapter 4) and this event are good evidence of this ambiguity; the shock event at -9 hrs ET in the Chapter 4 example (Figure 4.7) is preceded by around two days of very active conditions both in the solar wind and the magnetosphere, whereas this example is preceded by two days of relatively calm conditions. This is testament to the complexity of the outer belt electrons' nature, though both cases are apparently linked by substorm injections of electrons over a large range of energy sometime between 1 and 3 days prior to the time in which the flat gradients are observed.

A.2.3 Event Type-6: Apparent PSD Peak

The final, and most rare, type of distinct event is that where a distinct peak is observed in the PSD for higher energy electrons after the shock impact. The peaks are not just spikes between data points but display coherent and continuous increases and decreases in the PSD over several measurements after the shock impact. Once again, since particles are being transported inwards past the spacecraft taking measurements, the PSD temporal profile for electrons with constant μ immediately after the event is the same as part of the PSD radial profile beyond GEO. Thus, a peak in the temporal profile (see PSD results in Figure A.6) is evidence of a peak in the PSD radial profile, which would pinpoint the location of in situ heating. From Figure A.6, one can see from the Type-6, red curves with 'x' marks that peaks are visible in the profiles for electrons with μ = 200, 750, and 2000 MeV/G but not for 50 MeV/G. This is also similar to the results from the

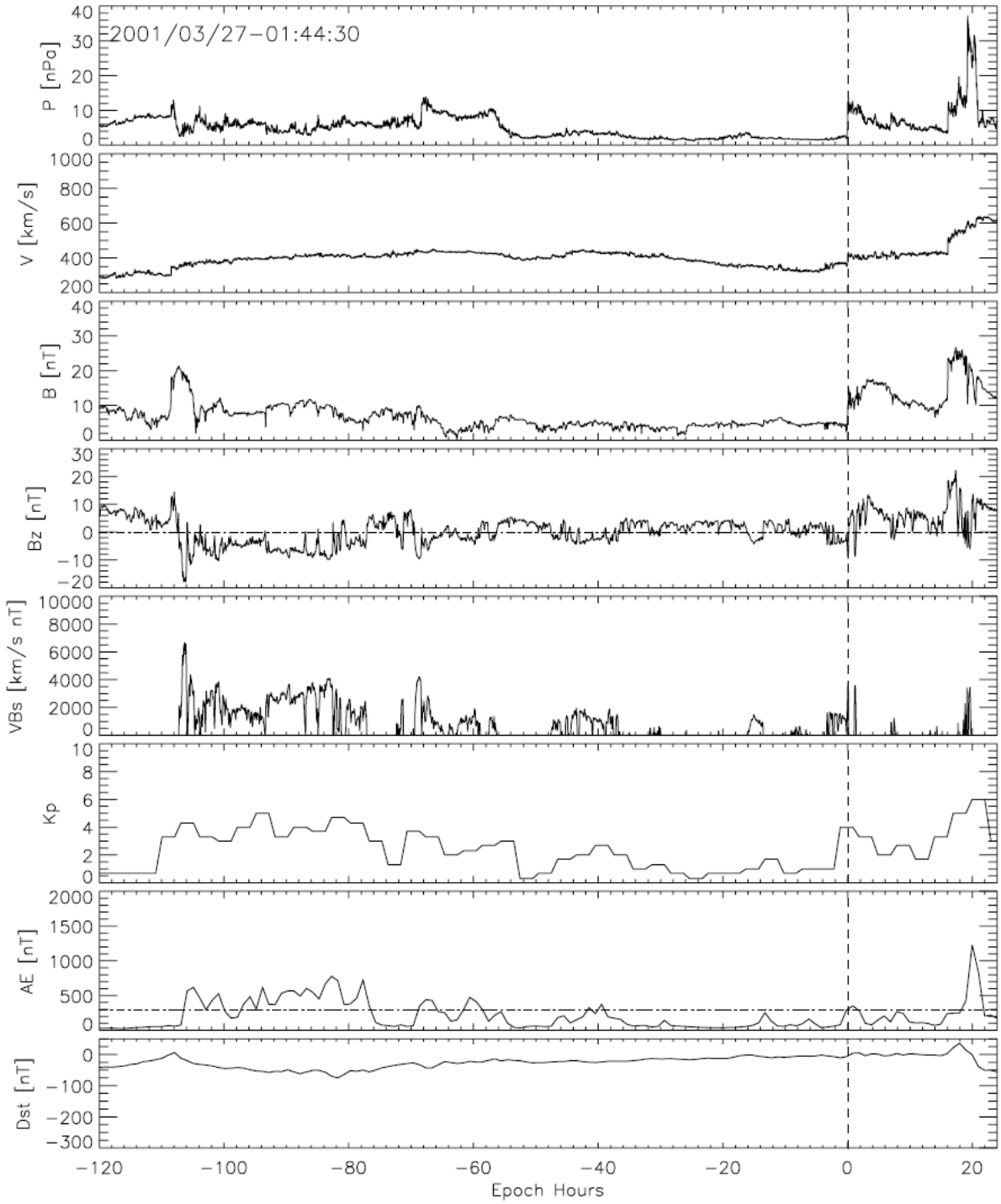

Figure A.3: Solar wind and geomagnetic conditions for five days before and one day after an event on 27 March 2001. Epoch time is given in the top left.

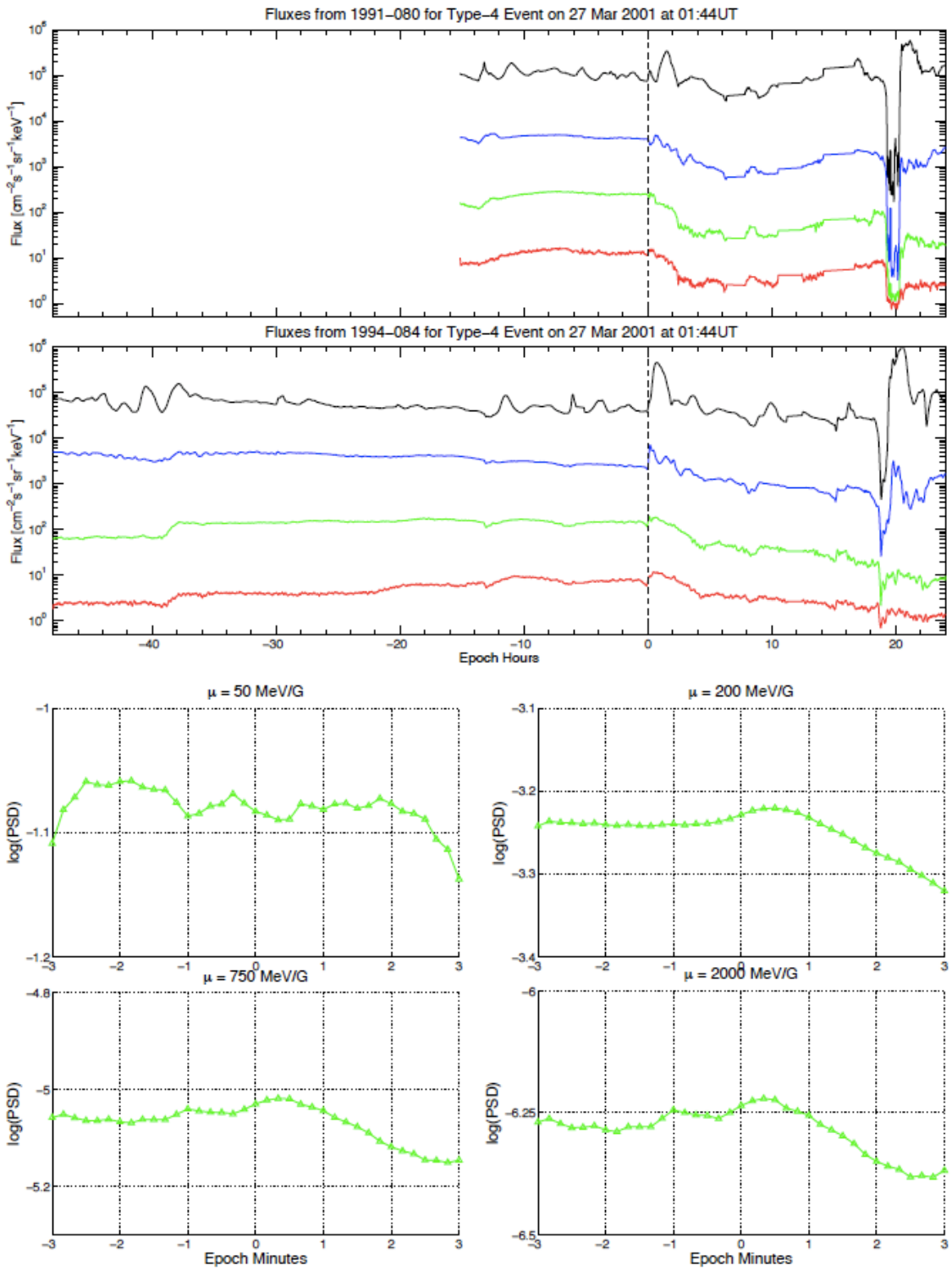

Figure A.4: (top and middle) Electron fluxes from LANL satellite 1991-080 and 1994-084 for the 27 March 2001 event. Epoch time is the same as that for Figure 4.7. Fluxes are shown from four different energy channels: 50-75 keV (black), 150-225 keV (blue), 500-750 keV (green), 1.1-1.5 MeV (red). For further details, see discussion in text. (bottom) Phase space density results from this event shown in the same format as Figure 4.6.

second case in which a peak is evident: peaks are visible in the μ = 750 and 2000 MeV/G profiles but not in the 50 or 200 MeV/G ones.

Concerning the preconditions to this event, Figure A.5 shows the solar wind and geomagnetic index data. Note that overall, the solar wind conditions in the days leading up to the event are calm, with average solar wind speeds and no significant pressure enhancements, though IMF-Bz is most often southward during the time shown. This southward IMF is likely responsible for the considerable and increasing levels of the AE and Kp indices leading right up to the event itself. Substorm activity is also evident in the last two days leading up to the event from the LANL flux data shown in Figure A.6. After the event, the flux data sees massive fluctuations, which are likely due to the spacecraft transitioning between regions of open and closed electron drift paths.

A.3 Discussion

A.3.1 All-Negative Gradients

Each of the 86 events evaluated for this study can be classified into one of six distinct "types" based on their PSD results for electrons with different μs. The first type of event, referred throughout as Type-1, is that in which the PSD gradient is negative for electrons with μ = 50 MeV/G, 200 MeV/G, 750 MeV/G, and 2000 MeV/G but there is no indication of loss at higher L^* due to magnetopause shadowing for several days before the event. Negative gradients beyond GEO with no evidence of loss at higher L^* could either imply that there is a source inside of GEO for these electrons or that there was a source at higher L^* that was stronger at some previous time but then got weak resulting in a peak inside of GEO (see discussion for Type-6 events below and in *Chen et al.* [2007b]), though from the results presented here, it appears that the former is most likely the case since AE activity is strong prior to Type-1 events.

As discussed briefly in the Conclusion section of Chapter 4, the all-negative gradient events in which there is no evidence of magnetopause shadowing prior to the observations can also be explained by electrons at L-shells higher than GEO undergoing bifurcated drift orbits, called Sha-

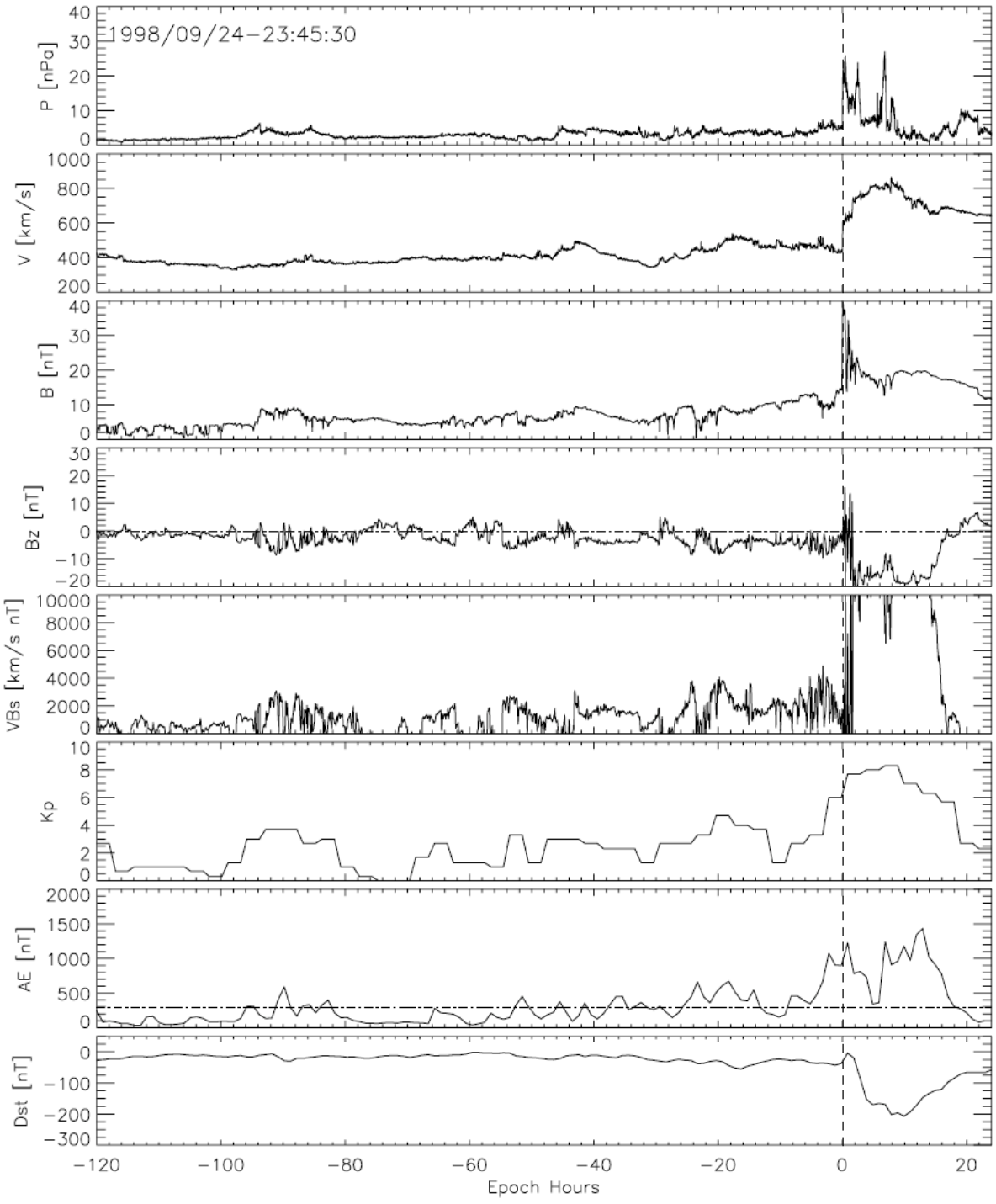

Figure A.5: Solar wind and geomagnetic conditions for five days before and one day after an event on 24 September 1998. Epoch time is given in the top left.

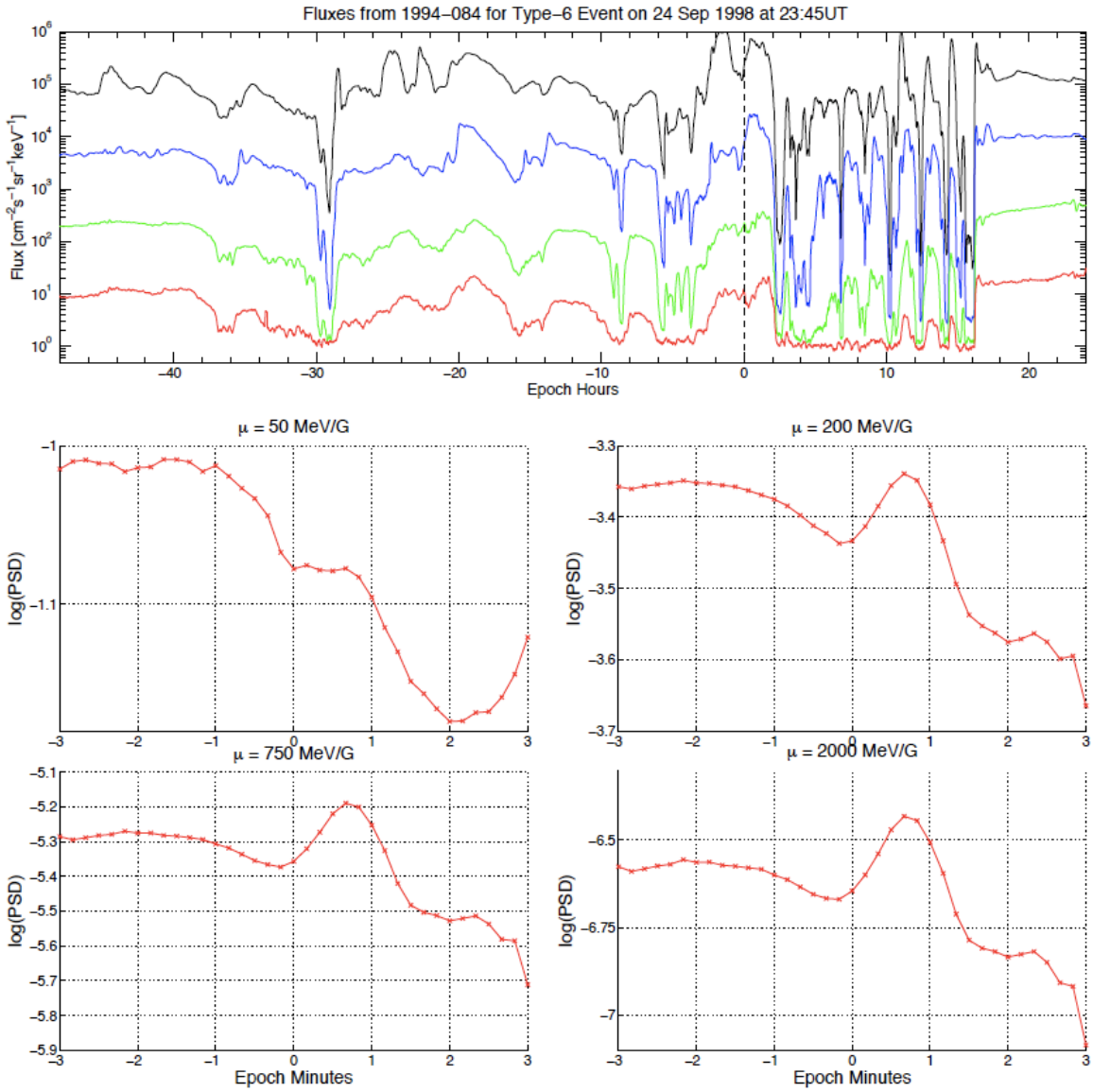

Figure A.6: (top) Electron fluxes from LANL satellite 1994-084 for the 24 September 1998 event. Epoch time is the same as that for Figure 4.7. Fluxes are shown from four different energy channels: 50-75 keV (black), 150-225 keV (blue), 500-750 keV (green), 1.1-1.5 MeV (red). For further details, see discussion in text. (bottom) Phase space density results from this event shown in the same format as Figure 4.6.

bansky orbits [*Shabansky and Antonova*, 1968], on the dayside magnetosphere. When the dayside magnetosphere is compressed to a state in which the minimum B_{Tot}, i.e. B_{min}, locations are shifted off the traditional magnetic equator (magnetic latitude of 0°), trapped particles at the L-shells affected will bounce around these off-equatorial B_{min} pockets. Thus, if the pitch angle distributions are peaked around 90°, a spacecraft at magnetic latitude of 0° will actually measure lower fluxes than it would closer to the latitudes where the B_{min} pockets are located. So for the study described in Chapter 4, if electrons are transported radially inwards near the equatorial plane, the flux measurements from higher-L can be affected by these Shabansky orbits in such a way that could result in all-negative PSD gradient events that cannot be explained by previous loss at high-L to the magnetopause.

A.3.2 All-Flat Gradients

The results from the two Type-4 events discussed here (Type-4 event example and the Type-4 event that occurred at -9 hrs ET in the all-negative event example from Chap. 4) demonstrate the very different conditions that can result in relatively flat gradients beyond GEO. The vast differences in preconditions leading up to Type-4 events explain the ambiguity in the superposed epoch results when they are included. Part of this may be from event misclassification as Type-4 if the PSD after the shock does not change by at least 10% of the pre-shock average. For example, of the 4 red events (mixed Type-4 and Type-5) that lie above the AE^* > 300 nT line in the superposed epoch analysis, only one of them, the Type-5 on 12 October 2000, has a positive change in PSD for 2000 MeV/G electrons; the other four see a negative change in PSD, just not enough to qualify them as a negative gradient event. However, nearly flat gradients imply that radial diffusion, either inward or outward, has smoothed the gradient beyond GEO.

A.3.3 Evidence of a Peaked Gradient

The results from two events show a peak in the radial gradient for electrons with energies above a couple hundred keV though not for electrons at lower energies; these have been classified

as a sixth type of event. Discussions in *Green and Kivelson* [2004] and *Chen et al.* [2007b] present some of the situations that might lead to a peak in PSD at higher L^*. If the PSD gradient is originally positive, a loss at higher L^* can create a peak in PSD [see Figure 3 and discussion in *Green and Kivelson*, 2004]. Another scenario producing a PSD peak is when a source population in the plasma sheet increases for some time and then decreases. This scenario brings the source PSD at higher L^* up initially and then drops it, leaving a high peak at some lower L^* [see Figure 1 and discussion in *Chen et al.*, 2007b]. A third scenario is that in which local heating of electrons results in a peak in PSD at the L^* where the heating is taking place. The example Type-6 event discussed here has relatively calm solar wind preconditions, and the PSD peak is not apparent in the 50 MeV/G electron results (see Figure A.6). These likely rule out the first scenario, in which loss at higher L^* results in a peak. Concerning the second scenario, there is evidence of substorm activity, evident from the AE index and flux data in Figures A.5 and A.5 , in the days leading up to the event, though this stays high up to the event time, so the increase-decrease scenario is unlikely. This leaves local acceleration as the most likely candidate. In support of the local acceleration scenario, there is significant substorm activity in the days leading up to the event, which is indicative of enhanced whistler-mode chorus and magnetosonic wave activity [e.g. *Meredith et al.*, 2001; *Shprits et al.*, 2007b; *Meredith et al.*, 2008]. This is supported by data displayed in Figure A.7, which shows VLF measurements taken from Halley Station, Antarctica (L∼4.3) for 5 of the 6 example events. Here, omni-directional intensities are shown for narrow passband filters centered on frequencies of 1 kHz (black) and 3 kHz (red). *Smith et al.* [1996] use VLF measurements from Halley Station to study 243 substorm-related chorus events in 1992, and *Horne et al.* [2005b] use Antarctic ground measurement of VLF to provide evidence of chorus waves near the magnetic equator, since it is there that the waves are generated. The diurnal variation in the data (most evident for the Type-1 event) is from measurements taken during daylight (lower) and nighttime (higher) [*Horne et al.*, 2005b]. For the Type-6 event, note the strong enhancement in 3 kHz data in the days leading up to the event. *Meredith et al.* [2001] discuss how chorus emissions are strongest during active conditions (AE $>$ 300 nT) and outside of the plasmapause ($3 < L < 7$), and L_{pp} stays inside of 4.5 R_E in the

five days leading up to this event according to the models of *Carpenter and Anderson* [1992] and *O'Brien et al.* [2003]. If this peak in PSD is indeed the result of local acceleration by wave-particle interactions, it is important to note that it occurs outside of GEO. This is well beyond the distance, L $\sim$ 4-5, at which others have reported evidence of peaks [e.g. *Green and Kivelson*, 2004; *Chen et al.*, 2005, 2007a, b], but the recent findings of *Li et al.* [2009] show that chorus activity can be strong at L $>$ 7 on the dayside. Based on the results here, these peaks in PSD beyond GEO are probably not common occurences.

The second Type-6 event (results not shown) is much more ambiguous. There is a strong solar wind pressure enhancement at around -40 hours epoch time, which is accompanied by $\sim$15 hours of high AE ($>$ 300 nT). In the last $\sim$35 hours leading up to the event, the pressure returns to normal levels and the AE drops below 300 nT. Thus, the first two peak-generating scenarios listed above cannot be ruled out for this case, though it is interesting to note that the PSD results for this event reveal a positive gradient for 50 MeV/G and 200 MeV/G electrons with evidence of a peak only apparent in the 750 MeV/G and 2000 MeV/G results.

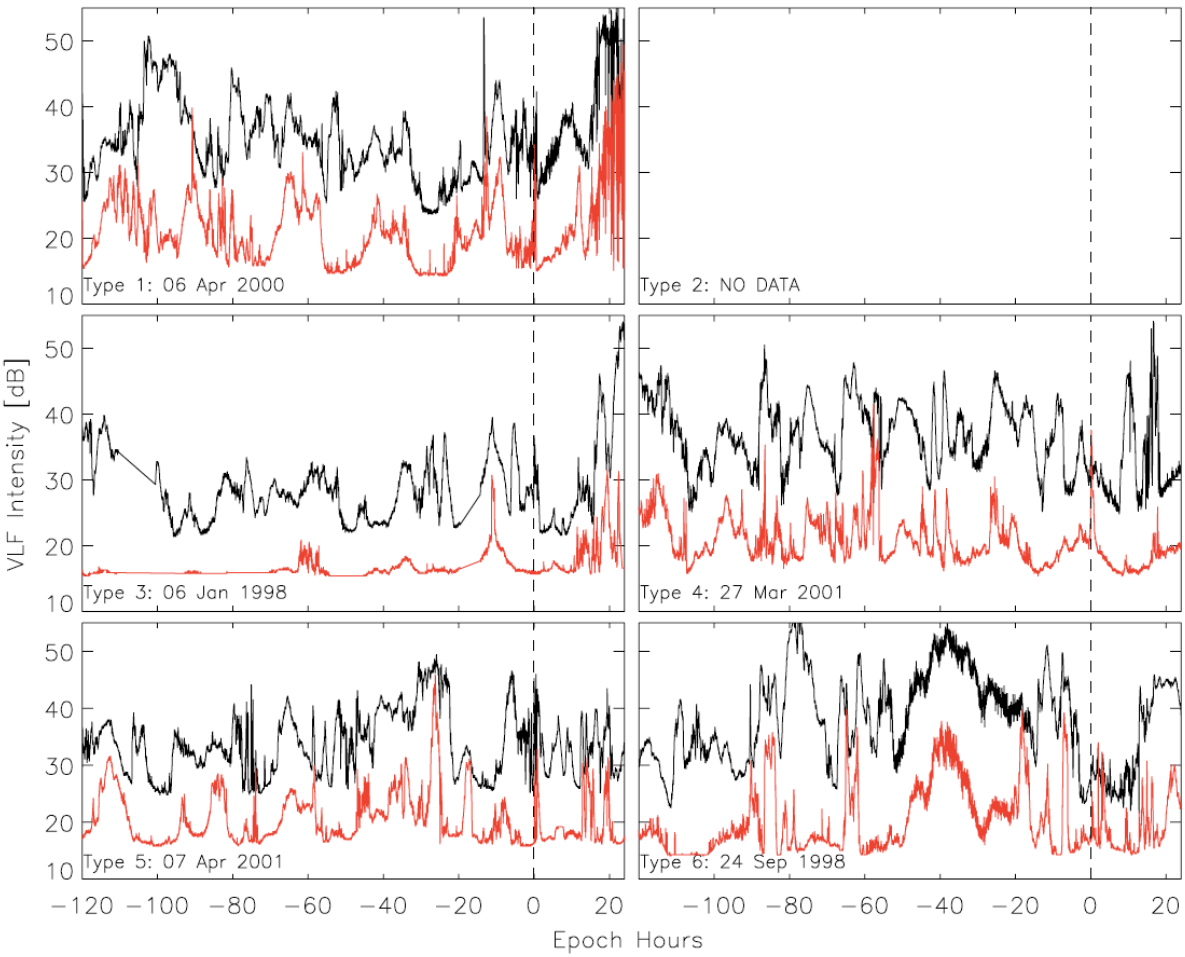

Figure A.7: Omni-directional VLF intensities from narrow passband filters centered around 1 kHz (black) and 3 kHz (red) measured at Halley Station, Antarctica for the six example events. Epoch times are the same times used for each event example.

Appendix B

Additional Details from the L^*_{max} Study

B.1 Approximating L^*_{max} as a Function of Two Quantities

To determine the independent variations in L^*_{max} for both the Kp index and solar wind dynamic pressure, we look at the relationship between L_{max} and each parameter for times when the other parameter is near to it's long term average. First, we compare L_{max} and Kp for times when the solar wind dynamic pressure is within 0.25 nPa of its average value from June 2007 - June 2009, which is 1.68 nPa. Figure B.1 shows the results. Here, each * shows the average of the L_{max} observations for each corresponding Kp. The numbers above the error bars display the amount of data points that contributed to each point shown. This data is best fit using least squares and a quadratic equation of the form seen in Figure B.1. A quadratic fit to Kp results in smaller residuals and better overall results than either a linear or power law fit. Note that the statistics here are weak, and ultimately so is the fit, which is evidence that L_{max} has a weak relation to Kp. However, as previously mentioned, adding the Kp dependence in this quadratic form does help the model results overall.

Figure B.2 shows the results for L_{max} compared with the solar wind dynamic pressure when the Kp index is within 0.5 of 1.34, its average from June 2007-June 2009. As *Shue et al.* [1997] found for the magnetopause location, the radial distance of the last closed drift shell on the nightside can be best-fit using a power law form for solar wind dynamic pressure. Unlike Figure B.1, we have not averaged L_{max} for bins of dynamic pressure since the pressure can have a broad range of values while the Kp index values are restricted. Based on these results, we can establish an analytical

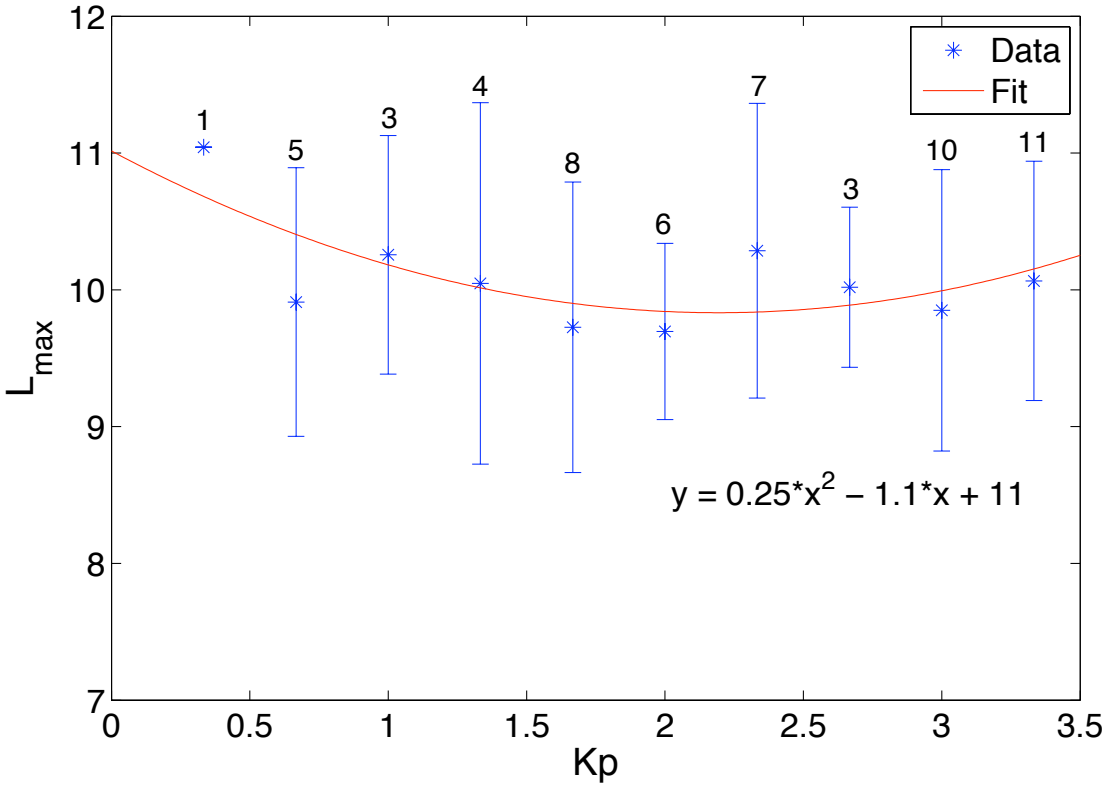

Figure B.1: L_{max} fit to Kp when P_{dyn} is held constant. Standard deviation error bars are shown since each data point is an average of the different L_{max} values for the each Kp. The number of points going into those averages are shown above the standard deviation bars. A quadratic fit is also shown.

form for the last closed drift shell radius using a combination of both the quadratic fit for the Kp index and the power law fit for the dynamic pressure:

$$L_{model} = [a * (Kp)^2 + b * Kp + c] * P^{\gamma} \tag{B.1}$$

where L_{model} is the L_{max} in R_E to the last closed drift shell, Kp is the Kp index, P is the one hour average of the solar wind dynamic pressure, and a, b, c, and γ are tuneable parameters.

To tune the parameters for this multi-variable equation, we resort to a simplex routine that maximizes the prediction efficiency of the results when compared to the original observations. Using the simplex routine to optimize a, b, and c for a range of different γ's, the best PE, PE = 0.23, results when a = 0.1378, b = -0.8977, c = 9.9501, and γ = -0.0369. For comparison with the other models, the standard deviation of the error when the model is compared to the observations is 0.79 R_E.

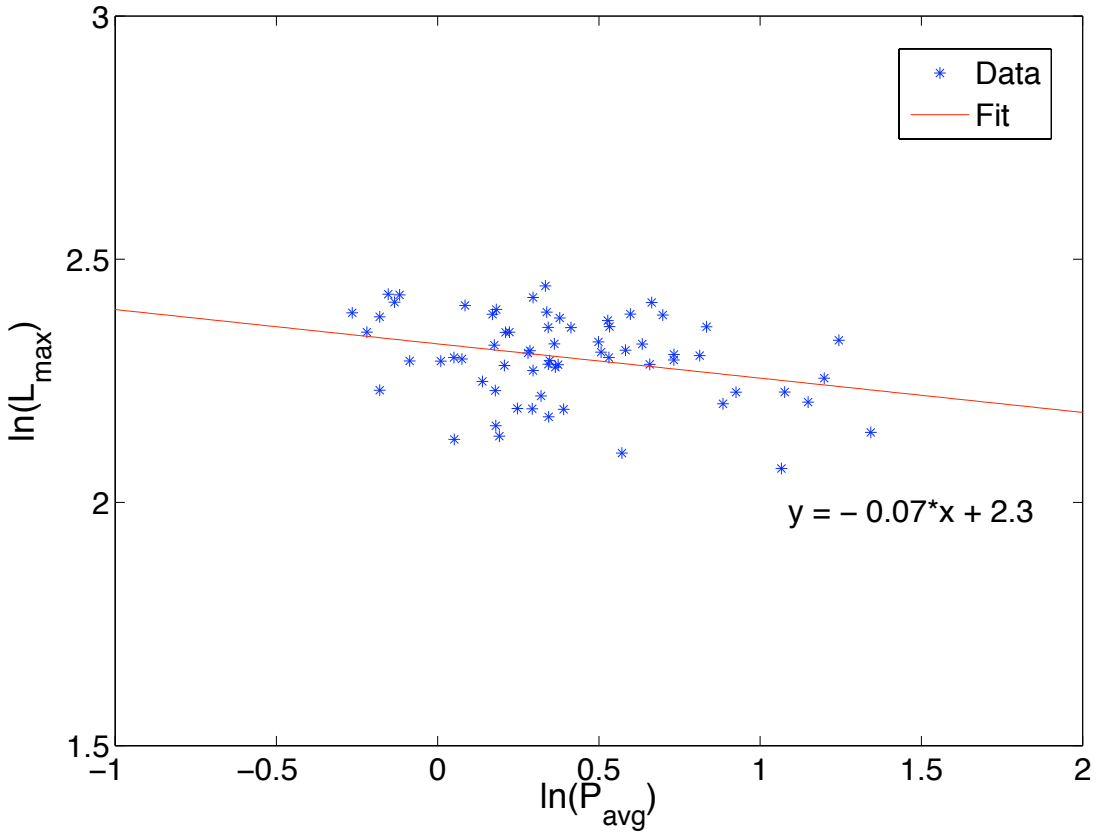

Figure B.2: L_{max} fit to P_{dyn} when Kp is held near its long-term average. A linear fit to the log-log results is also shown.

Appendix C

***THEMIS multi-spacecraft observations of a magnetopause disturbance exhibiting distinct plasma flows and an abnormal compression of plasma density* by D. L. Turner et al., under review for JGR**

C.1 Introduction

This work is a result of my work on the last closed drift shell using THEMIS. I noticed this event in the data and marked it as something interesting to show some people who were more expert in the field. With their support, I ended up writing the following paper, which allowed me to venture outside of my radiation belts comfort zone and explore the area of magnetopause disturbances. I include this work here as an example of how versatile and useful multi-spacecraft missions, like THEMIS and the upcoming RBSP missions, truly are to space science.

C.2 *THEMIS multi-spacecraft observations of a magnetopause disturbance exhibiting distinct plasma flows and an abnormal compression of plasma density* by D. L. Turner, S. Eriksson, W. Tu, W. Liu, T. D. Phan, X. Li, V. Angelopoulos, J. P. McFadden, and K. -H. Glassmeier, under review for JGR

C.2.1 Abstract

Large-scale magnetopause disturbances can result from several different types of events, such as flux transfer events (FTEs), foreshock cavities, hot flow anomalies, and solar wind pressure pulses. Here, we report on multipoint THEMIS observations of a magnetopause disturbance along

the dawn-side, equatorial flank that exhibits distinct flows in the magnetospheric plasma being displaced around it and an abnormally strong compression of the plasma density throughout its center, which peaks at $> 7\times$ the density of the near-Earth solar wind. In this observational report, we discuss the event's features, investigate the plasma distributions associated with the flows, and provide some speculation on the observation of the intense density compression associated with this disturbance. We find that the fastest ion and electron flows are related to two different processes: the ion flows resulting from plasma being displaced around the disturbance and the electron flows related to magnetic reconnection. We conclude that the event is most likely the result of a region of compressed sheath plasma at the edge of a foreshock cavity. We present a relatively simple schematic of the event that explains many of the observed features and discuss possibilities for the intense density enhancement. We propose that the most likely scenario is that the enhancement was the result of enhanced compression as this foreshock cavity interacted with the magnetosheath and magnetopause. However, an alternative scenario presents an interesting question: if the same feature in the IMF resulted in both a foreshock cavity and a FTE, how would the two features interact? We suggest that reconstruction and detailed simulations of this event should prove to be particularly beneficial to our understanding of magnetopause disturbances and the complex nature of solar wind - magnetosphere interactions.

C.2.2 Introduction

Several types of transient events that occur near or at the magnetopause can result in large-scale magnetopause deformation. Such events are important to solar wind - magnetosphere interactions because they can result in plasma mixing between the magnetosheath and the magnetosphere. Magnetopause disturbances can result from any of several different phenomena such as flux transfer events (FTEs) [e.g. *Owen et al.*, 2008], foreshock cavities [e.g. *Sibeck et al.*, 2002], hot flow anomalies (HFAs) [e.g. *Jacobsen et al.*, 2009], and solar wind pressure pulses [e.g. *Sibeck*, 1990]. There is still a great deal of uncertainty in determining the causes of magnetopause disturbances due to the ambiguity in various observations of these different phenomena. This ambiguity can

arise from similar features in the different phenomena, a lack of multipoint measurements, and/or a lack of near-Earth solar wind or magnetosheath measurements. The following subsection briefly introduces each of the different types of phenomena before we lead into this observational report of an interesting magnetopause disturbance observed on 21 November 2008.

C.2.2.1 Magnetopause Disturbances

Flux Transfer Events: FTEs have been the subject of intense investigations in the past 30 years since they were first observed and modeled [*Russell and Elphic*, 1978]. FTEs appear frequently in observations from spacecraft crossings of the dayside magnetopause [*Kawano and Russell*, 1997] and display characteristic features that have provided insight into their origin and nature. Based on observations, simulations, and theory, FTEs are thought to be signatures of magnetic reconnection[e.g. *Russell and Elphic*, 1978; *Sibeck et al.*, 2008]. This is further supported by statistical studies, which reveal that FTEs occur more frequently on the dayside during periods of southward interplanetary magnetic field (IMF) [e.g. *Kawano and Russell*, 1997, and references therein]. The reconnection process converts magnetic energy stored in the field to plasma energy by reconfiguring the magnetic field topology resulting in particle jets, and as this region of distorted fields (i.e. the FTE) moves along the magnetopause, fast plasma flows develop around it [*Korotova et al.*, 2009]. Some FTE models [i.e. *Lee and Fu*, 1985; *Southwood et al.*, 1988; *Scholer*, 1988a] proposed that extended reconnection X-lines (either multiple or single) can result in FTEs that are extended along the magnetopause. These extended FTEs could potentially complicate the interpretation of spacecraft data. Many models of FTEs exist, with each being proposed to explain features of FTEs observed in-situ by various spacecraft; for a good discussion on the various FTE models, see *Fear et al.* [2008].

The most characteristic feature in observations of FTEs is a bipolar signature in the magnetic field component in the direction normal to the magnetopause (B_N), and this coiled-field feature is often accompanied by enhancements in the total magnetic field strength [*Russell and Elphic*, 1978]. Reconnection that occurs from magnetospheric and magnetosheath field lines that have a

finite shear angle produces a strong guide field through the resulting FTE's core [*Scholer*, 1988b]. However, FTEs with weak core field strengths may also form; these are referred to as "crater" FTEs [e.g. *Sibeck et al.*, 2008, and references therein] due to their characteristic B_{Tot} field signatures with enhancements on either side of an overall depression. Recently, *Zhang et al.* [2010] have proposed that crater FTEs are simply the early stages of the more commonly observed FTEs with enhanced fields through their cores. They based this theory on statistical and individual event studies of FTEs observed between May and October of 2007.

FTEs have recently been simulated numerically [e.g. *Raeder*, 2006; *Omidi and Sibeck*, 2007; *Sibeck et al.*, 2008]. Of these, *Raeder* [2006] used a global MHD model to generate FTEs along the magnetopause and compare simulated spacecraft observations with real observations of FTEs. *Omidi and Sibeck* [2007] used 2.5-dimensional, global hybrid simulations to study FTEs and their interactions with the cusps, which disintegrate the FTEs through further reconnection. Both of these simulations reveal features of FTEs that are commonly observed by real spacecraft. However, strong density compressions, with factors of greater than eight times the density of the solar wind, are also observed within these simulated FTEs. These simulated compression factors are more than the expected factor of 4 in the magnetosheath resulting from the Rankine-Hugoniot jump conditions across the bow shock, and density enhancements on this order have not yet been observed from in-situ spacecraft measurements of FTEs along Earth's magnetopause.

Foreshock Cavities: The foreshock is the region upstream of Earth's bow shock characterized by particles flowing away from the bow shock (i.e. backstreaming) along the IMF field lines that intersect the shock. Foreshock cavities are a relatively common phenomenon that result from kinetic interactions between foreshock and solar wind plasmas [e.g. *Sibeck et al.*, 2002]. Near the bow shock, these cavities of depressed density and field strength, which result from expanding regions of enhanced fluxes of suprathermal ions backstreaming along field lines connected to the bow shock, can form between regions of field lines that are disconnected from the bow shock. In such cases, kinetic interactions result in the solar wind upstream of the bow shock being modified such that it produces crater like features in the total magnetic field strength and number density

as the regions on either side of the expanding, lower-density cavity undergo compression. *Thomas and Brecht* [1988] presented a model consistent with this in which hybrid simulations were used to demonstrate how a beam of backstreaming ions could produce such features in solar wind plasma. Foreshock cavities are not uncommon features, which was a result demonstrated by *Sibeck et al.* [2001], who conducted a study of the foreshock using IMP 8 data from January to August 1995 and found 292 foreshock cavities during this period. Foreshock cavities need not be associated with IMF discontinuities [*Sibeck et al.*, 2002], though such IMF variations can move a foreshock cavity past a spacecraft [e.g. *Sibeck et al.*, 2000].

Fairfield et al. [1990] presented observational evidence that pressure changes in the solar wind resulting from the foreshock (i.e. foreshock cavities) can propagate through the bow shock and magnetosheath and impinge on the magnetosphere. Similar to solar wind dynamic pressure variations (discussed below), the pressure variations generated by a foreshock cavity result in magnetopause motion, either inward or outward depending on the variation, to maintain the pressure balance at the boundary [e.g. *Sibeck et al.*, 2000]. The features generated by such pressure variations and consequent magnetopause motion would be similar to those described for solar wind pressure variations, which have been mistaken previously for features associated with FTEs [*Sibeck*, 1992].

Hot Flow Anomalies: Hot flow anomalies (HFAs) were first discussed in *Schwartz et al.* [1985] and *Thomsen et al.* [1986]. They are associated with current sheets in the solar wind that form along discontinuities in the IMF, and when these features encounter the magnetosphere, they can result in large-scale motion of the magnetopause. For example, *Jacobsen et al.* [2009] presented an observational report of a HFA on 30 October 2007. For their event, the THEMIS constellation observed a very large magnetopause deformation in which the magnetopause moved outward by close to 5 R_E in just under one minute. They concluded that the magnetopause deformation was the result of a HFA formed upstream of the bow shock and observed by THEMIS-B. HFAs contain hot plasma (10^6 -10^7 K) in their central regions, which also have disturbed magnetic fields, ion flux enhancements in the keV energy range, significant dynamic pressure dropouts, and densities the same as or lower than that of the surrounding solar wind [*Schwartz et al.*, 1985; *Thomsen*

et al., 1986]. These disturbances move along the magnetopause as the IMF current sheet passes over the magnetosphere, and to a spacecraft near the magnetopause, the resulting observations can closely resemble a FTE. HFAs are also very similar to foreshock cavities, particularly in the way they are generated. However, HFAs and foreshock cavities differ in that HFAs result in large reductions or deflections of plasma flow velocities through the events, nearly isotropic and Maxwellian distributions through the events, and large ion temperature variations [*Thomsen et al.*, 1986; *Sibeck et al.*, 2002]. One critical condition for HFA formation is that the convection electric field on at least one side of the IMF discontinuity should be pointing toward the discontinuity to drive reflected ions into it [*Thomsen et al.*, 1993]. *Facsko et al.* [2008] conducted a statistical study of 33 HFAs, and they found much evidence supporting the previously recognized formation conditions required for HFAs. These formation conditions included: 1) a crater-like feature in the magnetic field strength with sharp edges compared to the non-perturbed solar wind on either side of it, 2) a drop in the solar wind speed with a velocity turned away from the Sun-Earth line, 3) an increase in temperature up to several 10's of millions of Kelvin, 4) a crater-like feature in the solar wind number density. However, they also proposed a new condition for HFAs, namely that fast solar wind is essential to HFA formation.

Transient Pressure Pulses in the Solar Wind: The magnetopause is the boundary where the magnetic pressure from Earth's magnetic field balances the dynamic pressure of the solar wind. Thus, variations in the solar wind dynamic pressure result in variations on the magnetopause. *Sibeck* [1990, 1992] and *Sibeck and Smith* [1992] discussed how the effects of a sudden solar wind dynamic pressure pulse could be mistaken for a crater FTE because the pressure pulses can cause disturbances along the magnetopause with draped magnetic fields (resulting in a bipolar B_N signature) and a total field strength enhancement on either side of a depression. Also, like magnetopause disturbances resulting from each of the other phenomena mentioned here, magnetopause disturbances generated by solar wind pressure pulses result in clear ionospheric signatures called magnetic impulse events [*Glassmeier*, 1992; *Sibeck et al.*, 2003], which are distinct variations in the magnetic field associated with traveling magnetospheric convection vortices and field-aligned

currents. Thus, FTEs, foreshock cavities, HFAs, and solar wind pressure pulses can all result in magnetopause deformations with many similar features as observed by space- and ground-based instrumentation.

C.2.2.2 Overview

In this paper, we present observations of an abnormally strong compression of the plasma density through the center of a large-scale magnetopause disturbance that occurred on 21 November 2008. We begin by discussing the data sets employed and observations of the event. Solar wind measurements at Earth are available for this event from THEMIS-B (TH-B), and the magnetopause disturbane itself is observed by three of the other THEMIS spacecraft, TH-A, -D, and -E, which are distributed along the dawn flank of the magnetopause at the time of the event. We present evidence against the feature being the result of a pressure pulse in the solar wind or a hot flow anomaly and show that the observations are most consistent with a foreshock cavity. Additionally, we find insufficient evidence to argue that a FTE is present. We provide an analysis of the various features associated with this magnetopause disturbance, including the plasma distributions of the fast flows around it and the pressure balance associated with the density compression.

Taking the available observational evidence into account, we conclude that the disturbance is most likely the result of a foreshock cavity, and we speculate on the reason for the intense density enhancement. We speculate that the intense density enhancement is most likely the result of an abnormally strong compression associated with the foreshock cavity, perhaps due to some enhanced compression in the magnetosheath along the magnetopause. However, this case also introduces an interesting scenario; namely, if the same feature in the IMF generates both a foreshock cavity and a FTE, how would the two features interact as they both evolve along the magnetopause? In the discussion, we pose this question as well as some other interesting ones that arise from this study. From the complex features presented in this observational report, we suggest that this event be further analyzed using reconstruction techniques and/or detailed global simulations, which should prove beneficial in addressing the interesting nature of this particular event and improving our

overall understanding of magnetopause disturbances.

C.2.3 Observations

Launched on 17 February 2007, the Time History of Events and Macroscale Interactions during Substorms (THEMIS) mission, consists of an extensive network of ground-based instruments and five small, identical spacecraft [*Angelopoulos*, 2008]. In 2008, these spacecraft were in a set of orbits with different altitudes at apogee ranging from 10 - 30 R_E, and throughout the year, these orbits allowed the spacecraft to sample a massive range of Earth's magnetosphere, magnetosheath, and the near-Earth solar wind. On 21 November 2008, the THEMIS constellation had apogees on Earth's dawn side. Figure C.1 shows the locations of the 5 THEMIS spacecraft at 17:20 UT, just before three of the probes observe a disturbance near the magnetopause. The intersection of the *Shue et al.* [1997] magnetopause, calculated using the TH-B solar wind conditions at 17:20 UT, with each plane is shown with the dashed lines. TH-A, -D, and -E are located around 08:00 MLT near the magnetopause, and they all observe the disturbance. As can be seen in Figure C.1, TH-A and -D straddle the magnetic equator close to the same distance in X_{GSM}, while TH-E is within 0.3 R_E of the magnetic equator and slightly further down-tail. TH-C is still in the inner magnetosphere and is not used in this study. Finally, TH-B is near the dawn-dusk meridian and well outside of the magnetopause.

Figure C.2 shows fluxgate magnetometer [*Auster et al.*, 2008] and electrostatic analyzer (ESA) [*McFadden et al.*, 2008] data from the three THEMIS spacecraft that observe the disturbance: TH-A, -D, and -E. Magnetic fields and velocities here show the magnitudes (black) and components (colors) in LMN coordinates, in which N is the magnetopause normal direction (positive outward), M lies in the equatorial plane, and L completes the right-handed coordinate system [*Russell and Elphic*, 1978]. Thus, on the dawn(dusk)-side, equatorial magnetopause, the M-direction has an antisunward (sunward) component, with the L-direction primarily in the expected direction of the field just inside the magnetosphere. The LMN components displayed in Figure C.2 are calculated based on a statistical magnetopause [i.e. *Shue et al.*, 1998]. The magnetopause disturbance in

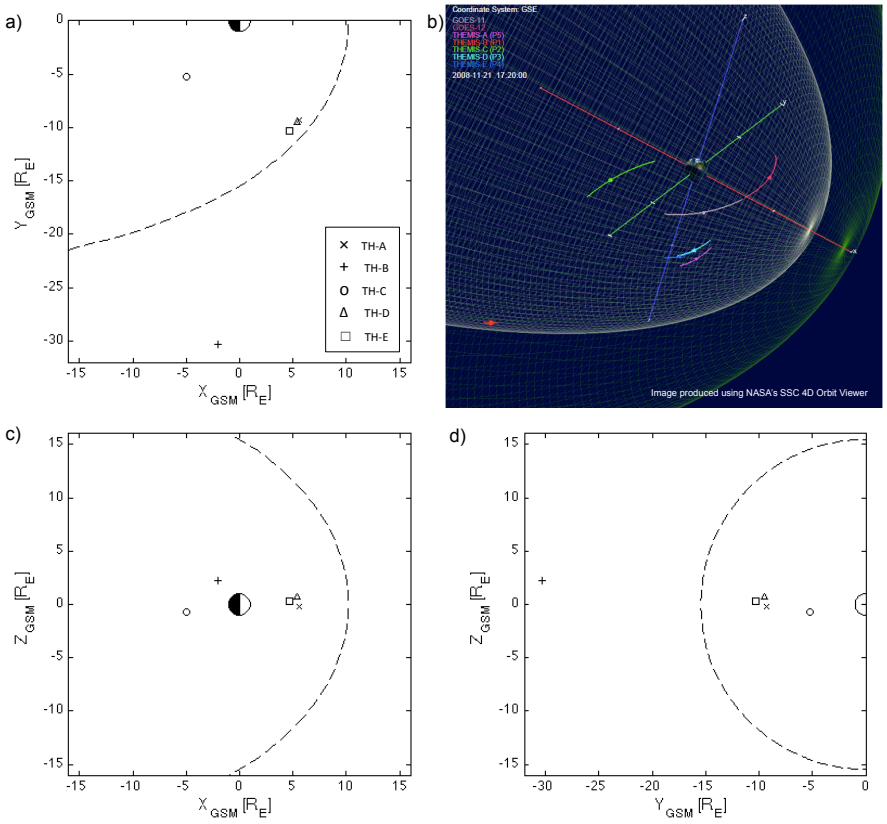

Figure C.1: a), c), and d) TH-A (×), -B (+), -C (·), -D (△), and -E (□) GSM locations at 17:20 UT with the *Shue et al.* [1997] magnetopause shown where it intersects each plane (dashed line). b) 3-D orbit view in GSE coordinates of the THEMIS and GOES spacecraft at 17:20 UT with orbital tracks for ± 2 hours. Model magnetopause and bow-shock are also shown as wireframes.

question here is first observed by TH-A and -D at around 17:20:55 and 17:21:05 UT respectively and then later by TH-E at 17:21:16 UT. In Figure C.2, the data from each of the three spacecraft is displayed in the columns from left to right. For each of the spacecraft in Figure C.2, the highest resolution data available are shown for 17:20 - 17:24 UT, when the disturbance is observed.

The effects of the event itself are clearly visible in Figure C.2 as the large disturbance in all of the data. Prior to the disturbance, conditions are calm and normal for the near-magnetopause magnetosphere. The magnetic field is primarily in the L-direction as observed by all three spacecraft, and the magnitude of the field ranges from ∼30 nT (TH-E) to ∼40 nT (TH-D), which also confirms that TH-E is closest and TH-D is farthest from the magnetopause. When the event is observed, TH-A and TH-D observe weaker B_L associated with an enhancement in B_M. TH-A observes a significant, double-peaked enhancement of plasma density up to ∼10 cm^{-3}, and TH-D observes significantly less change in the plasma density. The average ion and electron temperatures are inversely correlated with the densities. Both spacecraft also observe dropouts in the more energetic fluxes and enhancements of lower-energy fluxes for both ions and electrons. One of the clearest features in the TH-A and -D observations are the fast ion flows (in V_M and V_N) that flank the features of the main disturbance (i.e. those associated with the enhancements in B_M and low-energy flux). Similar flows are also seen in the electron velocities, though these are not shown in Figure C.2. Associated with these flows are lower-energy flux enhancements visible in the energy-time spectrograms, which we will discuss later in this paper and are referred to throughout as "wings" in the flux spectrums. TH-A observes a negative-to-positive turnover in V_N with a strong tripolar signature in V_M, revealing increased negative flows on either side of the disturbance and a strong positive V_M through the center of the encounter. V_L reveals an opposite tripolar signature to that of V_M. TH-D observes very similar features, though the total velocity associated with the center of the encounter is not as fast as that observed by TH-A. The maximum total velocities observed by TH-A and -D are just under 400 km/s, and the times these occur are indicated with the dashed vertical lines for all three spacecraft.

TH-E observes a longer encounter with the event and many of the features observed by

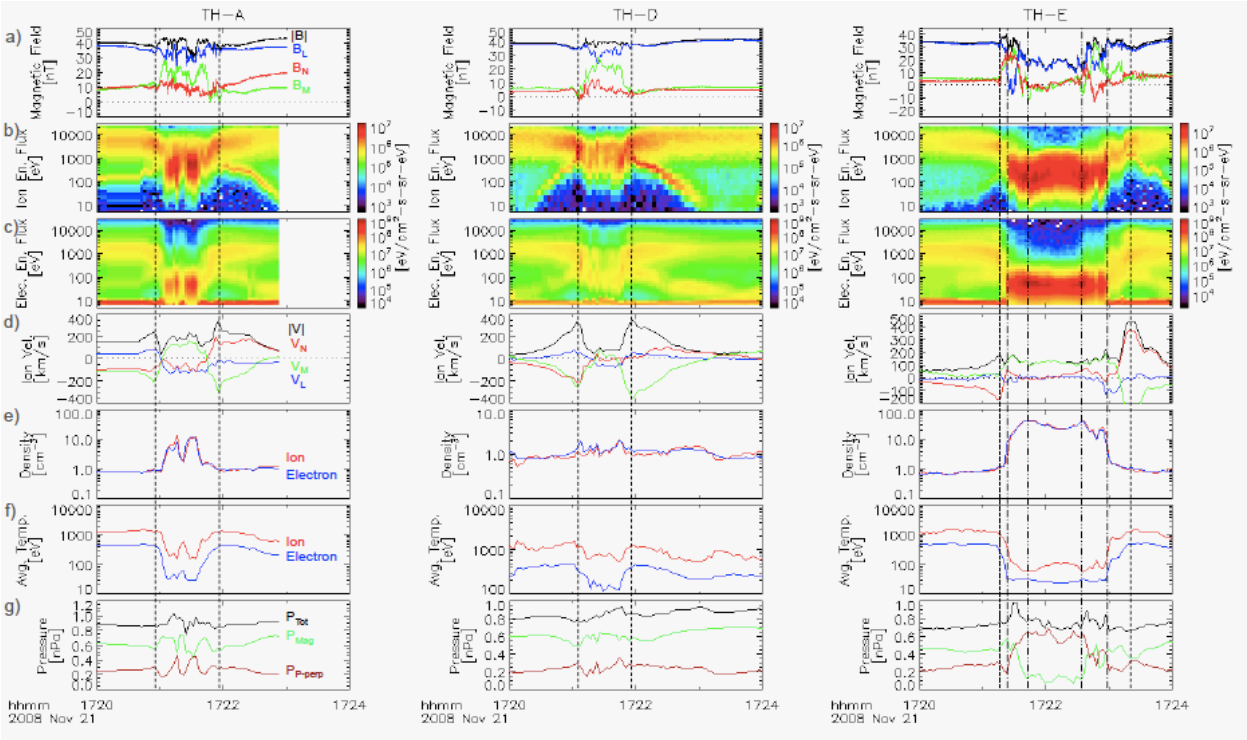

Figure C.2: TH-A, -D, and -E observations (columns 1-3 respectively). The rows of plots show a) the total magnetic field and the field components in LMN, b) and c) the ion and electron energy-time flux spectrograms, d) ion total velocity and components in LMN coordinates, e) and f) plasma density and average temperature, and g) calculated pressures. TH-A observations are cut short due to the end of burst-mode data. Various dashed vertical lines are used for reference and are described in the text.

this spacecraft are more extreme than those observed by TH-A and -D. During the main part of the disturbance, as seen in Figure C.2, TH-E observes crater-like features in total magnetic field strength, with a strong overall dropout through the center of the encounter and enhanced total strength and B_N signatures observed at the edges of this dropout. Strong positive B_M enhancements are also seen on either edge of the center of the encounter. Through the center of the encounter (i.e. the period occurring between the vertical dash-dot-dot lines), B_M and B_N undergo a clear negative-to-positive turnover, while B_L is the dominant component. The density enhancement observed by TH-E occurs within the times marked by the vertical dash-dot lines. This enhancement is very strong, going from normal magnetospheric levels of less than 1 cm^{-3} to a peak value of over 40 cm^{-3} through this portion of the encounter. A strong drop in ion temperature is also clearly visible through this portion of the encounter. The associated dropouts in the energetic ion and electron fluxes and enhancements in the low-energy fluxes are more clear than those observed by TH-A and -D, though the observations of the plasma "wings" on the flanks of the encounter are not as clear. Finally, the velocities observed by TH-E are faster upon exiting the disturbance than upon entering it, and the maximum velocity gets up to ~450 km/s.

Examining the data after the initial disturbance, there are some additional features that should be noted in the TH-E observations. Figure C.3 shows TH-E magnetic fields, ion quantities, and pressures for the 10-minute period from 17:20-17:30 UT. Note that after the disturbance is first observed, the magnetic field strength undergoes an overall enhancement followed by another dropout before returning to approximately its pre-event level just shortly after 17:28 UT. Associated with these magnetic field features are ion flux enhancements, including another feature that is similar to the "wings" seen before, enhanced velocities, and variations in the magnetic and plasma pressures. In the next section, we will analyze these particular features as well as those mentioned above from all three spacecraft to provide evidence concerning the underlying nature of this event.

Figure C.4 shows data from the magnetic field and plasma instruments on TH-B from 17:05 - 17:35 UT. From the strength and components (in GSM) of the magnetic field and the plasma energy fluxes and density, it is clear that TH-B is in the solar wind. Note here that the density plot

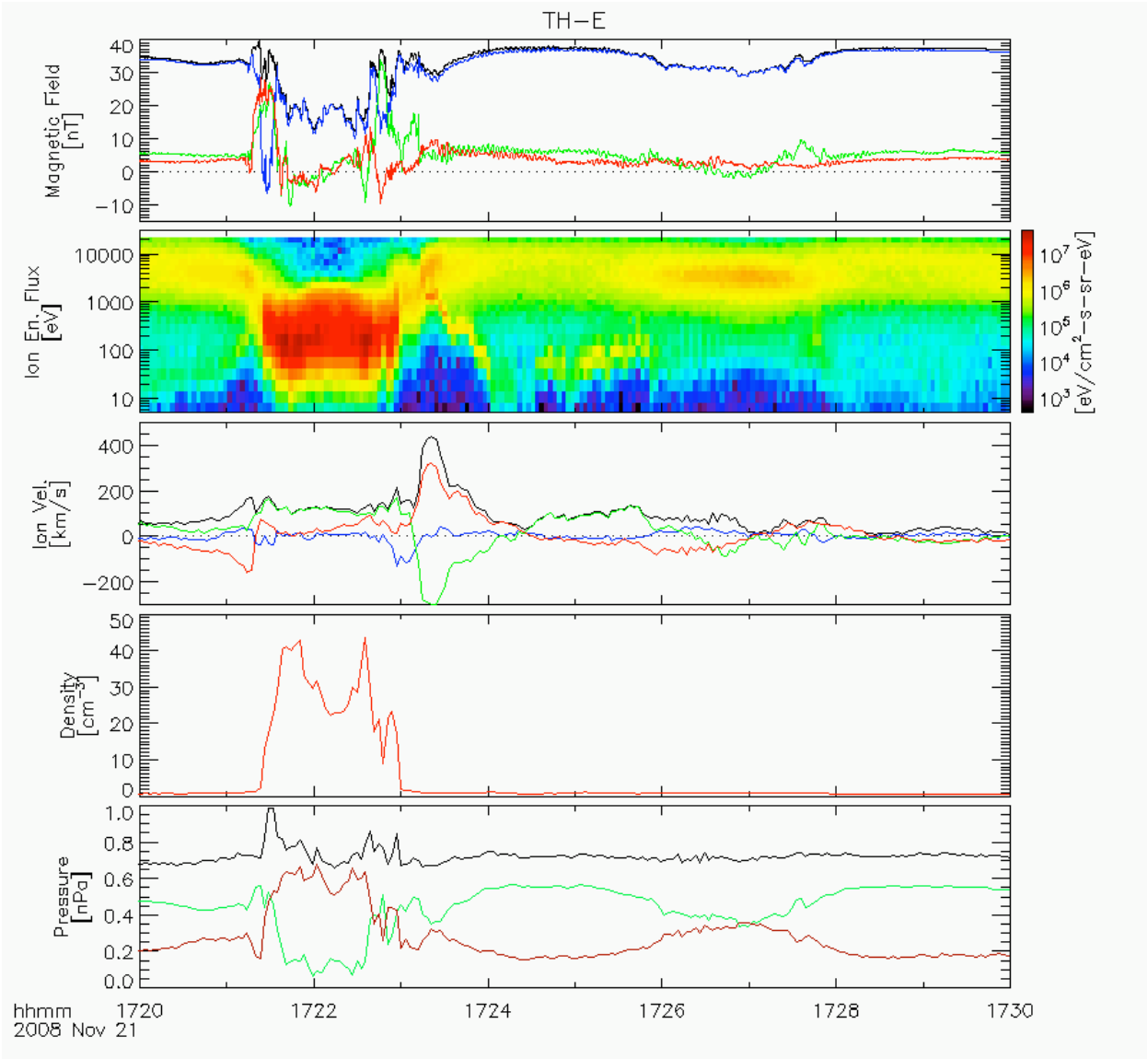

Figure C.3: TH-E observations from 17:20-17:30 UT. Magnetic field and velocity components are shown in LMN coordinates, and the line colors all correspond to those from Figure C.2. For the plasma quantities (i.e. ion energy fluxes, velocity, and density), reduced resolution data are shown. Note also that the density plot scale is linear, unlike in Figure C.2. The last row shows the total, magnetic, and perpendicular plasma pressures.

includes WIND-SWE ion densities (with times adjusted by 89 minutes from ballistic propagation to account for the offset from WIND being upstream in the solar wind) and that the TH-B ion density has been corrected based on the electron density since the ESA instrument was taking solar wind measurements while still in magnetosphere mode and cannot necessarily resolve the narrow solar wind beam. For this correction, the ion densities are simply multiplied by 1.62, which is the ratio of the average electron to ion densities during this 30-minute period. Under these conditions, the electron density is more accurate than that for the ions [see *McFadden et al.*, 2008]. It should also be noted that the magnitude of the ion temperature is unreliable, and the velocity directions (V_Y and V_Z) may be inaccurate (though the magnitude is accurate). Conditions are generally calm prior to the abrupt dawn-ward turning of the IMF B_Y at ~17:19:30 UT. This IMF turning apparently sets the appropriate conditions to put TH-B into the foreshock region from ~17:19:30 - 17:30:20 UT, when it observes suprathermal ions and depressed plasma density and dynamic pressure. Another IMF discontinuity at ~17:30 UT apparently changes the conditions such that TH-B is no longer in the foreshock. Upon exiting the foreshock region, TH-B observes crater-like features in the total field strength, density, and dynamic pressure from ~17:28-17:31 UT, before they return to levels observed earlier in the solar wind. Note also that the IMF B_Z is primarily southward prior to the discontinuity at ~17:30 UT.

C.2.4 Analysis and Interpretation

C.2.4.1 Event Classification

Solar Wind Pressure Pulse: WIND-SWE data are available at the time of this event (courtesy of R. Lin of UC-Berkeley and K. Ogilvie of NASA-GSFC and NASA's CDAWeb online database). They are consistent with the TH-B solar wind measurements and confirm that the solar wind density and velocity show no signs of a dynamic pressure pulse that would result in a significant compression of the magnetosphere. It should be noted here that we have greater confidence in the adjusted TH-B ion density measurements based on their good agreement with

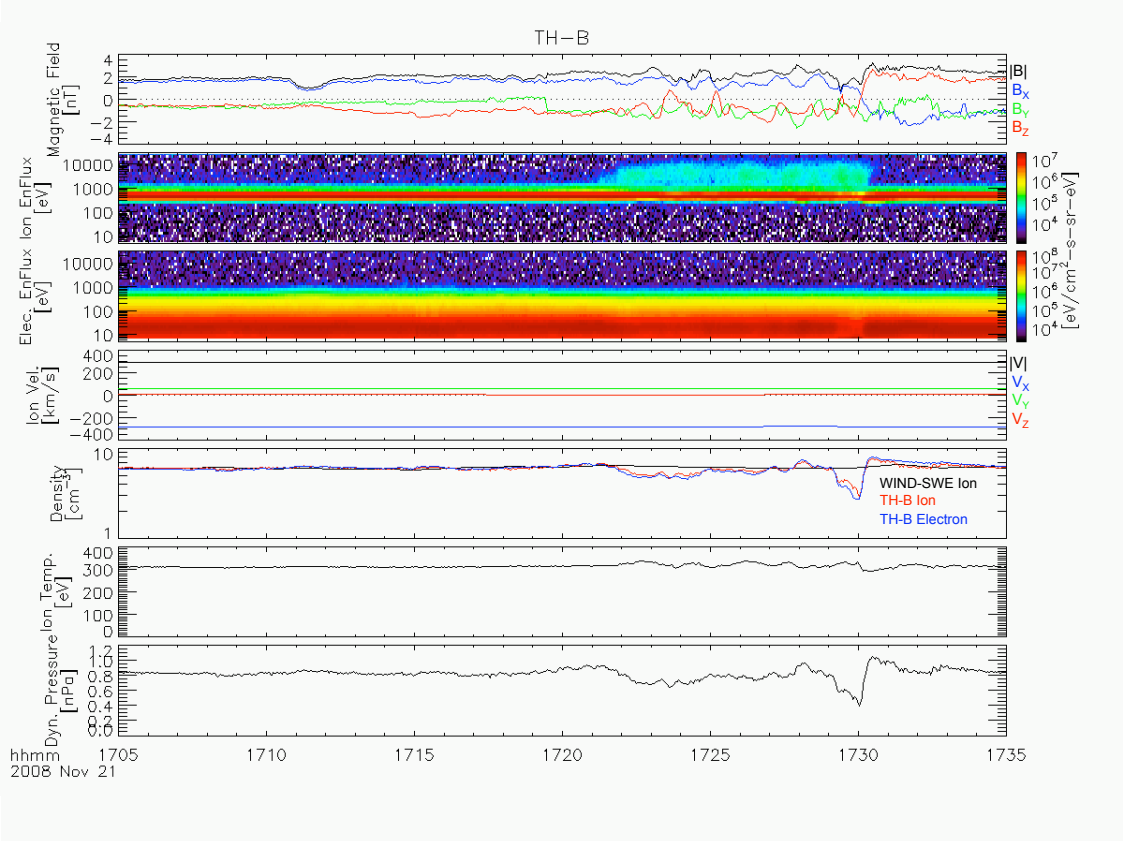

Figure C.4: TH-B observations: magnetic field and velocity components are in GSM with X_{GSM} in blue, Y_{GSM} in green, and Z_{GSM} in red, with the magnitude displayed in black. The plots from top to bottom correspond to the same parameters shown in rows a-e and g respectively from Figure C.2, except the bottom plot displays dynamic pressure only. WIND ion densities from the SWE instrument are also shown in black on the density plot.

the WIND ion densities as is shown in Figure C.4. Magnetic fields measured at geosynchronous orbit by the GOES-11 and -12 spacecraft (not shown; courtesy of H. Singer of NOAA-SWPC and NASA's CDAWeb) further confirm this, as they are both on the dayside at ∼09:00 and ∼13:00 MLT respectively and reveal no clear signs of a field compression at the time of the event. However, both GOES spacecraft do observe what appear to be ULF pulsations, which could result from magnetopause disturbances. Regardless, we already know there was a magnetopause disturbance from the THEMIS observations, and based on there being no evidence of a transient pressure pulse in the solar wind measured by either WIND or TH-B, we believe that this is likely not the cause of the event that occurred on 21 November 2008.

Hot Flow Anomaly: Based on the characteristics of HFAs, we can further establish that the event was not the result of a HFA. Starting around the same time that the disturbance is first observed by TH-A, -D, and -E, hotter ion fluxes are measured by TH-B in Figure C.4. These are likely diffuse back-streaming ions from the ion foreshock region [*Russell and Hoppe*, 1983] resulting from the IMF turning at ∼17:19:30 UT and TH-B being in the vicinity of the bow shock. The IMF-B_Y field discontinuity at ∼17:19:30 UT has no corresponding temperature spike, ion or electron flux enhancements, decrease in dynamic pressure, or change in the number density. However, the discontinuity occurring at ∼17:30 UT could have resulted in either a foreshock cavity or a HFA around the time that TH-A first observed the event given the correct orientation of the discontinuity. TH-B observes this second IMF discontinuity around 9 minutes after the magnetopause disturbance is first observed by TH-A. A minimum variance analysis (MVA) [e.g. *Sonnerup and Scheible*, 1998] using the TH-B data is employed to determine the orientation of the IMF discontinuity, which reveals a discontinuity normal direction with XYZ_{GSM} coordinates of (-0.7976, -0.2661, -0.5412) R_E. This seems appropriate as the fields measured by TH-B change mostly in the X and Z directions indicating a current with a strong Y-component.

Using the discontinuity normal direction calculated above from MVA and the $-\mathbf{V} \times \mathbf{B}$ electric field before and after the discontinuity (calculated with TH-B at 17:29:00 and 17:30:45 UT respectively), we find that the electric field after the discontinuity passes is indeed directed back

towards it, which is a necessary condition for HFA formation. However, as stated before, the velocity components (V_Y and V_Z) from TH-B at these times are not necessarily accurate. Also upon further analysis, there are several inconsistencies with previous works on HFAs, and a HFA does not explain all of the features observed in this event. First, there is no plasma temperature spike observed by TH-B associated with this feature. Though the magnitude of the TH-B temperature data may be inaccurate due to the instrument being in the wrong mode, TH-B still observes very little variation in the temperature during the event. A temperature spike should be apparent independent of a magnitude offset. Next, there is no significant change in the solar wind velocity direction in either the ground-derived data (shown in Figure C.4) or the spacecraft moment velocities (not shown here), which are available at higher time resolution. Also concerning the solar wind velocity, *Facsko et al.* [2008] found that fast solar wind speed is an essential condition for HFA formation. They found no HFAs for solar wind speeds less than 400 km/s, and for the event here, the solar wind speed is just under 300 km/s.

Foreshock Cavity: The features observed by TH-B are not consistent with a HFA, but they are consistent with a foreshock cavity. A foreshock cavity in the solar wind consists of a central region of depressed field strengths and plasma density flanked on either side by compressed regions with enhanced fields and density, which result in crater-like features in these quantities as observed by a spacecraft passing through them. TH-B is apparently in the foreshock from shortly after 17:21 UT until the IMF discontinuity at ~17:30 UT. Associated with this discontinuity are crater-like signatures in the total field strength, density, and dynamic pressure, which is highly consistent with previous observations of foreshock cavities [e.g. *Sibeck et al.*, 2002; *Schwartz et al.*, 2006; *Billingham et al.*, 2008]. Outside of the bow shock, the features associated with foreshock cavities diminish rapidly [*Sibeck et al.*, 2004]. However, the pressure changes associated with the different foreshock cavity regions can propagate through the magnetosheath and result in a disturbance along the magnetopause [*Sibeck et al.*, 2000].

Observing a passing foreshock cavity, a spacecraft inside the magnetosphere should measure opposite field signatures than those measured by spacecraft in the sheath or solar wind near the bow

shock. On either edge of such an event, a spacecraft in the magnetosphere near the magnetopause would observe field depressions as the enhanced densities in the sheath pushed the magnetopause closer to the spacecraft, while through the center, when the densities in the cavity itself are depressed in the sheath, the spacecraft would observe an enhancement in field strength as the magnetopause moved outward. From ∼17:21-17:28, this picture is consistent with what TH-E observes (refer to Fig. C.3) with the exception that apparently the magnetopause actually passes over TH-E from ∼17:21:30-17:23:00, leaving the spacecraft in the sheath during this period. TH-B observes a much shorter encounter. The crater-like features it observes are consistent with a foreshock cavity passing by in the solar wind near the bow shock, the features and duration of which would be diminished compared to an observation of the same event in the sheath.

Figure C.5 is a sketch displaying the scenario in which a foreshock cavity moves along the magnetopause with the IMF discontinuity. Assuming propagation at ∼205 km/s, which is the component of the solar wind speed along the discontinuity normal direction as calculated above, with a separation between TH-E and TH-B along this normal direction of -9.8 R_E, the discontinuity would take only around five minutes to travel from TH-E to TH-B. Next, if we assume that the foreshock cavity is approximately symmetric about the IMF current sheet, which is also consistent with a similar scenario presented in *Sibeck et al.* [2000], then we can approximate whether the timing in the observations is consistent with a foreshock cavity moving with the IMF discontinuity. TH-E encounters the center of the cavity shortly before 17:25 UT, corresponding to the local maximum in total field strength. Meanwhile, TH-B encounters the center of the cavity shortly before 17:30 UT, which is a difference of around 5 minutes. Thus, the IMF discontinuity could indeed be responsible for moving a foreshock cavity past TH-A, -D, and -E along the magnetopause.

If a foreshock cavity is the cause of the magnetopause disturbance observed by the three THEMIS spacecraft, then TH-E should simply pass into the magnetosheath as a result of the effect of the first compressed region. Indeed when TH-E passes into the disturbance itself (see the first dash-dot line in Fig. C.2), it does observe initially southward field that then turns abruptly northward with the L-component (corresponding well to Z_{GSM}) becoming dominant. This is qual-

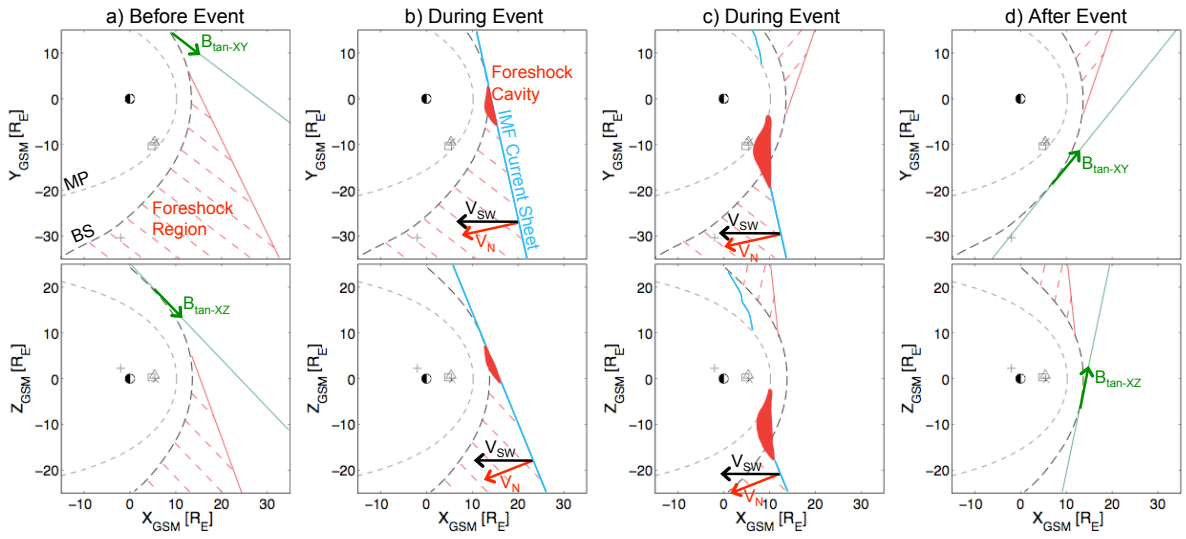

Figure C.5: Sketch depicting the passage of the current sheet in the IMF observed by TH-B at ~17:30 UT. Cross-sections in the XY and XZ GSM planes are shown for four different times: a) before the event is observed, with the pre-event tangential IMF shown and an estimated foreshock region; b) when the IMF discontinuity (blue line marked "IMF Current Sheet") first impacts the bow shock, possibly generating a foreshock cavity (red shaded region); c) around the time when the event is observed at TH-A, -D, and -E; and d) after the discontinuity has passed leaving behind it a new orientation of IMF and thus a different location of the foreshock region.

itatively similar to what TH-B observes in the IMF discontinuity at ∼17:30 UT. However, when these features are aligned based on the times when B_Z is minimum immediately prior to the positive turnover and their respective clock angles are compared in Figure C.6, the features observed by TH-E and TH-B are quantitatively quite different. In Figure C.6, TH-B data (top) has been shifted back by 8 minutes and 23 seconds to align and compare with the TH-E data. Here, the time axis is the UT measured by TH-E with observations starting at 17:21:27 UT. Thus, the aligned TH-B observations shown here were measured by TH-B starting at 17:29:50 UT. The TH-E data shown in the middle plot in Figure C.6 is in GSM with the same dash-dot-dot lines from Figure C.2 marking the center of the encounter. Analogous to the LMN fields shown in Figure C.2, B_Z here is dominant (like B_L in Fig. C.2), and there is a clear rotation in B_X and B_Y (like B_M and B_N). Note that the turnover time for the field to go from southward to northward is much longer for TH-B than for TH-E. The clock angles calculated from each of the spacecraft field measurements are shown in the bottom plot, and these confirm that the two fields do not quantitatively agree. The angles start off more than 60 degrees apart and eventually approach each other, but significant variations continue after they do become more aligned. Variations encountered in the magnetosheath may be the reason for the lack of agreement between the TH-E and TH-B fields if TH-E really did just enter into pure sheath plasma.

Flux Transfer Event: We will now compare the observations made by TH-A, -D, and -E to observations of crater FTEs from previous studies to show that the disturbance on 21 November 2008 has some features consistent with crater FTEs, though none that are definitive. All three spacecraft are near ∼08:00 MLT when they observe the disturbance (see Fig. C.1), and based on the statistical study of *Kawano and Russell* [1997], the solar wind conditions measured by TH-B meet the criteria (i.e. $|B_Y| < 4.505$ nT and an FTE showing dawnward motion) for which the majority of FTEs are observed between 06:00 and 12:00 MLT. Additionally, based on the simulations of *Sibeck and Lin* [2010], for these solar wind conditions, an FTE observation along the dayside, dawn flank is not unexpected considering the weakly negative IMF B_Y and weakly southward IMF B_Z. As observed by TH-E, it is clear from the magnetic field data in Figure C.2

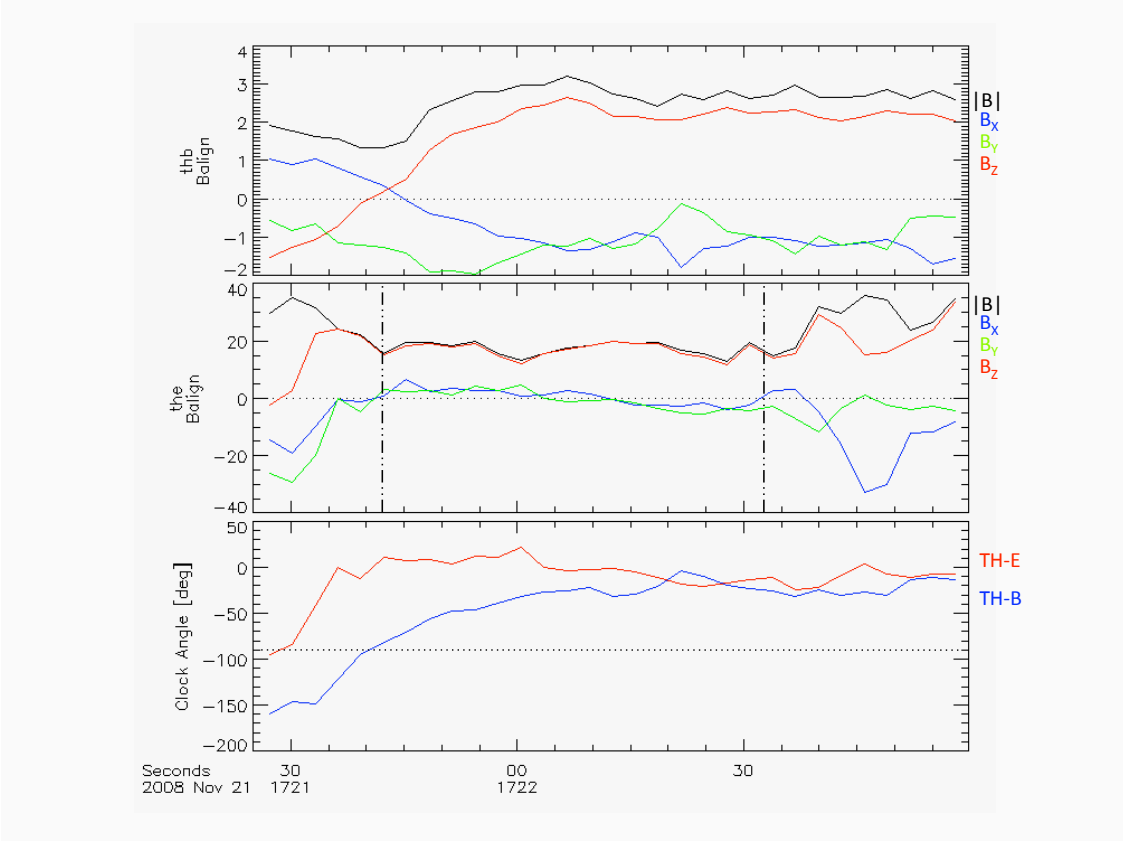

Figure C.6: Top: TH-B magnetic field in GSM with the time aligned to TH-E. The TH-B observed initial time for this aligned period is actually 17:29:50 UT. Middle: TH-E magnetic field in GSM starting at 17:21:27 UT. The times here correspond to the observed TH-E times. Bottom: Clock angles for TH-B and TH-E magnetic fields in GSM; 0 degrees is northward. The dashed line at -90 degrees delineates between northward (clock angles >-90 deg as shown here) and southward (clock angles <-90 deg as shown here) fields.

that the total field strength drops significantly through the center of the encounter but is slightly enhanced at the edges, which is the defining feature of crater FTEs. However, foreshock cavities have very similar magnetic field signatures. Additionally, the N-component of the magnetic field undergoes several turnovers, and over the full encounter, there is no clear bipolar feature that is typically used for identifying FTEs.

From the flux spectrograms in Figure C.2, TH-A and -E (and TH-D to a lesser extent) observe dropouts in the energetic magnetospheric electrons through the center of their encounters with the initial disturbance, which indicates that the spacecraft have moved onto open field lines. This, however, would also be the case for the spacecraft simply moving into the sheath. The plasma flow bursts of several hundreds of km/s seen in the energy-time flux spectrograms and velocity plots in Figure C.2 are consistent with the magnetospheric flows around FTEs discussed in *Korotova et al.* [2009], yet as discussed below, these should be typical features of any transient event on the magnetopause. Additionally, field-aligned electrons are observed by TH-E on the edges of the initial disturbance (discussed further below), which are indicators of reconnection along the magnetopause and can indicate a separatrix layer around FTEs [e.g. *Owen et al.*, 2008]. This evidence of reconnection is consistent with the southward IMF, but it is not clear evidence of a FTE being present as these field-aligned electrons would result from any reconnection, whether it be steady, which should not result in a FTE, or time-varying, which could result in a FTE.

Finally, we can estimate a minimum scale size of the disturbance in the direction of its velocity (i.e. primarily in the +M direction) by taking into account the spacecraft separations at a time when all three spacecraft observe the event simultaneously. At 17:21:30 UT, all three spacecraft observe the event, with TH-A and -D near the end of their encounters and TH-E at the beginning of its encounter. At this time, 0.890 R_E separates TH-A and -D, 1.114 R_E separates TH-A and -E, and 0.799 R_E separates TH-D and -E. This reveals that the scale size of this cross-section of the disturbance is $\sim$1 R_E, which is also consistent with previous studies of FTEs [e.g. *Hasegawa et al.*, 2006; *Lui et al.*, 2008] though not definitive.

C.2.4.2 Fast Plasma Flows

Concerning the plasma flow bursts, *Korotova et al.* [2009] completed a detailed study of FTE velocities and plasma flows around FTEs. As with many of the other features associated with magnetopause disturbances, the flows around disturbances generated by different types of transient events should be similar. The findings of *Korotova et al.* [2009] for the plasma flows observed around FTEs are indeed consistent with the TH-A, -D, and -E observations discussed here. *Korotova et al.* [2009] describe the flow signatures of an entry into the core of an FTE from a direct impact as a bipolar V_N signature associated with a monopolar V_L or V_M. TH-E observes these features upon encountering the initial magnetopause disturbance on 21 Nov. 2008: V_N displays a bipolar signature at the same time as a strong increase in V_M, which stays positive until after TH-E exits the disturbance and observes the fast flows around it (more explanation of this is in the Discussion section). This strong, positive V_M encountered through the core of the disturbance is likely from the plasma moving through or with the event itself. Note that both TH-A and TH-E observe these fast, positive V_M flows ($V_M >\sim 100$ km/s) through most of the center of their respective encounters, but TH-D observes the same only very briefly.

Korotova et al. [2009] also discussed the flow signatures that spacecraft taking a glancing impact by an FTE (or other transient feature along the magnetopause) should observe; these include a bipolar signature in V_N and a tripolar signature in V_L or V_M. TH-A and TH-D observe just this, both observing a bipolar V_N throughout the full encounter accompanied by a very clear tripolar signature in V_M. These fast plasma flows are evidence of the plasma being forcefully diverted around the disturbance and are also visible in the flux enhancements associated with the "wings" on either side of the disturbance in rows b) and c) of Figure C.2. Note too that all three spacecraft observe positive V_L signatures on the flanks of the disturbance. This indicates that the event is also moving in a slightly southward direction along the magnetopause. The negative V_L signatures observed by all three spacecraft in the disturbance itself further support this.

From Figure C.2, the ion fluxes associated with these fast plasma flows are enhanced when

compared to the fluxes at the same energies before and after the disturbance passes, and for the low-energy population, the magnitude of this enhancement and the energy at which it occurs are both correlated with the magnitude of the velocity of the flow. This is attributed to the cold plasma being heated as it is compressed ahead of and accelerated around the passing magnetopause disturbance. These "wings" are simply signatures of the magnetopause motion [e.g. *Sauvaud et al.*, 2001]. The $-\mathbf{V} \times \mathbf{B}$ electric field associated with the maximum velocity (as observed by TH-D) is calculated as 13.7 mV/m and is primarily in the negative N-direction (the statistical magnetopause LMN components at 17:21:55 UT are: [1.4, -0.2, -13.6] mV/m). Similar "wing" features are also evident in the electron distributions (see Fig. C.2), though they are less prominent than their ion counterparts.

When pitch angle distributions are examined for the fast ion flows, they are not field-aligned, which is further proof that they are indeed plasma being displaced around the disturbance. Figure C.7 shows the pitch angle flux spectrograms for TH-A, -D, and -E. Figure C.7a is compiled of ion and electron fluxes from energy ranges corresponding to the cold plasma "wings", while Figure 7b is the same format but for energy ranges corresponding to the hot magnetospheric plasma. Using Figure 7a, we see that the lower-energy ions are perpendicular to the field and likely associated with plasma being displaced around the disturbance as it passes by the spacecraft. However, it is significantly different for the electrons featured here, which are field-aligned and bidirectional both just before and after each spacecraft encounters the disturbance. From Figure C.7a, note that the peak fluxes of these field-aligned electrons are closest to the crossing boundary itself (i.e. between the white-dashed lines indicating the peaks in ion velocity, which are magnetospheric flows, and the disturbance itself, which has the highest low-energy ion and electron fluxes associated with it), and this is consistent with the idea that these are electrons residing along a separatrix-layer that are remnants of some previous magnetic reconnection or ongoing reconnection along the boundary. From Figure C.7b, it is apparent that there are also peaks in the higher energy fluxes corresponding to the peak ion velocities, and these peak fluxes consist of both electrons and ions with local pitch angles nearly perpendicular to the field. These too are magnetospheric plasma being diverted

around the disturbance, but the pitch angle distributions for these higher energies are more spread out than for the lower energy plasma populations.

C.2.4.3 Density Enhancement

Finally, we look at the density enhancement through the center of the magnetopause disturbance. TH-E observes the most significant density enhancement, which reaches a peak level of over 44 cm^{-3}. This is a factor of greater than 7× the near-Earth solar wind density as measured by TH-B (∼6 cm^{-3}) and the upstream solar wind measured by WIND. In the magnetosheath, a density enhancement of 4× is expected across the subsolar bow shock based on the Rankine-Hugoniot jump conditions. However, TH-E is not near the subsolar bow shock, and according to the *Spreiter et al.* [1966] model, the sheath density near the magnetopause at ∼08:00 LT should only be a factor of 2 to 3 times higher than that of the solar wind. The agreement between the TH-B ion densities corrected to the electron density when compared to those measured by WIND (see Fig. C.4) provides additional confidence in the accuracy of the solar wind density magnitude. Thus, the event on 21 November 2008 reveals a compression of plasma density that, to our knowledge, has not yet been reported.

The peaks in the ion density observed by TH-E occur around the start and stop times of the B_M and B_N bipolar signature observed through the middle of the encounter (see period between the dash-dot-dot lines in Figs. C.2 and C.6). These maxima also roughly mark the start and stop times of the depression in the crater-like B_{Tot} observations. They occur just after the first peak in total pressure and just before the second peak is observed (the peaks in total pressure occur between the dash-dot and dash-dot-dot lines on either side of the disturbance in Fig. C.2). These peak locations are interesting in that they imply that there is a confined region of compressed plasma along some boundary of the disturbance itself. We speculate on this more in the Discussion section. The density through the very center of TH-E's encounter actually dips to just over 20 cm^{-3}. Thus, the density here also shows a crater-like feature, though it does not align with the magnetic field crater signature.

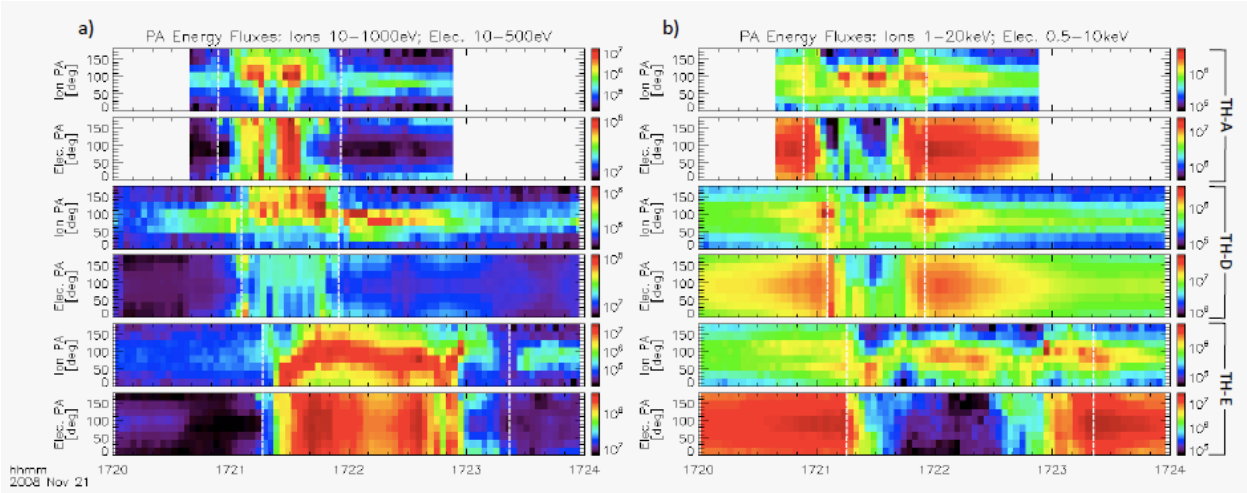

Figure C.7: a) Pitch angle flux spectrograms for ions ranging from 10-1000 eV and electrons ranging from 10-500 eV, representing the lower-energy "wings." b) Same as a) but for ions ranging from 1-20 keV and electrons ranging from 0.5-10 keV, representing the background magnetospheric plasma. For both a) and b), fluxes (units of eV/cm^2-s-sr-eV) are shown in color, and TH-A, -D, and -E results are shown from the top to the bottom with ion spectrograms appearing first and those for electrons appearing immediately below for each spacecraft. White dashed lines correspond to the times when the peak ion velocities (see Fig. C.2) are observed by each spacecraft both before and after the main disturbance is encountered. Note: the color scales for all plots are different here so as not to lose any information.

Concerning the peaks in total pressure, row g) of Figure C.2 shows the magnetic (green) and perpendicular thermal (red) pressures as well as their sum (black) through the event. Particularly evident in the TH-E data, the perpendicular thermal pressure becomes significantly stronger than the magnetic pressure through the core of the disturbance. Note that at either edge of their encounters with the disturbance, TH-A and -E, observe local maxima in total pressure. These total pressure increases are consistent with the spacecraft moving through the low-latitude boundary layer (LLBL), which should be bunched up in a boundary layer around the magnetopause disturbance and was shown to have an excess of total pressure corresponding to a peak in magnetic pressure in [*Phan and Paschmann*, 1996]. The thermal pressure dominating over magnetic pressure through the core is consistent with TH-E going into sheath-like plasma. Note too that the total pressure through the center of the disturbance observed by TH-E is not enhanced overall. The magnetic tension of the draped fields around the disturbance, the evidence of which is particularly clear in the B_M enhancements observed by all three spacecraft, must also be recognized when considering the pressure balance through the event.

C.2.5 Discussion

Based on the observations, we believe that TH-A and -D take glancing impacts from the disturbance, while TH-E takes a direct impact and penetrates into the core of it. TH-D probably does not encounter the event as closely as TH-A does based on the results from the pressure balance and the lack of a density enhancement. TH-A and -D encounter the disturbance first, and around 0.9 R_E down tail from TH-A, TH-E is the last to encounter it. TH-E makes clear measurements of the crater-type nature of this disturbance as well as the internal field structure and abnormal density enhancement in its core. After the initial disturbance, TH-E observes an overall enhancement followed by another depression in the total magnetic field strength. When the details of these observations are more closely examined, the large magnetopause disturbance observed by TH-A, -D, and -E on 21 November 2008 presents an intriguing scenario.

The IMF discontinuity observed by TH-B at 17:30 UT could have resulted in a foreshock

cavity, which is depicted in Figure C.5 and explains many of the features observed by the three THEMIS spacecraft along the magnetopause. During the period from ∼17:19 to ∼17:30 UT, the IMF orientation is consistent with TH-B being located in the foreshock region. Indeed, TH-B observes hot ions that are characteristic of the foreshock from ∼17:21 to ∼17:30 UT, when the IMF discontinuity occurs. As TH-B moves through the foreshock boundary, it observes crater-like features in the total field strength, plasma density, and dynamic pressure, which are all characteristic features of foreshock cavities. Given the results of a minimum variance analysis on the IMF discontinuity, the solar wind velocity, and our current understanding of foreshock cavities, the effects of a foreshock cavity moving with the discontinuity could have been observed by TH-A, -D, and -E starting shortly before 17:21 UT. Ground magnetometer observations from the THEMIS network of stations reveal some very clear magnetic impulse events (MIEs). These signatures (not shown here; see Inuvik and Bettles stations for clear examples) have been used previously to identify magnetopause motion resulting from pressure variations in the sheath [e.g. *Sibeck et al.*, 1989]. However, *Glassmeier* [1992] pointed out that MIEs could occur for any type of magnetopause motion.

Concerning the observations of the initial disturbance at the magnetopause, Figure C.8 is a simple picture of the disturbance that explains many of the features observed by TH-A, -D, and -E during their encounters from 17:20-17:24 UT. Figure C.8 shows a cartoon depicting a cross-section of the scenario in the M-N plane, and it can be used as a visual reference for the following discussion on what TH-A, -D, and -E observed as they each encountered different parts of this disturbance. Starting with TH-D (triangle) in Figure C.8, the spacecraft observes the clearest plasma flow signatures (dashed blue lines in Fig. C.8) and apparently just barely penetrates into the boundary layer between the magnetosphere and the disturbance (shaded gray region). This picture explains why it observes the strong negative V_M and V_N flows initially as the magnetospheric plasma is being redirected around the disturbance. The weak positive V_M flows through the center are representative of the plasma flow of the event itself (being in the +M-direction) and are slow since TH-D is still near the magnetopause. When TH-D re-enters the magnetosphere, it again encounters the negative V_M magnetospheric flows, which have a weaker, though slightly positive N-component

on the trailing side of the disturbance. The lack of a density enhancement through the middle of the encounter is explained by TH-D never really leaving the magnetopause boundary layer. The magnetic fields around the event must also be distorted to have stronger M and N components, which TH-D also observes and is consistent with the TH-A and -E observations when they are also in this boundary layer.

TH-A (symbol x in Fig. C.8) makes similar observations to TH-D though apparently skirts closer to the edge of the disturbance. Based on the picture in Figure C.8, TH-A starts to encounter the disturbance with observations of the displaced plasma flows, with their strong negative V_M and V_N components consistent with plasma being redirected around the incoming feature. Next, it enters into the boundary layer between purely magnetospheric field and the field in the disturbance itself. We propose that TH-A never fully enters into the disturbance since it doesn't observe a reversal in the B_M and B_N components like TH-E, though it probably gets close based on the similarity to the TH-E total velocity, density, temperature, and pressure observations in Figure C.2. Upon exiting the boundary layer, TH-A once again observes the fast plasma flows around the disturbance, though now they are in the positive V_N and negative V_M directions.

The picture in Figure C.8 is also useful in explaining many of the features observed by TH-E (square) between 17:20 and 17:24. As the spacecraft begins to encounter the magnetopause disturbance, it observes fast plasma flows that are primarily in the negative N-direction due to its closer proximity to the magnetopause and, thus, more perpendicular angle of incidence. Also just as it starts to encounter the disturbance, TH-E observes a positive V_L in the magnetospheric flows indicating that the event is moving with a slight negative V_L component. Upon entering the boundary layer, TH-E observes the distorted magnetospheric and sheath fields, with enhanced M- and N-components and a significantly weak L-component. In Figure C.2, TH-E would be passing through this boundary layer during the periods between the dash-dot and dash-dot-dot lines. Going fully through the boundary layer, the spacecraft sees a reversal in the M- component of the field, which is indicative of entering a new region of plasma. In the boundary region, V_L turns negative, but through the core of the event (i.e. the period between the two dash-dot-dot lines in Fig. C.2),

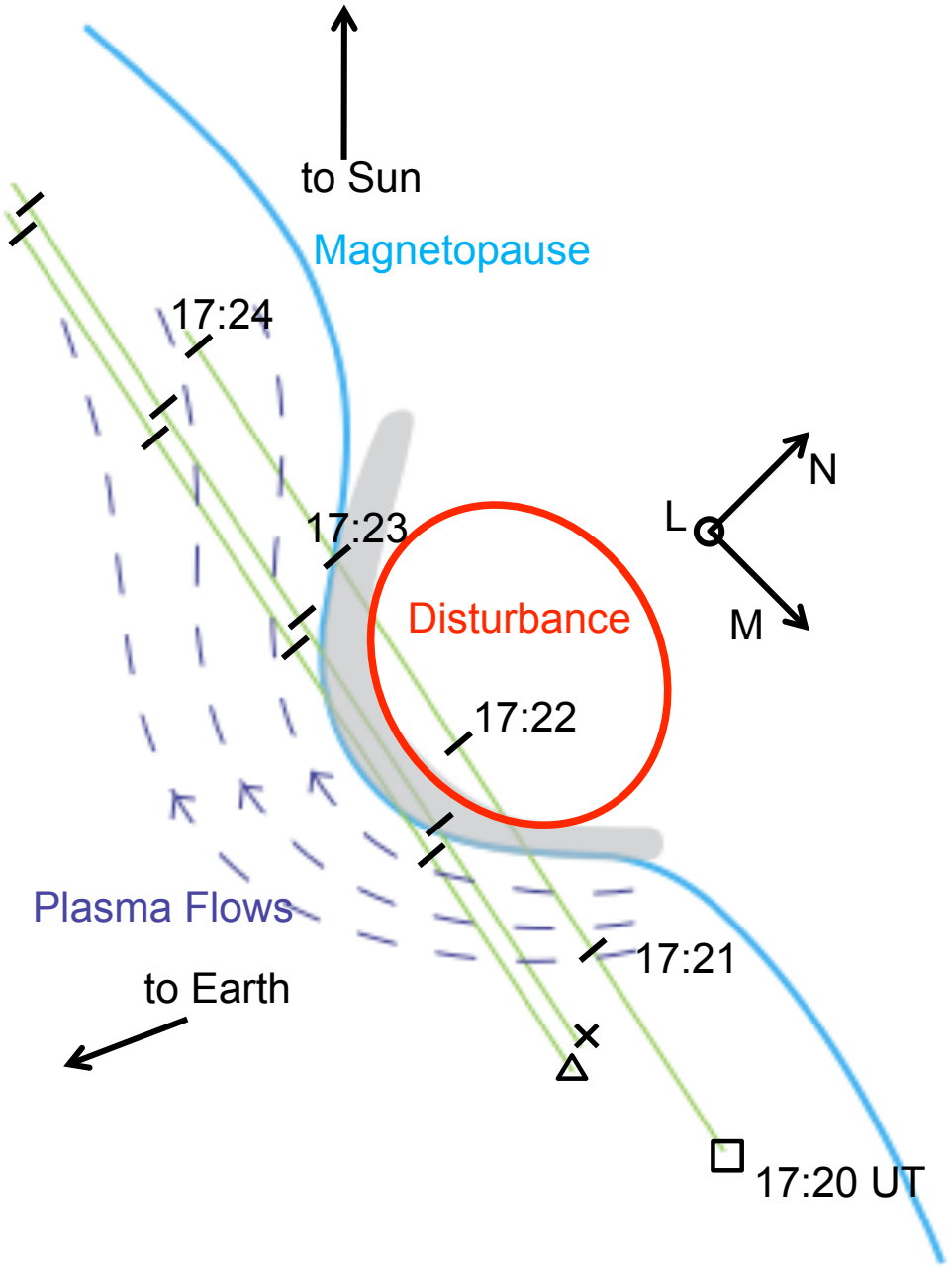

Figure C.8: Cartoon depicting a cross-section of the scenario in the M-N plane and moving with the event. TH-A (×), -D (△), and -E (□) are shown at 17:20 UT with the same symbols as used for them as in Figure C.1. Their estimated tracks through the event are shown with green lines and each minute after 17:20 UT is marked with black bars and labeled along TH-E's track. The magnetopause boundary is shown with light blue and a representation of the disturbance's cross-section is shown with red. The shaded gray region represents the boundary region between the magnetopause and the disturbance. The dark blue dashed lines and corresponding arrows denote plasma streamlines and flow directions respectively.

V_L is very weak and slightly positive. Also, it is at the transition between the boundary and core regions, as indicated by the dash-dot-dot lines in Figure C.2, that TH-E observes the abnormally strong peaks in the plasma density. Through the core region, TH-E observes a slow turning over of the M- and N- components of the field, which is further evidence of a complex internal structure. Upon exiting the disturbance again through the boundary layer and into purely magnetospheric field, TH-E observes the draped magnetospheric fields with their positive B_M and negative B_N components. The fields and velocities measured by TH-E through its encounter indicate a complex structure with several different plasma regions indicated by the various dashed lines in the TH-E observations in Figure C.2. After TH-E has passed through the event shortly after 17:23 UT, it again encounters the fast plasma flows being diverted around the disturbance, and these flows display a positive V_N and negative V_M, which remains consistent with the picture in Figure C.8.

The simplest explanation for this event is that the current sheet in the solar wind swept a foreshock cavity past the four THEMIS spacecraft used in this study. Indeed, the crater-like features observed by TH-B and the observations by TH-E from ~17:21-17:28 are consistent with both theory [*Thomas and Brecht*, 1988] and observations [e.g. *Sibeck et al.*, 2002] of foreshock cavities. TH-B observes a shorter and less intense encounter with the event, which is consistent with its location in the solar wind outside of the bow shock. In the magnetosheath, this foreshock cavity is apparently asymmetric concerning the intensity of its compressed edges. From TH-E, the initial compression region is encountered from ~17:21-17:24. During this part of the event, the magnetopause is moved inwards over TH-A, -D, and -E, and TH-E apparently penetrates through into the compressed region itself, which exhibits the intense enhancement in plasma density. The cavity region, which results in the magnetopause moving back radially outwards, is encountered by TH-E from ~17:24-17:26, and the trailing compression region is apparently encountered from ~27:26-17:28. This second compression region does not result in any of the three magnetospheric THEMIS spacecraft from entering into the sheath. Additionally, the southward and tail-ward motion of the event as observed by TH-A, -D, and -E is consistent with how a foreshock cavity moving with the current sheet would move along the magnetopause.

Based on the TH-E observations of the extreme density enhancement associated with this event, we speculate that this could result from the combined factors of the enhanced density in the magnetosheath itself along with the enhanced densities at the edges of a foreshock cavity. Furthermore, it seems as though the enhanced plasma density associated with the foreshock cavity is bunched up against the LLBL, with its enhanced total pressure and distorted magnetic fields. This might further magnify the enhancement. If this is indeed the case, it introduces some interesting questions. Does the LLBL truly play a role in the enhancement? How strong can such an enhancement get?

It has already been recognized that foreshock cavities can set off reconnection on the magnetopause [see discussion in *Sibeck et al.*, 2002], and there is evidence of reconnection for the event in question, namely the southward IMF B_Z and field-aligned electrons observed along the event boundary. However, there is no definitive evidence to show that the event was the result of a FTE. There is no clear bipolar B_N signature observed by TH-A, -D, or -E, and reconnection prior to the event observation may have been steady, which would not have resulted in a FTE. For these reasons, we propose that the disturbance is most likely the result of a foreshock cavity generated by the IMF discontinuity. However, it is of interest here to discuss how just such a discontinuity could also potentially result in the generation of a FTE by way of a varying reconnection rate that creates a magnetic bubble containing a flux-rope [e.g. *Southwood et al.*, 1988]. In fact, *Jacob and Cattell* [1993] showed that exactly this type of IMF feature, i.e. a sudden southward to northward turning of B_Z, may be important to the generation of some FTEs. Two of the FTEs described in *Jacob and Cattell* [1993] were accompanied by variations in the solar wind density, magnetic field, and pressure, which they attributed to foreshock effects. Such a scenario presents an interesting question: if two different transient magnetopause events (i.e. a foreshock cavity and a FTE) are generated by the same solar wind feature, then how do these features interact? Essentially, how would each feature evolve in order to reach pressure balance between the coiled fields (i.e. magnetic tension), plasma pressure, and magnetic pressure associated with each? Could these interactions result in an abnormal density enhancement like that observed by TH-E? If this were not the case,

as it seems for the 21 Nov. 2008 event, then what about this particular foreshock cavity resulted in such a strong density enhancement along the magnetopause? The most direct way to address the questions presented here is with detailed numerical simulations [e.g. *Omidi and Sibeck*, 2007] and reconstruction efforts [e.g. *Hasegawa et al.*, 2006], using spacecraft observations for input and validation.

C.2.6 Conclusions

The magnetopause disturbance observed by three of the THEMIS spacecraft on 21 November 2008 presents a complex yet interesting case with several clear and detailed features. In this observational report, we have presented the evidence and propose that the most likely cause of this event is a foreshock cavity associated with a discontinuity in the IMF. We have gone into detail analyzing the fast plasma flows encountered around the initial disturbance, and we find that the fast ion flows are mostly perpendicular to the field and are the result of plasma being displaced around the disturbance itself as it moves along the magnetopause. This is consistent with the work of *Korotova et al.* [2009], yet here we have also analyzed the pitch angle flux spectrograms associated with these flows. The "wing" signatures in the ion flux distributions are simply evidence of the magnetopause motion. The low-energy electrons associated with the highest-speed electron flows are field-aligned, unlike their ion counterparts, and are consistent with separatrix-layer electrons that are associated with a reconnection neutral line.

In addition to these fast plasma flows and clear "wings" in the plasma flux distributions, the initial disturbance displays an abnormal compression of plasma density throughout its central core up to 44 cm^{-3}, which is more than 7× the density of the near-Earth solar wind and is significantly higher than the factor of 4 expected in the subsolar magnetosheath from the Rankine-Hugoniot jump conditions across the bow shock. This type of density enhancement has been presented previously in global MHD and hybrid simulations of FTEs but, to our knowledge, has not been reported previously with in-situ observations of magnetopause disturbances resulting from either foreshock cavities or FTEs. We conclude that this enhancement is most likely an extreme density

enhancement associated solely with a foreshock cavity, perhaps resulting from a combination of compression effects in the magnetosheath. An interesting, though less likely, alternative scenario is that the density enhancement results from some complex interaction between a FTE and foreshock cavity both generated by the same IMF feature. In either case, the density enhancement and the detailed and asymmetric features associated with this foreshock cavity event are intriguing, and we propose that these THEMIS observations on 21 November 2008 should prove useful for detailed reconstruction and simulations, both of which may prove to be particularly beneficial to our understanding of magnetopause disturbances and the complex nature of solar wind - magnetosphere interactions.

Appendix D

Additional Details from the Forecast Studies

D.1 Additional Details Concerning Statistical Asynchronous Regression

D.1.1 Comparing SAR Mapping Results Using Different CCDF Libraries

When I first started working with mapping fluxes around GEO using SAR, I investigated the effects of compiling CCDF libraries using different solar wind parameters and bin sizes. I compiled CCDF libraries for solar wind speed using 10 different bin sizes, IMF B_z, dynamic pressure, number density, and a combination of solar wind speed and B_z. Based on the PEs and LCs from the resulting mapped fluxes for the year 2000, I found that the most effective parameters were B_z north vs. south, solar wind speed, and the combination of these two. Figure D.1 shows the results from using four of these libraries. Note that all four perform similarly and have similar features concerning performance vs. local hour. Their maximum PEs are all around dawn and fall between 0.84 and 0.86. Any of these libraries can be used with the SAR mapping tool that has been developed to work with the forecast models. For simplicity, I only use the solar wind speed binned by ± 25 km/s for the paper in Chapter 7. Based on their comparable performances, I think any of the libraries shown here would perform adequately for the SAR mapping.

D.1.2 Determining which Solar Wind Forecast to use for SAR

To determine whether to use the Wang-Sheely-Arge forecast or simple persistence to estimate "tomorrow's" solar wind velocity for SAR mapping, I compared the results of such mapping for

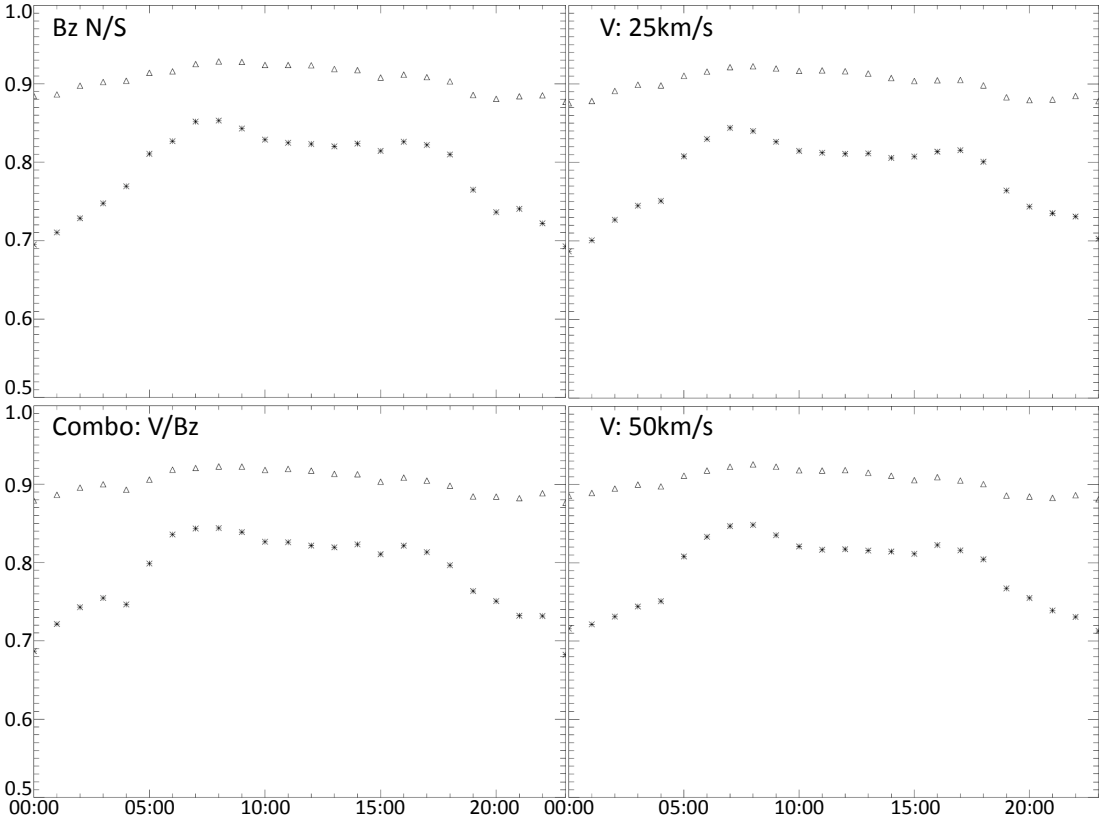

Figure D.1: Comparing results from SAR mapping using different CCDF libraries. Shown are PE (*'s) and LC (triangles) on the Y-axes for all 24 local hours around GEO on the X-axis. The four plots are for CCDF libraries compiled using IMF Bz north or south (Bz N/S), solar wind speed for two different bin sizes, 25 km/s and 50 km/s, and a combined library using both IMF Bz and solar wind speed.

different periods in the solar cycle. Figure D.2 shows the results for 2007-2008. I compare the results from WSA and persistence to a "cheating" model that uses "tomorrow's" actual solar wind measurement, since this is possible using historical data. From this study, I determined that simple persistence yields consistently higher PEs for fluxes mapped to all local times compared to those using the WSA model. This is consistent throughout the solar cycle. Note that I conducted this study before the STEREO-B study. Based on the results from that study (discussed in the first part of Chapter 7, it would ideally be best to use solar wind speeds from a spacecraft ahead of Earth in the Parker spiral. However, I have not performed the analysis to determine the limit on how far ahead a spacecraft can be before simple persistence with today's measurement is more effective.

D.2 Results from the Combined Forecast Model

Figures D.3 and D.4 show the results from the combined forecast model run for the first half of 2003 and 2009. PEs are shown for all of the input models, and it is clear that this combination model significantly improves the forecast results during the more active 2003 period. During the inactive 2009 period, the combination model performs just as well as the best individual model (i.e. the internal source model). These clearly show the benefits of the weighted combination model.

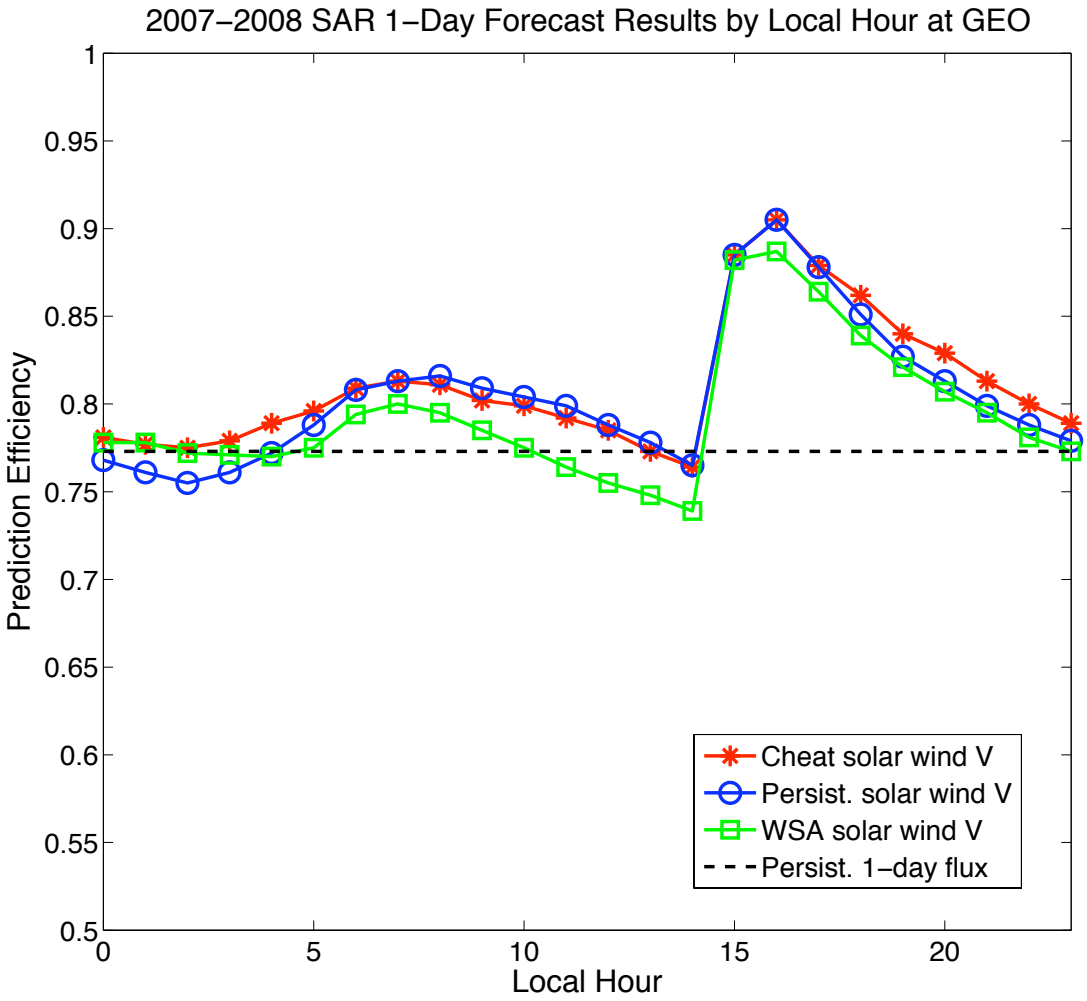

Figure D.2: Results from SAR run for 2007-2008 with three different solar wind "forecasts": the Wang-Sheeley-Arge (WSA) model, simple persistence, and a cheating model that uses the actual value. Fluxes are forecast using the *Li* [2004] model for 1600 LT, and the daily averaged persistence PE is also shown with the dashed black line.

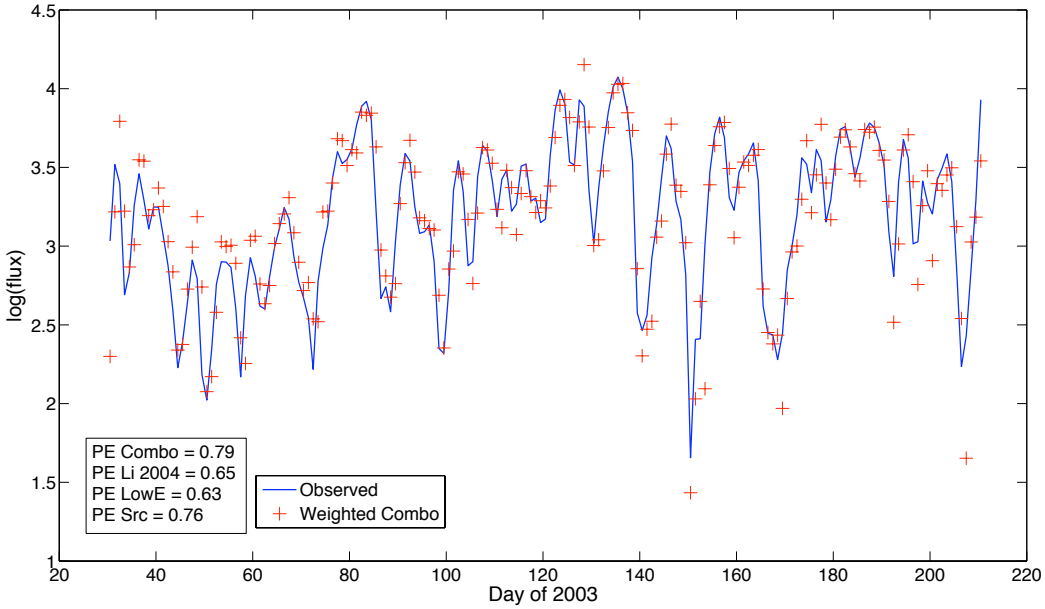

Figure D.3: Combined forecast results (red +'s) for the first half of 2003. PEs for each model are shown with the legend.

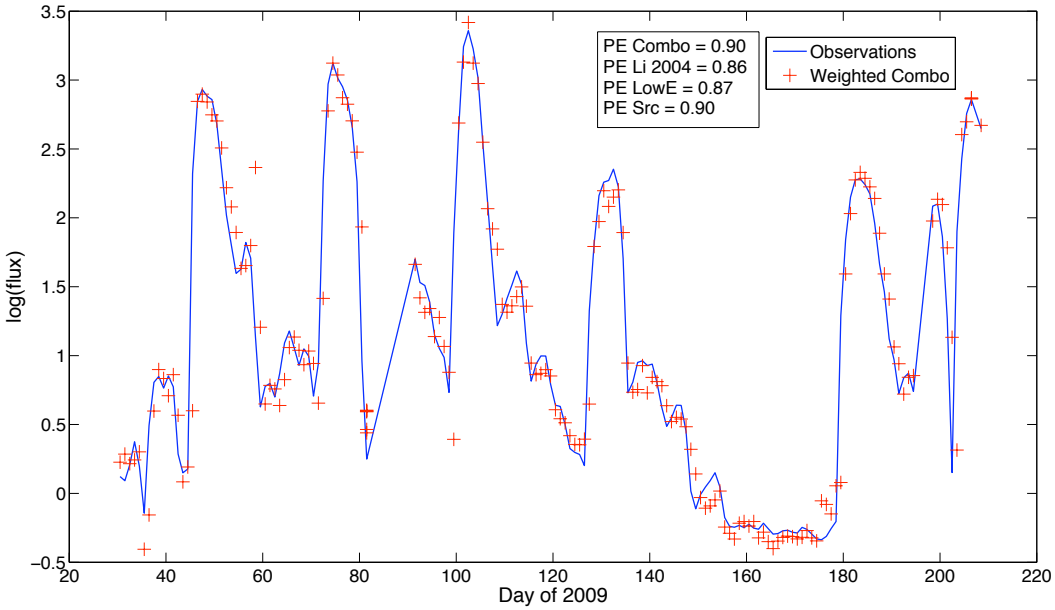

Figure D.4: Combined forecast results (red +'s) for the first half of 2009. PEs for each model are shown with the legend.